Università degli studi Roma Tre

Department of Mathematics and Physics
Ph.D. Program in Physics – XXXIII cycle

Mapping the circumnuclear matter in obscured active galactic nuclei via X-ray spectroscopy and polarimetry

A dissertation submitted in partial fulfillment
of the requirements for the degree of
Doctor of Philosophy

Author:
Dr. Alessandra Zaino

Advisor:
Prof. Giorgio Matt

Coordinator of the Doctoral Program:
Prof. Giuseppe Degrassi

December 2020

“Twenty years from now you will be more disappointed
by the things you didn’t do than by the ones you did do.
So throw off the bowlines.
Sail away from the safe harbor.
Catch the trade winds in your sails.
Explore. Dream. Discover.”

(H. Jackson Brown Jr.)

Acknowledgements

Giunti alla fine di questo percorso sarebbero tante le persone da ringraziare, troppe per poter essere contenute in poche righe. Vi ringrazierò personalmente quando ci incontreremo di nuovo. In quest'ultimo anno ci siamo dovuti inventare un modo diverso di vivere, ma l'importante è non perdere mai la speranza e la voglia di costruire insieme un mondo migliore, facendo tesoro di tutte le difficoltà affrontate.

Non posso però esimermi dal citare alcune persone. Rivolgo il mio grazie in primis al mio relatore Giorgio Matt, che ha guidato il mio lavoro in questi tre anni e senza il quale questa tesi non sarebbe stata possibile. Inoltre, è doveroso da parte mia ringraziare anche Stefano Bianchi per la pazienza che ha sempre dimostrato nel risolvere i miei dubbi e per la gentilezza con cui mi ha sempre dato consigli utili a migliorare il mio modo di fare ricerca. Grazie a entrambi per avermi dato la possibilità di sfruttare tante opportunità di crescita, di entrare in una collaborazione internazionale e di portare il mio lavoro fino nell'emisfero australe. Grazie anche ad Andrea Marinucci per l'aiuto fornito in numerose occasioni e per il fondamentale ruolo che ha avuto all'inizio di questo mio percorso.

Un ringraziamento speciale è poi rivolto alla mia famiglia, senza la quale non sarei diventata la persona che sono. Come tutti ho pregi e difetti, ma se i difetti sono colpa mia, le qualità sono certamente merito dell'educazione e dell'amore che ho ricevuto. Un ringraziamento speciale lo voglio rivolgere anche ai miei nonni che sono certa siano fieri di me anche lassù e felici per il raggiungimento di questo nuovo traguardo.

Grazie a Cristian Vignali per essersi sempre interessato al mio lavoro, anche dopo il mio trasferimento a Roma. Grazie a Paola, Roberto e Lucia che, seppur lontani fisicamente, sono sempre stati presenti nella mia vita con affetto e simpatia.

Grazie ai tanti amici, dottorandi e non, incontrati in questi anni. In particolare, voglio ringraziare Federica, che ha allietato tante mie giornate, così come io spero di avere fatto con lei, e Riccardo, con cui ho condiviso tante esperienze, lavorative e di svago. Non posso poi dimenticare Davide, amico prezioso e sempre disponibile; sono certa che l'amicizia che ci lega oggi possa continuare a lungo, sorretta da una sincera stima reciproca.

Infine, grazie a chi ha fatto parte della mia vita anche solo per un momento perché, come diceva Gandhi: "Ogni persona che incontri è migliore di te in qualcosa; in quella cosa impara".

Part of this work has been presented at the following conferences:

- **AGN and Polarimetry Conference: Towards a panchromatic understanding of the polarization of Active Galactic Nuclei**
  Virtual Conference, Strasbourg, December 1-11th, 2020
  Ref: https://polagn.astro.unistra.fr/style/Abstract_booklet.pdf, p.17

- **EAS 2020: European Astronomical Society Annual Meeting**
  Virtual Conference, Leiden, June 29th - July 3rd, 2020
  Ref: https://eas.kuoni-congress.info/2020/programme/abstract/333

- **X-ray Astronomy 2019: Current Challenges and New Frontiers in the Next Decades**
  Bologna, September 8-13th, 2019
  Ref: https://indico.ict.inaf.it/event/720/contributions/5647

- **From the Dolomites to the event horizon: sledging down the black hole potential well**
  Sexten (BZ), July 1-5th, 2019

- **IXPE meeting: one day of discussion on astrophysics**
  Roma, May 30th, 2019

- **TORUS 2018: The many faces of AGN obscuration**
  Puerto Varas, December 10-14th, 2018
  Ref: https://www.torus2018.org/TALKS/18.12.11-S4.4-Zaino.pdf

- **1st IXPE Science Collaboration Meeting**
  Roma, November 7-8th, 2018

- **AGN 13: Beauty and the Beast**
  Milano, October 9-12th, 2018
  Ref.: https://ui.adsabs.harvard.edu/abs/2018agn..confE..43Z/abstract

- **FERO 9: Finding Extreme Relativistic Objects**
  Heraklion, May 23-25th, 2018
  Ref.: http://fero9.physics.uoc.gr/AZaino.pdf

Summary

According to the most widely accepted paradigm, active galactic nuclei (AGN) are powered by accretion of matter onto supermassive black holes (SMBHs) located in galactic centers (Lynden-Bell 1969), which is the only viable explanation to their high bolometric luminosities, ranging from 10^{41} to 10^{48} erg s^{-1} and able to outshine the emission of the host galaxy.

The AGN emission extends over the whole electromagnetic spectrum from γ-ray to radio wavelengths. The complexity of the AGN spectral energy distribution (SED) is due to the different physical processes taking place in regions at various distances from the central BH, each of which dominates at different wavelengths. Typically four main components are observed: i) the Big Blue bump, representing the emission in the optical-UV band coming from the accretion disk; ii) the Compton-hump, due to the interaction of the optical and UV radiation with the hot corona; iii) the infrared bump, due to the thermal emission of dust around the nuclear region; iv) the synchrotron radio emission, which may be more or less significant (leading to the division between radio-quiet and radio-loud AGN, respectively). Although most of the AGN radiation is emitted in the optical and UV bands, X-rays are actually the most suitable energy range to study the structure and the physical properties of AGN because they minimize the host galaxy contribution allowing to directly observe the nuclear region of these objects.

The origin of the X-ray emission is ascribed to thermal Comptonization processes in the corona, a hot optically thin region above a cooler accretion disk (Haardt & Maraschi 1991), through which the UV disk photons gain energy by the inverse Compton process. This mechanism can explain both the observed power-law shape of the primary continuum and its high-energy cut-off (Rybicki & Lightman 1979).

In the first approximation, the emission of the hot corona can be assumed isotropic; therefore, any cold, optically-thick matter close to the accreting black hole, such as the accretion disk, the broad line region (BLR) or the torus, can intercept and reprocess some fraction of the primary continuum emission, thereby imprinting atomic features into the observed spectrum. This process of "X-ray reflection" primarily gives rise to the iron fluorescence line at 6.4 keV and to a broad reflection bump, the so-called Compton hump, peaking at $\sim$30 keV (George & Fabian 1991; Matt et al. 1991; Reynolds 1998).

Nowadays, it is well known that most AGN are "obscured" in the X-rays (e.g. Matt 2002a; Bianchi et al. 2012 and references therein; Ramos Almeida & Ricci 2017) and their observed spectrum depends on the column density N_H of the neutral gas intercepted along the line of sight. In particular, AGN are classified as "Compton-thick" if $N_H \geq 1.5 \times 10^{24}$ cm^{-2}, and "Compton-thin" if the column density is smaller but still in excess with respect to the Galactic absorption (Matt et al. 2003).

One of the most consolidated properties of AGN is their variability observed across all the electromagnetic spectrum. In particular, the X-ray flux exhibits variability on time-scales shorter than any other energy band, indicating that this emission originates from a small region very close to the SMBH. Moreover, as explained above, a large fraction of AGN are obscured and part at least of their observed X-ray variability is thought to be due to the variations of the circumnuclear medium surrounding the central engine (e.g. Risaliti et al. 2002; Yang et al. 2016). According to the most popular AGN unification model (Antonucci 1993; Netzer 2015), this obscuring medium is optically thick, composed of dust and gas and arranged in an axisymmetric dusty structure with luminosity dependent dimensions of 0.1-10 pc (i.e. the "torus"). However, although X-ray studies have confirmed, to first order, the widely accepted unified scheme, the location, geometry and physical state of the absorbing material are still widely debated (Bianchi et al. 2012).

In particular, the observation of short timescale variations (∼days or even ∼hours) in the absorption column density in several nearby bright sources, such as NGC 1365 (Risaliti et al. 2005; Rivers et al. 2015a), NGC 4151 (Puccetti et al. 2007), NGC 4388 (Elvis et al. 2004) and NGC 7582 (Bianchi et al. 2009; Rivers et al. 2015b), implies that the obscuring medium has a clumpy geometry, consisting of a series of discrete clouds likely at sub-pc scales. Although the density of this absorbing matter likely increases towards the equatorial plane (e.g. Nenkova et al. 2008a and 2008b), these variations are at odds with the classical torus geometry, which invokes a smooth distribution of dust and gas in a uniform toroidal structure (Pier & Krolik 1992 and 1993; Fritz et al. 2006).

Therefore, despite AGN are the most energetic long-lived objects in the Universe and are thought to play a fundamental role in galaxy evolution, surprisingly little is known about the physical processes acting in these objects on parsec and sub-parsec scales. Thus, a study of the X-ray variability from a spectroscopic point of view, such as the one at the basis of this thesis work, is of paramount importance to probe the extreme physical processes acting in the innermost regions of these sources and to better understand the relationship between the AGN and the host galaxy. Indeed, connecting the active galactic nucleus with its host galaxy, the circumnuclear matter is not only responsible for feeding the black hole, but it can also provide crucial information on the feedback that nuclear activity produces on the galaxy. Looking at the structure and kinematics of the material surrounding the accreting SMBHs is thus of paramount importance to directly probe the AGN-host galaxy connection (Ramos Almeida & Ricci 2017).

On the other hand, different information on the nature and geometry of the circumnuclear matter in AGN can be obtained from future X-ray polarimetry missions, such as the *Imaging X-ray Polarimeter Explorer* (*IXPE* – Weisskopf et al. 2016a and 2016b), scheduled to be launched at the end of 2021. Expected to deliver outstanding science, *IXPE* will detect linear polarization from several astronomical sources belonging to different classes, giving new insights on their emission mechanism and geometry. In particular, since the X-ray emission in Compton-thick AGN is dominated by reflection from the circumnuclear matter in the 2-8 keV working band of the polarimeters on board this mission, a high polarization degree, dependent on the inclination and level of symmetry of the matter, is expected, with the polarization angle related to the symmetry axis. A comparison of such an axis to those of the spatially resolved inner tori and of the ionization cone will shed further light on the structure of the circumnuclear matter in heavily obscured AGN.

This thesis work is structured as follows.

- **Chapter 1** consists in an overview on AGN, where their structure, classification and unification model are discussed.
- **Chapter 2** focuses on the X-ray emission of AGN. The various components of their complex X-ray spectrum are presented in detail. The importance of obscured sources and the role of the X-ray variability are also discussed.
- **Chapter 3** is dedicated to the current X-ray observatories, giving an overview of the satellites whose data are analyzed in this thesis: *NuSTAR*, *Swift*, *XMM-Newton*, *Suzaku* and *Chandra*.
- **Chapter 4** focuses on the X-ray spectral analysis of the Compton thick Seyfert 2 galaxy NGC 1068, based on a *NuSTAR* monitoring performed in 2017-2018. The detection of one unveiling and one eclipsing event due to Compton-thick matter located in the innermost part of the torus or even further inward provides further evidence of the clumpy structure of the circumnuclear matter in this source. Furthermore, the detection of a new flaring ULX at a distance of about 2 kpc from the nuclear region of NGC 1068 is also discussed.
- **Chapter 5** focuses on the X-ray spectral analysis of the Compton thin Seyfert 2 galaxy NGC 4507, based on a *NuSTAR* monitoring performed in 2015. Regarding the physical properties of the circumnuclear matter, the *NuSTAR* findings are also compared to the previous configuration observed with *Suzaku* in 2007.
- **Chapter 6** is dedicated to a short introduction on X-ray polarimetry and to the *IXPE* mission that will shed light on polarimetry in the X-rays after more than 40 years.
- **Chapter 7** focuses on the expected polarimetric X-ray view of the brightest Compton-thick AGN in the sky, i.e. the Circinus Galaxy. The future planned *IXPE* observation is discussed together with the best observational strategy needed to disentangle the contribution of the AGN to the polarization signal from the one due to contamination from other X-ray sources within the field of view.
- **Chapter 8** is devoted to the conclusions drawn by the analyses discussed throughout this thesis work.

Contents

List of Figures

List of Tables

1
Active galactic nuclei

Contents

The term "Active Galactic Nucleus" (AGN) refers to the existence of highly energetic phenomena within the central regions of galaxies that cannot be attributed clearly and directly to stellar processes (Peterson 1997).

From an observational point of view an object can be classified as AGN if it shows at least one of the following properties (Netzer 1990):

- a compact nuclear region, much brighter than the nucleus of galaxies of the same morphological classification;
- non-thermal continuum nuclear emission;
- nuclear emission lines indicating excitation by a non-thermal continuum;
- continuum and/or emission lines variability.

A short introduction on AGN is proposed in §1.1, with a particular attention on both the accretion mechanism and the overall emission of these sources. Then, §1.2 and §1.3 are devoted to illustrate the several components that constitute an AGN and the different classes to which these sources can belong, respectively. Finally, the unification scheme is summarized in §1.4. It is worth to note that, since the whole thesis work is focused on the analysis of radio-quiet sources, this class of AGN will receive the most attention throughout the first two chapters.

1.1 Introduction to active galaxies

According to a widely accepted paradigm, AGN are powered by accretion of matter onto supermassive black holes (SMBHs) located in galactic centers (Lynden-Bell 1969), which is the only viable explanation to their high bolometric luminosities, ranging from 10^{41} to 10^{48} erg s^{-1} and able to outshine the emission of the host galaxy.

The overall AGN emission extends over several orders of magnitude in frequency, from radio to γ-rays, giving origin to the so-called "triple hump" (Figure 1.1), since it often peaks in the UV, but significant luminosity is revealed also in the X-ray and infrared bands. It is spatially unresolved except in the radio band, where some evidences of collimated outflows at relativistic speeds are sometimes observed. The complexity of the AGN spectral energy distribution (SED) is due to the different physical processes taking place in regions at various distances from the central black hole, each of which dominates at different wavelengths. Typically, four main components are observed:

- the Big Blue bump, representing the emission in the optical-UV band coming from the accretion disk (see §1.2.2);

- the infrared bump, due to the thermal emission of dust around the nuclear region (see §1.2.5);

- the Compton-hump, due to the interaction of the optical and UV radiation with the hot corona. A detailed analysis of this part of the spectrum is discussed in Chapter 2;

- the radio emission, due to synchrotron mechanism. It may be negligible or contribute substantially to the overall AGN emission leading to the radio-quiet and radio-loud dichotomy (see §1.3).

1.2 AGN structure

The typical structure of an AGN is shown in Figure 1.2.

In the following, I will discuss the main components constituting an AGN, namely the supermassive black hole (§1.2.1), the accretion disk (§1.2.2), the hot corona (§1.2.3), the broad line region (BLR – §1.2.4), the molecular torus (§1.2.5), the narrow line region (NLR – §1.2.6), and the relativistic jet (§1.2.7).

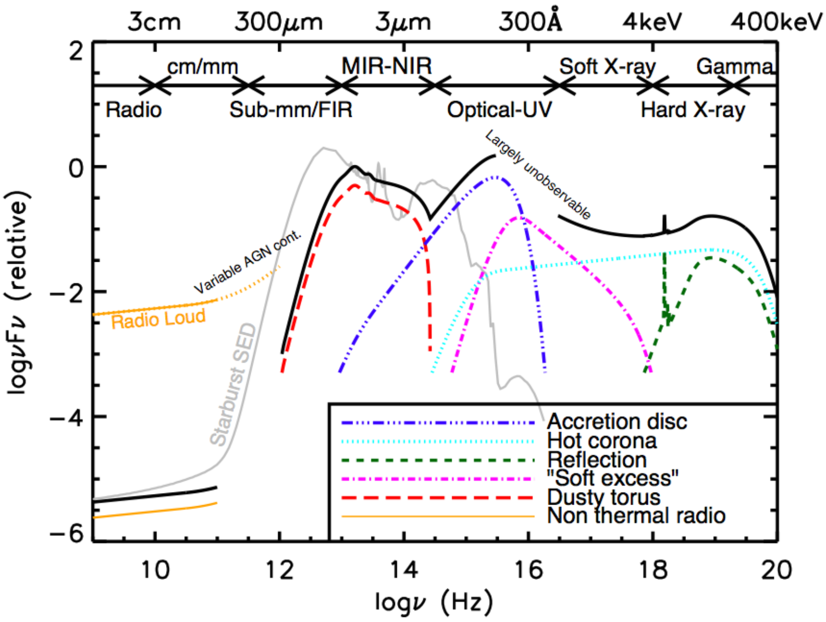

Figure 1.1. Schematic representation of the spectral energy distribution (SED) of an AGN (Harrison 2014). The solid black line reproduces the overall AGN emission, while the colored lines represent the main physical components. For comparison purposes, also the SED of a star-forming galaxy is shown (gray curve).

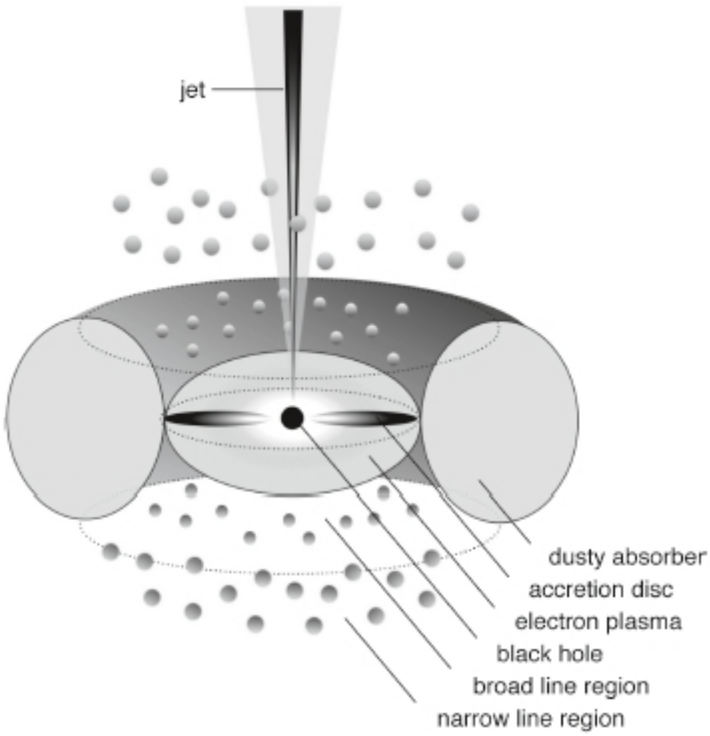

Figure 1.2. Schematic representation (not in scale) of the typical structure of AGN. Adapted from Beckmann & Shrader (2012).

1.2.1 The supermassive black hole

The presence of SMBHs in the center of AGN was firstly predicted by Lynden-Bell (1969) and later confirmed by several experimental evidences, such as variability measurements, orbital velocities, the $M-\sigma$ relation or the reverberation mapping technique.

According to the General Relativity theory formulated by Einstein in 1916, a black hole is completely described by three quantities: the mass M, the charge Q, and the angular momentum J. In astrophysics, black holes are assumed to be electrically neutral, so $Q=0$ and, thus, they can be described by only two quantities (Maio et al. 2003). The SMBH masses span from $\sim 10^6\ M_\odot$ up to $10^{10}\ M_\odot$ (e.g. Marconi et al. 2009), while the angular momentum is described by the adimensional quantity "spin", which is defined as $a = Jc/GM_{BH}^2$, where c is the speed of light, G the gravitational constant, and M_{BH} the mass of the compact object. The spin can assume any value from $|a|=0$ to $|a|=1$, representing the former a non-spinning BH, while the latter describes a maximum rotating BH, with positive and negative spins indicating a black hole rotating in the same (corotating BH) or opposite (counter-rotating BH) direction as the accreting material, respectively.

The most general description of astrophysical black holes is given by the Kerr solution to Einstein's general relativity (Kerr 1963):

$$\begin{aligned} ds^2 = &-\left(1-\frac{2GM_{BH}r}{\Sigma c^2}\right)c^2dt^2 - \frac{4GM_{BH}rasin^2\theta}{\Sigma c^2}dtd\phi + \frac{\Sigma}{\Delta}dr^2 + \Sigma d\theta^2 + \\ &+\left(r^2+a^2+\frac{2GM_{BH}ra^2sin^2\theta}{\Sigma c^2}\right)sin^2\theta d\phi^2, \end{aligned} \tag{1.1}$$

where the functions Σ and Δ are defined by $\Sigma := r^2 + a^2cos^2\theta$ and $\Delta := r^2 - \frac{2GM_{BH}r}{c^2} + a^2$.

In the limit $a \to 0$, Equation 1.1 reduces to the Schwarzschild solution to Einstein's general relativity (Schwarzschild 1916), which describes the metric of space-time around a non-rotating black hole:

$$ds^2 = -\left(1-\frac{2GM_{BH}}{rc^2}\right)c^2dt^2 + \frac{dr^2}{1-\frac{2GM}{rc^2}} + r^2(d\theta^2 + sin^2\theta d\phi^2). \tag{1.2}$$

A fundamental characteristic of a black hole is the presence of the event horizon, defined as the region out of which matter and light cannot escape. In general, the radius of the event horizon depends on both its mass M_{BH} and angular momentum J, and is given by:

$$R_{evt} = \frac{GM_{BH}}{c^2}(1+\sqrt{1-a^2}), \tag{1.3}$$

(see red solid line in Figure 1.3), leading to the Schwarzschild radius $R_{Sch} = 2GM/c^2$ for a not spinning BH and to the gravitational radius $R_G = GM/c^2$ for an extreme Kerr (i.e. |a|=1) BH.

The minimal radius at which stable circular motion is still possible identifies the so-called innermost stable circular orbit (ISCO). In particular, $R_{ISCO} = 6R_G$ for a Schwarzschild BH, while $R_{ISCO} = R_G$ or $R_{ISCO} = 9R_G$, in case of a corotating or counter-rotating Kerr BH, respectively (Narayan 2005), as shown with the dash-dotted blue lines in Figure 1.3.

Accretion mechanism can release a large amount of energy, depending on the compactness of the accreting object, which is defined as the ratio between its mass and its radius. Thus, the accretion of matter onto a BH is the most efficient mass-energy conversion process actually known.

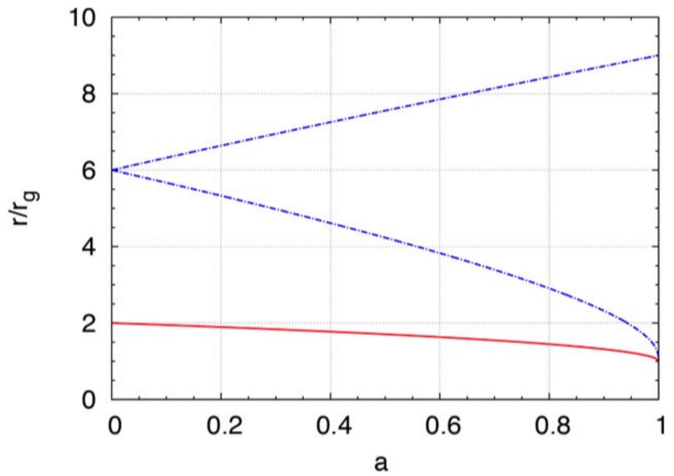

Figure 1.3. Radius of both the event horizon (red solid line) and the ISCO (blue dash-dotted line) of a black hole, expressed in unit of gravitational radii, as a function of the spin parameter a. As concerns R_{ISCO}, the upper curve refers to counter-rotating orbits and the lower curve to corotating orbits (Bambi 2018).

To have a qualitative idea of the amount of energy produced in AGN, the average efficiency η of the conversion of rest mass energy into radiation is usually assumed to be $\sim$10% (Fabian 1999), while nuclear burning releases at most 0.7% of the mass-energy, which is at least a factor 10 lower than AGN accretion. From more detailed calculations, we actually know that, in case of accretion onto a black hole, the efficiency of the conversion of rest mass energy into radiation depends solely on the BH spin and is given by:

$$\eta = 1 - E_{ISCO}, \tag{1.4}$$

where $E_{ISCO} = \sqrt{1 - 2/(3r_{ISCO})}$ is the specific energy of a gas particle in the innermost stable circular orbit, with r_{ISCO} expressed in terms of R_G (e.g. Volonteri 2013). Thus, according to Equation 1.4, the theoretical efficiency of the accretion mechanism in AGN can assume a wide range of values, from $\sim$ 4% (for a counter-rotating BH) up to $\sim$ 42% (for a corotating BH), with $\eta \sim 6\%$ for a non-spinning BH (see Figure 1.4 and Table 1.1).

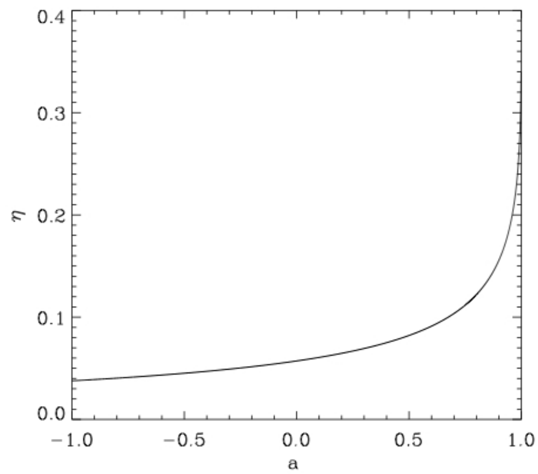

Figure 1.4. Radiative efficiency as a function of the BH spin (Zhang 2013).

However, it is worth noting that the BH capture cross-section is greater for photons with angular momentum opposite to that of the BH (i.e negative momentum), with respect to photons with positive angular momentum. Thus, in case of accretion, the black hole preferentially swallows negative angular momentum photons emitted by the accretion flow, limiting the spin to a=0.998 (Thorne 1974). A summary of the main characteristics of a BH described above is reported in Table 1.1.

Table 1.1. Main characteristics of spinning or not spinning black holes.

	not spinning BH	fast rotating BH †	maximum rotating BH
spin ^{a}	0	0.998	1
R_{ISCO} ^{b}	6	$\sim 1.236^{d}$, $\sim 8.994^{e}$	1^{d}, 9^{e}
η ^{c}	~ 0.057	$\sim 0.321^{d}$, $\sim 0.038^{e}$	$\sim 0.423^{d}$, $\sim 0.057^{e}$
metric	Schwarzschild	Kerr	Kerr

Notes. † It corresponds to the maximum rotating BH in case of accretion. ^{a} Adimensional angular momentum per unit mass, defined by $a = Jc/GM_{BH}^2$. ^{b} Radius of the innermost stable circular orbit, in units of R_G, according to Bardeen et al. (1972). ^{c} Radiative efficiency, defined by Equation 1.4, whose trend is shown in Figure 1.4. ^{d} In case of a corotating BH ^{e} In case of a counter-rotating BH.

1.2.2 The accretion disk

Due to the conservation of the angular momentum, matter spiralizing around the SMBH cannot fall directly into the compact object, giving origin to an accretion disk emitting thermally because of viscosity.

The simplest configuration is the α-disk model described by Shakura & Sunyaev (1973), in which matter orbiting around the SMBH with Keplerian motion gives origin to an optically thick and geometrically thin disk of cold matter ($T \sim 10^5 - 10^6$ K). Due to viscosity forces, the angular momentum of the gas is transferred outward, causing the spiralizing of matter into the center. During this process, the accreting matter looses a considerable fraction of its gravitational energy which is in turn converted into radiation, with the efficiency given by Equation 1.4. If the viscosity is mainly due to turbulence driven by the magneto-rotational instability, the kinematic viscosity coefficient ν_* follows the so-called "α prescription":

$$\nu_* \sim l_0 v_o, \tag{1.5}$$

where l_0 is the correlation length of turbulence and v_0 is the mean turbulent speed. Assuming that the latter cannot exceed the sound speed ($v_0 < c_S$), and that the typical size of the turbulent elements cannot be greater than the disk thickness ($l_0 < h$), one gets:

$$\nu_* = \alpha h c_S, \tag{1.6}$$

where α is the efficiency of the angular momentum transport mechanism assumed by Shakura & Sunyaev to be a constant and providing the solution of the equations of the disk structure for different radial ranges. The dimensionless coefficient α can assume any values ranging from 0 to 1, where the lowest value correspond to a scenario in which there is no accretion, while the highest one reproduces a disk accreting at the maximum rate.

The α-disk model is assumed to be radiatively efficient, since all the heat generated by viscosity at a given radius is immediately radiated away. In particular, the energy flux radiated from a surface unit of the disk with radius r in the unit of time is given by:

$$Q = \frac{3}{8\pi} \frac{GM_{BH}\dot{M}}{r^3} \left[1 - \left(\frac{R_{in}}{r} \right)^{1/2} \right]; \tag{1.7}$$

where R_{in} is the inner radius of the disk, while $\dot{M}$ is the accretion rate. In case of radiative vertical transport, each element of the optically thick disk ($\tau >> 1$) radiates as a blackbody with an effective temperature given by

$$Q = \sigma_{SB} T^4, \tag{1.8}$$

where σ_{SB} is the Stefan-Boltzmann constant. Therefore, simply combining Equations 6.4 and 1.8, one can obtain the surface temperature profile of the disk:

$$T(r) = \left\{ \frac{3GM_{BH}\dot{M}}{8\pi r^3 \sigma_{SB}} \left[1 - \left(\frac{R_{in}}{r} \right)^{1/2} \right] \right\}^{1/4}, \tag{1.9}$$

which depends only on the product between the black hole mass and the accretion rate, and not on the kinematic viscosity coefficient.

According to Equation 1.9, the gas within the disk can assume a wide range of temperatures, depending of its distance from the SMBH. Therefore, the overall disk emission can be explained as a sum of blackbody spectra with different temperature (see Figure 1.5), where the maximum value is set by the inner boundary condition of the accretion disk. Moreover, peaking at UV wavelenghts, the emission from the accretion disk is thought to give origin to the Big Blue bump feature in the spectral energy distribution of AGN (Sanders et al. 1989).

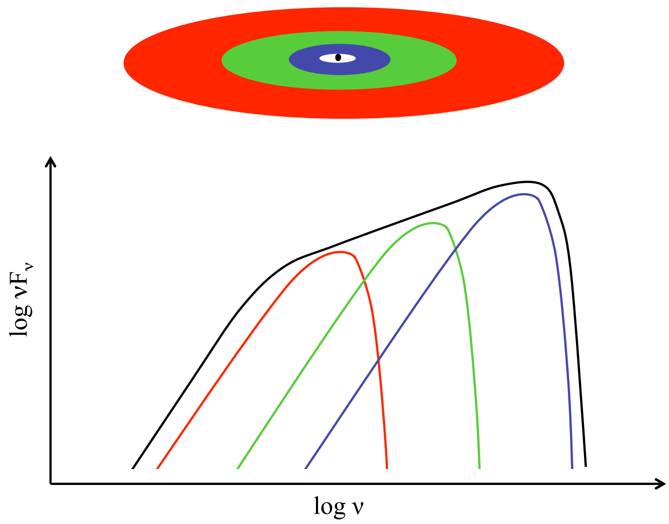

Figure 1.5. Spectral energy distribution of a standard accretion disk. Red, green and violet solid lines represent the different contributions to the spectrum from different annuli of the disk, while the total emission is shown in black.

The total energy released by accretion in the unit of time is given by:

$$L_{acc} = \eta \dot{M} c^2, \tag{1.10}$$

where $\dot{M}$ is the accretion rate (in $M_\odot/yr$), η is the radiative efficiency defined by Equation 1.4, and c is the speed of light.

The maximum luminosity in case of spherical accretion is given by the Eddington luminosity, which is defined as the value by which the radiation pressure ($F_{rad} = \frac{L_{acc}\sigma_T}{4\pi c r^2}$) equals the gravitational attraction force ($F_{grav} = \frac{GM_{BH}m_p}{r^2}$) and depends only on the mass of the BH:

$$L_{Edd} = \frac{4\pi c M_{BH} m_p}{\sigma_T} \sim 1.3 \times 10^{38} \frac{M_{BH}}{M_\odot}\ erg\ s^{-1}, \tag{1.11}$$

where m_p is the mass of the proton and $\sigma_T = 6.65 \times 10^{-25}$ cm^2 is the Thomson cross-section.

Accretion is a self-regulated process: when the luminosity exceeds the Eddington limit, the radiation pressure balances the gravitational force and the accretion stops. The ratio between the bolometric luminosity of a disk and the Eddington limit is given by the Eddington ratio:

$$\lambda_{Edd} = \frac{L_{bol}}{L_{Edd}}, \tag{1.12}$$

leading to the distinction between sub-Eddington ($\lambda_{Edd} < 1$) and super-Eddington accretion ($\lambda_{Edd} > 1$), which is possible since spherical accretion is only an approximation and does not represent the physical situation of an accreting object.

1.2.3 The hot corona

The accretion disk solely cannot explain the high X-ray emission of AGN, because even in case of warm disks their emission is not supposed to exceed few hundreds eV; conversely, the presence around the accretion disk of an optically thin hot plasma ($T \sim 10^9$ K), the so-called hot corona, allows to explain the X emission at energies $E \sim 0.1 - 100$ keV observed in the spectra of AGN (see Figure 1.6). It is in fact now universally accepted that the origin of the primary emission component observed in AGN is due to the inverse Compton mechanism by which the UV photons coming from the accretion disk acquire energy following the interaction with the hot electrons of the corona.

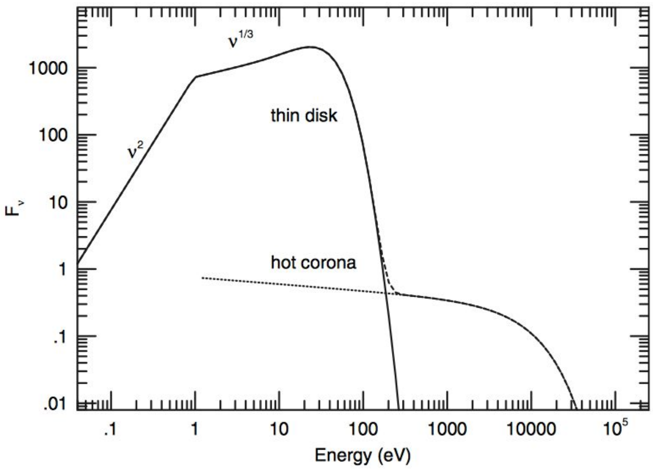

Figure 1.6. Schematic view of a spectrum produced by the combination of an optically thick geometrically thin disk with $T_{max} = 10^5$ K and an optically thin hot corona with $T_{cor} = 10^8$ K (Netzer 2006).

The origin, extension and geometric configuration of the hot corona are not yet well understood, although microlensing models have estimated a size of the order of a few gravitational radii (Chartas et al. 2009). Some possible geometries of the corona are shown in Figure 1.7, while some hypotheses about its origin are shortly discussed as follows.

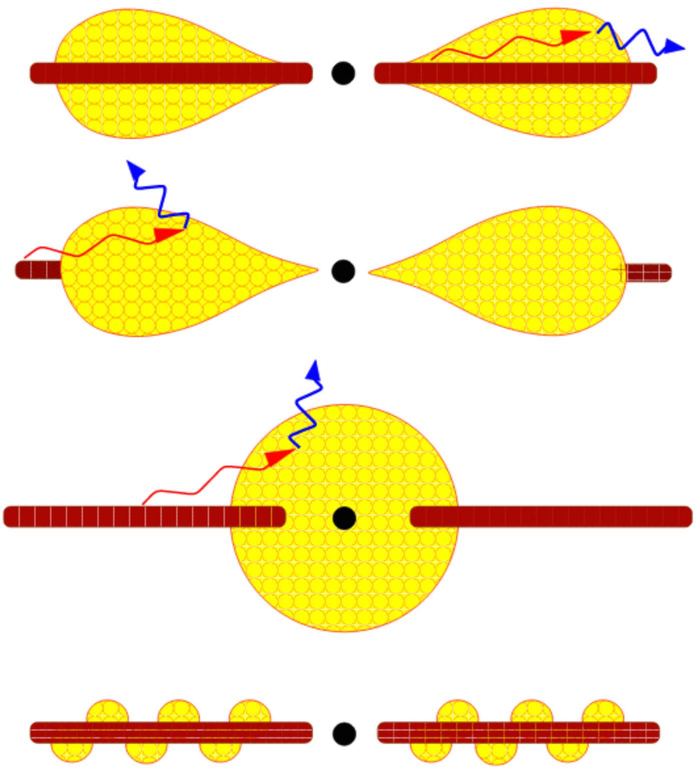

Figure 1.7. Some possible geometries for an accretion disk and Comptonizing corona (Reynolds & Nowak 2003). (a) "slab" geometry, where the corona sandwiches the accretion disk. Being relatively easily Compton cooled, this type of corona cannot easily reach high temperatures, thus predicting spectra softer than observed; (b) and (c) "sphere+disk" geometries, in which the corona is not strongly Compton cooled, thus remaining very hot and producing hard spectra; (d) "patchy corona", known also as "pill box" model (Stern et al. 1995).

Magnetic flares – A possible explanation for the heating of the electrons required to Comptonize the soft photons emitted from the accretion disk is related to a magnetic reconnection mechanism. In particular, the presence of magnetic flares above the accretion disk can heat the electrons, which then emits the primary X-ray emission by Comptonization of the UV photons from the disk, resulting in a reasonably working hypothesis to model X-ray spectra and variability (Haardt et al. 1994). Moreover, this scenario may be supported from the possible evidence for hot spots corotating with the disk (Dovčiak et al. 2004a; Iwasawa et al. 2004).

Clumpy disks – The hypothesis of inhomogeneous, clumpy discs able to explain the X-ray properties of accreting black holes was firstly proposed by Guilbert & Rees (1988) and then pursed over the years by many authors (Celotti et al. 1992; Collin-Souffrin et al. 1996; Kuncic et al. 1997; Krolik 1998; Malzac & Celotti 2002; Merloni et al. 2006). This scenario requires the presence of a highly inhomogeneous accretion flow with a two-phase structure which is able to explain both the primary and the reprocessed emission. In particular, a hot and optically thin phase is responsible for the primary emission, while a cold optically thick phase provides the seed photons for the Comptonization, and is responsible for the reprocessed emission.

Aborted jets – The idea that the primary emission could originate from jets propagating only for a short distance on the black hole axis (i.e. aborted jets) was firstly introduced by Henri & Petrucci (1997), and later pursued by Ghisellini et al. (2004), which attributed the jet failure to a velocity lower than the escape one. When the jet fails, it can collide with other blobs produced later and still moving outwards. Through these collisions, the kinetic energy of the blobs can be converted into internal energy, heating the plasma where Comptonization can occur. It is worth noting that this scenario is not necessarily alternative to the most popular "disk-corona" model because, at least in part, both processes could be responsible of the high energy emission.

1.2.4 The broad line region

The broad line region (BLR) is composed of gas clouds under the gravitational influence of the SMBH, which extends from 0.01 pc up to 1 pc from the nuclear region. Orbiting at high velocities around the central black hole, the clouds intercept and reprocess part of the ionizing radiation produced by the disk through emission lines significantly wider than those produced by star formation. The widths of AGN broad lines span over two order of magnitudes ranging from Δv_{FWHM} ~500 km s^{-1} to Δv_{FWHM} ~10^4 km s^{-1}, with typical values of Δv_{FWHM} ~5000 km s^{-1} (Peterson 1997).

The strongest lines observed in the typical spectra of AGN are those of the hydrogen Balmer series (Hα, Hβ and Hγ), the hydrogen Lyα, and lines from abundant ions (MgII, C[III], and CIV), whose main properties are reported in Table 1.2. In addition to them, there are also several lines which are blended because of their large Doppler widths (see Table 1.3).

Table 1.2. Typical emission line strenghts in AGN (Peterson 1997).

Line	Relative flux †	Equivalent width (Å)
Lyα λ1216 + NV λ1240	100	75
CIV λ1549	40	35
C[III] λ1909	20	20
MgII λ2798	20	30
Hγ λ4340	4	30
Hβ λ4861	8	60

Notes. † Normalized flux, assuming Lyα + NV = 100.

From the observed emission lines, we can estimate the physical properties of the gas. From one hand, the line intensities give information on the gas temperature, which results to be of the order of $T \sim 10^4$ K. Such a temperature leads to a velocity dispersion for the gas of the order of

$$v \sim \left(\frac{k_B T}{m_p}\right)^{1/2}, \tag{1.13}$$

Table 1.3. Selected blended broad lines in AGN (Peterson 1997).

Feature	Contributing lines
Lyβ + OVI λ1035	Lyβ λ1026; OVI $\lambda\lambda$1032, 1038
Lyα + NV	Lyα λ1216; NV $\lambda\lambda$1239, 1243
SiIV + O[IV]	SiIV $\lambda\lambda$1394, 1403; O[IV] λ1402
CIV λ1549	CIV $\lambda\lambda$1548, 1551
HeII + O[III]	HeII λ1640; O[III] λ1663
C[III] + Si[III]	AlIII λ1857; Si[III] λ1892; C[III] λ1909
Small blue bump	Balmer continuum ($\lambda < 3646$ Å); FeII (many lines)
MgII λ2798	MgII $\lambda\lambda$2796, 2803
FeII λ4570 + HeII	FeII (multiplets 37, 38, and 43); HeII λ4686
Hβ	Hβ λ4861; FeII $\lambda\lambda$4924, 5018
FeII $\lambda\lambda$5190, 5320	FeII (multiplets 42, 48, 49, and 55)

where k_B is the Boltzmann constant and m_p is the mass of the proton. Therefore, thermal broadening can only account for velocity dispersions of the order of ~10 km s^{-1}, well below the typical widths observed in AGN, which are instead due to bulk motion of the individual clouds. On the other hand, the presence or the absence of particular emission lines enable us to obtain some limits to the electron density within the BLR. In particular, since essentially all forbidden lines are collisionally suppressed, we can set $n_e \sim 10^8$ cm^{-3} as the lower limit to the electron density (Osterbrock & Ferland 2006), while an upper limit of $\sim 10^{14}$ cm^{-3} is consistent with the critical density for collisional de-excitation of the broad lines (Ilic et al. 2010).

Moreover, reverberation mapping studies of low redshift AGN have shown that the inner radius of the BLR scales with the monochromatic continuum luminosity at 5100 Å:

$$\frac{R_{in,BLR}}{lt-days} = (32.9^{+2.0}_{-1.9}) \left[\frac{\lambda L_\lambda(5100\text{Å})}{10^{44}\ erg\ s^{-1}} \right]^{0.700\pm0.033} \tag{1.14}$$

(Kaspi et al. 2000). On the other hand, since the BLR is a dust-free region, its outer limit $R_{out,BLR}$ is set by the dust sublimation radius R_d:

$$R_{out,BLR} = R_d = 1.3 \left(\frac{L_{UV}}{10^{46}\ erg\ s^{-1}} \right)^{0.5} \left(\frac{T_{gr}}{1500\ K} \right)^{-2.8} pc, \tag{1.15}$$

where L_{UV} is the UV luminosity and T_{gr} is the temperature below which dust grains sublimate (Barvainis 1987). Moreover, due to its proximity to the SMBH, the BLR is expected to be always detected in unobscured sources, while its direct view can be hidden by the molecular torus in obscured AGN.

1.2.5 The molecular torus

At parsec distances from the SMBH, it is now universally accepted the existence of an optically thick toroidal structure, composed of molecular gas and dust, which absorbs and reprocesses the radiation from the accretion disk and from the corona (Jaffe et al. 2004; Burtscher et al. 2013). The reprocessed radiation is then re-emitted in the mid infrared, giving rise to an emission peak around 10-30 μm, the so-called Infrared Bump.

Several theoretical works over the years have proposed various geometries for this absorbing medium in order to explain the broad infrared spectral energy distribution observed in AGN. The main configurations were first the uniform one (smooth dust distribution – Pier & Krolik 1992 and 1993; Fritz et al. 2006) followed by the discrete (clumpy distribution – Nenkova et al. 2008a and 2008b) and the composite ones (two-phase distribution - Stalevski et al. 2012), which are shortly summarized as follows. However, although they give rise to different spectral energy distributions, the differences between them seem to be mainly due to the assumptions underlying the adopted models (e.g. distribution of the primary emission, chemical composition of the dust) and not to the different distribution of the absorbing material (Feltre et al. 2012).

Smooth dust distribution (Pier & Krolik 1992 and 1993; Fritz et al. 2006): this model requires a simple toroidal structure with a uniform distribution of gas and dust (see panel (a) in Figure 1.8). The size of the torus is defined by the angular opening angle θ and by the outer radius R_{max}, while the inner radius is defined by the sublimation temperature of the dust grains under the influence of the strong nuclear radiation field. In such a configuration, the temperature distribution of the absorbing material depends on its distance from the BH, with a profile decreasing roughly linearly for increasing distances from the central source. Moreover, a source is obscured only if the line of sight intercepts the torus; otherwise the nuclear region can be seen directly. A typical expected feature in this configuration is a strong silicate 9.7μm absorption if the total optical depth at this wavelength exceeds unity (Netzer 2015).

Clumpy distribution (Nenkova et al. 2008a and 2008b): this model consists of a series of discrete clouds, probably with a greater distribution on the equatorial plane (see panel (b) in Figure 1.8). With respect to the homogeneous model, additional parameters are required to accurately describe this configuration, such as the column density, the radial distribution, the filling factor and the density distribution of the individual clumps. In such a model, the clouds can have different temperatures even if they are at the same distance from the BH. Moreover, since the illuminated and back sides of individual clumps radiate at different temperatures, the dark side of a cloud close to the AGN can be as warm as the bright side of a farther cloud allowing the same dust temperature to occur at different distances. The probability of intercepting the torus is maximum on the equatorial plane, but it can assume finite values elsewhere, thus not excluding the possibility to have a direct view of the nuclear region also for edge-on sources. This model can account for several observational properties of AGN and appears to be strongly supported by recent X-ray observations that directly reveal the clumpiness of the absorbing medium (e.g. Risaliti et al. 2005; Bianchi et al. 2009; Markowitz et al. 2014; Rivers et al. 2015a and 2015b).

Clumpy two-phase distribution (Stalevski et al. 2012): being a combination of smooth and clumpy models, it could perhaps represent the most realistic configuration of the torus structure. In this case, there is no empty space between the clumps, being this volume filled with diluted dusty gas which absorbs part of the incident optical-UV radiation and part of the locally emitted NIR and MIR radiation (see panel (c) in Figure 1.8). Thus, the two-phase distribution allows to preserve the main features of the pure clumpy case, taking also into account the additional attenuation by the inter-cloud dust and gas.

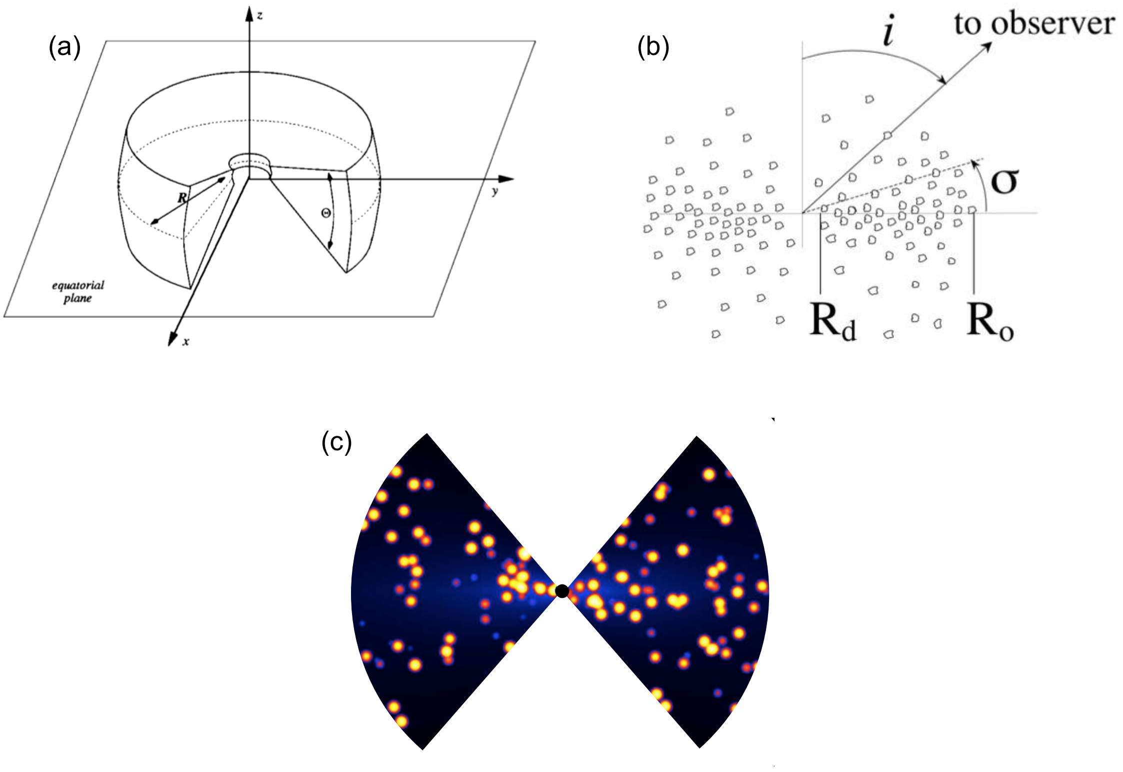

Figure 1.8. Different torus configurations: smooth (panel (a) – Fritz et al. 2006), pure clumpy (panel (b) – 2008b) and two-phase clumpy (panel (c) – Stalevski et al. 2012) dust distributions. More details about the assumptions on each of them are discussed throughout the text.

1.2.6 The narrow line region

Extending from some hundreds of parsecs, the narrow line region (NLR) represents the outermost region which can be photoionized by the radiation produced in the nuclear zone. Unlike the BLR, it is composed of clouds made of gas and dust, whose electron density is low enough ($n_e \sim 10^4$ cm^{-3}) to allow the formation of forbidden lines, which are strong gas coolants and dominate the NLR emission-line spectrum (Groves 2007). A list of the most prominent emission lines produced in the NLR and observed in Seyfert 2 spectra together with their typical relative intensities with respect to $H\beta$, are reported in Table 1.4. Since this region lies outside the dominating influence of the central black hole, the line velocity widths are much lower than values observed in the BLR. The typical full width at half maximum for narrow emission lines lies in the range $200 < \Delta v_{FWHM} < 900$ km s^{-1}, with most values falling around 350-400 km s^{-1}.

Table 1.4. Strong narrow emission lines observed in Seyfert 2 spectra (Peterson 1997).

Line	Relative flux
Lyα λ1216	55
CIV λ1549	12
[CIII] λ1909	5.5
MgII λ2798	1.8
[NeV] λ3426	1.2
[OII] λ3727	3.2
[NeIII] λ3869	1.4
Hβ λ4861	1.0
[OIII] λ4959	3.6
[OIII] λ5007	11
Hα λ6563	3.1
[NII] λ6583	2.9
[SII] λ6716	1.5

Being located on kpc scales, the NLR can be detected in both obscured and unobscured AGN; however, since it is well beyond the dust sublimation radius, the spectroscopic analysis of this region can be complicated by the presence of significant quantities of dust (Peterson 1997). Moreover, the NLR is the only AGN component which is spatially resolved through optical observations, revealing an axisymmetric morphology composed of two opposite ionization cones centered into the nuclear source (e.g. Pogge 1988; Malkan et al. 1998).

1.2.7 The relativistic jet

In about 10% of AGN, the development of highly collimated jets is observed. Consisting of plasma moving at relativistic speeds, they extend perpendicularly to the accretion disk on scales of hundreds of kiloparsec emitting mainly in the radio band through synchrotron mechanism. The origin of these jets is still debated, but the currently adopted model requires the presence of a strong magnetic field whose lines of force are twisted together due to the strong rotation of the accreting material, giving rise to a magnetic tower from which the relativistic plasma is expelled (Kato et al. 2004). This model requires both the rotation of the disk as well as the central black hole.

1.3 AGN taxonomy

Despite the large number of classes and subclasses in which AGN are actually divided, a simplified classification can be based on only two parameters: the radio-loudness and the width of the optical emission lines (Urry & Padovani 1995), as shown in Table 1.5.

Table 1.5. Simplified scheme of AGN classification, based on both the radio loudness parameter and optical emission line properties (adapted from Padovani 1997).

Radio emission	Radio loudness	Optical emission lines properties		
		Type 0 (unusual)	Type 1 (broad lines)	Type 2 (narrow lines)
Radio-quiet	$R_o \sim 0 - 1$		Sy1 QSO	Sy2 QSO
Radio-loud	$R_o \sim 10 - 1000$	Blazars	BLRG FSRQ/SSRQ	NLRG
		increasing angle with respect to the line of sight –>		

Even though all AGN emits at radio wavelenghts, only a small fraction of them (i.e. ~10%), the so called radio-loud AGN, is expected to have a strong radio emission if compared with the optical one (see Figure 1.9); otherwise AGN are classified as radio-quiet. The radio loudness parameter R_o is usually used to determine if an AGN is radio-quiet or radio-loud. It is defined as the ratio between the 5 GHz radio luminosity and the optical luminosity in the optical B-band at 440 nm:

$$R_o = \frac{L_\nu(5GHz)}{L_\nu(B)}. \tag{1.16}$$

Analyzing data from the Palomar Bright Quasar Survey, Kellermann et al. (1989) were the first to highlight a bimodal distribution of the radio loudness parameter suggesting the existence of two classes of AGN: radio-quiet (RQ, $R_o \sim 0.1 - 1$) and radio-loud (RL, $R_o \sim 10 - 1000$) sources, with $R_o \sim 10$ being the discriminating value (Kellermann et al. 1994).

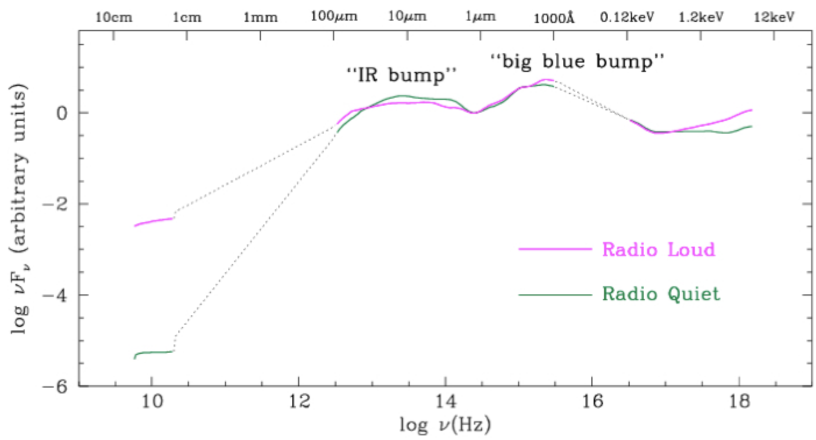

Figure 1.9. A schematic representation of a typical spectral energy distribution of radio-quiet (green) and radio-loud (magenta) AGN (Elvis et al. 1994).

An alternative way to distinguish between radio-quiet and radio-loud AGN is given by the ratio between the radio luminosity at 5 GHz and the X-ray luminosity in the 2-10 keV energy band:

$$R_X = \frac{\nu L_\nu(5GHz)}{L_X(2-10\ keV)}. \tag{1.17}$$

This method has the advantage that R_X can be measured also for highly absorbed nuclei (i.e. $N_H >> 10^{23}$ cm^{-2}), which would be totally obscured at optical wavelengths. In this case the boundary between radio-loud and radio-quiet object corresponds to $logR_X = -4.5$ (Terashima & Wilson 2003).

1.3.1 Radio-quiet AGN

Radio-quiet AGN are characterized by a weak radio emission (if compared to the optical one), and include three different types of sources:

- **radio-quiet quasars (RQ QSOs)**: characterized by a high brightness of the nucleus ($M_B \leq 23$ mag), whose emission dominates that of the host galaxy;
- **Seyfert galaxies (Sy)**: low luminosity objects ($M_B \geq -23$ mag) in which both the emission due to the AGN and to the host galaxy can be appreciated;
- **Low Ionization Nuclear Emission Regions (LINERs)**: characterized by optical spectra similar to those of Seyfert galaxies, but dominated by low ionization emission lines (Heckman 1980). Their classification as low luminosity AGN is still under investigation, since the observed lines could be also due to shock processes within the galaxy.

As concerns Seyfert galaxies, they were firstly divided into two unique categories, depending on the width of the Balmer lines observed in their optical spectra. In particular, the presence of broad lines identifies Seyfert 1 galaxies, while only narrow lines were observed in Seyfert 2s (Khachikian & Weedman 1974), as shown in Figure 1.10, where the typical optical spectra of Seyfert 1 and Seyfert 2 galaxies are drawn. The former have a bright continuum, wide permitted emission lines ($v_{FWHM} \sim 10^3 - 10^4$ km s^{-1}) produced in a high density medium (BLR – $n_e \geq 10^8$ cm^{-3}) and narrow forbidden lines ($v_{FWHM} \sim 10^2 - 10^3$ km s^{-1}) produced in a low density medium (NLR – $n_e \sim 10^3 - 10^6$ cm^{-3}), while the latter show a weak continuum and only narrow emission lines. It is worth noting that the same differences occur for objects with higher brightness (type 1 and type 2 QSOs).

Then, some different Seyfert galaxies were discovered, which could not be classified in neither of the two previous classes. These intermediate types of AGN, which are summarized in Table 1.6, were classified using the Hβ to [OIII]-5007Å optical emission line ratio (Winkler 1992).

A further subclass is constituted by the so-called Narrow Line Seyfert 1 (NLSy1), characterized by having allowed optical lines only slightly wider than those forbidden (see Figure 1.10), strong Fe II emission lines or presence of lines of highly ionized iron and a [OIII]-Hβ ratio lower than 3 (Osterbrock & Pogge 1985).

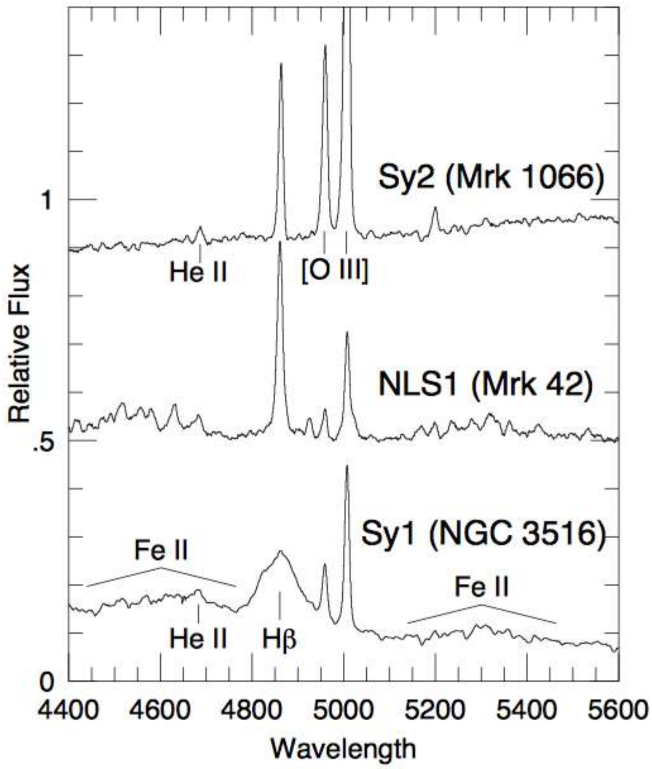

Figure 1.10. Optical spectra in the $H\beta$ region relative to the Sy1 NGC 3516, the NLS1 Mrk 42, and the Sy2 Mrk 1066 (Pogge 2000).

Table 1.6. Main characteristics of the optical spectra of the different Seyfert classes.

Seyfert type	Hβ to [OIII]-5007Å line ratio	Emission line features observed in the optical spectrum
1	$>$5.0	narrow and broad emission lines
1.2	2.0 - 5.0	weaker Hβ component than Seyfert 1
1.5	0.33 - 2.0	comparable strengths of the broad and narrow Hβ components
1.8	$<$0.33	very weak broad components, but detectable both in Hβ and Hα
1.9	—	broad component is detected only in the Hα line
2	—	narrow emission lines only

1.3.2 Radio-loud AGN

Representing $\sim 10\%$ of AGN, radio-loud sources are tipically associated with a collimated relativistic jet or with regions where a jet has collided with the surrounding material (Fabian 1999). They are characterized by intense radio emission, and include the following types of objects:

- **radio galaxies**: divided into broad line (BLRGs) and narrow line (NLRGs) radio galaxies depending on the width of the Balmer lines observed in their optical spectra. Moreover, according to their radio brightness at 178 MHz, radio galaxies are also divided into low power (Fanaroff-Riley type I – FR I) and high power (Fanaroff-Riley type II – FR II) objects, being $L_{178MHz} = 2 \times 10^{25}$ W Hz^{-1} sr^{-1} the threshold value that divides the two classes (Fanaroff & Riley 1974);

- **radio-loud quasars (RL QSOs)**: classified on the basis of the value of the radio spectral index α into Flat-Spectrum Radio Quasars (FSRQs – $\alpha < 0.5$) and Steep-Spectrum Radio Quasars (SSRQs – $\alpha > 0.5$);

- **blazars**: highly variable objects that emit highly polarized radiation. They are divided into BL Lac objects (named after the prototype BL Lacertae) and Optically Violent Variable quasars (OVVs). The former are characterized by the absence of strong emission or absorption lines in their spectra, while the latter show a high variability ($>$ 0.1 mag in optics) on very short scale times ($\sim$days).

1.4 The unification model

Despite the existence of several AGN classes, each with their peculiar characteristics, the idea that all AGN are powered by the same mechanism, namely the accretion of matter onto a SMBH, is nowadays commonly accepted. This assumption is at the basis of an AGN unification model for both radio-loud and radio-quiet AGN able to explain the observational differences in the various AGN classes as due to the orientation of the object with respect to the line of sight. Figure 1.11 shows how in this context radio-quiet AGN differ according to the role played by the obscuring torus (Antonucci 1993), while the subdivision into the various radio-loud AGN classes depends on the orientation of the jet with respect to the line of sight (Urry & Padovani 1995).

As concerns radio-quiet AGN, the first important step towards a unification model was done in the late '70s, when Rowan-Robinson (1977) proposed a unique scheme for several AGN classes and attributing the different emission properties observed in type 1 and type 2 AGN as due to the presence of strong dust obscuration in the latter. Few years later, also Osterbrock (1981) attributed a key role to the dust surrounding the central engine, explaining in this way the variations in the Balmer widths observed in intermediate Seyfert galaxies. However, in this context the milestone was the detection of both broad Balmer ($v_{FWHM} \sim 7500$ km s^{-1}) and FeII lines in the optical spectrum of the archetypal Seyfert 2 galaxy NGC1068, when observed in polarized light (Miller & Antonucci 1983; Antonucci & Miller 1985 – see Figure 1.12). Having an equivalent widths similar to those typically observed in Seyfert 1s, Balmer lines were assumed to be produced by reflection of the radiation emitted in the BLR. At the same time, the presence of FeII was crucial in establishing the origin of this broad emission in clouds of very high optical depth. The obvious conclusion to be drawn was that the BLR was also present in Seyfert 2 galaxies,

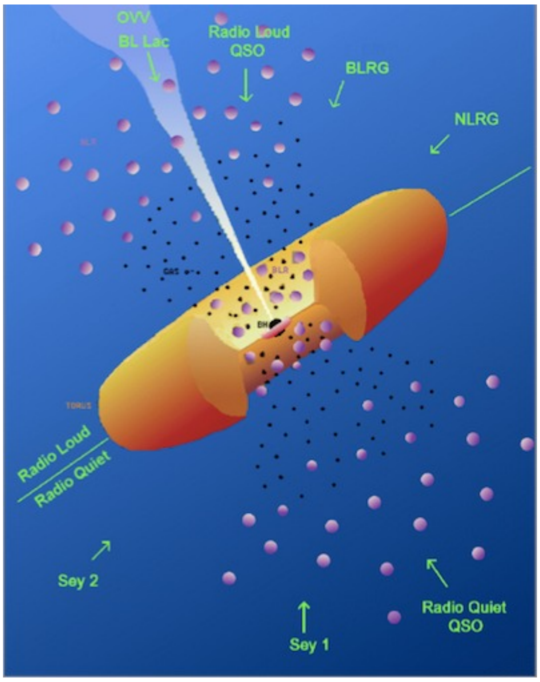

Figure 1.11. Typical scheme of both radio-quiet and radio-loud AGN. Green arrows indicates the line of sight for each subclass. Adapted from Urry & Padovani (1995).

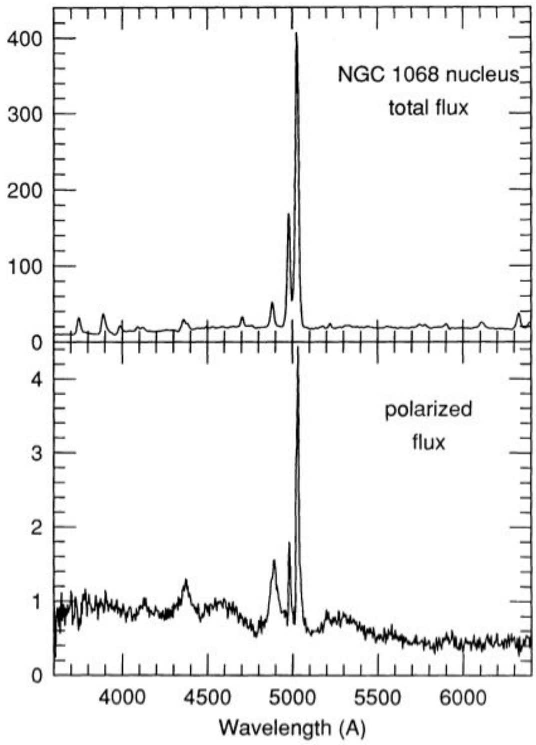

Figure 1.12. Spectropolarimetry of the nucleus of NGC 1068, showing the total flux (top panel) and the polarized flux (bottom panel) between 3600 Å and 6400 Å (Miller et al. 1991).

but it was visible only through scattering due to the presence of absorbing matter along the line of sight preventing its direct view. This obscuring medium is assumed to be optically thick, composed of dust and gas and arranged in a toroidal axisymmetric structure with column density large enough to completely obscure the central source in some directions (Antonucci 1993; Netzer 2015). This was the first observational evidence able to confirm the idea that all AGN could share the same structure and that the differences found in their spectra could be explained by inclination effects. In this scheme, type 1 AGN are observed at low angles with respect to the torus axis, allowing a direct view on the nuclear region and thus observing both the broad and the narrow features produced in the BLR and NLR, respectively. Conversely, type 2 AGN are observed at high inclinations, with the nuclear region completely hidden by absorbing matter in the line of sight. In this latter case, the BLR cannot be observed due to the torus obscuring wall and the only observable features come from the NLR.

However, a radio-quiet unification scheme based solely on the inclination angle of the system and on the presence of an homogeneous donut-shaped absorbing morphology appears to be an oversimplification (Elvis 2012). Indeed, although X-ray studies have confirmed, to first order, the widely accepted unified scheme, the location, geometry and physical state of the absorbing material are still widely debated (Bianchi et al. 2012). In particular, the observation of short timescale variations ($\sim$days or even $\sim$hours) in the absorption column density in several nearby bright sources, such as NGC 1365 (Risaliti et al. 2005; Rivers et al. 2015a), NGC 4151 (Puccetti et al. 2007), NGC 4388 (Elvis et al. 2004) and NGC 7582 (Bianchi et al. 2009; Rivers et al. 2015b), implies that the obscuring medium has a clumpy geometry, consisting of a series of discrete clouds likely at sub-pc scales. Although the density of this absorbing matter likely increases towards the equatorial plane (e.g. Nenkova et al. 2008a and 2008b), these variations are at odds with the classical torus geometry, which invokes a smooth distribution of dust and gas in a uniform toroidal structure (Pier & Krolik 1992 and 1993; Fritz et al. 2006).

2

The X-ray emission of AGN

Contents

Although most of the radiation is emitted in the optical and UV bands, X-rays are actually a fundamental tool to probe the physical conditions of the innermost regions of AGN because they minimize the host galaxy contribution allowing to directly observe their nuclear region. Furthermore, the X-ray emission, which typically extends from the cut-off energy due to the Galactic absorption at energies $E \sim 0.1$ keV up to $E \sim 300$ keV, appears to be ubiquitous in AGN and its contribution can reach a considerable fraction of their bolometric luminosity ($\sim 5 - 40\%$, Ward et al. 1987).

In the following, I will discuss the spectral features of AGN when observed in the X-rays. It is worth noting that the X-ray non-thermal emission is not considered here because this component is relevant only for radio-loud AGN (e.g. Celotti 2004), while this thesis work focuses on radio-quiet sources. The complexity of the typical X-ray spectrum of AGN (see Figure 2.1) is described in §2.1, where the different observed components such as the primary emission, the soft-excess, the reprocessed emission and the role of absorption are discussed. The X-ray view of obscured AGN on which this thesis focuses is instead discussed in §2.2, while §2.3 is devoted to the analysis of the most common main drivers of the variability often observed in the X-rays. Finally, §2.4 focuses on the reasons why this thesis work was conceived.

2.1 The complex X-ray spectrum of AGN

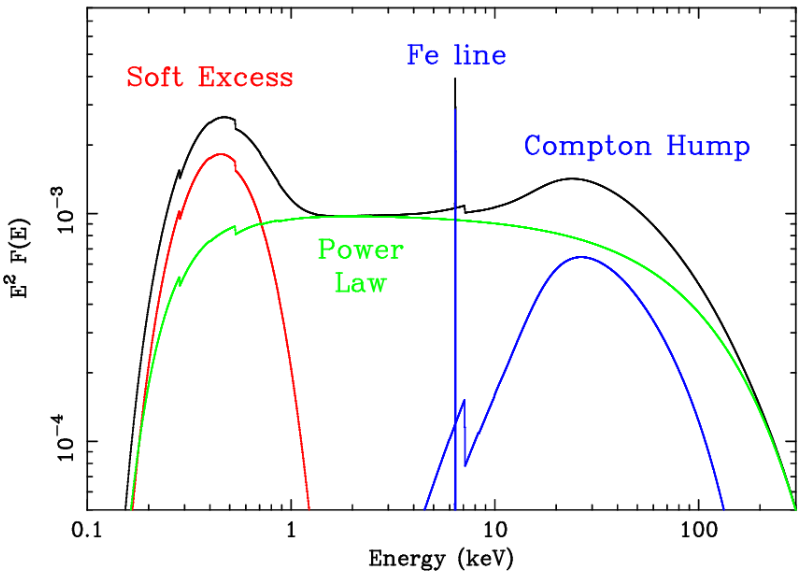

Figure 2.1. Typical X-ray spectrum of an unobscured AGN (black line) subdivided into its main components: soft excess (red), primary emission due to Comptonization (green), reflection continuum and the most relevant narrow line feature (blue), namely the iron Kα emission line at 6.4 keV (Fabian & Miniutti 2005).

2.1.1 The primary emission

The origin of the X-ray emission in AGN is ascribed to thermal Comptonization processes taking place in the hot corona, where the optical-UV photons emitted by the accretion disk are upscattered at X-ray energies by the hot electrons through inverse Compton scatterings.

The spectral shape of the X-ray emission depends by only the electron temperature and the optical depth of the medium. In particular, the dimensionless electron temperature due to the balance between Coulomb heating and Compton cooling rates is given by

$$\Theta = \frac{kT_e}{m_e c^2} \tag{2.1}$$

while the medium optical depth is defined as

$$\tau = n_e \sigma_T R \tag{2.2}$$

where n_e is the electron number density, σ_T is the Thomson cross section, and R is the typical size of the upscattering region (Ishibashi & Courvoisier 2010).

Titarchuk & Lyubarskij (1995) showed that a power-law spectrum, characterized by the spectral index α, or the photon index $\Gamma = \alpha + 1$, is the exact solution of the radiative kinetic equation, obtaining an analytical solution for the spectral slope, both in the non-relativistic and relativistic limit. In the general case, the spectral index is given by:

$$\alpha = \frac{\beta}{ln[1 + \frac{(\alpha+3)\Theta}{1+\Theta} + 4d_0^{1/\alpha}\Theta^2]} \tag{2.3}$$

where the coefficient $d_0(\alpha)$ is computed through a transcendental equation, while β is uniquely determined by the geometry (plane or spherical) and the Thomson optical depth τ_0 of the plasma according to the following relations:

$$\beta = \frac{\pi^2}{12(\tau_0 + 2/3)^2}(1 - e^{-1.35\tau_0}) + 0.45e^{-3.7\tau_0} ln\frac{10}{3\tau_0} \quad \text{for disks} \tag{2.4}$$

$$\beta = \frac{\pi^2}{3(\tau_0 + 2/3)^2}(1 - e^{-0.7\tau_0}) + e^{-1.4\tau_0} ln\frac{4}{3\tau_0} \quad \text{for spheres} \tag{2.5}$$

Equation 2.3 leads to the non relativistic (i.e. $\Theta << 1$) solution:

$$\alpha = \sqrt{\frac{9}{4} + \frac{\beta}{\Theta}} - \frac{3}{2} \tag{2.6}$$

and to the relativistic (i.e. $\Theta >> 1$) solution:

$$\alpha = \frac{\beta - ln[d_0(\alpha)]}{ln(4\Theta^2)} \tag{2.7}$$

As the energy of the photons becomes comparable to the thermal energy of the electrons, the inverse Compton processes no longer take place giving origin to the high energy cut-off observed in AGN at $E_C \sim 3kT_e$. Thus, as a result of the thermal Comptonization process, the primary continuum of AGN can be well approximated by a power-law with a high-energy exponential cut-off (Rybicki & Lightman 1979), whose flux, as a function of the energy, is given by:

$$F(E) = AE^{-\Gamma} exp\left[-\frac{E}{E_c}\right] \quad photons\ cm^{-2}\ s^{-1}\ keV^{-1} \tag{2.8}$$

where A, Γ, and E_C are the normalization at 1 keV, the photon index, and the rollover energy of the cut-off power-law.

Both the photon index and the high-energy cut-off have been measured in several AGN samples, obtaining typical values of $\Gamma = 1.5 - 2.5$ (e.g. Nandra & Pounds 1994; Reeves & Turner 2000; Piconcelli et al. 2005; Page et al. 2005; Bianchi et al. 2009) and $E_c = 70 - 300$ keV (e.g. Matt 2001; Perola et al. 2002; Risaliti & Elvis 2004; Tortosa et al. 2018 and references therein), respectively.

2.1.2 The soft excess

In addition to the main power-law continuum component, the X-ray spectra of AGN often contain a soft emission (hereafter, soft excess) raising smoothly below 1 keV above the extrapolated 2-10 keV emission (e.g. Arnaud et al. 1985; Turner & Pounds 1988), as shown in Figure 2.2.

Although several studies have been made on this topic, nowadays the origin of this soft excess component is still an open issue. Being fairly featureless, it appears as a continuum component which was first believed to originate in the inner part of the accretion flow and thus emitting as a blackbody (Zheng et al. 2001; Czerny et al. 2003). However, the characteristic energy range in which the soft excess arises is at too high values ($E \sim 0.1 - 0.2$ keV) to be simply the high energy tail of the accretion disc emission.

Trying to solve this issue, a further parametrization of the soft excess based on a Comptonization model (Magdziarz et al. 1998; Page et al. 2004; Dewangan et al. 2007) was

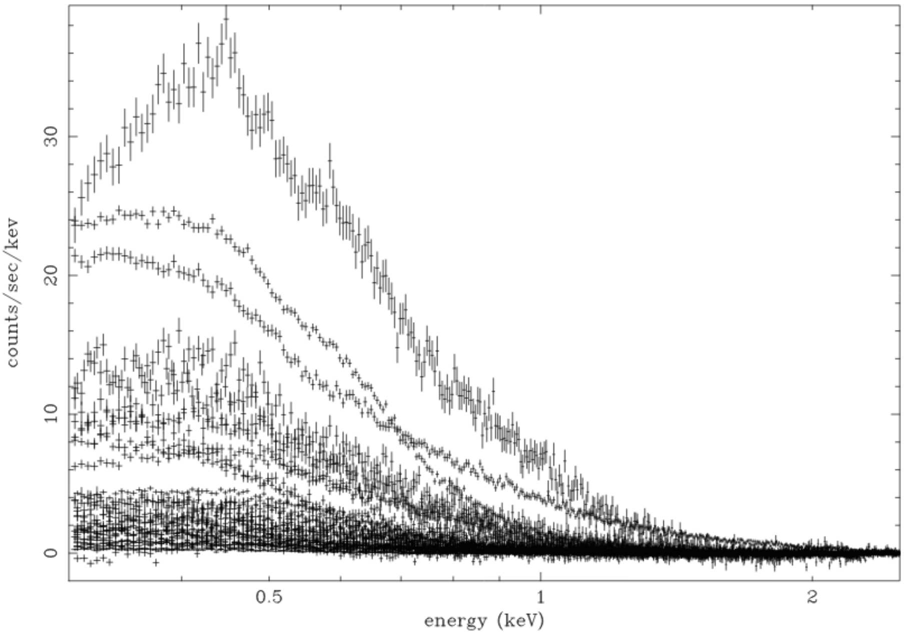

Figure 2.2. Residuals observed in 34 Seyfert 1 galaxies, most of them from the Palomar-Green sample, when modelled with a power-law only. The soft excess component is clearly evident in most of the sources (Crummy et al. 2006).

hypothesized. This scenario requires the presence of a second colder ($kT \sim 0.2$ keV) and optically thick Comptonization region able to scatter the disk photons at softer energies with respect to the hotter, optically thin region producing the high energy power-law emission discussed in §2.1.1. However, also this first attempt of attributing the origin of the soft excess to the emission of a warm corona has been ruled out, due to the quite similar temperatures observed in the XMM-Newton survey of PG quasars spanning a range of over a factor 10 in disc temperature (Gierliński & Done 2004).

The quite constant temperature would seem to point towards an origin in atomic rather than continuum processes. In particular, the soft excess could be related to the large increase in opacity in the 0.7-3 keV energy range, due to OVII/OVIII and Fe L shell absorption (Done et al. 2007). In this case, the rise of the soft emission can be due to an increase in reflected or transmitted flux below 0.7 keV, due to optically thick matter located out of the line of sight and seen via reflection (e.g. from an accretion disc) or optically thin matter within the line of sight seen in absorption (e.g. a wind above the disc), respectively. However, even though an absorption origin appears more physically plausible, both scenarios require quite extreme parameters to explain the characteristics of the soft excess, making its origin still uncertain (Sobolewska & Done 2006).

Recently, the "two-coronae" scenario assuming two Comptonization regions accounting for the UV-soft X-rays and hard X-rays, respectively, was found to be able of producing spectra in agreement with the observed soft X-ray excess spectral shape. In particular, a slightly patchy corona with $kT \sim 0.1 - 2$ keV and $\tau \sim 20$ in radiative equilibrium above a non-dissipative accretion disk resulted to have spectral properties similar to those observed in the soft X-rays in type 1 AGN (Petrucci et al. 2020 and references therein), suggesting that warm Comptonization can be considered as a valuable model to explain the origin of the soft X-ray excess.

2.1.3 The reprocessed emission

In the first approximation, the emission of the hot corona can be assumed isotropic; therefore, any cold, optically-thick matter close to the accreting black hole, such as the accretion disk, the broad line region (BLR) or the torus, can intercept and reprocess some fraction of the primary continuum emission, thereby imprinting atomic features into the observed spectrum (see Figure 2.1). This process of "X-ray reflection" primarily gives rise to a broad reflection bump, the so-called Compton hump, peaking at $\sim$30 keV (George & Fabian 1991; Matt et al. 1991; Reynolds 1998) and to the the iron fluorescence line at approximately 6.4 keV. A further typical feature usually observed in the X-ray spectra of AGN is the Fe K-shell absorption edge at E=7.112 keV (Bearden & Burr 1967), which is due to the increase in the absorption cross-section for photons with energies just beyond the binding energy of the innermost electron shell.

The observed spectral shape of the reflection component is the results of the competition between two physical processes: photoelectric absorption and Compton scattering. The cross section of the former decreases significantly with increasing energy becoming less than the Compton cross-section at energies $\geq$10 keV, where Compton scattering dominates (Morrison & McCammon 1983) and the reflection component appears, originating an hardening in the X-ray spectrum (Lightman & White 1988).

From an observational point of view, the shape of the reflected spectrum is also affected by the ionization state and the chemical composition of the scattering material, as shown in Figure 2.3. The ionisation parameter can be defined as:

$$\xi = \frac{L_{ion}}{nR^2}, \tag{2.9}$$

where L_{ion} is the ionizing luminosity between 13.6 eV and 13.6 keV, n is the hydrogen number density of the reflecting material, and R is the distance of the ionized matter from the SMBH (Tarter et al. 1969).

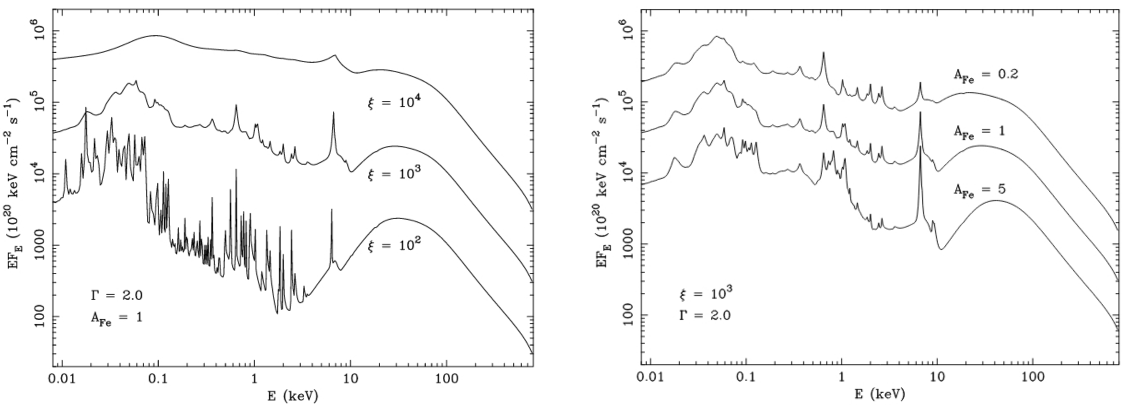

Figure 2.3. *Left panel.* Reflected spectra for three values of the ionization parameter, with $\xi = 10^2$ (bottom curve), $\xi = 10^3$ (middle curve), and $\xi = 10^4$ (top curve), in units of erg cm s^{-1}. In each case, the incident spectrum has a photon index $\Gamma = 2.0$, and iron has solar abundance ($A_{Fe} = 1$). *Right panel.* Reflected spectra for three values of the iron abundance, with $A_{Fe} = 0.2$ (top curve), $A_{Fe} = 1$ (middle curve), and $A_{Fe} = 5$ (bottom curve) times solar abundance. In each case, the incident spectrum has $\xi = 10^3$ erg cm s^{-1} and $\Gamma = 2.0$, with successive spectra offset by factors of 5 for clarity purposes, only (Ross & Fabian 2005).

The Compton hump

The main feature of the reflection continuum due to neutral matter consists in a broad bump peaking at ~ 30 keV, with two cut-offs at low ($E \sim 4-5$ keV) and high energies ($E \sim$ few tens of keV), being the first due to the photoelectric absorption of the lower energy incident radiation, while the second is caused by the decrease in the scattering cross section which allows the higher energy photons to penetrate further into the disk, increasing their probability to be absorbed.

The reflection efficiency in the 2-10 keV range is a small fraction (typically a few percent) of the primary emission, but it can reach about 30% at the energy of the Compton hump in presence of an optically thick reflective material covering a significant fraction of the solid angle (Ghisellini et al. 1994). It is usually described with the parameter R, which is given by

$$R = \frac{\Omega}{2\pi}, \tag{2.10}$$

and represents the solid angle Ω of the cold material visible from the Comptonizing source, in units of 2π (Magdziarz & Zdziarski 1995). The value of R depends on the inclination angle at which we observe the system, as clearly shown in Figure 2.4. In particular, the smaller is the value of the inclination angle, the larger will be the resulting reflection component.

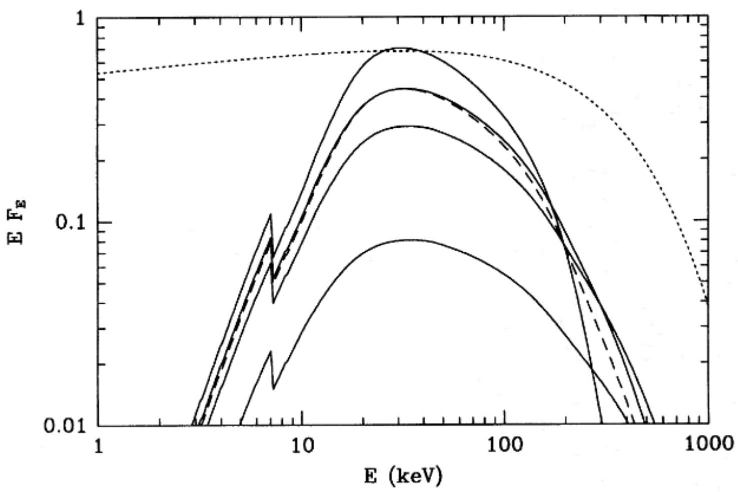

Figure 2.4. Dependence of the reflection continuum (solid curves) from μ, the cosine of the viewing angle. From top to bottom, $\mu = 0.95,\ 0.45,\ 0.25,\ 0.05$, respectively. The dashed curve gives the angle-averaged reflection spectrum, while the dotted line represent a cut-off power-law with photon index $\Gamma = 1.9$ and cut-off energy $E_c = 300$ keV, reproducing the primary emission (Magdziarz & Zdziarski 1995).

The iron Kα line

The most prominent feature often associated with the reflection component is the iron Kα fluorescence line, which is a doublet with energies $E_{K\alpha_1} = 6.404$ keV and $E_{K\alpha_2} = 6.391$ keV and a branching ratio of 2:1 (Palmeri et al. 2003). However, as this feature is actually unresolved with the X-ray instruments on board the current X-ray observatories, it is usually assumed as a single narrow line at the mean rest-frame energy $E_{K\alpha} = 6.4$ keV.

A sketch of the emission mechanism is shown in Figure 2.5. Due to the photoelectric absorption of an X-ray photon by an iron atom, one of the two electrons inside the shell K (n=1) is expelled. In turn, the electrons of the nearby orbitals tend to redistribute themselves to bring the atom back to its ground state. When an electron from an upper shell fills the vacancy, an X-ray photon is emitted giving rise to a fluorescence line with energy equal to the energy difference between the two shells. Although the Kα transition from the L shell (n=2) to the K shell is more likely ($\sim$90%), it may happen that the gap is filled by an electron coming from the M shell (n=3); in this case we observe the Kβ transition at energy $E_{K\beta} = 7.058$ keV, with an Fe Kβ to Fe Kα branching ratio of 0.135 (Palmeri et al. 2003; Kallman et al. 2004). It is worth to note that fluorescence can occur for several elements, but iron has a higher abundance than other metals and is also favored for what concerns the losses due to the Auger effect.

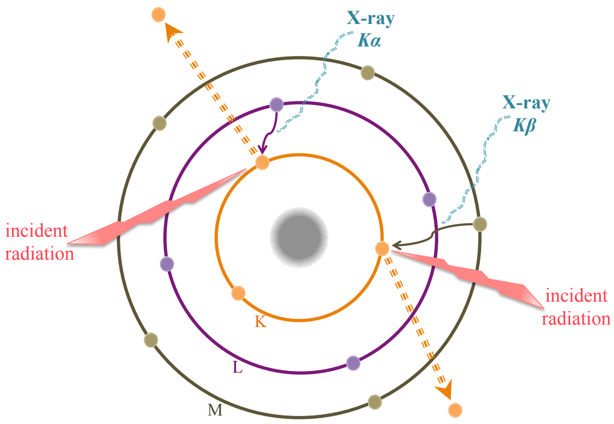

Figure 2.5. Sketch of the emission mechanism of X-ray fluorescence lines. When incident radiation hits an atom, a photoelectron of the innermost K shell can be expelled. To bring the atom back to its ground state, the electron of the upper shells redistribute filling the vacancy. Since the energy of the transition corresponds to the energy difference between the two shells, if the gap is filled by an electron coming from the L (or M) shell, a Kα (or Kβ) transition occurs.

The profile of the iron Kα line is intrinsically narrow; however, if this transition is produced by reflection from the innermost parts of the accretion disk, it can show a broad profile deformed by relativistic effects, as shown in Figure 2.6 (Fabian et al. 2000). In a non-relativistic disk, each ring produces a symmetrical double-horned line profile, where the lowest (redshifted) and highest (blueshifted) energy peaks represent the emission from the receding and approaching material, respectively (see panel (a) in Figure 2.6). The relativistic effects that come into play near the nuclear zone enhances the blue peak (see panel (b) in Figure 2.6), while the effects due to both the transverse Doppler effect and the gravitational redshift causes a shift of the line at lower energies (see panel (c) in Figure 2.6).

The different profile shown by the line in different physical conditions can therefore be used to study the dynamics of the innermost regions of AGN. Figure 2.7 illustrates how it varies according to the emissivity profile and to the inclination of the accretion disk, in case of both a non-spinning or extreme Kerr BH. In particular, the blue peak of the line is a strong function of the inclination while the redwards peak mainly depends on the inner radius of the emitting annulus (Fabian et al. 2000). Thus, their shape can provide

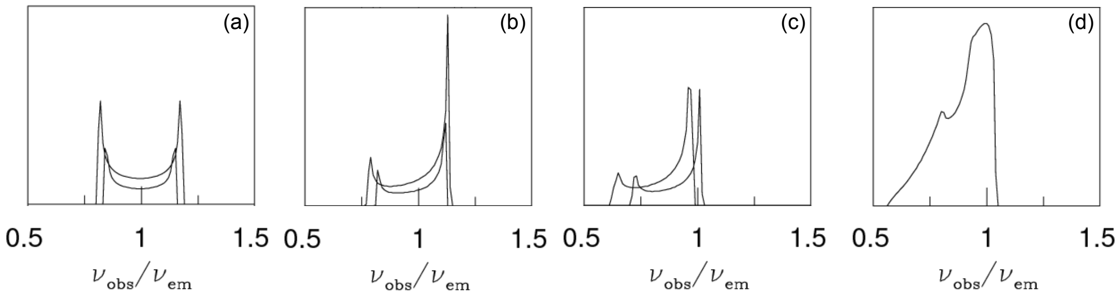

Figure 2.6. Effects of the transverse Doppler shifts, relativistic beaming, and gravitational redshifting on the profile of a broad line. Panel (a) shows the symmetric double-peaked from two narrow annuli on a nonrelativistic disk. Panel (b) included the effects of transverse Doppler shifting and relativistic beaming, while panel (c) takes into account also gravitational redshifting. Finally, panel (d) shows the resulting skewed line profile. Image adapted from Fabian et al. (2000).

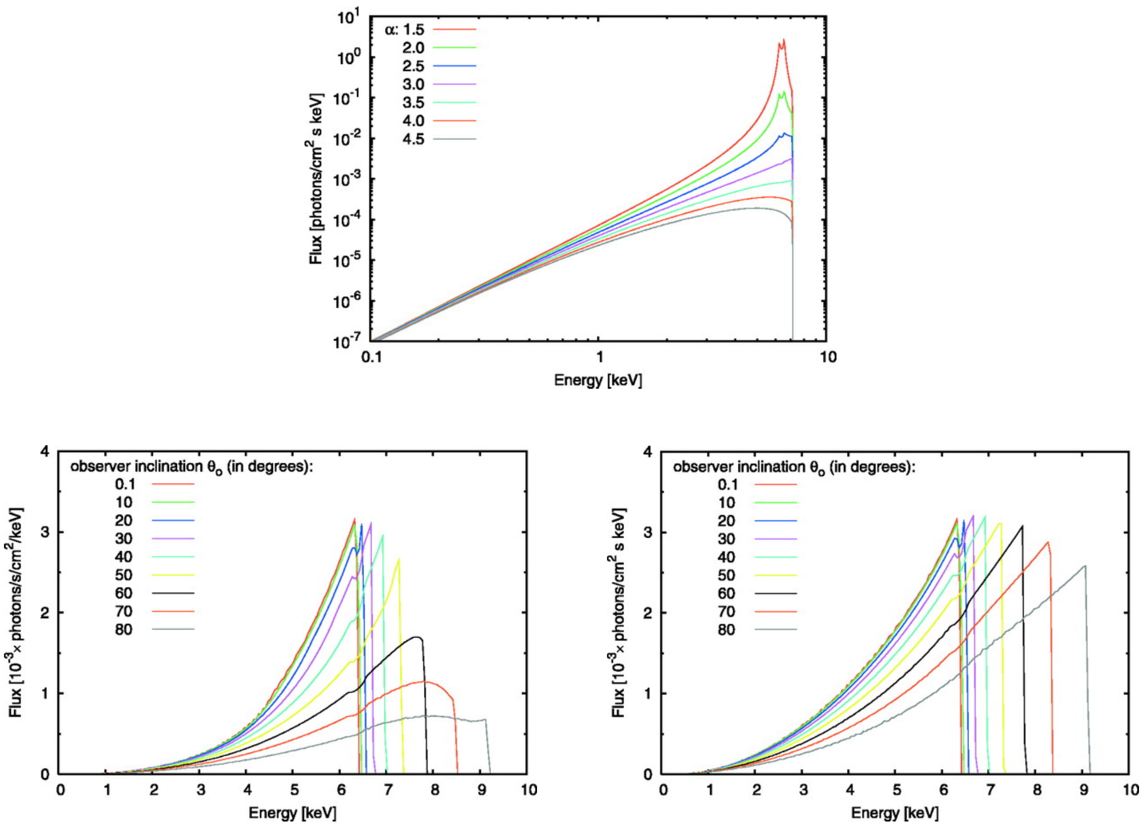

Figure 2.7. Dependence of the relativistic profile of the $K\alpha$ line on the emissivity profile (top panel) and on the inclination of the accretion disk for a Schwarschild (bottom left panel) or an extreme Kerr (bottom right panel) BH (Dovčiak et al. 2004b).

a robust measurement of both the inclination of the accretion disk and the nature of the BH, respectively (see Figure 2.8).

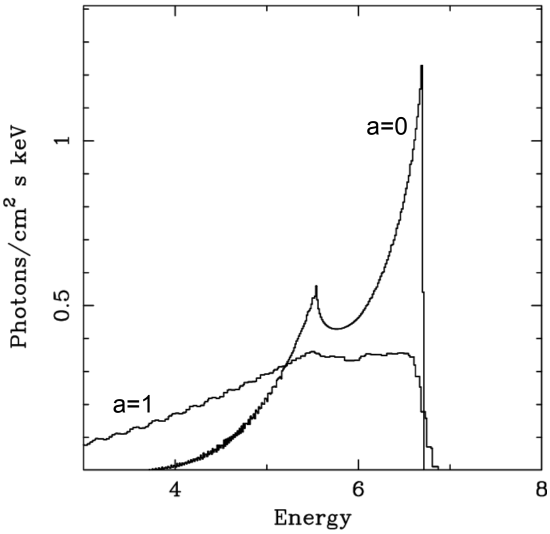

Figure 2.8. Relativistic iron line profiles produced from an accretion disk around a Schwarzschild black hole (narrower, peaky line) or a extreme Kerr black hole (broader line). Image adapted from Fabian et al. (2000).

2.1.4 The absorption component

The presence of any kind of material along the line of sight may significantly affect the X-ray spectra, providing important information on the nature of the circumnuclear medium in AGN. When crossing our line of sight, both neutral and ionized matter may give origin to different absorption features which are shortly discussed as follows.

Absorption from neutral matter

The presence of cold and neutral matter along the line of sight introduces a sharp photoelectric absorption cutoff in the power-law spectrum emitted by the nuclear source, which depends on the column density N_H of the neutral gas intercepted by the observer (see Figure 2.9). Therefore, by measuring the energy of the photoelectric absorption, it is possible to accurately determine the column density of the absorbing material. In particular, AGN are classified as "Compton-thick" if the X-ray obscuring matter has a column density which is equal to or larger than the inverse of the Thomson cross-section ($\sigma_T \sim 1.5 \times 10^{24}$ cm^{-2}), and "Compton- thin" if the column density is smaller but still in excess with respect to the Galactic absorption (Matt et al. 2003). Otherwise, they are considered as unobscured sources. A more detailed analysis about the observed X-ray spectra of Compton-thin and Compton-thick AGN is discussed in §2.2.2.

It is worth noting that cold absorption in the X-ray band is due to metals and solar abundances are usually assumed to infer the equivalent hydrogen column density (i.e. N_H). However, it is well know that most AGN can display super-solar abundances (e.g Hamann & Ferland 1999; Hamann et al. 2002; Nagao et al. 2006; Baldwin et al. 2003); therefore, as a consequence, the hydrogen column densities inferred from X-ray spectra can be often overestimated (Maiolino & Risaliti 2007).

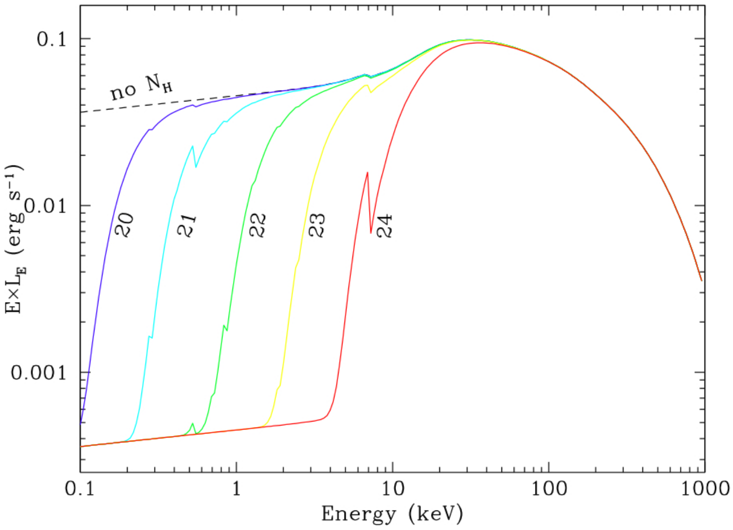

Figure 2.9. Typical AGN X-ray spectrum composed of a power-law with $\Gamma = 1.9$ and a high-energy cutoff at 300 keV, a Compton reflection hump peaking at ~30 keV, and photoelectric absorption. Each number indicates the amount of absorption of the corresponding spectrum, given as $logN_H$, with N_H in units of atoms cm^{-2}. It appears clearly evident that, for increasing values of the column density, the cut-off due to photoelectric absorption is observed at higher energies (Treister & Urry 2012).

Absorption from ionized matter

About 50% of AGN spectra are affected by soft X-ray absorption features, the so-called warm absorbers (WAs - in red in Figure 2.10), which are due to the presence of ionized material between the source and the observer (Reynolds 1997). The typical parameters describing these structures are shown in Figure 2.10 (red circles); in particular, their ionization parameter is usually in the range of $log[\xi/(erg\ cm\ s^{-1})] \sim 0 - 3$, while the equivalent hydrogen column density is of the order of $N_H \sim 10^{20} - 10^{22}$ cm^{-2}. Moreover, the absorption features due to the WAs are often blue-shifted, indicating that the gas is outflowing with velocities of the order of $v_{out} \sim 10^2 - 10^3$ km s^{-1}.

The detection of absorption lines at energies $E \sim 7 - 10$ keV are associated with transitions relative to the iron K shell (Tombesi et al. 2010; Gofford et al. 2013). Observed in a large number of AGN, they suggested the presence of highly ionized material ($log[\xi/$(erg cm s^{-1})]$\sim 3 - 6$) moving with mildly relativistic speeds ($v_{out} \sim 10^4 - 10^5$ km s^{-1}, corresponding to $0.03 - 0.33c$). These extreme absorbers are usually called Ultra Fast Outflows (UFOs - blue circles in Figure 2.10) and believed to originate in the innermost region of the accretion disk, within a hundred gravitational radii from the SMBH. Moreover, UFOs are thought to significantly affect the evolution of galaxies via AGN feedback, and a positive correlation between their outflowing velocity and the X-ray luminosity of the AGN has been observed (e.g. Matzeu et al. 2017; Pinto et al. 2018), as expected in a radiatively driven wind scenario. Both WAs and UFOs, initially considered to be of different origin, could therefore represent different parts of a single stratified outflow observed at different distances from the central SMBH (see Figure 2.11 - Tombesi et al. 2013).

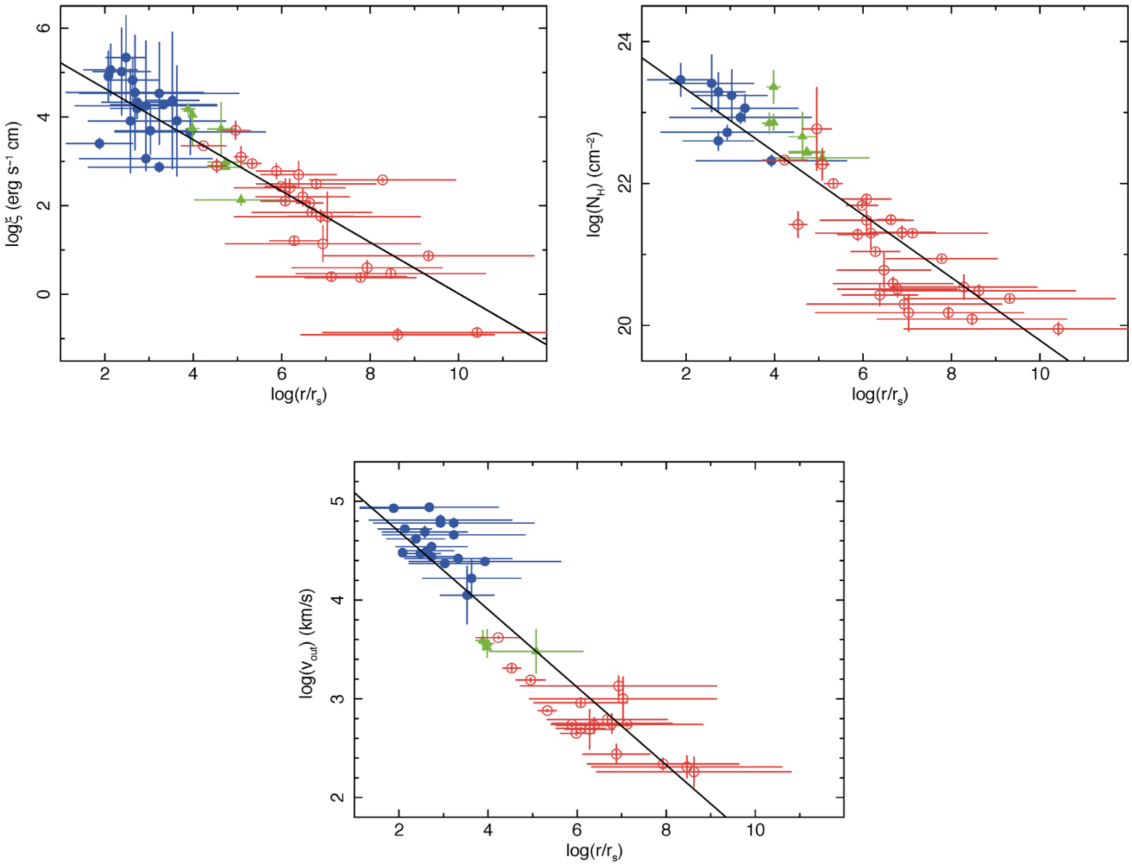

Figure 2.10. Ionization values (top left panel), equivalent hydrogen column densities (top right panel) and outflow velocities (bottom panel) as a function of the distance from the SMBH, in units of Schwardschild radii. Red and blue circles represent warm absorbers and ultra fast outflows, respectively, while green triangles indicate highly ionized absorbers with $v_{out} < 10^4$ km s^{-1} (Tombesi et al. 2013).

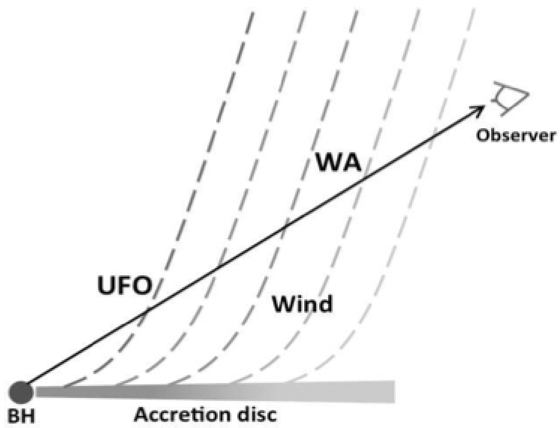

Figure 2.11. Schematic representation of a stratified accretion disk wind. In this scenario, WAs and UFOs can be identified with the same global outflow observed at different locations along the line of sight (Tombesi et al. 2013).

2.2 Obscured AGN

Obscured AGN are composite systems where the nuclear region cannot be directly observed due to the presence of material between the source and the observer. In a general framework, obscuration can be defined as any kind of matter absorbing and/or scattering a large fraction of the primary emission away from the line of sight of the observer. However, in AGN, the obscuring medium is typically composed of dust and/or gas, with the first dominating the absorption at UV-IR wavelenghts, while the latter is the most relevant source of obscuration at X-rays.

The vast majority of the AGN population are obscured: they dominate both the number density and luminosity density of accretion onto SMBHs (e.g. Ueda et al. 2014; Aird et al. 2015; Buchner et al. 2015). However, the absence of direct emission from the nuclear region makes obscured AGN more challenging to identify than unobscured sources for two key reasons (Hickox & Alexander 2018):

- diminished emission: the AGN emission can be heavily reduced, and in some cases completely extinguished, by the presence of matter along the line of sight;
- host-galaxy dilution: some physical processes taking place in the host galaxy, such as star formation, can dilutes or overwhelms the AGN emission, making the active galaxy indistinguishable from a normal one in some extreme cases.

The impact of these two effects is mainly dependent on the amount of obscuration, on the ratio between the AGN and the galaxy emission, and on the wavelength at which these systems are observed.

2.2.1 How to select obscured AGN in the X-ray band?

Obscuration in AGN can occur on a wide range of scales and physical conditions. If we assume an hydrogen cloud with radius R, its column density is given by $N_H = n_H R$, where n_H is the number density. In terms of the mass of the hydrogen atom m_H, the total mass of gas is thus given by $M_{gas} = m_H n_H \frac{4}{3}\pi R^3$. As a result, $N_H \propto R^{-2}$ for a given mass of gas; thus, the highest column densities will occur on relatively small scales and only modest amounts of obscuration can be expected over larger scales (Buchner & Bauer 2017).

Since most of the obscuring matter lies under the gravitational influence of the SMBH, X-rays appears as the most promising energy band to study obscured sources. As concerns the X-ray band, a typical criterion for identifying an AGN is to search for X-ray luminosity higher than expected from stellar processes. The usually assumed value is given by $L_X > 10^{42}$ erg s^{-1}, measuring the X-ray luminosity in the 0.5-10 keV energy band. Then, once AGN have been identified, obscured sources are characterized by several properties, such as:

- an equivalent hydrogen column density $N_H > 10^{22}$ cm^{-2};
- a low ratio of observed X-ray luminosity to intrinsic AGN luminosity, with the latter inferred from infrared or optical data;
- a prominent iron Kα line with equivalent width up to values >1 keV.

It is worth to note that obscuration in the X-ray band is a function of the rest-frame energy, with lower-energy X-ray photons more easily absorbed than higher-energy X-ray photons, due to the increase of the optical depth with decreasing energy (Wilms et al. 2000). Moreover, the X-ray emission from other astrophysical sources is typically weak if compared with the one observed in AGN, making the host galaxy contamination an issue only for heavily obscured objects. Thus, the combination of the low optical depth and the high contrast between AGN and other astrophysical sources makes X-ray observations one of the most reliable and complete methods to select obscured AGN.

2.2.2 Compton-thin vs. Compton-thick AGN

As already discussed in §2.1.4, obscured AGN can be divided into two subclasses, depending on the equivalent hydrogen column density of the material located along the line of sight. In particular, if N_H exceeds the value for which the Compton scattering optical depth becomes equal to unity (i.e. $\sigma_T^{-1} = 1.5 \times 10^{24}$ cm^{-2}), AGN are called Compton-thick; otherwise, they are called Compton-thin. Figure 2.12 shows how the observed spectrum of obscured AGN changes according to the value assumed by the absorbing column density.

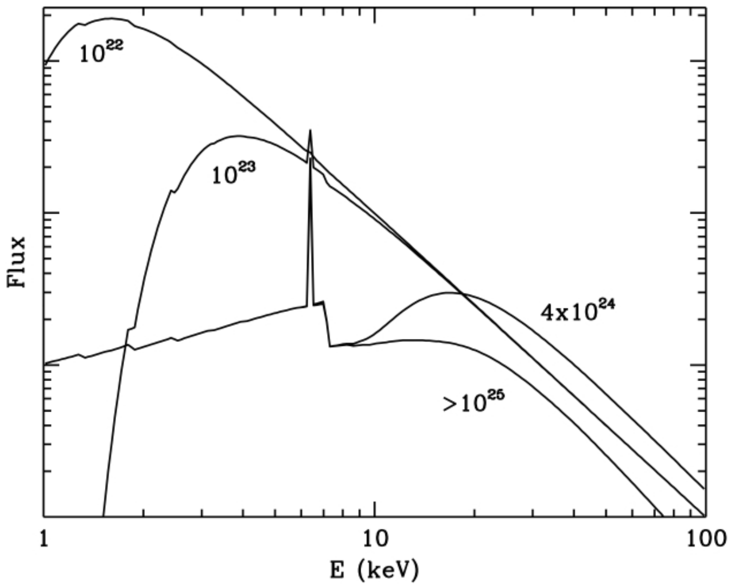

Figure 2.12. Typical spectra of obscured AGN. For increasing values of the column density, the cut-off due to photoelectric absorbtion is observed at higher energies and the observed $K\alpha$ emission line becomes more prominent (Matt et al. 2003).

Due to the distinctive absorption features affecting the X-ray spectra of AGN already discussed in §2.1.4, X-ray spectroscopy provides one of the most accurate methods of identifying obscured source and measure their level of absorption, at least up to the Compton-thin regime, where the nuclear spectrum can be directly observe above a few keV and an iron Kα fluorescent line with equivalent width up to ~ 100 eV is produced (see Figure 2.13 – right panel). On the other hand, the increase of the obscuration level up to Compton-thick values make the absorption features more challenging to detect in heavily obscured sources. One of the most important signature of Compton-thick absorption is the observation of a reflection-dominated spectrum below 10 keV, being the primary X-ray radiation completely absorbed at lower energies by the high column density of the circumnuclear matter. However, as long as the column density of the gas does not exceed 10^{25} cm^{-2}, the primary radiation is still transmitted and observable at higher energies (see Figure 2.12).

Conversely, if $N_H > 10^{25}$ cm^{-2}, the primary X-ray radiation is totally absorbed at any energy (Matt et al. 1997). Figure 2.13 shows two further clear signatures of Compton-thick absorption, namely a strong reflection component at $E > 10$ keV and a prominent Fe Kα emission line at 6.4 keV produced by the visible part of the inner wall of the torus and showing an equivalent width typically >1 keV (e.g. Mushotzky et al. 1993).

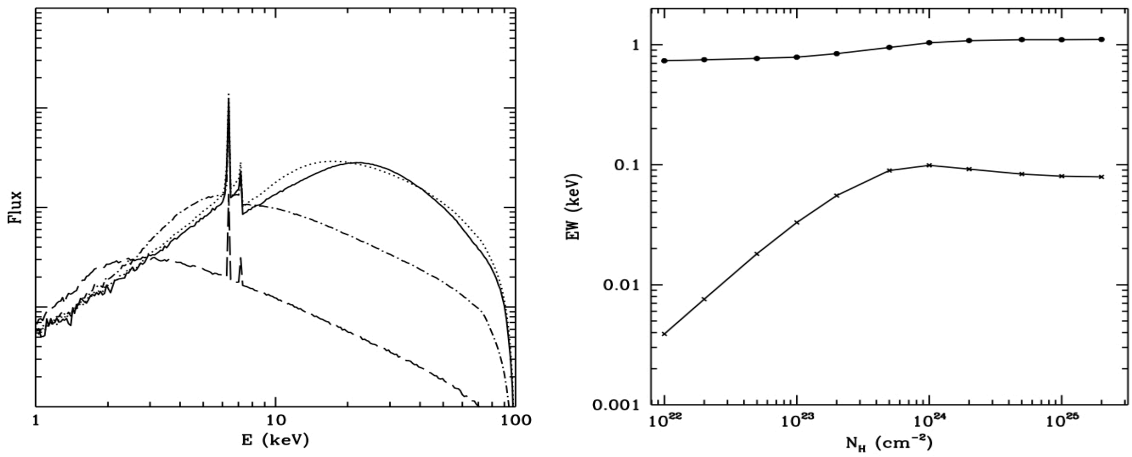

Figure 2.13. *Left panel.* Reflection spectra for different column densities: $N_H = 2 \times 10^{22}$ cm^{-2} (dashed line), $N_H = 2 \times 10^{23}$ cm^{-2} (dot-dashed line), $N_H = 2 \times 10^{24}$ cm^{-2} (dotted line) and $N_H = 2 \times 10^{25}$ cm^{-2} (solid line). *Right panels.* Equivalent width of the iron $K\alpha$ line, measured with respect to the pure reflection component (upper data) or to the total continuum (lower data). Images are taken from Matt et al. (2003).

Some examples of both Compton-thin and Compton-thick sources are analyzed in the next chapters.

2.3 Variability in the X-rays

One of the most consolidated properties of AGN is their variability observed across all the electromagnetic spectrum. In particular, the X-ray flux exhibits variability on timescales shorter than any other energy band (Vaughan et al. 2003; McHardy 2013), indicating that this emission originates from a small region very close to the SMBH. With only a few exceptions, such as in case of external irradiation or when the emitting region is moving relativistically towards the observer (e.g. Gaskell & Klimek 2003), no variability can be observed on timescales shorter than the light crossing time of the source; thus, an upper limit to the size of the emitting region is given by $R \leq c\Delta t$ (Mushotzky et al. 1993). Moreover, the combination of both the enormous amount of energy released and the very small size of the emitting regions is at the basis of the current AGN paradigm, which assumes that these sources are powered by the accretion of matter onto SMBHs.

The X-ray variability observed in several AGN can be due to multiple factors, such as a change in the intrinsic X-ray luminosity of the source, variations of the amount of the absorbing gas along the line of sight, or a combination of both. As concerns the intrinsic variability, it can be induced by any variations in the seed photons for the Comptonizing medium or might arise from processes which involve the coronal heating mechanism (Nandra 2001). Some possibilities can be related to an intrinsically hot portion of the accretion flow (e.g. Shapiro et al. 1976; Narayan & Yi 1994), or to magnetic reconnection creating hot flaring regions above the accretion disk (e.g. Nayakshin & Melia 1997; Poutanen & Fabian 1999). Further explanations include unstable accretion disks, in which local dynamo processes drives angular momentum loss in the form of an outflow (King et al. 2004), or a flare/spot scenario in which the X-ray emission is generated both in hot magnetic loops above the accretion disk and in bright spots created under the loops by strong irradiation (Czerny et al. 2004).

On the other hand, as explained above, a large fraction of AGN are obscured and part at least of their observed X-ray variability is thought to be due to the variations of the circumnuclear medium surrounding the central engine (e.g. Risaliti et al. 2002; Yang et al. 2016; Liu et al. 2017). Two different physical reasons can account for such a scenario:

- changes in the ionization state of the absorber, due to variations in the ionizing radiation;
- variations in the amount of absorbing gas along the line of sight.

If the former possibility could be consistent with an homogeneous absorber whose variability should be correlated with a change in the intrinsic flux, the variations observed in the latter case are at odds with the classical torus geometry and requires a different distribution of the absorbing matter. In particular, the observation of short timescale variations (∼days or even ∼hours) in the absorption column density in several nearby bright sources, such as NGC 1365 (Risaliti et al. 2005; Rivers et al. 2015a), NGC 4151 (Puccetti et al. 2007), NGC 4388 (Elvis et al. 2004), and NGC 7582 (Bianchi et al. 2009; Rivers et al. 2015b), has been explained assuming a clumpy geometry for the obscuring medium, consisting of a series of discrete clouds likely at sub-pc scales. A sketch of such a scenario, in which the observed X-ray variability is correlated with the typical crossing time of an absorbing cloud along the line of sight, is shown in Figure 2.14.

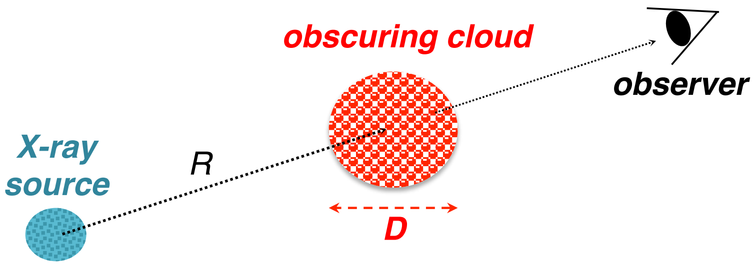

Figure 2.14. Sketch (not in scale) of a physical scenario in which the obscuring medium is composed of individual spherical clouds orbiting with Keplerian velocities around the SMBH.

Moreover, from the timescale of the observed X-ray variability, we can infer some information about the absorbing clouds, as for example their distance from the nuclear region. By considering the typical timescale of variation Δt to be the crossing time of a discrete cloud across the line of sight, and assuming the obscuring material composed of individual spherical clouds orbiting with Keplerian velocities around the nuclear region, their distance R from the SMBH is given by

$$R = \frac{GM_{BH}}{v^2}, \tag{2.11}$$

where G is the gravitational constant, M_{BH} is the BH mass and v is the transverse velocity of the obscuring matter, which is related to both the cloud dimension D and the crossing time Δt by the relation $v = D/\Delta t$, where D is in turn given by the ratio between the column density and the gas density of the absorbing cloud.

In the next chapters, some examples of AGN that can be described by such a physical scenario are discussed in detail, and some physical constraints on the circumnuclear matter within them are inferred by exploiting information obtained analyzing their observed X-ray variability.

2.4 Why studying the AGN nuclear obscuration in the X-rays?

Despite AGN are the most energetic long-lived objects in the Universe and are thought to play a fundamental role in galaxy evolution, surprisingly little is known about the physical processes acting in these objects on parsec and sub-parsec scales. Thus, the study of the reprocessed and absorbed X-ray radiation, which is the focus of this thesis work, can provide some useful information on the structure and physical properties of the circumnuclear material.

In the X-ray band the nuclear obscuration is produced by multiple absorbers on various spatial scales (see Figure 2.15), giving rise to several reflection features, the most important of which are the iron Kα line at 6.4 keV and the Compton hump peaking at about 30 keV, as we have already discussed in Section §2.1.3.

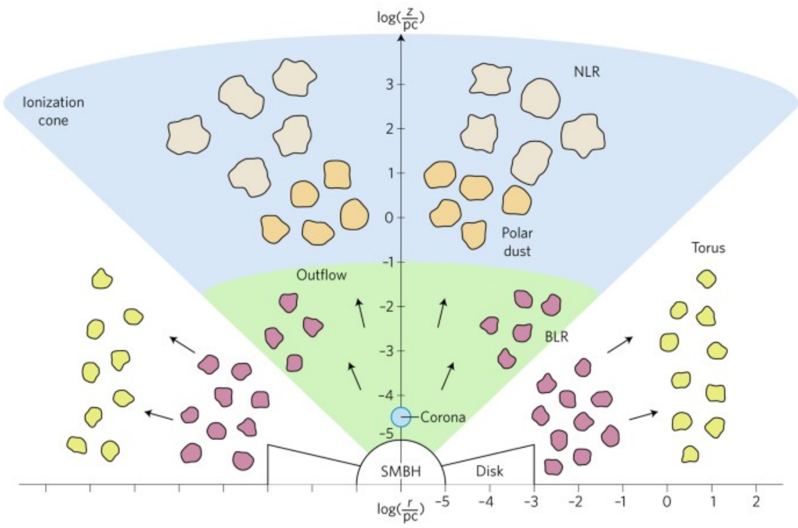

Figure 2.15. Sketch of the main AGN structures seen along the equatorial and polar direction. The different colors indicate different compositions or densities (Ramos Almeida & Ricci 2017).

Both features are almost ubiquitous in AGN, but their origin is still widely debated. Indeed, even though we know that the the iron Kα line likely arises from material with $N_H = 10^{21} - 10^{23}$ cm^{-2}, while the Compton hump originates by the reprocessing of the X-ray photons in Compton-thick material, something is still unclear, such as:

- is the origin of the narrow Kα line related to the torus (Nandra & Pounds 1994), to the BLR (Bianchi et al. 2008), or to an intermediate region between the two (Gandhi et al. 2015)?

- what fraction of the Compton hump arises from the accretion disk and what from material associated to the BLR or the torus?

Moreover, in Compton-thick material some of the iron Kα line photons are down scattered, giving rise to the so called "Compton shoulder". While the shape of this feature carries important information on the geometry and physical characteristics of the material surrounding the SMBH (Matt 2002b), the spectral resolution of the current facilities has not yet allowed to study it in detail.

In this context, a study aimed at mapping the circumnuclear matter in obscured AGN through X-ray spectroscopy, such as the one at the basis of this thesis work, is definitely useful to improve our current knowledge of the physical properties of the material surrounding the SMBH, allowing to probe the extreme physical processes acting in the innermost regions of these sources. Furthermore, it will also enable us to better understand the relationship between the AGN and the galaxy in which it resides. Indeed, connecting the active galactic nucleus with its host galaxy, the circumnuclear matter is not only responsible for feeding the black hole, but it can also provide crucial information on the feedback that nuclear activity produces on the galaxy. Looking at the structure and kinematics of the material surrounding the accreting SMBHs is thus of paramount importance to directly probe the AGN-host galaxy connection (Ramos Almeida & Ricci 2017).

3
Current X-ray observatories

Contents

In the following, the current X-ray observatories providing data for this research work are shortly described. In particular, §3.1, §3.2, §3.3 and §3.4 are devoted to describe the main characteristics of *NuSTAR*, *Swift*, *XMM-Newton* and *Suzaku*, whose data were used to describe the physical properties of the circumnuclear matter in NGC 1068 and NGC 4507 discussed in Chapter 4 and 5, respectively. Finally, §3.5 focuses on the *Chandra X-ray Observatory*, which will be useful to track the ULX population activity in the Circinus Galaxy in order to correct the polarization signal induced by the AGN for the presence of these contaminating sources (see Chapter 7 for more details).

3.1 *NuSTAR*

The *Nuclear Spectroscopic Telescope Array* (*NuSTAR* – Harrison et al. 2013) mission, which is part of the NASA's Small Explorer (SMEX) program, led for the first time a focusing high-energy X-ray telescope in orbit. Operating in the 3-79 keV energy range, this observatory extended the sensitivity of focusing far beyond the ∼10 keV high-energy cutoff achieved by all previous X-ray satellites.

NuSTAR was launched on June 13, 2012 from the Reagan Test Site on the Kwajalein Atoll in the South Pacific in a compact, stowed configuration on a Pegasus XL vehicle, and placed into a 600 km, near-circular, 6° inclination orbit. Nine days after launch an extendible mast was deployed allowing to achieve the 10.14 m instrument focal length. Both stowed and extended configurations are shown in Figure 3.1, while the satellite performances are listed in Table 3.1.

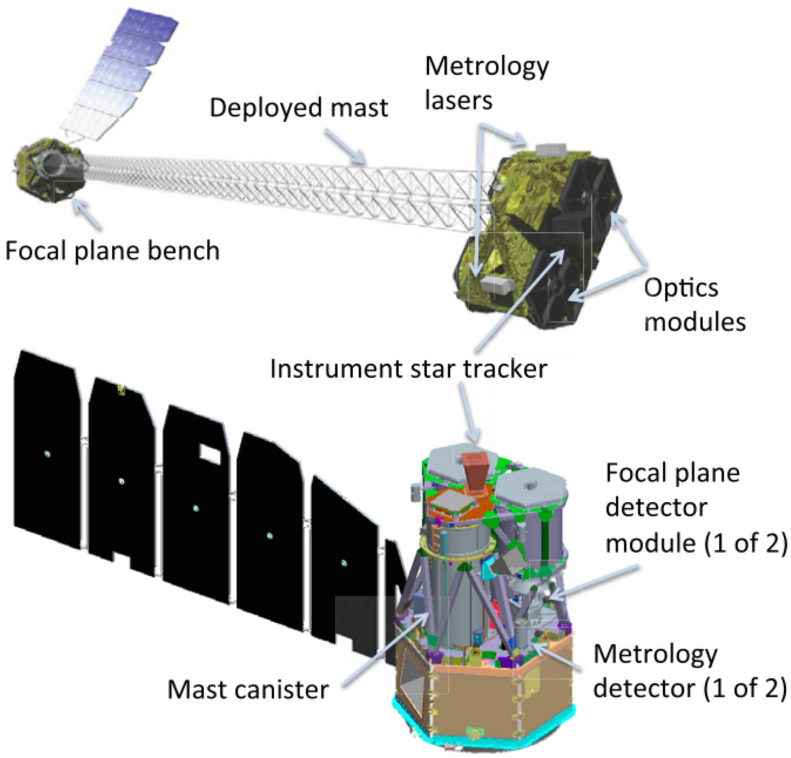

Figure 3.1. *NuSTAR* observatory in the stowed (bottom) and deployed (top) configurations (Harrison et al. 2013).

NuSTAR was designed such that one side of the observatory always faces the Sun, and pointing to a celestial target is achieved by rotating the observatory about the Sun-Earth vector, allowing to simplify the thermal design. Having no consumables, the satellite lifetime is only limited by the orbit decay, resulting in a re-entry in about 10 years.

3.1.1 Science instrument

The *NuSTAR* science instrument consists of two depth-graded multilayer-coated Wolter-I conical approximation X-ray optics (Hailey et al. 2010), focusing onto two independent solid-state focal plane detectors. The two benches that support the optics and the focal

Table 3.1. *NuSTAR* performance parameters. Adapted from Harrison et al. (2013).

Parameter	Value
Energy range	3-78.4 keV
Energy resolution (FWHM)	400 ev @ 10 keV; 900 eV @ 68 keV
Angular resolution	18 arcsec (FWHM); 58 arcsec (HPD)
Temporal resolution	2 μs
Field of view (FoV)	10 arcmin @ 10 keV ; 6 arcmin @ 68 keV
Sensitivity (6-10 keV) (10^6 s, 3σ, ΔE/E=0.5)	2×10^{-15} erg cm^{-2} s^{-1}
Sensitivity (10-30 keV) (10^6 s, 3σ, ΔE/E=0.5)	1×10^{-14} erg cm^{-2} s^{-1}
Background in HPD (10-30 keV)	1.1×10^{-3} counts s^{-1}
Background in HPD (30-60 keV)	8.4×10^{-4} counts s^{-1}

plane systems, respectively, are then separated by a ∼10 m focal length through a deployable composite mast consisting in 57 bays locked into a stiff structure by tensioned steel cables.

The optics area as a function of the off-axis source position decreases with increasing photon energy (see Figure 3.2 – left panel). Also the effective FoV (i.e. the furthest off-axis position that has 50% of the on-axis effective area) decreases with energy, resulting to be 10 arcminutes at 10 keV and 6 arcminutes at 68 keV.

The optics are coated with depth-graded multilayer structures having two different material combinations. The inner 89 shells are coated with depth-graded Pt/C multilayers reflecting efficiently below the Pt K-absorption edge at 78.4 keV, while depth-grade W/Si multilayers that reflect efficiently below the W K-absorption edge at 69.5 keV are used for the outer 44 shells (Christensen et al. 2011). The combination of the low graze angle X-ray optics and the multilayer coatings enables to achieve a significant collecting area out to 78.4 keV, as shown in the right panel of Figure 3.2.

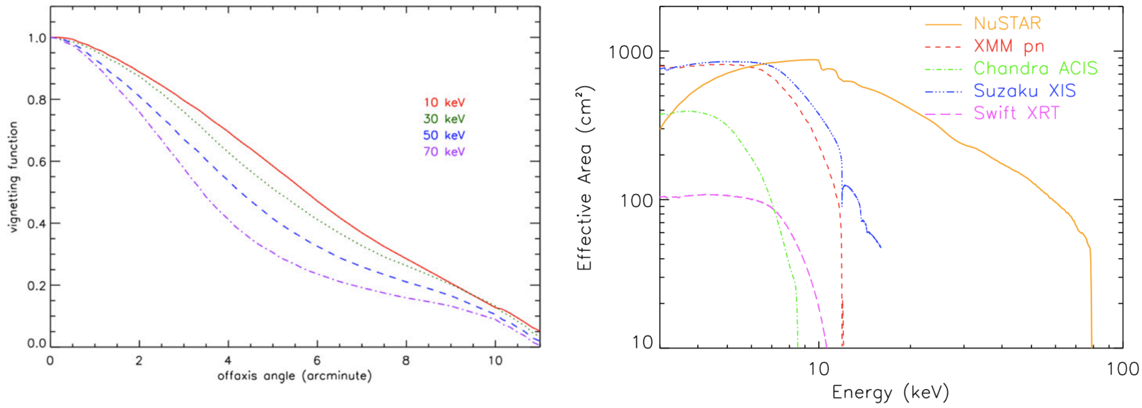

Figure 3.2. Effective collecting area of *NuSTAR* compared to selected operating focusing telescopes. We note that *NuSTAR* provides good overlap with these soft X-ray observatories and extends focusing capability up to 79 keV. (Harrison et al. 2013).

Each telescope has its own focal plane module, named FPMA and FPMB, respectively. Both of them consist of a two-by-two array of CdZnTe pixel detectors, each with 32×32 pixels 0.6 mm in size providing a 12 arcmin FoV, surrounded by a CsI anti-coincidence shield. Events resulting in a simultaneous energy deposition in both the anti-coincidence shield and the detector are rejected on board by a processor as background.

3.1.2 The *NuSTAR* background

On orbit, the background in the 3-79 keV energy band mainly depends from the geomagnetic latitude. This is the reason why the *NuSTAR* instrumental background dominating at high energies appears as lower and more stable with respect to other missions with a higher inclination orbit, which result in a larger range of geomagnetic latitudes and in more frequent passages within the South Atlantic Anomaly (SAA).

Figure 3.3 shows the typical background spectra for FPMA (in green) and FPMB (in blue). At energies below 15-20 keV, the background is dominated by diffuse cosmic flux entering through the aperture stop. Since this component is not uniform across the FoV, some care is needed in choosing regions for background subtraction at low energies for faint sources. At higher energies, the instrumental background dominates. This latter component is spatially uniform across a given detector chip, while varying from detector to detector. It consists of multiple factors, such as the albedo from Earth's atmosphere, fluorescence lines produced within the CsI anti-coincidence shield and lines mainly activated by interaction between the detectors and particle trapped in the SAA (Wik et al. 2014). The strongest instrumental lines are due to activation lines in the 22-25 keV energy range and K-shell fluorescence of Cesium and Iodine residing in the anti-coincidence shield at 28 keV and 31 keV, respectively.

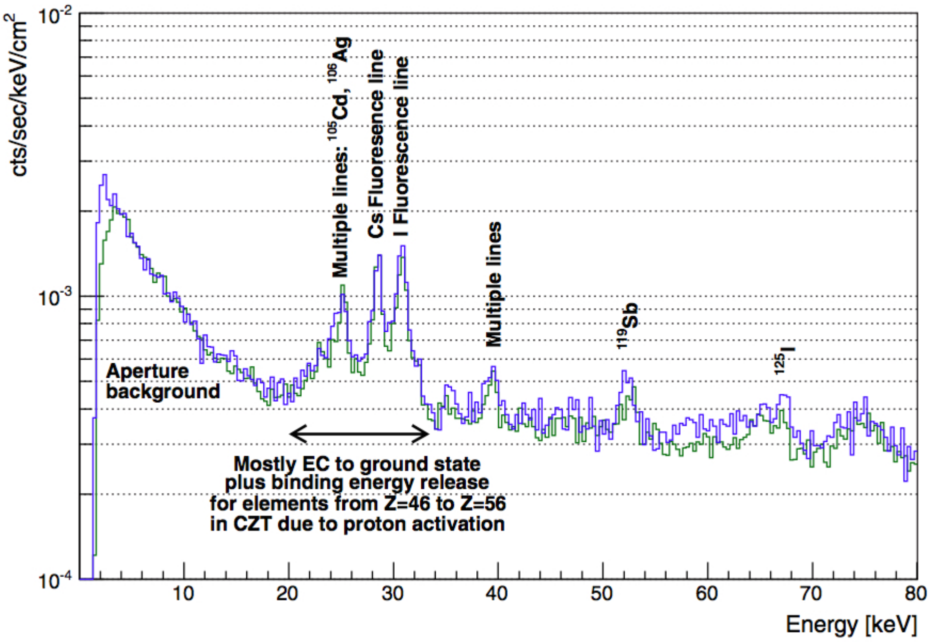

Figure 3.3. Background spectra for focal plane module A (green) and B (blue) from observations of the Extended Chandra Deep Field South (ECDFS). At energies below 15-20 keV, the background is dominated by leakage through the aperture stop, while at higher energies atmospheric albedo and activation components dominate. Several prominent emission lines, due to fluorescence from the anti-coincidence shield or activation processes, can be seen in the 20-40 keV band. Above these energies, weaker lines are still present, but the continuum dominates (Harrison et al. 2013).

3.2 *Swift*

The *Swift* mission (Gehrels et al. 2004) is a multiwavelength observatory for gamma-ray burst (GRB) astronomy, which is part of NASA's medium explorer (MIDEX) program. Successfully launched on November 20, 2004 from Cape Canaveral on a Delta 7320 rocket, it was placed into a low-Earth orbit with a period of ~90 minutes, an altitude of 600 km and an inclination of 22°.

Swift's science payload consists of three instruments mounted onto an optical bench (see Figure 3.4): a wide-field gamma-ray Burst Alert Telescope (BAT – §3.2.1) and two sensitive, coaligned narrow-field instruments, i.e. the X-ray Telescope (XRT – §3.2.2) and the Ultraviolet/Optical Telescope (UVOT – §3.2.3).

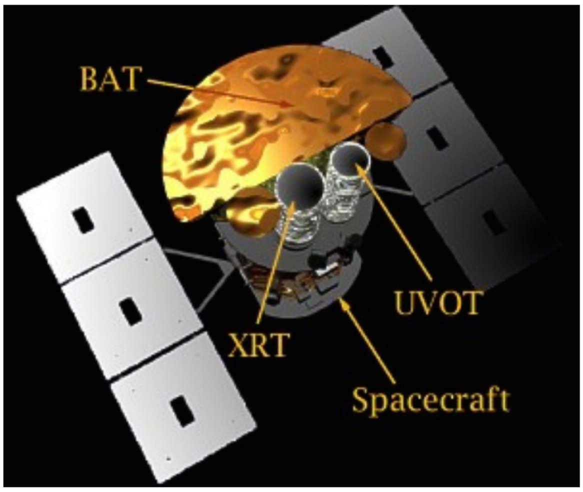

Figure 3.4. Artistic view of the multiwavelenght Swift observatory.

The primary scientific objectives of the mission are to determine the origin of GRBs and to pioneer their use as probes of the early universe. In particular, BAT scans the sky to search for new GRBs rapidly sending positions of arcminute accuracy to the spacecraft upon discovery, and triggering an autonomous spacecraft slew to observe the burst with both XRT and UVOT. Through the combination of the three instruments, Swift is thus able to rapidly determine the GRBs positions with arcsecond accuracy, measuring lightcurves and redshifts of the bursts and afterglows. In addition to the GRB science, the mission is performing the most sensitive hard X-ray all-sky survey ever made, and is able to rapidly respond with sensitive gamma-ray, X-ray, UV, and optical observations to most events on the sky (e.g. AGN flares, X-ray transients, pulsar glitches).

3.2.1 Burst Alert Telescope

The Burst Alert Telescope (BAT – Barthelmy et al. 2005), whose main characteristics are listed in Table 3.2, is a highly sensitive coded-mask instrument designed to search for GRBs over the whole sky. It consists of a coded aperture mask located 1 m above the detector plane composed of 32768 CdZnTe (CZT) detector elements and front-end electronics. The combination of the 4 mm square CZT pieces, plus the 5 mm square mask cells and the 1-m detector-to-mask separation yields an instrumental PSF of 17 arcmin FWHM. A graded-Z fringe shield, composed of 4 layers of Pb, Ta, Sn and Cu, is located on the side walls between the mask and the detector plane and under the detector plane to reduce both the instrumental and the cosmic diffuse background, while a control system with a thermal radiator is used to keep the detector plane at its nominal operating temperature of (20±1)°C.

Table 3.2. *Swift*-BAT instrument parameters. Adapted from Barthelmy et al. (2005).

Parameter	Value
Energy range	15-150 keV
Energy resolution	~7 keV
Aperture	Coded mask
Detecting area	5240 cm^2
Detector material	CdZnTe
Detector element	256 modules of 128 elements each
Detector element size	4.0×4.0×2.0 mm^3
Coded mask cell size	5.0×5.0×1.0 mm^3
Field of view (FoV)	1.4 sr (half-coded)
Point spread function (PSF)	17 arcmin
Source position accuracy	1-4 arcmin

According to the two major types of data, the BAT instrument can run in two different modes: a burst mode producing burst positions, or a scan-survey mode collecting hard X-ray survey data. Most of the BAT's time is spent accumulating events in the detector plane looking for increases in the count rate over a range of time scales as a hint of a burst. When the trigger algorithm is satisfied, the burst mode starts. Otherwise, the instrument performs continuous surveys of the hard X-ray sky accumulating detector plane maps (i.e. an energy spectrum in each detector elements) every 5 minutes with a sensitivity of the order of $\sim 2 \times 10^{-11}$ erg cm^{-2} s^{-1} in the 15-150 keV band.

3.2.2 X-ray Telescope

The X-Ray Telescope (XRT – Burrows et al. 2005) is a sensitive X-ray imaging spectrometer designed to measure afterglow positions with accuracy better than 5 arcseconds within 100 s of a burst alert from the BAT instrument, and to perform long-term monitoring of the events for days or weeks, providing moderate resolution spectroscopy, and lightcurves with high timing resolution. Its main characteristics are listed in Table 3.3.

XRT consists of a grazing incidence Wolter I telescope with 12 concentric gold-coated electroformed Ni shells focusing X-rays onto a thermoelectrically cooled e2v CCD-22 detector, similar to those used by the XMM-Newton EPIC MOS cameras. To prevent thermal gradients in the mirror module that could distort the PSF, a thermal baffle is mounted in front of the mirrors providing a warm environment at a temperature T=(18±0.5)°C. A further thermal radiator coupled to a thermo-electric cooler (TEC) was mounted on the anti-solar side of the spacecraft with the aim of cooling the detector at a temperature of -100°C on orbit, to ensure low dark current and to reduce sensitivity to radiation damage. Unfortunately, the TEC failed to activate after lunch and the CCD can be now cooled only passively to temperatures ranging from about -50°C to about -70°C through the Heat Rejection System (HRS). Operation of the CCD at a suboptimal temperature is expected to result in a gradual degradation of the XRT spectral resolution and line sensitivity over the life of the mission. Finally, to block optical light, a thin filter is installed in front of the CCD, similar to those used on the *Chandra*/ACIS and *XMM-Newton*/EPIC instruments.

Table 3.3. *Swift*-XRT instrument parameters. Adapted from Burrows et al. (2005).

Parameter	Value
Telescope	JET-X Wolter 1 (3.5 m focal lenght)
Detector	e2v CCD-22, 600 × 600 pixels
Pixel size	40 μm × 40 μm
Pixel scale	2.36 arcsec/pixel
Detector operation	photon counting, integrated imaging, and timing
Field of view (FoV)	23.6 × 23.6 arcmin
Point spread function (PSF)	18" HPD @ 1.5 keV ; 22" HPD @ 8.1 keV
Position accuracy	3 arcsec
Time resolution	0.14 ms, 1.8 ms, or 2.5 ms
Energy range	0.2-10 keV
Energy resolution	140 eV @ 5.9 keV (at launch)
Effective area	$\sim$125 cm^2 @ 1.5 keV ; $\sim$20 cm^2 @ 8.1 keV
Sensitivity	2×10^{-14} erg cm^{-2} s^{-1} in 10^4 s

The XRT readout modes are designed to allow spectroscopy for sources up to $\sim 6\times10^{-8}$ erg cm^{-2} s^{-1} in the 0.2-10 keV range, while brighter sources should be affected by pile up even in the fastest readout mode. On-board software allows fully automated observations, with the instrument selecting an appropriate observing mode for each object, based on the measured count rate.

Image mode: depending on the source flux, it uses either 0.1 or 2.5 second exposures to obtain a rapid position of a new GRB. All the accumulated charge from the target is read without any X-ray event recognition. For typical GRBs, images are highly affected by pile up; so no spectroscopic data are produced, but accurate positions and good flux estimates are provided for source with fluxes between 25 mCrabs and at least 45 Crabs.

Photodiode mode: fast timing mode designed to produce accurate information for extremely bright sources. Providing a high-speed light curve with time resolution of about 0.14 ms, this mode is useful for incident fluxes up to 60 Crabs. Since the count rates are integrated over the entire CCD, no spatial information are provided.

Windowed timing mode: it provides a 1.8 ms time resolution for a 200 column window covering the central 8 arcminutes of the FoV. It is useful for fluxes below 5000 mCrabs, and has minimal pileup below 1000 mCrabs.

Photon-counting mode: it retains full imaging and spectroscopic resolution, but time resolution is only 2.5 seconds. PC mode uses a "normal" CCD readout sequence, in which the entire CCD is read out every 2.5 seconds, and processed on-board by subtracting a bias map and searching for X-ray events in 5 x 5 pixel "neighborhoods" around each local maximum pixel. It is useful for fluxes below 1 mCrab.

3.2.3 Ultraviolet/Optical Telescope

The Ultraviolet/Optical Telescope (UVOT – Roming et al. 2005) is mounted on the *Swift* optical bench with the BAT and the XRT and is co-aligned with the XRT. Its main characteristics are reported in Table 3.4.

Based on the Optical Monitor instrument onboard *XMM-Newton* (see §3.3.2), it consists of a modified Ritchey-Chrétien reflector with a 30 cm primary mirror and a 7.2 cm

Table 3.4. *Swift*-UVOT instrument parameters. Adapted from Roming et al. (2005).

Parameter	Value
Telescope	Modified Ritchey-Chrétien (30 cm diameter)
Detector	MCP intensified CCD
Detector operation	photon counting
Detection element	256 × 256 pixels
Pixel scale	0.5 arcsec
Filters	11
Wavelenght range	170-600 nm
Field of view (FoV)	17 × 17 arcmin^2
Point spread function (PSF)	0.9 arcsec FWHM @ 350 nm
Sensitivity	B=24 in white light in 1000s

secondary mirror, placed at 45 degrees in the path of the incoming beam to steer light onto one of the two micro-channel plate intensified CCD detectors (MICs). Each MICs lies behind an identical 11-position filter wheel, which provides low-resolution UV/optical grism spectra of sources brighter than 17^{th} magnitude, and broadband photometry in the V (5440Å), B (4390Å), U (3450Å), UVW1 (2510Å), UVM2 (2170Å), and UVW2 (1880Å) bands.

UVOT can operate in six different modes, which are summarized as follows.

Slewing: the instrument control unit cleanly shuts down any current observation and performs several technical checks. When the spacecraft slews to a new target, no observations are done to preserve detector from damages due to bright sources falling within the FoV.

Settling: as the spacecraft is within 100 arcmin of the target, the observation starts. Since the target rapidly moves within the FoV, no images are collected, and the positional accuracy is only known to a few arcminutes based on BAT's centroided position.

Finding chart: it is used to localize a GRB. A 100s exposure in the V filter provides an accuracy of ∼0.3" relative to the background stars in the FoV. The finding chart provides useful information for both subsequent automated target exposures and ground-based observatories.

Automated targets: this operating mode consists in two different sequences of exposures for bright or dim GRBs chosen according to the optical profile of the afterglow and to time since the initial burst.

Preplanned targets: UVOT operates in this mode when no automated targets have to be observed. A wide range of exposure times (from 10 s to 1000 s) is possible, and photons can be collected in event and/or image modes. Pre-planned targets include previous automated targets, targets of opportunity (ToO), and survey target.

Safe pointing targets: predetermined locations on the sky considered as observationally safe for UVOT, which are used when neither automated nor preplanned targets can be pointed due to observing constraints.

3.3 *XMM-Newton*

The space satellite *XMM-Newton* (Jansen et al. 2001) was launched on December 10, 1999 from the space base of Kourou (French Guiana), and positioned on a highly elliptical orbit having a period of 48 hours, an inclination of 40 degrees, a perigee of 7000 km and an apogee of 114000 km. Initially known with the acronym *XMM* (*X-ray Multi-Mirror*) due to its configuration, it was renamed *XMM-Newton* on February 9, 2000, in honor of Sir Isaac Newton.

With a weight of 3800 kg, a length of 10.8 meters and a maximum width of over 16 meters with fully deployed photovoltaic panels, *XMM-Newton* (see Figure 3.5) is the largest scientific satellite of the European Space Agency (ESA). It is equipped with three X-ray telescopes and an optical/UV telescope allowing simultaneous observations in the respective bands of the electromagnetic spectrum. The scientific instruments on board the satellite, which can operate independently and simultaneously, are:

- European Photon Imaging Camera (EPIC – Strüder et al. 2001; Turner et al. 2001): three CCD cameras for imaging, moderate resolution spectroscopy, and photometry in the X-ray band;

- Reflection Grating Spectrometer (RGS – den Herder et al. 2001): two spectrometers for high resolution X-ray spectroscopy and spectro-photometry;

- Optical Monitor (OM – Mason et al. 2001): a 30-cm optical/UV telescope for imaging and grism spectroscopy in the optical and UV band.

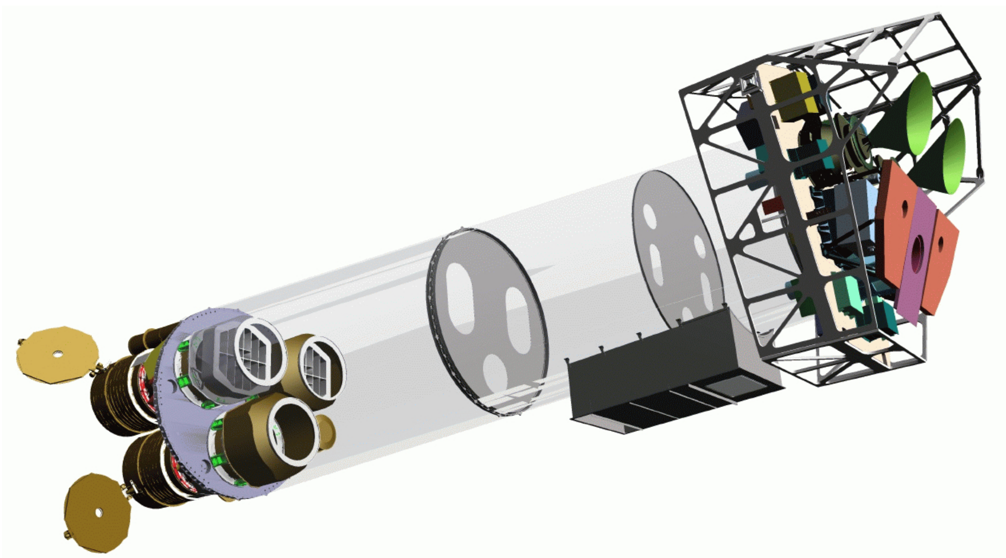

Figure 3.5. The payload of *XMM-Newton*. The three X-ray telescopes are visible at the lower left. At the right end of the assembly, the focal instruments are shown: the EPIC-MOS cameras with their radiators (black/green "horns"), the radiator of the EPIC-pn camera (in violet) and those (in light blue) of the RGS receivers (in orange). The black box at the bottom of the bus is the outgassing device. Credit: ESA/*XMM-Newton*.

3.3.1 The X-ray telescopes

The three X-ray telescopes onboard the *XMM-Newton* observatory are co-aligned with an accuracy of about 1-2 arcseconds across the full FoV. Each of them consists of 58 mirror shells with a Wolter-I type configuration, which are nested in a coaxial and confocal configuration providing a large collecting area over a wide energy band (Aschenbach & Braeuninger 1988). The mirror characteristics are listed in Table 3.5.

Table 3.5. Specifications of the three X-ray telescopes onboard the *XMM-Newton* observatory.

Parameter	Description
Telescope focal lenght	7500 mm
Number of mirrors per telescope	58
Inner/outer mirror radius	153 mm / 350 mm
Inner/outer mirror thickness	0.47 mm / 1.07 mm
Mirror substrate material	nickel
Reflective coating	gold

In the focal planes of the X-ray telescopes reside the three EPIC cameras and the two detectors of the RGS spectrometers. One telescope has a pn camera at the focus, while the remaining two are each equipped with a MOS camera and an RGS unit, which in turn consists of a Reflection Grating Assembly (RGA) and an RGS Focal Camera (RFC). The optical paths of the three X-ray telescopes are shown in Figure 3.6. The pn camera receives 100% of the incident radiation, while the MOS cameras collect only 44% of the incoming photons. Due to the presence of an RGA grating, part of the incident radiation (40%) is indeed deflected onto a secondary focus towards the RFC camera. The remaining light (16%) is instead absorbed by the support structures of the RGAs.

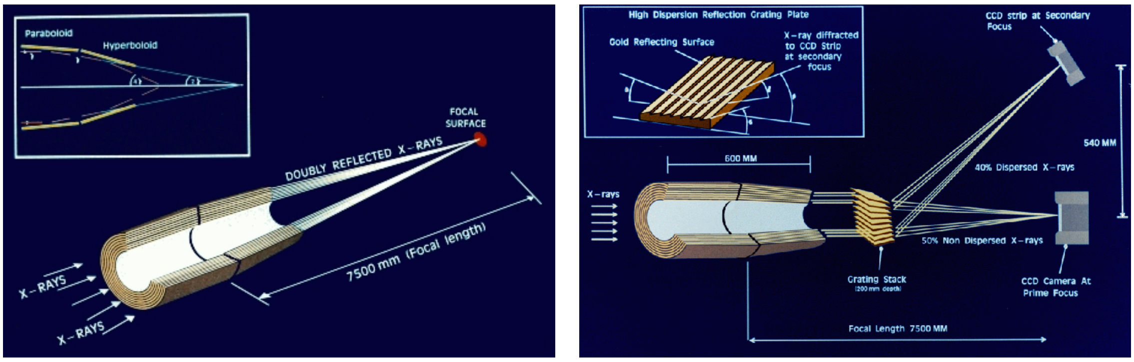

Figure 3.6. Optical paths of the X-ray telescopes equipped with pn (left image) and MOS (right image) cameras (not to scale). 100% of the incoming light focused by the multi-shell grazing incidence mirrors is directed onto the pn camera, while only 44% is collected in the MOS cameras, due to the presence of grating assemblies in their light paths, diffracting part of the incoming radiation onto their secondary focus. Credit: ESA/*XMM-Newton*.

3.3.2 The scientific instruments

The six scientific instruments (pn, MOS1, MOS2, RGS1, RGS2 and OM) are shortly described in the following, while their main characteristics are listed in Table 3.6.

Table 3.6. Main characteristics of the scientific instruments onboard the *XMM-Newton* observatory.

	EPIC MOS	EPIC pn	RGS	OM
Bandpass	0.15-12 keV	0.15-12 keV	0.35-2.5 keV	180-600 nm
Orbital target visibility ^{a}	5-135 ks	5-135 ks	5-135 ks	5-145 ks
Sensitivity ^{b}	$\sim 10^{-14}$ ^{c}	$\sim 10^{-14}$ ^{c}	$\sim 8 \times 10^{-5}$ ^{d}	20.7 mag ^{e}
Field of view	30’	30’	$\sim 5'$	17’
PSF (FWHM/HEW)	5"/14"	6"/15"	—	1.4"-2.0"
Timing resolution ^{f}	1.75 ms	0.03 ms	0.6 s	0.5 s
Spectral resolution ^{g}	$\sim$ 70 eV	$\sim$ 80 eV	0.04/0.025 Å	180

Notes. ^{a} Total time available for science per orbit. ^{b} After 10 ks. ^{c} In the range 0.15-12.0 keV, in units of erg s^{-1} cm^{-2}. ^{d} O VII 0.57 keV line flux in photons cm^{-2} s^{-1}, for an integration time of 10 ks and a background of 10^{-4} photons cm^{-2} s^{-1} keV^{-1}. ^{e} 5-σ detection of an A0 star in 1000 s. ^{f} In fast data acquisition mode, i.e. timing mode for EPIC, spectroscopy mode for RGS1, and fast mode for OM. ^{g} At 1 keV energy.

The European Photon Imaging Cameras

The three X-ray telescopes onboard *XMM-Newton* are equipped with an EPIC camera that offers the possibility to obtain images over a field of view of about 30 arcminutes and in the 0.15-12 keV energy band with a moderate spectral and angular resolution, as shown in detail in Table 3.6. Two of them carries an EPIC MOS (Metal Oxide Semi-conductor) CCD arrays, while the third is equipped with an EPIC pn camera. The two types of cameras (pn and MOS) are fundamentally different, both for what concerns the configuration of the CCDs (see Figure 3.7), as well as for their properties, as shortly summarized in the following.

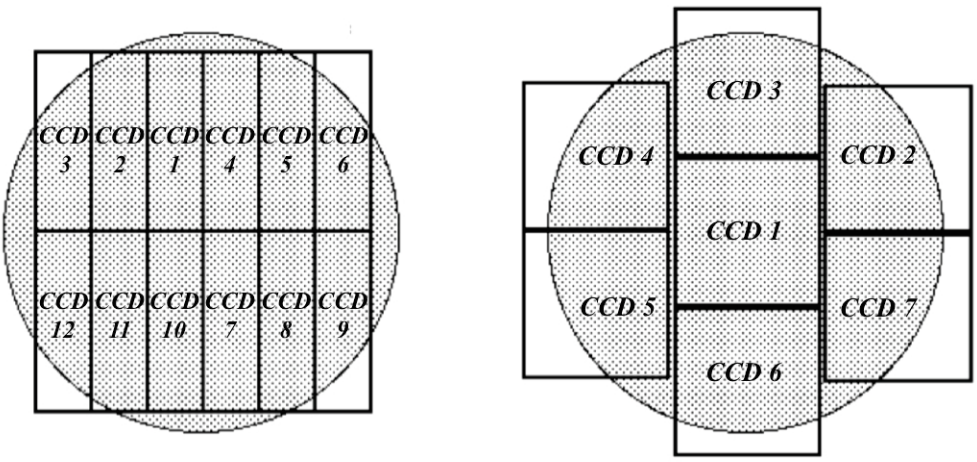

Figure 3.7. Sketch of the CCD configuration for EPIC pn (left image) and MOS (right image) cameras.

- **CCD configuration**: the chip geometry for both pn and MOS cameras is shown in Figure 3.7. The pn camera consists of twelve $13.6' \times 4.4'$ coplanar back-illuminated CCDs, while the two MOS cameras are rotated by 90° with respect to each other and each of them carries seven $10.9' \times 10.9'$ non-coplanar front-illuminated CCDs.

- **Operating science modes**: the different science modes that can be used for EPIC cameras are listed below. It is worth to note that in the case of MOS the outer ring of 6 CCDs remain in standard imaging mode, while the central MOS CCD can be operated separately.

  - **Full Frame mode**: all pixels of all CCDs are read out, thus covering the whole FoV. An Extended Full Frame mode is available for EPIC pn only, where the frame time is longer with respect to the normal Full Frame mode.
  - **Partial Window mode**: this operating mode may be useful to minimize the effects of pile-up, when very bright sources are observed. For EPIC pn, only half area of each of the 12 CCD (Large Window) or only part of the CCD 4 (Small Window) is used. For MOS cameras, only part of the central CCD is read out, with Large Window and Small Window mode depending on the extension of the CCD active area.
  - **Timing mode**: spatial information is acquired in only one dimension in order to speed up the readout. For pn, the full width of CCD 4 is used, whereas for the MOS cameras the active area is reduced to about 100 columns around the aimpoint. An additional mode (Burst Mode) is available for EPIC pn only, which offers very high time resolution (7 μs), but has a very low duty cycle of 3%.

  The optimal operating mode for a given source depends on its characteristics as well as on the scientific case.

- **Readout time**: the design of the EPIC pn provides a readout node for each column of pixels, allowing a much faster readout time with respect to the MOS cameras (Table 3.7), in which at most two readout nodes are available for each CCD.

Table 3.7. Temporal resolution of the EPIC pn and MOS cameras in different operating modes.

Science mode	EPIC pn	EPIC MOS
Full Frame mode	73.4 ms	2.6 s
Extended Full Frame mode	199.1 ms	—
Large Window Mode	47.7 ms	0.9 s
Small Window Mode	5.7 ms	0.3 s
Timing mode	0.03 ms	1.75 ms
Burst mode	7 μs	—

Due to its high temporal resolution, the pn camera is also optimized for photometric studies of highly variable sources.

The Reflection Grating Spectrometers

Prior to reach the MOS cameras, about half of the X-ray radiation reflected by the mirrors is deflected onto a secondary focus by the Reflection Grating Spectrometers (RGSs – den Herder et al. 2001). Each RGS consists of an RGA composed of 182 identical gratings diffracting the incoming light towards nine back-illuminated MOS CCDs, which detect the dispersed spectra in single photon counting mode. The RGS design is optimized for the detection of the K-shell transitions of carbon, nitrogen, oxygen, neon, magnesium, and silicon, as well as the L shell transitions of iron. CCDs are nominally cooled to -80°C to reduce the dark current. By lowering the temperature to -120°C, also the increase in their charge transfer inefficiency due to radiation damage can be reduced.

The position of the X-ray on the detector gives the wavelength of the incoming radiation through the dispersion equation:

$$m\lambda = d(\cos\beta - \cos\alpha), \tag{3.1}$$

where $m = -1, -2, ...$ is the spectral order, d is the groove spacing, while α and β are the angles of the incident and dispersed light, respectively, both measured from the grating plane (see Figure 3.8).

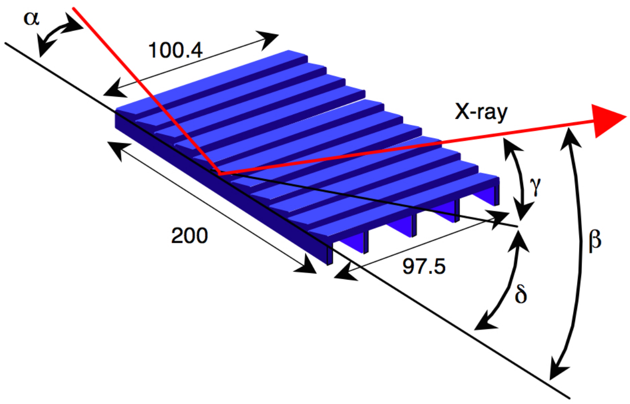

Figure 3.8. RGS diffraction geometry: the X-ray radiation strikes the gratings at an angle of incidence α with respect to the plane of the grating, and emerges at an angle β related to the radiation wavelenght by Equation 3.1 (den Herder et al. 2001).

The RGSs can be used in three different operating modes:

- **Spectroscopy**: the nine CCDs are read out sequentially in frame transfer mode, resulting in an accumulation time of about 5.7 s;
- **High time resolution**: only one CCD is read out, providing the shortest accumulation time (∼15 ms);
- **Diagnostic**: data are transferred to the ground without any on-board data processing. This operating mode is used for dark current and system noise level verification.

The Optical Monitor

Providing coverage between 170 nm and 650 nm of the central 17 arcmin square region of the X-ray field of view, the Optical/UV Monitor Telescope (OM – Mason et al. 2001) allows to simultaneously observe *XMM-Newton* targets in the X-ray and ultraviolet/optical bands.

The OM is equipped with a 30-cm diameter Ritchey Chrétien telescope, whose light path is shown in Figure 3.9. The incoming radiation collected by the primary mirror is reflected onto a hyperboloid secondary mirror, which in turn reflects the light onto a rotatable 45° flat mirror located behind the primary. X-rays are then directed onto one of the two redundant detector chains that are both composed of a 11-aperture filter wheel and a microchannelplate-intensified CCD detector.

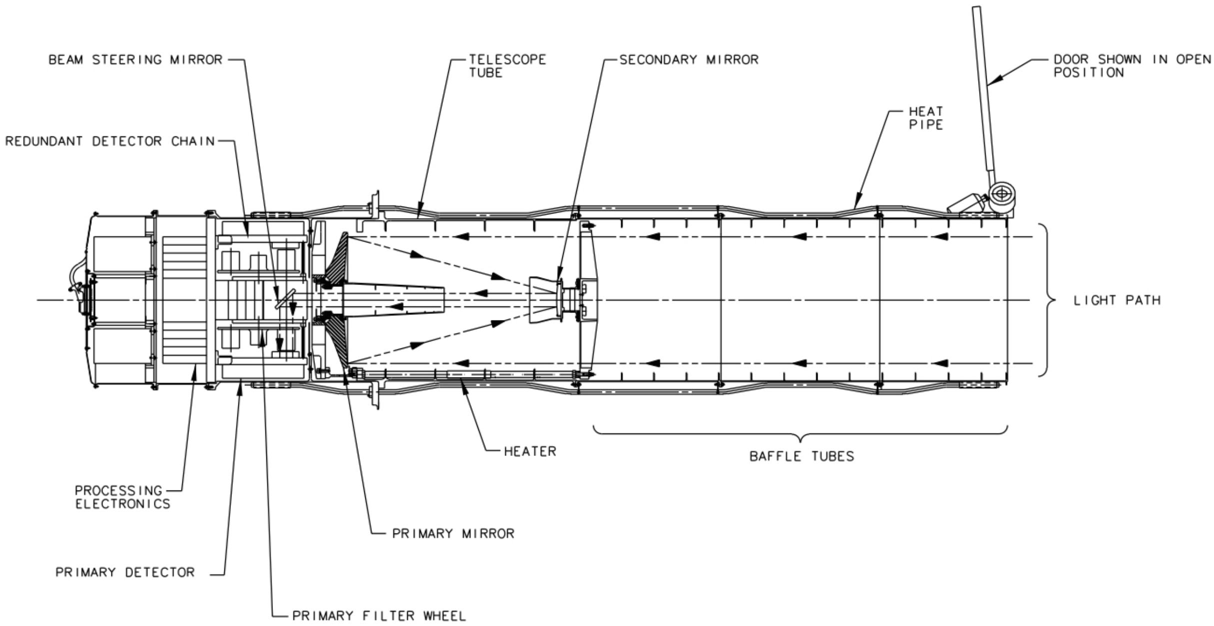

Figure 3.9. Schematic view of the OM telescope module showing the light path from the primary mirror to the detectors (Mason et al. 2001).

The filter wheel is composed of:

- a blanked filter used as a shutter to prevent light from reaching the detector;
- six optical (V, U, B) and UV (UVW1, UVW2, UVW3) filters covering wavelenghts between 180 nm and 580 nm;
- a white filter, which transmits light over the full range of the detector to give maximum sensitivity to point sources;
- two grisms for low-resolution spectroscopy, one optimised for the UV (grism 1) and the other for the optical range (grism 2);
- a magnifier, which provide high spatial resolution of the central portion of the FoV in the 380-650 nm band.

The OM can operate in two different modes depending on whether spatial coverage (image mode) or timing information (fast mode) are required.

3.4 *Suzaku*

Suzaku (Mitsuda et al. 2007), formerly known as *Astro-E2*, was born as recovery mission for *Astro-E*, which did not achieve orbit during launch in February 2000 due to the failure of the first stage motor. Launched by Japan Aerospace Exploration Agency (JAXA) with the M-V launch vehicle from JAXA's Uchinoura Space Center (USC) on 2005 July 10, it was placed into a near circular orbit at 570 km altitude with an inclination angle of 31°.

A schematic view of the satellite is shown in Figure 3.10. The scientific payload was initially composed of three distinct co-aligned scientific instruments: an X-ray Imaging Spectrometer (XIS – see §3.4.1), a hard X-ray detector (HXD – see §3.4.2) and an X-ray micro-calorimeter (XRS – see §3.4.3), which failed shortly after launch.

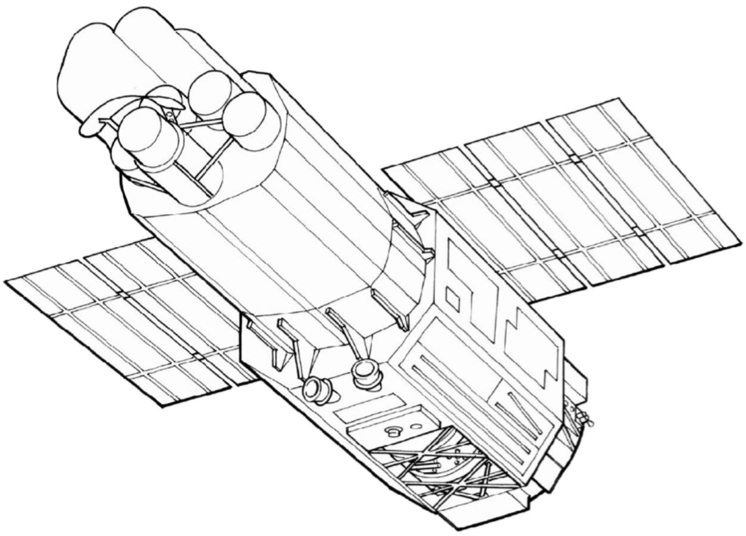

Figure 3.10. Schematic view of the *Suzaku* satellite in orbit (Mitsuda et al. 2007). The X-ray telescope (XRT-S) for the X-ray spectrometer (XRS), and the four X-ray telescopes (XRT-Is) for the X-ray CCD camera (XIS) are clearly visible on the top.

3.4.1 The X-ray Imaging Spectrometer

The X-ray Imaging Spectrometer (XIS – Koyama et al. 2007) is composed of four X-ray sensitive imaging CCD cameras located in the focal plane of a dedicated X-ray telescope (XRT-I – Serlemitsos et al. 2007). XRT-Is are grazing-incidence Wolter I telescopes with 175 tightly nested, thin-foil conical mirror shells, providing a moderate imaging capability in the 0.2-12 keV energy range. As concerns the CCD cameras, three of them (XIS0, XIS2, and XIS3) are front illuminated (FI), while the other (XIS1) is back-illuminated (BI). A three-stage thermo-electric cooler (TEC) is used to cool the CCDs to their nominal operating temperature of -90°C, while a radiation shielding prevents damages when the spacecraft passes through the South Atlantic Anomaly (SAA). The main characteristics of both XRT-I and XIS are listed in Table 3.8, while the effective area of the XRT+XIS system is shown in Figure 3.11.

Nowadays, only two of the XIS-FI are still operating, while XIS2 suffered a catastrophic damage on 2006 November 9, presumably due to a collision by a micro-meteorite.

Table 3.8. Main characteristics of the XRT-I+XIS system onboard the *Suzaku* observatory. Adapted from Koyama et al. (2007).

Parameter	Value
Field of view	$18' \times 18'$
Energy range	0.2-12 keV
Detector	MOS-type CCD, 1024×1024 pixels
Pixel size	24μm$\times 24\mu$m
Energy resolution	∼130 eV (FWHM) @5.9 keV
On-axis effective area	∼330 cm^2 (FI), ∼370 cm^2 (BI) @ 1.5 keV ∼160 cm^2 (FI), ∼110 cm^2 (BI) @ 8 keV

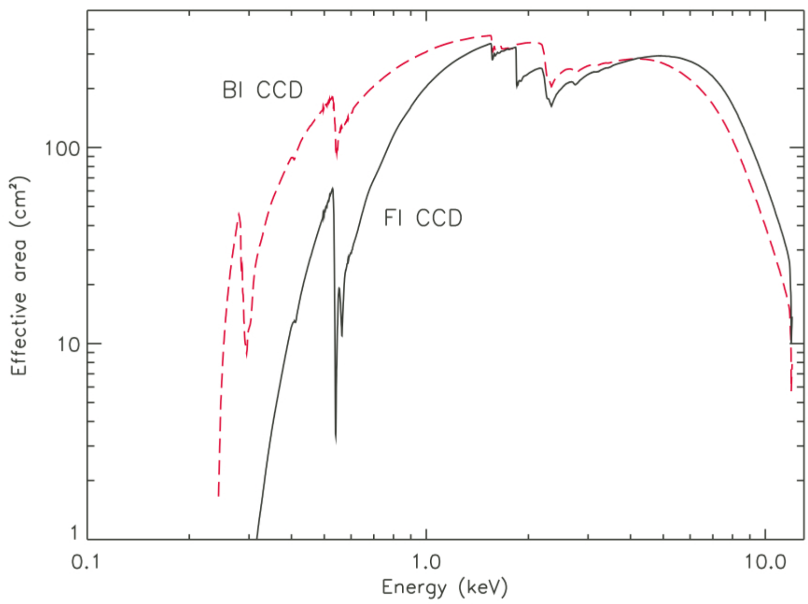

Figure 3.11. Effective area of the XRT-I+XIS system, for both the FI (XIS0, XIS2, and XIS3) and BI (XIS1) CCDs (Mitsuda et al. 2007).

3.4.2 The hard X-ray detector

The hard X-ray detector (HXD – Takahashi et al. 2007) is a non-imaging, collimated hard X-ray scintillating instrument sensitive in the 10-600 keV energy range, whose main characteristics are listed in Table 3.9. HXD is composed of a sensor part (HXD-S), an analog (HXD-AE) and a digital electronics system (HXD-DE). Taking advantage from both a "well-type active shield" and a "compound-eye configuration" (i.e. each unit is also an active shield for adjacent units), HXD allows to minimize the background level, achieving a higher sensitivity than any previous instrument above 10 keV.

Table 3.9. Main characteristics of the HXD system onboard the *Suzaku* observatory (Takahashi et al. 2007).

Parameter	Value
Field of view	34×34 arcmin^2 (E$\lesssim$100 keV); 4.5×4.5 deg^2 (E$\gtrsim$100 keV)
Energy range	10-600 keV (total band); 10-70 keV (PIN); 40-600 keV (GSO)
Energy resolution (FWHM)	$\sim$3 keV (PIN); $7.6/\sqrt{E_{MeV}}$ %
Effective area	$\sim$160 cm^2 @ 20 keV; $\sim$250 cm^2 @ 100 keV
Time resolution	61 μs or 31 μs

HXD-S is a compound-eye detector instrument composed of 16 main detectors arranged as a 4×4 array surrounded by 20 BGO anti-coincidence shield counters. Each detector unit consists of a combination of GSO/BGO well-type phoswich counter and four PIN silicon diodes located in front of the GSO scintillator, whose effective area is shown in Figure 3.12. The PIN diodes are mainly sensitive below 60 keV, while the GSO/BGO scintillators are sensitive above 30 keV. All the units work independently at an operating temperature of -20°C, which reduce the leakage current at few nA. As well as for background shielding, the outer BGO anti-coincidence scintillators can also be used as a Wide-band All-sky Monitor (WAM) to detect bright X-ray transients, γ-ray bursts, and solar flares.

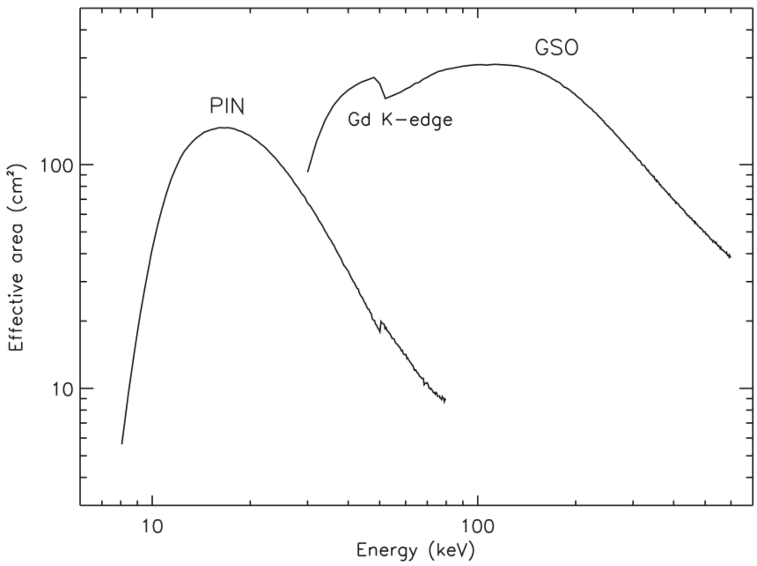

Figure 3.12. Total effective areas of the PIN and GSO constituting each HXD detector unit, as a function of the energy. (Mitsuda et al. 2007).

3.4.3 The X-ray spectrometer

Suzaku's X-ray Spectrometer (XRS – Kelley et al. 2007) was supposed to be the first X-ray microcalorimeter to fly onboard an orbiting observatory. Its design was composed of 30 active pixels in a 6×6 geometry, with the four corner pixels plus two further ones that are inactive (see Figure 3.13). Each pixel size is 625 μm × 625 μm, covering a sky area of roughly 2.9×2.9 arcmin^2. The typical gap size between the pixels is 16 μm, resulting in a filling factor of about 95%.

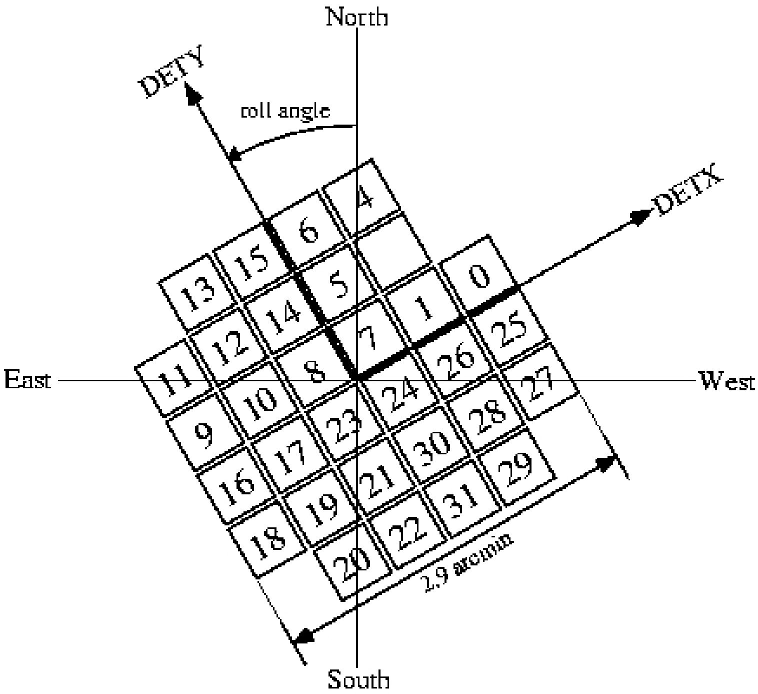

Figure 3.13. The XRS microcalorimeter array, showing the layout of the pixels as projected onto the sky. The unlabeled pixel is inactive. Credit: NASA/GSFC.

A silicon PIN anti-coincidence detector beneath the microcalorimeter array was expected to detect the background particles in order to reject their associated events for later data analysis.

The detector assembly, also known as Front End Assembly (FEA) should have been kept at a temperature of 65 mK to operate at the maximum performance, providing an unprecedented energy resolution of 7 eV (FWHM) over the 0.3-12 keV energy band. To this aim, XRS was contained in an insulated dewar cooled to 65 mK by an helium tank filled with 25 litter liquid helium at about 1.5 K surrounded by a neon tank filled with 100 litter solid neon at a temperature of about 17 K. The FEA was placed inside the helium tank, which was thermally connected to the Adiabatic Demagnetization Refrigerator (ADR), cooling the system down to 65 mK. Unfortunately, XRS prematurely lost all its liquid helium cryogen one month after launch and is no longer operative.

3.5 *Chandra*

The *Advanced X-Ray Astrophysics Facility* (*AXAF*), renamed the *Chandra X-ray Observatory* (*CXO* – Weisskopf et al. 2000) in honor of Subrahmanyan Chandrasekhar is the X-ray component of NASA's Great Observatory Program, which includes the infrared *Spitzer Space Telescope* (*SST*) officially decommissioned on January 30, 2020, the *Hubble Space Telescope* (*HST*) for observations in the optical band, and the no longer operational *Compton Gamma-Ray Observatory* (*CGRO*).

Launched on 1999, July 23 by the Space Shuttle Columbia, *Chandra* was placed in an highly elliptical orbit with a period of ~ 64 hours, which is stable for decades and yields a high observing efficiency. Both the fraction of the sky occulted by the Earth and the time of high background due to the passage of the satellite into Earth's radiation belt are small over the most orbital period; thus, more than 70% of the time is useful and uninterrupted observations lasting more than 2 days are possible.

The different components constituting the *CXO* are shown in Figure 3.14. Apart from the spacecraft module, which provides the support structure and the environment necessary for the telescope and the science instruments to work, *Chandra* is composed of two main parts: the telescope system, and the Integrated Science Instrument Module (ISIM). The former is composed of the High Resolution Mirror Assembly, two transmission gratings and a 10-meter-long Optical Bench Assembly (OBA), while the latter houses the High-Resolution Camera (HRC) and the Advanced CCD Imaging Spectrometer (ACIS).

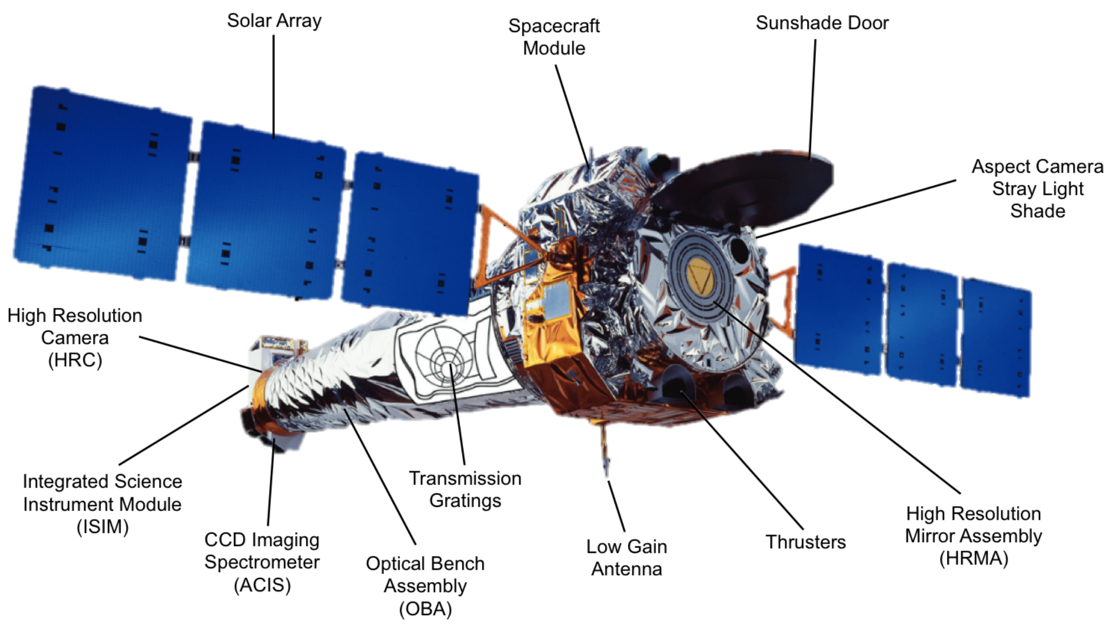

Figure 3.14. The *CXO* flight system, which include the spacecraft, the X-ray telescope and the science instruments onboard *Chandra*, is shown. Credit: NASA/CXC.

Chandra was designed to provide significant advances over previous X-ray observatories with regards to spatial and spectral resolution. With its combination of large mirror area, accurate alignment and efficient X-ray detectors, *Chandra* has eight-times greater resolution and is 20 to 50 times more sensitive than any previous X-ray telescope.

3.5.1 The telescope system

The whole telescope system is composed of three main parts: the X-ray optics, two Objective Transmission Gratings (OTGs) that can be inserted into the X-ray path, and a 10-m-long optical bench. A reflective multi-layer insulation allows to keep a constant temperature of 21°C on orbit to preserve the HRMA from damages. By maintaining a precise temperature, the mirrors within the telescope are indeed not subjected to expansion and contraction, thus ensuring greater accuracy in observations.

The High Resolution Mirror Assembly

The principal element of the telescope system is the High Resolution Mirror Assembly (HRMA – van Speybroeck et al. 1997), which is separated from the ISIM by a 10-meter-long composite structure, known as Optical Bench Assembly (OBA). The HRMA consists of 4 pairs of concentric thin-walled, grazing-incidence Wolter Type-I mirrors. The front mirror of each pair is a paraboloid, while the back one is a hyperboloid (see Figure 3.15). All of them are coated with iridium on a binding layer of chromium to enhance reflectivity at X-ray wavelengths. The main characteristics of the HRMA are listed in Table 3.10.

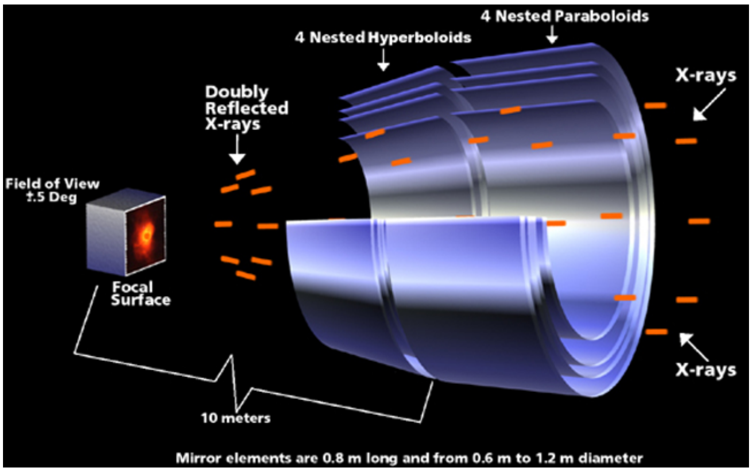

Figure 3.15. Design and functioning of the High Resolution Mirror Assembly (HRMA) onboard *Chandra*. Credit: NASA/CXC.

Table 3.10. Main characteristics of the HRMA onboard the *Chandra X-ray Observatory*.

Characteristics	Description
Optics	Wolter Type-I
Mirror coating	Iridium
Mirror Lenghts	84 cm
Total Lenght	276 cm
Focal lenght	10.070 ± 0.003 m
PSF FWHM (with detector)	<0.5 arcsec
	800 cm^2 @ 0.25 keV
Effective area	400 cm^2 @ 5.0 keV
	100 cm^2 @ 8.0 keV
Field of view	30 arcmin diameter

Low energy and high-energy transmission gratings

Aft of the HRMA are two OTGs dedicated to high resolution spectroscopy: the Low-Energy Transmission Grating (LETG – Brinkman et al. 1987) and the High-Energy Transmission Grating (HETG – Canizares et al. 2005), which can be inserted behind the mirrors through a positioning mechanism. Either OTG holds hundreds of gold transmission gratings able to intercept and diffract the X-rays reflected from the mirrors, changing their direction by amounts that depend sensitively on the X-ray energy. The diffracted X-ray radiation is then detected by one of the two focal-plane science instruments (HRC or ACIS – described in §3.5.2), which provide a precise determination of its energy (see Figure 3.16).

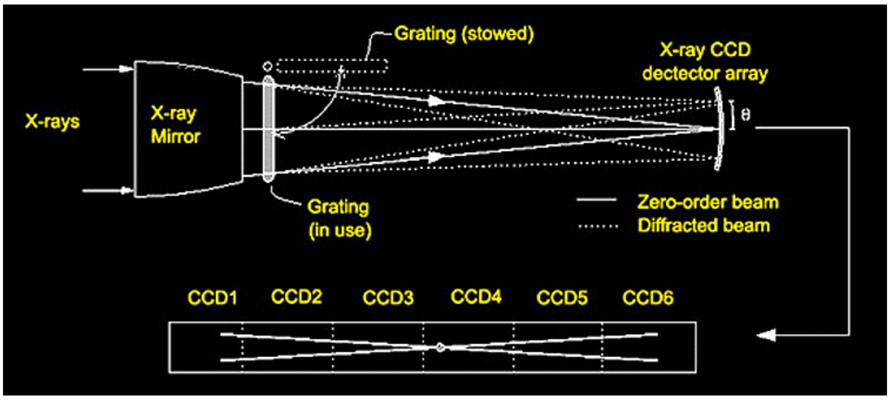

Figure 3.16. Sketch of the operating mechanism of LETGS/HETGS. Each spectrometer is activated by swinging an assembly into position behind the mirrors. The X-rays reflected from the mirrors are diffracted by the gratings and detected by HRC or ACIS. Credit: NASA/CXC.

In operation with the High Resolution Mirror Assembly (HRMA) and a focal-plane imager (HRC-S or ACIS-S – §3.5.2), these science instruments are referred to as the Low-Energy Transmission Grating Spectrometer (LETGS) and High-Energy Transmission Grating Spectrometer (HETGS), whose main characteristics are listed in Table 3.11.

Table 3.11. Main characteristics of the LEGTS and HETGS onboard *Chandra*.

Characteristics	LETGS	HETGS	
		MEG	HEG
Grating material	Gold	Gold	Gold
Thickness	2.5 μm	3600 Å	5100 Å
Width	68 μm	2080 Å	1200 Å
Energy range	0.07-10 keV †	0.4-10 keV	
	0.2-10 keV ‡	0.4-5.0 keV	0.8-10 keV
Resolution ($\Delta\lambda$, FWHM)	0.05 Å	0.023	0.012
Resolving power ($\lambda/\Delta\lambda$)	$\geq$1000 (50-160 Å)	970-80	1070-65
	$\sim 20 \times \lambda$ (3-50 Å)	660 @ 15 Å	1000 @ 12.4 Å
Effective area	1-25 cm^{-2} †	7 cm^{-2} @ 0.5 keV	
		59 cm^{-2} @ 1.0 keV ⋆	
	1-100 cm^{-2} ‡	200 cm^{-2} @ 1.5 keV ⋆	
			28 cm^{-2} @ 6.5 keV

Notes. †with HRC-S. ‡with ACIS-S. ⋆MEG+HEG first orders, with ACIS-S.

3.5.2 The Integrated Science Instrument Module

The Integrated Science Instrument Module (ISIM) houses the two focal-plane science instruments onboard *Chandra*, i.e. the High-Resolution Camera and the Advanced CCD Imaging Spectrometer, which are shortly described as follows.

High resolution camera

The High Resolution Camera (HRC – Murray et al. 1997) is a microchannel plate (MCP) instrument comprised of two detectors, one optimized for wide-field imaging (HRC-I) and the other (HRC-S) serving as read-out for the Low Energy Transmission Grating (LETG). With two Micro-Channel Plates (MCPs), consisting of a 10 cm^2 cluster of 69 million tiny lead-oxide (PbO_2) glass tubes that are about 10 μm in diameter and 1.2 mm long, the HRC is designed to accurately records the position, number, and energy of X-rays. The tubes have a special coating that causes the release of electrons when they are struck by X-rays, while the camera is shielded from UV and optical radiation. Accelerated at high voltage down the tubes, each electron triggers the release of other electrons, that strike a grid of wires at the end of the tubes. By detecting the electronic signal, the position of the original X-ray is determined with high precision, thus producing a detailed map of the X-ray source with an unprecedented resolution of 0.5 arcseconds (Figure 3.17).

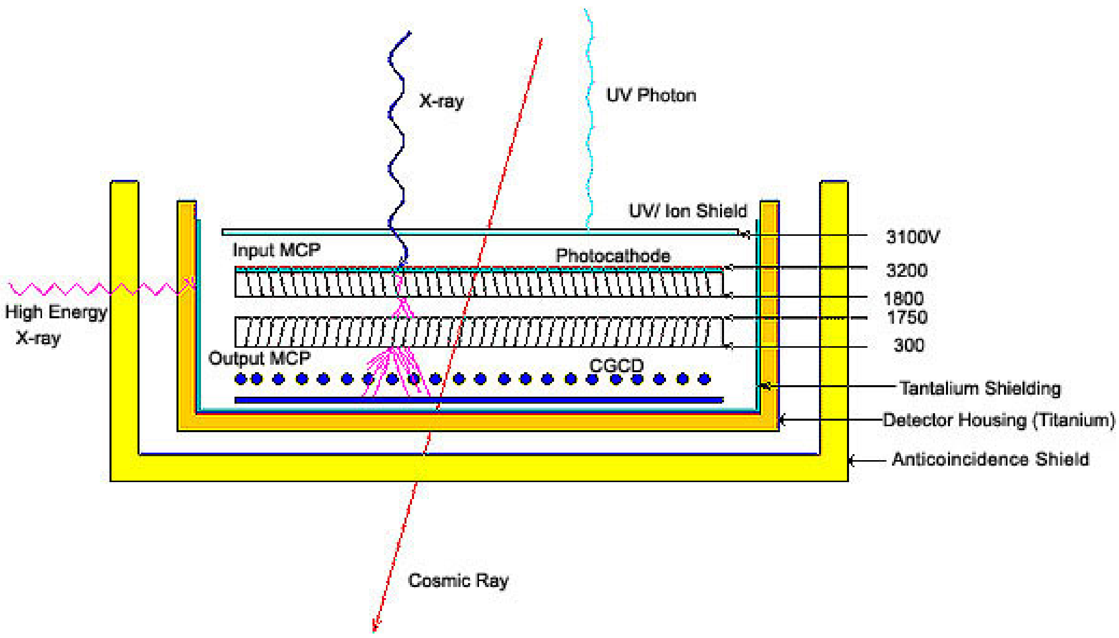

Figure 3.17. Schematic of the HRC microchannel plate detector. Credit: NASA/CXC.

The HRC-I provides the largest field-of-view ($\sim$ 30 $\times$ 30 arcmin^2) of any detector onboard Chandra, and its response extends to energies below the sensitivity of ACIS, even though the spectral resolution is lower. The HRC-S is instead optimized to be used with the LETG in the so-called Low Energy Transmission Grating Spectrometer (LETGS). Also the time resolution of the HRC detectors (τ=16 μs) is the best on the CXO, but it can only be exploited in certain operation mode.

Advanced CCD imaging spectrometer

The Advanced CCD Imaging Spectrometer (ACIS – Garmire et al. 2003) offers the capability to simultaneously acquire high-resolution images and moderate resolution spectra. It is composed of 10 planar, 1024×1024 pixel CCDs arranged in two different arrays and providing position and energy information. Each CCD have an "active" or imaging section, which is directly exposed to the incident radiation, and a shielded "frame store" region, where the charge is transferred to identify the position and amplitude of any events (see Figure 3.18).

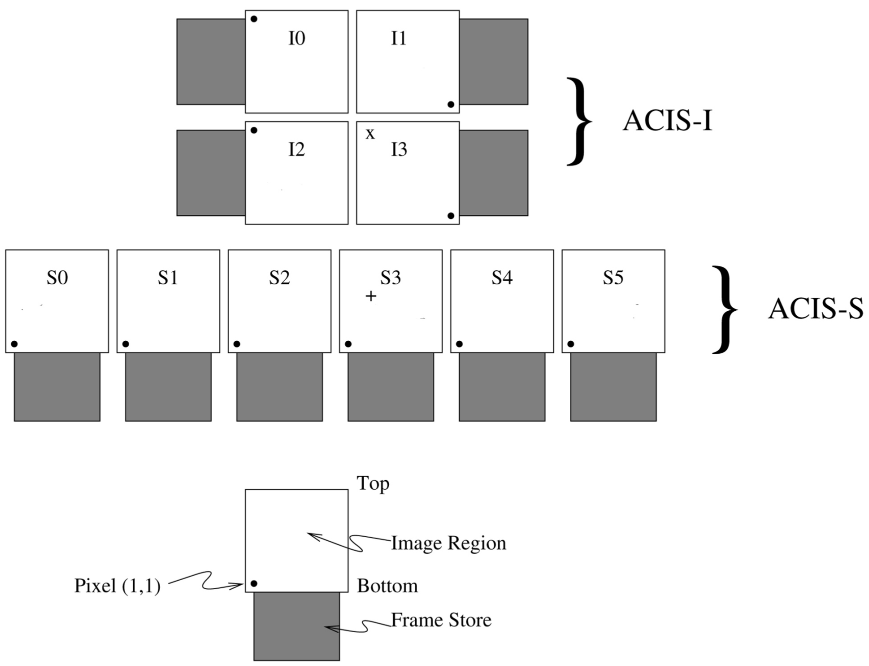

Figure 3.18. ACIS schematic layout overhead view to illustrate the location of the imaging (ACIS-I) and spectroscopic (ACIS-S) arrays of CCD ships. Chips S1 and S3 are back-illuminated chips; all of the other chips are front-illuminated. Credit: NASA/CXC.

The imaging array (ACIS-I) is composed of four front-illuminated CCDs arranged in a 2×2 configuration, which is optimized for spectrally resolved, high-resolution imaging over a 16.9 × 16.9 arcminute field-of-view. The spectroscopic array is instead composed of 6 CCDs (4 FI and 2 BI) in a 1×6 configuration, which is used either for imaging or for a grating spectrum read-out. When used in conjunction with the HETG in the so-called High Energy Transmission Grating Spectrometer (HETGS), ACIS-S provides high-resolution spectroscopy with a resolving power (E/ΔE) up to 1000 over the 0.4-8 keV energy band.

4

A deep *NuSTAR* view of the buried AGN in NGC 1068

Contents

This chapter focuses on the physical properties of the absorbing circumnuclear medium in NGC 1068 obtained through the analysis of the latest *NuSTAR* monitoring campaign performed between July 2017 and February 2018 (Zaino et al. 2020).

In §4.1 a short overview on NGC 1068 is discussed. §4.2 is devoted to the introduction of the model discussed in Bauer et al. (2015) and used as a baseline model in the following analysis. The X-ray observations and the data reduction are discussed in §4.3, with §4.3.1 and §4.3.2 devoted to *NuSTAR* and *Swift*-XRT data, respectively. The X-ray spectral analysis is discussed in §4.4, with §4.4.1, §4.4.2 and §4.4.3 focused on the detection of a new Ultra-Luminous X-ray source (ULX), the broadband spectral analysis and the calibration issues affecting the iron $K\alpha$ line energy range, respectively. Finally, in §4.5 the results of the *NuSTAR* analysis are discussed and compared to the previous X-ray results, while §4.6 is devoted to the future possibilities offered by the new X-ray observatories that will be launched in the next years.

4.1 Introduction

NGC 1068 (D_L = 14.4 Mpc; Tully 1988) is one of the best known Seyfert 2 galaxies partly because the unification model was first proposed to explain the presence of broad optical lines in its polarized light (Antonucci & Miller 1985). According to its classification, the nucleus of NGC 1068 is heavily obscured by dust. Near- and mid-infrared observations spatially resolved the dust structures within this galaxy, revealing a torus consistent with a two-component dust distribution. In particular, *VLTI*/VINCI observations for the first time favored a multi-component model for the torus intensity distribution. Taking into account also K-band speckle interferometry, these data showed that a part of the flux originates from scales clearly smaller than ∼0.4 pc, arising from substructures of the dusty torus or from the central accretion flow viewed through moderate extinction, and another part of the flux from larger scales of the order of ∼3 pc (Wittkowski et al. 2004, and references therein). MIDI observations confirmed this scenario; in particular, Jaffe et al. (2004) modelled the observed spectra using two components with different size and temperature, each of which is a two-dimensional Gaussian aligned with the axis parallel to the radio jet. They considered a central hot component (T>800 K) marginally resolved along the source axis and surrounded by a warm dust component (T∼320 K) in a structure 2.1 parsec thick and 3.4 parsec in diameter. More recent MIDI observations allowed resolution of the nuclear mid-infrared emission from NGC 1068 in unprecedented detail, with a maximum resolution of 7 mas (i.e. ∼0.5 pc at the distance of NGC 1068). In particular, Raban et al. (2009) found that the mid-infrared emission can be represented by two components, each with an elliptical Gaussian brightness distribution: a compact hot component (T∼800 K), 1.35 parsec long and 0.45 parsec thick in FWHM (i.e. the inner funnel of the obscuring torus), tilted by ∼45° with respect to the radio jet and with similar size and orientation to the observed water maser distribution (Gallimore et al. 2004), and a 3×4 pc warm component (T∼300 K) marking the colder and extended part of the torus-like structure.

Recent *ALMA* observations have been able to resolve the molecular torus in NGC 1068 over spatial scales of D=10-30 pc, demonstrating that there is radial density stratification as well as hints of counter-rotation and a high velocity outflow (Imanishi et al. 2018; García-Burillo et al. 2019; Impellizzeri et al. 2019). The observed physical parameters are significantly different depending on which line transition used to image the torus, highlighting its many faces. In particular, the CO(2-1), CO(3-2) and HCO$^+$(4-3) maps provided a full-size of the torus $D_{CO(2-1)} = 28 \pm 0.6$ pc, $D_{CO(3-2)} = 26 \pm 0.6$ pc and $D_{HCO^+(4-3)} = 11 \pm 0.6$ pc, respectively (García-Burillo et al. 2019).

From an X-ray point of view, the multi-epoch X-ray spectra of NGC 1068 were analysed by Bauer et al. (2015) using different observatories, including a *NuSTAR* pointing in 2012, and spanning a time period of ∼16 years. The authors modeled the broadband emission of the source with a combination of a completely obscured transmitted power law ($\Gamma = 2.10^{+0.06}_{-0.07}$), scattering by both warm and cold reflectors, radiative recombination continuum and line emission, and off-nuclear point-source emission, being the latter due to the ULX population within the NGC 1068 field of view. In particular, the reflected emission is due to a multi-component reflector with three distinct column densities, in which the higher N_H component ($N_{H,1} \sim 10^{25}$ cm^{-2}) provides the bulk of the flux of the Compton hump, the lower N_H component ($N_{H,2} = (1.4 \pm 0.1) \times 10^{23}$ cm^{-2}) contributes primarily to the iron line emission and reproduces the curvature of the continuum around 10 keV, and a third reflector on more extended scales (>140 pc) provides almost 30% of the neutral iron Kα line flux (see §4.2 and Bauer et al. 2015 for further details).

NGC 1068 was observed again in 2014 and in 2015 with a joint *XMM-Newton* and *NuSTAR* monitoring campaign during which a transient excess above 20 keV was observed and ascribed to a Compton-thick unveiling event in which material with $N_H \geq 2.5 \times 10^{24}$ cm^{-2} moved temporarily out of our line of sight (see Figure 4.1), allowing the intrinsic radiation to pierce through the circumnuclear medium (Marinucci et al. 2016).

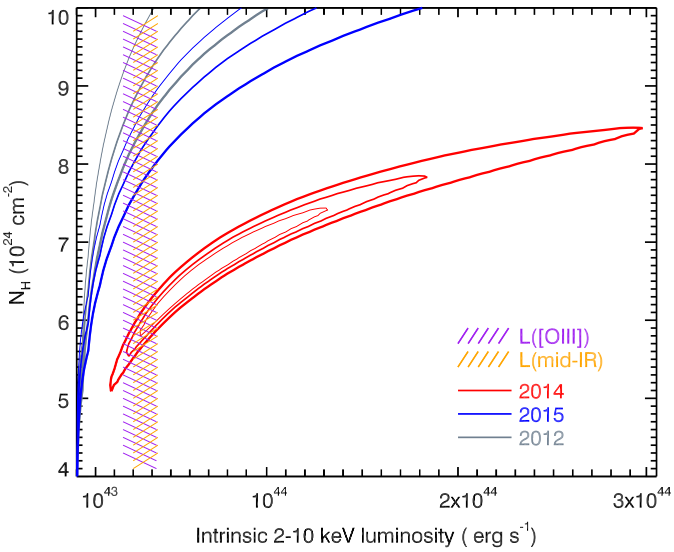

Figure 4.1. Confidence contours between the column density along the line of sight and the intrinsic 2-10 keV luminosity for 2012 (in grey), 2014 (in red) and 2015(in blue) data sets (Marinucci et al. 2016). Boldest to thinnest contours indicate 99 per cent, 90 per cent and 68 per cent confidence levels. Vertical orange and purple stripes indicate the 2-10 keV intrinsic luminosities inferred from the mid-IR (Gandhi et al. 2009) and [OIII] (Lamastra et al. 2009) observed luminosities.

VISIR and MIDI observations performed before and immediately after the X-ray variations showed constant behavior in the infrared emission of the nuclear region of NGC 1068, confirming the hypothesis that the observed change in the X-ray regime was not due to an intrinsic change in the luminosity of the central accretion disk, but to escaping emission through the patchy torus clouds (López-Gonzaga et al. 2017). However, due to the large separation of the *NuSTAR* observations (∼6 months), only an upper limit of ∼2 pc could be given on the location of such a variable absorber, which is consistent both with the BLR and the torus. In the latter case, the change in the absorbing column density along the line of sight required to explain the X-ray variability of the AGN in NGC 1068 could be associated with the small-scale structure of the molecular torus imaged by *ALMA* (García-Burillo et al. 2019).

4.2 The baseline model

In 2015, Bauer et al. (2015) characterized the multi-epoch X-ray spectra of NGC 1068 analyzing high-quality observations performed from 1996 until 2012 by different X-ray observatories. In particular, *NuSTAR* and *XMM-Newton* data were used to study in detail the total emission of the source, while the higher spectral and angular resolution of *Chandra* (HETG and ACIS, respectively) enabled the authors to remove potential host-galaxy contamination, spatially separating the nuclear spectrum from diffuse and off-nuclear point-source emission at least below 8 keV. *Swift*, *Suzaku* and *BeppoSAX* observations were used for points of comparison.

The broadband emission of NGC 1068 was modeled with a combination of a heavily Compton-thick transmitted power law, scattering by both warm and cold reflectors, radiative recombination continuum (RRC) and line emission, and off-nuclear point-source emission (see Figure 4.2 for the fractional contributions of the different spectral components). No angular dependence of the nuclear emission spectral shape is assumed (i.e. all scattering component have the same photon index), nor is relativistic reflection from the accretion disk considered, due to the inclination of the source and the dominance of scattering and absorption from cold distant material.

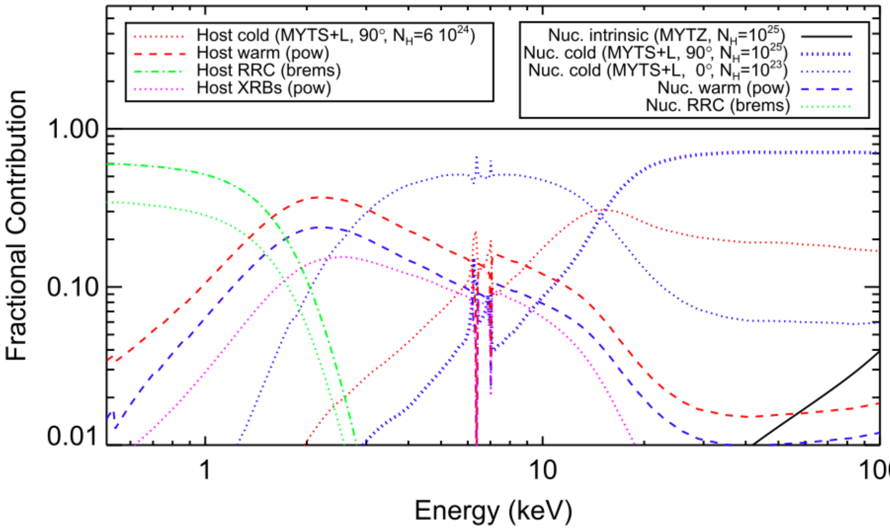

Figure 4.2. Fractional contributions from individual components of the baseline model. For clarity, all the Gaussian lines within the model were excluded when calculating fractional contributions, as their presence dramatically shifted the continuum contributions over small portions of the spectrum. Changes in the dominance of different continuum components as a function of energy are clearly visible (Bauer et al. 2015).

To construct a robust model for the nuclear X-ray spectrum of NGC 1068, both the point-like nuclear emission and the diffuse emission and point source contamination from the host galaxy must be taken into account. The extended emission can be effectively constrained below 8 keV by *Chandra* imaging, leaving considerable degeneracy at higher energies. Since the aim is to provide the best constraints on the properties of the reflectors, data below 2 keV are not considered, and all the spectral components that are well-constrained through a separate fit of the nuclear and host galaxy contribution (i.e. extranuclear point sources, RRC and line emission) are fixed during the combined fit (see Bauer et al. 2015 for the adopted values of each spectral component).

The AGN intrinsic continuum is well-described by a highly absorbed ($N_H = 10^{25}$ cm^{-2}) power-law with a photon index $\Gamma = 2.10^{+0.06}_{-0.07}$ and an energy cut-off $E_c = 128^{+115}_{-44}$ keV, while a multi-component reflector with three distinct column densities ($N_{H,1} \sim 10^{25}$ cm^{-2}, $N_{H,2} = (1.4 \pm 0.1) \times 10^{23}$ cm^{-2}, $N_{H,3} = (5.0^{+4.2}_{-1.9}) \times 10^{24}$ cm^{-2}) reproduces the complex structure of the circumnuclear matter (i.e. Model M2d in Bauer et al. 2015 – see Figure 4.3). The spectral features attributed to the $N_{H,1}$ and $N_{H,2}$ components arise from the central region, within 2 arcsec from the nucleus, while $N_{H,3}$ corresponds to regions outside the central 2 arcsec. In particular, the higher N_H component provides the bulk of the flux to the Compton hump, while the lower N_H component contributes primarily to the iron line emission and reproduces the curvature of the continuum around 10 keV, effectively decoupling the two key features of Compton reflection. The inclination angles of the two nuclear scatterers with respect to the line of sight are 90° and 0°, respectively, in order to reproduce a clumpy torus distribution with the edge-on scatterer accounting for the photons reprocessed by the obscuring material lying between the AGN and the observer, while the face-on scatterer mimics the reprocessed emission coming from back-side reflection. These latter photons have a smaller chance of being absorbed before reaching the observer, making the `MYTORUS` 0° component relevant in a patchy torus scenario (Yaqoob et al. 2015; Zhao et al. 2019). On the other hand, the third reflector on more extended scales (>140 pc) with an inclination of 0° provides almost 30% of the neutral iron Kα line flux and could represent material within the ionization cones.

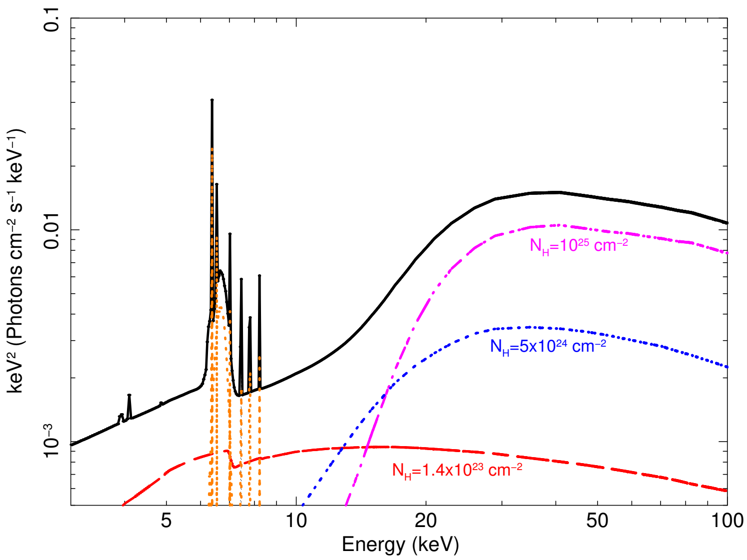

Figure 4.3. Theoretical best-fit model of NGC 1068 adopted by Bauer et al. 2015 (solid black line). Emission lines (orange dotted lines in the 6-9 keV energy range), nuclear (dashed red and dot-dashed magenta lines) and more distant (blue dotted line) reflectors represent the reflection components arising from different column densities, while the nuclear intrinsic emission is completely absorbed by heavily Compton-thick matter (Zaino et al. 2020).

4.3 Observations and data reduction

NGC 1068 was observed by *NuSTAR* (Harrison et al. 2013) with its two co-aligned X-ray telescopes, with corresponding Focal Plane Modules A (FPMA) and B (FPMB), during a monitoring campaign composed of four observations of about 50 ks each, performed between July 2017 and February 2018 (see Table 4.1).

Table 4.1. *NuSTAR* observation log for NGC 1068 (Zaino et al. 2020).

	obsID	Date	Detector	Net exposure time [a] [ks]	Net count rate [b] [counts s^{-1}] 3-5.5 keV	20-79 keV
OBS1	60302003002	2017-07-31	FPMA	50.0	0.0246±0.0007	0.0289±0.0009
			FPMB	49.8	0.0240±0.0007	0.0262±0.0008
OBS2	60302003004	2017-08-27	FPMA	52.5	0.0253±0.0007	0.0332±0.0009
			FPMB	52.4	0.0256±0.0007	0.0309±0.0009
OBS3	60302003006	2017-11-06	FPMA	49.7	0.0254±0.0007	0.0301±0.0009
			FPMB	49.5	0.0236±0.0007	0.0281±0.0008
OBS4	60302003008	2018-02-05	FPMA	54.6	0.0313±0.0008	0.0276±0.0008
			FPMB	54.5	0.0299±0.0008	0.0261±0.0008

Notes. [a] Net exposure time, after screening was applied on the data. [b] Net source count rate after screening and background subtraction, as observed in the 3-5.5 keV and 20-79 keV energy ranges.

4.3.1 *NuSTAR* data

The Level 1 data products were processed using the *NuSTAR* Data Analysis Software (`NuSTARDAS`) package (version 1.8.0). Event files (Level 2 data products) were extracted using the `nupipeline` task, adopting standard filtering criteria and the latest calibration files available in the *NuSTAR* calibration database (`CALDB 20180126`). The source spectra were extracted from circular regions of radius 50 arcsec, corresponding to an encircled energy fraction (EEF) of about 70%, from both FPMA and FPMB. The same radius was used to extract background spectra, selecting a region on the same chip, uncontaminated by source photons or background sources. The net exposure times and the total count rates after this process are reported in Table 5.1 for each spectrum and for both FPMA and FPMB.

Finally, the two *NuSTAR* spectra from each observation were binned in order not to oversample the instrumental energy resolution by a factor larger than 4 and to have a signal-to-noise ratio (SNR) greater than 7 in each background-subtracted spectral channel. This ensures the applicability of the χ^2 statistic to evaluate the quality of spectral fitting, avoiding a dramatic oversampling due to the high flux of the source. The same energy bins were used for both FPMA and FPMB.

4.3.2 *Swift* data

In our work we also analyzed two *Swift*-XRT archival observations performed simultaneously with *NuSTAR* in November 2017 and February 2018 and a ToO observation requested in June 2018 (see Table 4.2).

Table 4.2. *Swift*-XRT observation log for NGC 1068 (Zaino et al. 2020).

obsID	Start time	Exposure time [ks]	
0088104005	2017-11-06 08:40:57	2.0	(1)
0088104006	2018-02-05 05:27:57	2.1	(2)
0088104007	2018-06-15 16:13:48	1.6	(3)

Notes. (1) Simultaneous to OBS3. (2) Simultaneous to OBS4. (3) ToO observation.

To analyze the XRT observation taken in February 2018, we extracted a source spectrum from a circular region with a 20 arcsec radius centered on the ULX (see §4.4.1 for further details), ensuring that the nuclear emission of NGC 1068 is excluded. A background spectrum was also extracted from a source-free circular region with a 60 arcsec radius. We used identical extraction regions for the other two XRT spectra (November 2017 and June 2018), generating spectra with `XSELECT`, effective area files with `XRTMKARF`, and using the redistribution matrix file `swxpc0to12s6_20130101v014.rmf`. Finally, all the XRT spectra were rebinned in order to have at least 15 counts per energy bin.

4.4 X-ray spectral analysis

The X-ray spectral analysis of NGC 1068 was performed using `XSPEC 12.10.1` (Arnaud 1996) and the χ^2 statistic, apart from the ULX analysis (see §4.4.1), where the C-statistic (Cash 1976) was used. The photoelectric cross sections for all absorption components are those from Verner et al. (1996), while the element abundance pattern is from Wilms et al. (2000) and the metal abundance is fixed to solar. Unless stated otherwise, errors correspond to the 90 per cent confidence level for one interesting parameter ($\Delta\chi^2$=2.706). The four *NuSTAR* monitoring spectra are shown in Figure 4.4.

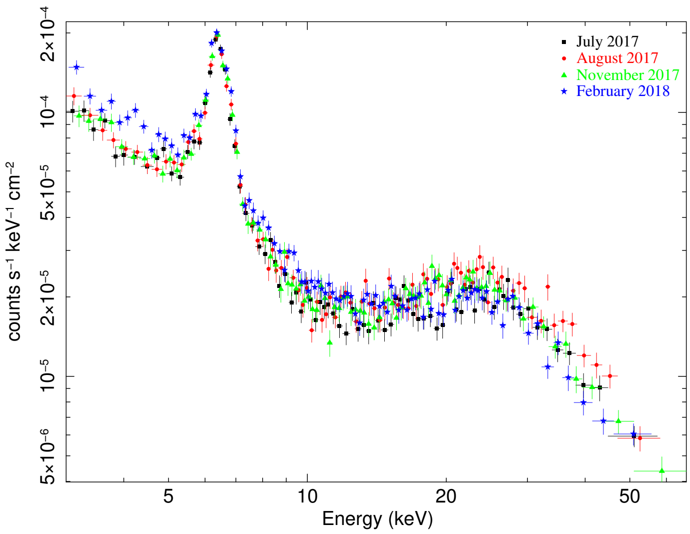

Figure 4.4. *NuSTAR* monitoring spectra taken in July 2017 (black squares), August 2017 (red circles), November 2017 (green triangles) and February 2018 (blue stars). FPMA and FPMB data of each observation are grouped together for clarity purposes only (Zaino et al. 2020).

4.4.1 A new ULX detection in NGC 1068?

NGC 1068 is not only one of the best known Seyfert 2 galaxies in the local universe, but also a powerful starburst galaxy with a star-formation rate $\dot{M} > 36\ M_{\odot}\ yr^{-1}$ (i.e. at least a factor of 7 greater than the SFR in our Galaxy). In particular, infrared observations indicate that the star formation in this galaxy is primarily distributed within the central $\sim$3 kpc in two very extended complexes, one located to the north and the other to the southwest of the nucleus (Telesco & Decher 1988).

Focusing on the soft X-ray band below 5.5 keV, we can observe an excellent agreement of the data taken in July, August and November 2017 (see black, red and green symbols in Figure 4.4, respectively). However, an unexpected increase of the flux by $25 \pm 2\%$ was observed in February 2018 with respect to the previous observations (see blue circles in Figure 4.4 and the count-rates in Table 5.1). On the other hand, the *NuSTAR* images taken in February 2018 in the 3-5.5 keV energy band suggest the presence of a transient object at a distance of ~30 arcsec from the nuclear region (see Figure 4.5). The analysis of the simultaneous *Swift*-XRT image confirms this hypothesis (see Figure 4.6), allowing us to ascribe the 3-5.5 keV excess observed in February 2018 to the appearance of a flaring source at a distance of ~2 kpc from the nucleus of NGC 1068 (at the distance of NGC 1068 1"=72 pc – Bland-Hawthorn et al. 1997).

To identify this flaring source, we overlaid the five point-like sources previously detected with *Chandra* (Smith & Wilson 2003), within 20 arcsec of its position, on the *Swift*-XRT 3-5.5 keV image (see Figure 4.6). Among these point-like objects, the brightest one (with more than 50 counts in the *Chandra* band and with a SNR>7) is CXOU J024244.0-000035, with a reported 0.4-8 keV luminosity $L_{0.4-8} = 6.8 \times 10^{38}$ erg s^{-1}, corresponding to a 2-10 keV luminosity $L_{2-10} = 4.8 \times 10^{38}$ erg s^{-1}, which is almost two orders of magnitude lower than the one observed during our monitoring. No known X-ray sources appear to lie closer than $d \simeq 8$ arcsec from the ULX centroid in the *Swift*-XRT image, neither the supernova exploded in NGC 1068 in November 2018 (Bostroem et al. 2019) matches the location of the ULX; therefore, we conclude that there is no robust identification with previously detected sources.

To obtain *NuSTAR* FPMA and FPMB spectra of the ULX, we computed difference spectra between the ones extracted from the February 2018 and November 2017 observations, already described in Section 4.3.1. Then, we rebinned the two spectra in order to have a SNR greater than 2σ in each spectral channel. With this requirement, no detected spectral bins are present above 16 keV and 12 keV for FPMA and FPMB, respectively.

We used the C-statistic to simultaneously fit the XRT, FPMA and FPMB spectra obtained in February 2018. An absorbed cut-off power-law provides an acceptable description of the data, with a fixed value for the Galactic column density ($N_H^{Gal} = 3 \times 10^{20}$ cm^{-2} – Kalberla et al. 2005), a photon index $\Gamma = 1.5 \pm 0.4$, a cut-off energy $E_c \geq 5$ keV and a normalization $N = (2.6^{+0.7}_{-0.6}) \times 10^{-4}$ ph cm^{-2} s^{-1} keV^{-1}. We retrieved a $C/dof = 43.3/45$ and our best fit is shown in Figure 4.7. The observed flux in the 2-10 keV band is $F_{2-10} = (9.4 \pm 1.0) \times 10^{-13}$ erg cm^{-2} s^{-1}, corresponding to an intrinsic luminosity $L_{2-10} = (3.0 \pm 0.4) \times 10^{40}$ erg s^{-1} at the distance of NGC 1068.

Since the source was not detected before (neither in this monitoring, nor in the previous X-ray observations), we requested and obtained a 1.5 ks ToO observation with *Swift*-XRT on June 15, 2018 (NGC 1068 was not observable before this date due to Sun occultation) to confirm the presence of this new source. Unfortunately, the transient source was no longer visible in the *Swift*-XRT image in the 3-5.5 keV band, and the spectrum extracted from a circular region of 20 arcsec centered on the position of the ULX, as observed in February 2018, showed a dramatic drop of the count-rate in the 2-10 keV band (i.e. about one order of magnitude, from 0.010 ± 0.002 counts/s in February 2018 to 0.0013 ± 0.0009 counts/s in June 2018). This prevented further detailed study of this transient source, allowing us to determine only a variability timescale less than ~ 3 months. However, we note that transient ULXs are already known (e.g. Middleton et al. 2012, 2013; Pintore et al. 2018), and that even high luminosity ULXs can vary on very short timescales, such as ULX1 in NGC 5907 (Walton et al. 2015).

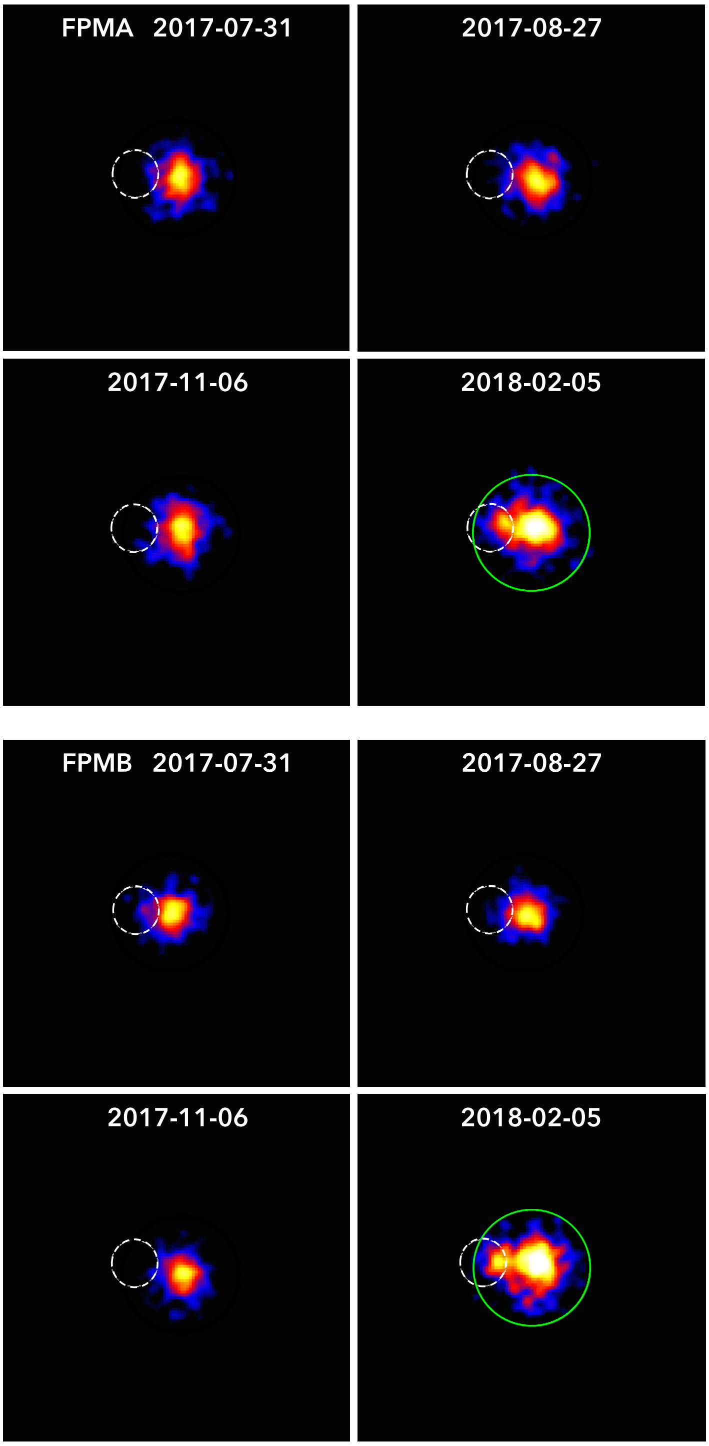

Figure 4.5. *NuSTAR* FPMA (top panels) and FPMB (bottom panels) images of the central 5’×5’ regions in the 3-5.5 keV band smoothed with a 3 pixels radius Gaussian filter (Zaino et al. 2020). The circular region with a radius of 50 arcsec used for extracting the source spectra is shown in OBS4 (green solid circle), while the 20 arcsec circular region used to extracted the *Swift*-XRT spectrum is overplotted in all panels (white dotted circles).

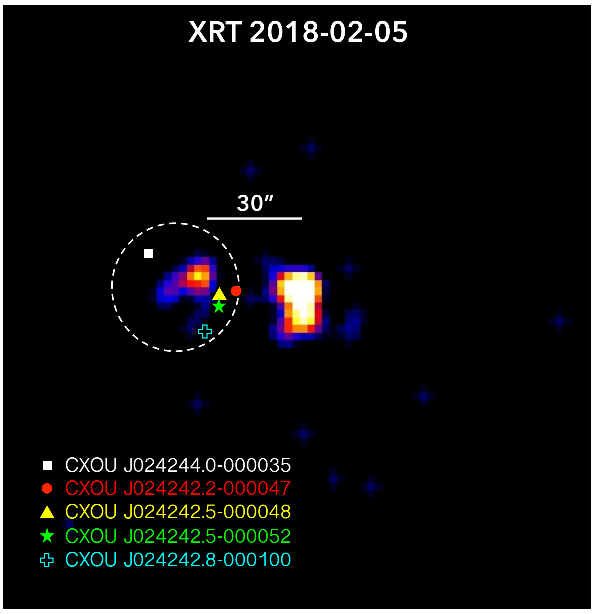

Figure 4.6. *Swift*-XRT image of the central 3'×3' region, obtained in February 2018, in the 3-5.5 keV band (Zaino et al. 2020). The dashed white circular region with a radius of 20 arcsec used for extracting the ULX spectrum is shown. We over-imposed the five different point-like sources previously detected with *Chandra* and located within a 20 arcsec radius region from the ULX, from Smith & Wilson (2003). The ULX is not detected in November 2017 nor in June 2018.

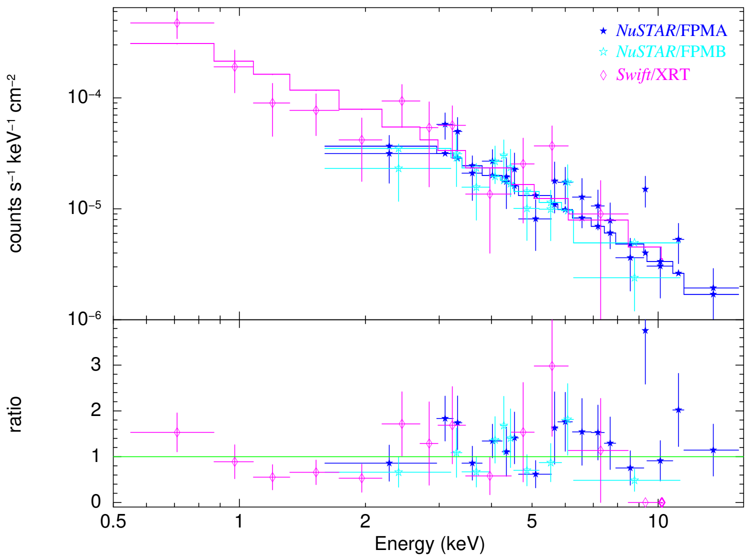

Figure 4.7. *Top panel.* XRT (magenta diamonds), FPMA (blue filled stars) and FPMB (cyan empty stars) ULX spectra taken in February 2018. *Bottom panel.* Data/model ratio with respect to a model (solid green line) composed of an absorbed power-law with a photon index $\Gamma = 1.5 \pm 0.4$ and a cut-off energy $E_c \geq 5$ keV (Zaino et al. 2020).

4.4.2 The broadband analysis

Considering the whole *NuSTAR* band (3-79 keV), we find that the iron line emission does not vary significantly during the whole monitoring (see Figure 4.4); however, the count-rate above 20 keV clearly varies by up to ∼20% between the observations (see Table 4.1). This behavior is similar to that observed three years previously; in particular, NGC 1068 was caught in a higher flux state in August 2014 and 2017 and in a lower one in February 2015 and 2018, as reported in Table 4.3. Additionally, we find excellent overlap of the spectral shapes in the high and low states during the two *NuSTAR* campaigns (see Figure 4.8). Both these findings suggest that we are observing eclipsing/unveiling events affecting only the spectrum above 10 keV, as found in Marinucci et al. (2016). The benefit of the current *NuSTAR* monitoring campaign is that we have two additional observations in July and November 2017 (see Table 4.1) that enable us to more accurately probe the variability of NGC 1068.

Table 4.3. Comparison between the higher and the lower flux states of NGC 1068 during 2014-2015 and 2017-2018 *NuSTAR* monitoring (Zaino et al. 2020).

High state		Low state	
Date	Count rate [1]	Date	Count rate [1]
FPMA			
Aug 2014	0.032 ± 0.001	Feb 2015	0.026 ± 0.001
Aug 2017	0.033 ± 0.001	Feb 2018	0.028 ± 0.001
FPMB			
Aug 2014	0.031 ± 0.001	Feb 2015	0.023 ± 0.001
Aug 2017	0.031 ± 0.001	Feb 2018	0.026 ± 0.001

Notes. [1] Net count rate in the 20-79 keV band, expressed in counts/s.

To model our data set, we adopted the best-fit model discussed in Bauer et al. 2015 (see §4.2 for a detailed description of the model), with an additional cut-off power-law component to account for the ULX contribution in OBS4 (Model A in Table 4.4), whose spectral analysis is described in §4.4.1. Due to the fact that ULXs break to very steep spectra above ∼10 keV (e.g. Stobbart et al. 2006, Gladstone et al. 2009, Pintore et al. 2017, Walton et al. 2018), we expect that this new source should have a negligible effect on the high-energy data from the nucleus. In our configuration, the reflected emission is reproduced by three distinct reflectors ($\theta_1 = 90°$, $N_{H,1} \geq 9.7 \times 10^{24}$ cm^{-2}; $\theta_2 = 0°$, $N_{H,2} = (1.4 \pm 0.1) \times 10^{23}$ cm^{-2}; $\theta_3 = 0°$, $N_{H,3} = (5.0^{+4.2}_{-1.9}) \times 10^{24}$ cm^{-2}) modeled with `MYTORUS` tables in a decoupled configuration (Yaqoob 2012), where the normalizations for the different angles vary independently, while the continuum and line components of a given angle are fixed, corresponding to a patchy torus distribution. Applying this model to our data set, the fit was not good ($\chi^2_r = 1.63$), mainly due to significant residuals at ∼6 keV (see panel (a) in Figure 4.9).

Taking advantage of previous *NuSTAR* observations, some of which were performed simultaneously with *XMM-Newton*, we argue that the significant residuals observed in Model A have no astrophysical origin, but are spurious calibration features (see §4.4.3 for a detailed analysis). We modeled this component out of the residuals adopting an additional emission line (i.e. a `gauss` component in XSPEC), whose parameters are reported in Table 4.4 (Model B), obtaining a significant improvement of the fit ($\chi^2_r = 1.18$ – see panel (b) in Figure 4.9). We stress that this further component does not affect our conclusions.

Table 4.4. Summary of the six models discussed in the text and differences with respect to the Bauer model summarized in §4.2 (Zaino et al. 2020).

Model A: Bauer model + ULX contribution in OBS4 (χ^2/dof = 1186/730)

$\Gamma_{\rm ULX}$	E_c [keV]	norm$_{\rm ULX}$ [ph cm^{-2} s^{-1} keV^{-1}]
1.5 ± 0.4	≥ 5	$(2.6^{+0.7}_{-0.6}) \times 10^{-4}$

Model B: Model A + `gauss` component at ∼6 keV (χ^2/dof = 840/714)

	$E_{\rm gauss}$ (FPMA/FPMB) [keV]	norm$_{\rm gauss}$ (FPMA/FPMB) [ph cm^{-2} s^{-1} keV^{-1}]
OBS1	6.1 ± 0.1 / 6.1 ± 0.1	1.7 ± 0.5 / 2.5 ± 0.5
OBS2	6.1 ± 0.1 / 6.1 ± 0.1	1.3 ± 0.5 / 2.3 ± 0.5
OBS3	6.0 ± 0.1 / 6.1 ± 0.1	2.1 ± 0.5 / 2.2 ± 0.5
OBS4	5.9 ± 0.1 / 5.9 ± 0.1	1.7 ± 0.4 / 1.9 ± 0.5

Model C: Model B with reflectors parameters free to vary, but fixed between the observations (χ^2/dof = 784/724)

Γ	$N_{H,1}$	$N_{H,2}$ [10^{24} cm^{-2}]	$N_{H,3}$	norm$_1$	norm$_2$ [ph cm^{-2} s^{-1} keV^{-1}]	norm$_3$
2.10 ± 0.01	$10^{\dagger}$	0.13 ± 0.01	≥ 4.3	$(3.0 \pm 0.2) \times 10^{-1}$	$(4.3^{+0.3}_{-0.4}) \times 10^{-2}$	$(0.9 \pm 0.3) \times 10^{-2}$

Model D: Model C with only N_H along the l.o.s. and intrinsic flux free to vary (χ^2/dof = 784/730)

	$N_H^{\rm l.o.s.}$ [10^{24} cm^{-2}]	norm$_{\rm intr}$ [ph cm^{-2} s^{-1} keV^{-1}]
OBS1	≥ 7.3	$5.0^{+2.1}_{-4.6}$
OBS2	$6.3^{+1.2}_{-1.0}$	$0.9^{+1.6}_{-0.5}$
OBS3	$4.6^{+1.4}_{-1.2}$	$0.12^{+0.28}_{-0.08}$
OBS4	$2.4^{\dagger}$	≤ 1.2

Model E: Model D with the same intrinsic luminosity during the monitoring (χ^2/dof = 793/733)

	$N_H^{\rm l.o.s.}$ [10^{24} cm^{-2}]	norm$_{\rm intr}$ [ph cm^{-2} s^{-1} keV^{-1}]
OBS1	$7.4^{+1.1}_{-1.0}$	
OBS2	$5.6^{+0.9}_{-0.8}$	$0.5^{+0.5}_{-0.2}$
OBS3	$6.2^{+1.0}_{-0.8}$	
OBS4	≥ 7.8	

Model F: Model D with the same absorbing column density during the monitoring (χ^2/dof = 793/733)

	$N_H^{\rm l.o.s.}$ [10^{24} cm^{-2}]	norm$_{\rm intr}$ [ph cm^{-2} s^{-1} keV^{-1}]
OBS1		$0.15^{+0.25}_{-0.10}$
OBS2	$5.9^{+1.0}_{-0.8}$	$0.7^{+0.8}_{-0.4}$
OBS3		$0.38^{+0.47}_{-0.20}$
OBS4		≤ 0.14

Notes. Model A. $\Gamma_{\rm ULX}$, E_c, norm$_{\rm ULX}$: photon index, cut-off energy and normalization of the cut-off power-law accounting for the contribution of the ULX discussed in Section 4.4.1. *Model B.* $E_{\rm gauss}$ and norm$_{\rm gauss}$: energy and normalization of the phenomenological line due to calibration issues modeled in `XSPEC` with $\sigma = 0$ and discussed in Section 4.4.3. *Model C.* Γ: photon index of the primary continuum; $N_{H,1}$, $N_{H,2}$, $N_{H,3}$ and norm$_1$, norm$_2$, norm$_3$: column densities and normalizations of the three reflectors, respectively. *Model D,E,F.* $N_H^{\rm l.o.s.}$: absorbing column density along the line of sight; norm$_{\rm intr}$: normalization of the intrinsic power law. χ^2/dof: ratio between χ^2 and the degrees of freedom of the model. † Unconstrained value. Errors correspond to the 90 per cent confidence level for one interesting parameter. In all models, ULX parameters are fixed to their best-fit values, while the column density along the line of sight and the intrinsic luminosity of the source are left free to vary (for clarity purposes, these values are not reported here for Model A,B,C). All the other parameters not shown in this table are fixed to the best-fit values reported in Bauer et al. (2015).

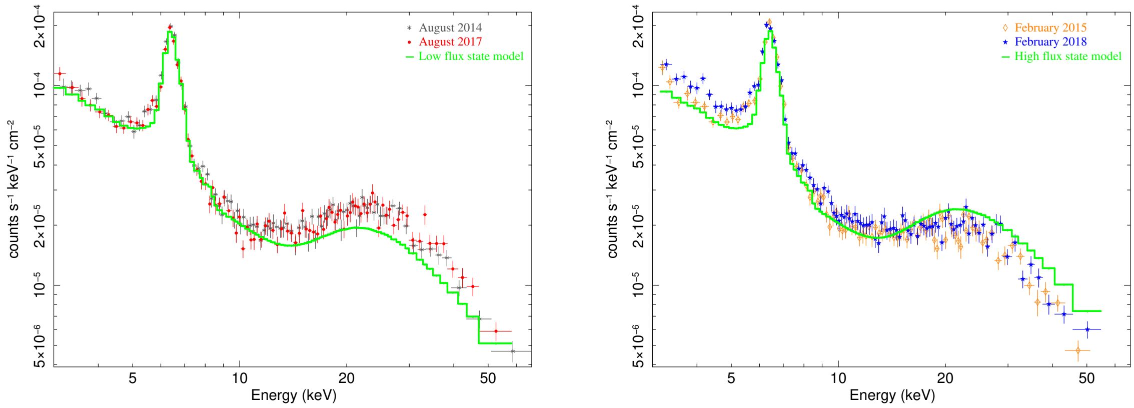

Figure 4.8. *NuSTAR* observations of NGC 1068 during the last two *NuSTAR* monitoring campaigns. *Left panel.* Comparison between OBSID 60002033002 (August 2014; grey asterisks) and OBS2 (August 2017; red circles), catching the source in a high flux state. *Right panel.* Comparison between OBSID 60002033004 (February 2015; orange diamonds) and OBS4 (February 2018; blue stars), observing the source in a low flux state. In both panels, the green solid line represents the modelling of the opposite flux state, and FPMA and FPMB data of each observation are grouped together for clarity purposes only (Zaino et al. 2020). The disagreement between blue data and the high flux model below 5.5 keV is due to the appearence of the ULX in February 2018. We refer to the text for further details.

Moreover, to better compare our findings to those obtained from the previous *NuSTAR* analyses, we decided to leave the column densities and normalizations of the reflection parameters free to vary (Model C - $\chi^2_r = 1.08$ – see panel (c) in Figure 4.9). This allowed us to check the good agreement between our values and those observed by Bauer et al. (2015) for the 2012 epoch and Marinucci et al. (2016) for the 2014-2015 epochs, as reported in Table 4.5. Since the highest column density reflector located within 2 arcsec of the nuclear region and providing the bulk of the flux of the Compton hump (i.e. $N_{H,1}$) was not constrained, we fixed its value to the best-fit one (i.e. 10^{25} cm^{-2}).

Then, due to the complexity of the model used to reproduce our data set (see §4.2 for a detailed description), we decided to follow the same approach used by Marinucci et al. (2016) in analyzing the 2014-2015 *NuSTAR* campaign. Therefore, we fixed the column densities and the normalizations of the three reflectors to the best-fit values previously found, leaving only the flux of the primary component and the column density along the line of sight free to vary (Model D). We obtained an improvement of the fit ($\chi^2_r = 1.07$ – see panel (d) in Figure 4.9), pointing out a variation in N_H between the observations. However, the column density along the line of sight in OBS4 is unconstrained and a significant spread in the intrinsic emission of the AGN is clearly visible during the monitoring (see Figure 4.10 and Model D in Table 4.4), although the large errors make the normalizations of the four observations consistent with each other.

For this reason, we tied together the normalizations of the intrinsic power-law during the whole monitoring, leaving only the column density along the line of sight free to vary (Model E - see Figure 4.11). Despite the χ^2_r being unchanged with respect to Model D, this modelling allowed us to avoid the degeneracy between variations in the absorbing column density and the intrinsic emission of the source resulting in better constraints on the column density in all the observations (see Model E in Table 4.4) and reproducing

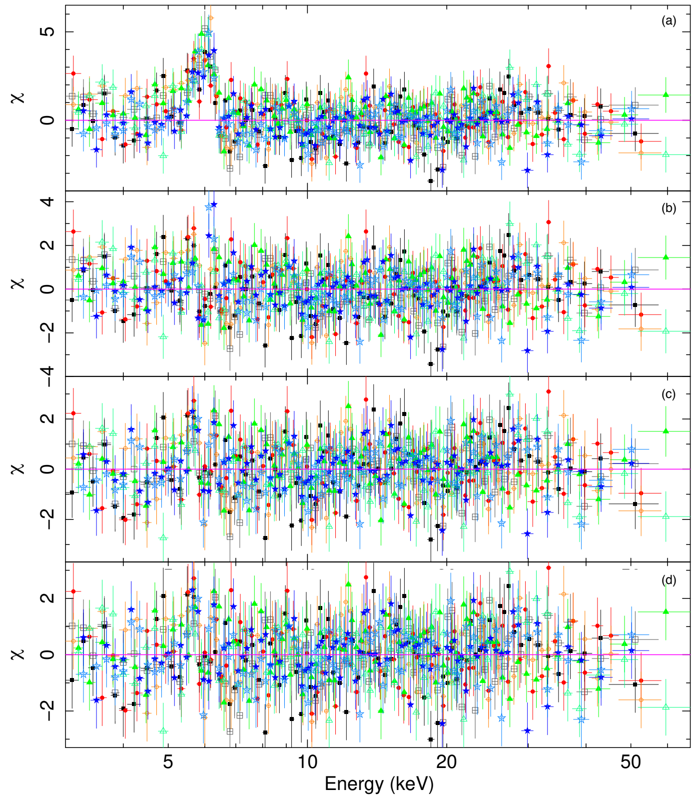

Figure 4.9. *From top to bottom.* Residuals with respect to Model A, B, C and D (solid magenta line in the four panels) plotted in terms of sigmas (Zaino et al. 2020). OBS1, OBS2, OBS3 and OBS4 are shown in black and grey squares, red and orange circles, green and dark green triangles and blue and light blue stars, while filled and empty symbols represent FPMA and FPMB data, respectively.

Table 4.5. Comparison between the reflectors parameters obtained in this work and in the previous ones (Zaino et al. 2020), when modeled through `MYTORUS` tables (Murphy & Yaqoob 2009).

	Bauer (2015)	Marinucci (2016)	This work (Model C)
Γ $^{(1)}$	$2.10^{+0.06}_{-0.07}$		2.10 ± 0.01
$N_{H,1}$ $^{(2)}$	≥ 9.7		$10^{\dagger}$
$norm_1$ $^{(3)}$	$(3.0 \pm 0.5) \times 10^{-1}$	all the parameters are fixed	$(3.0 \pm 0.2) \times 10^{-1}$
$N_{H,2}$ $^{(2)}$	0.14 ± 0.01	to the best-fit values	0.13 ± 0.01
$norm_2$ $^{(3)}$	$(3.6^{+0.3}_{-0.2}) \times 10^{-2}$	found in Bauer (2015)	$(4.3^{+0.3}_{-0.4}) \times 10^{-2}$
$N_{H,3}$ $^{(2)}$	$5.0^{+4.2}_{-1.9}$		≥ 4.3
$norm_3$ $^{(3)}$	$(1.0 \pm 0.2) \times 10^{-2}$		$(0.9 \pm 0.3) \times 10^{-2}$

Notes. $^{(1)}$ Photon index. $^{(2)}$ Column density of the reflector, in units of 10^{24} cm^{-2}. $^{(3)}$ Normalization of the reflected emission, in units of ph cm^{-2} s^{-1} keV^{-1}. †Fixed value.

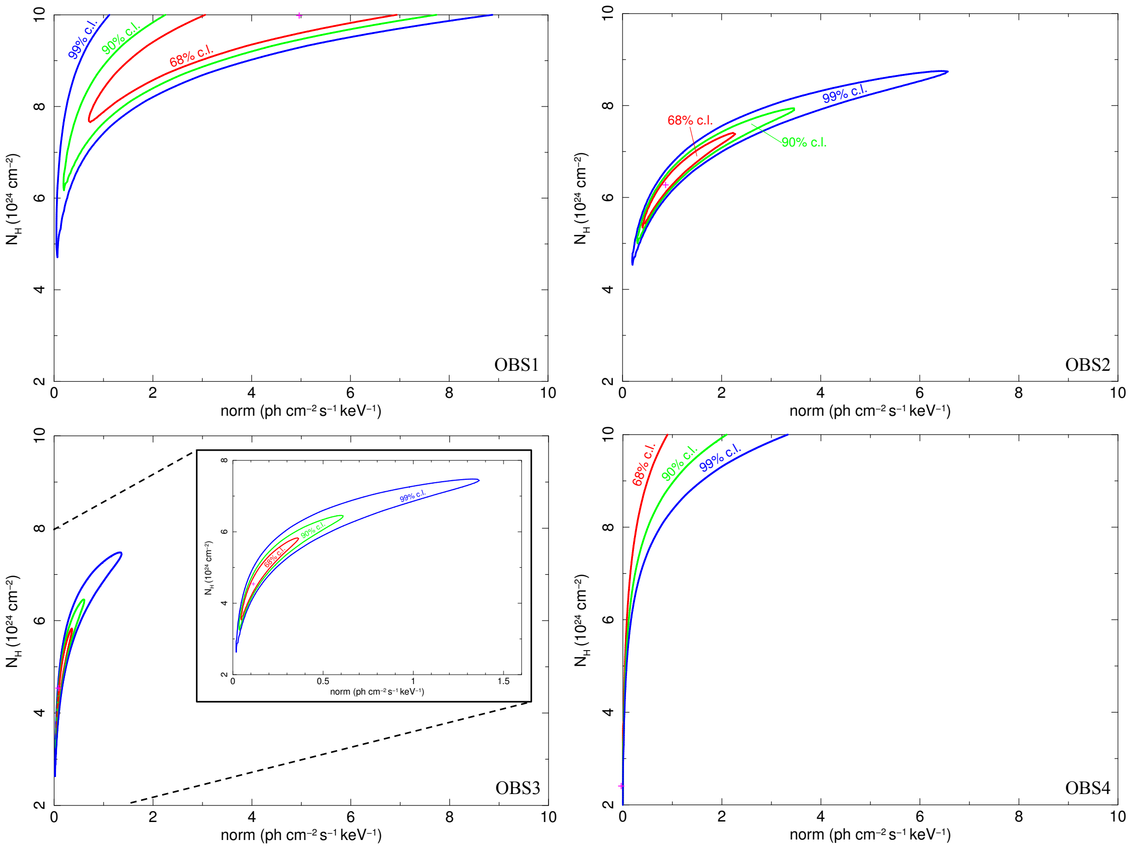

Figure 4.10. Confidence contours between the obscuring column density along the line of sight and the normalization of the primary power-law component for OBS1 (top left), OBS2 (top right), OBS3 (bottom left – a zoom is shown within the black box), and OBS4 (bottom right), when Model D is assumed (Zaino et al. 2020). A variation in N_H is clearly visible between the observations, even if the absorbing column density is unconstrained in OBS4, while the normalizations are consistent with each other despite a large spread in their values. Red, green and blue contours indicate 68 per cent, 90 per cent and 99 per cent confidence levels, while the magenta cross indicates the best-fit values.

well the behavior already shown in Figure 4.8. Using this parametrization, we obtained an intrinsic unabsorbed 2-10 keV luminosity $L_{2-10} = (3.5^{+3.6}_{-1.8}) \times 10^{43}$ erg s^{-1} at the distance of NGC 1068, in agreement with Bauer et al. (2015) and Marinucci et al. (2016), and fully consistent with the one inferred using the mid-IR (Gandhi et al. 2009) and [OIII] (Lamastra et al. 2009) observed luminosities.

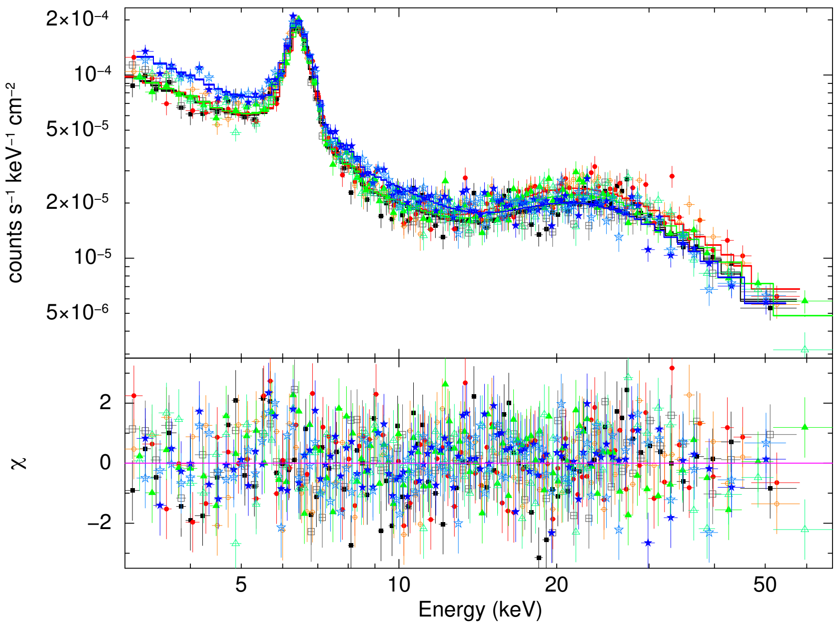

Figure 4.11. *NuSTAR* monitoring spectra (top panel) and residuals plotted in terms of sigmas (bottom panel) with respect to the best-fit model (Model E). Both the color code and the symbols are the same as in Figure 4.9 (Zaino et al. 2020).

On the other hand, the degeneracy between N_H and the intrinsic emission of the source could be also avoided assuming a uniform absorbing column density with an intrinsic variability in the accretion rate. Testing this scenario (Model F in Table 4.4), we obtained a fit equivalent to the previous one from a statistical point of view ($\chi^2_r = 1.08$), with an absorbing column density along the line of sight $N_H = (5.9^{+1.0}_{-0.8}) \times 10^{24}$ cm^{-2}, fully consistent with the values obtained in Model D only for two observations (OBS2 and OBS3). Furthermore, a variation between the normalizations of the intrinsic power-law in OBS3 and OBS4 is clearly visible. This corresponds to a change in the X-ray luminosity in the 2-10 keV band $\Delta L_{2-10} = (1.8^{+3.3}_{-1.4}) \times 10^{43}$ erg s^{-1}, suggesting a decrease in the normalized accretion rate of the source (i.e. L_{bol}/L_{Edd}) from 0.47 to 0.12 in a 3-month timescale.

However, due to the fact that the X-ray luminosity we obtain in the low-flux state of NGC 1068 (which characterises most of the observations) using Model F (i.e. $L_{2-10} \leq 9.8 \times 10^{42}$ erg s^{-1}) is much less than the one expected from other wavelengths, while the constant L_X - multiple N_H scenario provides an X-ray luminosity fully consistent with the one inferred using the mid-IR and [OIII] observed luminosities, we adopted Model E as our best-fit model.

4.4.3 Calibration issues

As reported in §4.4.2, when modelling the *NuSTAR* X-ray spectra of NGC 1068, we obtained significant residuals at ∼6 keV (see panel (a) in Figure 4.9). Comparing our monitoring observations with older data obtained during the previous *NuSTAR* monitoring campaign in 2014-2015, we find lack of temporal dependence of the iron line profile (see Figure 4.12). Assuming that the slight variations of the blue data are due to the appearence of the ULX in February 2018 (see Section 4.4.1), the line profiles are sufficiently similar to each other to conclude that their variance is purely statistical. We note that no issues were reported in Marinucci et al. (2016) because they only considered *NuSTAR* data above 8 keV, using simultaneous *XMM-Newton* data at lower energies.

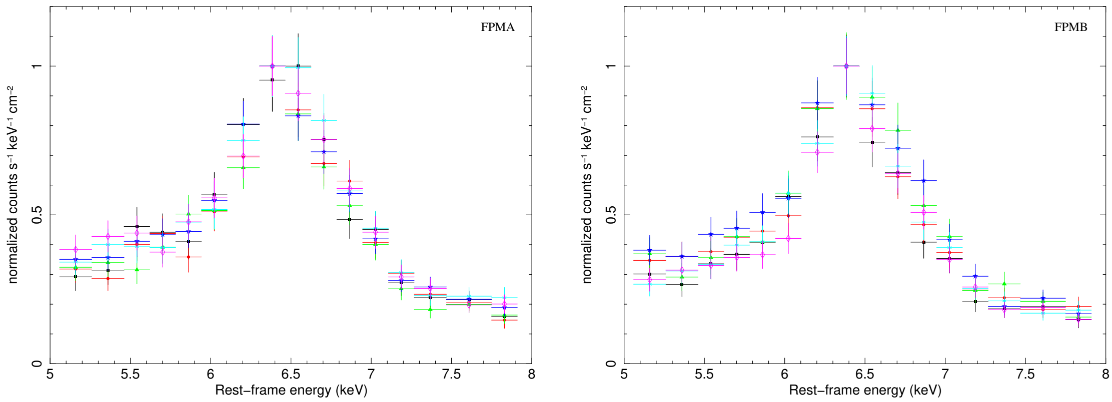

Figure 4.12. FPMA (left panel) and FPMB (right panel) spectra of NGC 1068 in the 5-8 keV range, normalizing to one the intensity of the highest channel (Zaino et al. 2020). Black squares, red circles, green triangles, blue stars, cyan asterisks and magenta diamonds represent OBS1, OBS2, OBS3, OBS4, August 2014 and February 2015 observations, respectively. For clarity purposes, all the observations have the same energy bins.

Fitting the residuals at ∼6 keV with a further emission line (i.e. a `gauss` component in `XSPEC`) with respect to Model A, we obtain energies and normalization values fully consistent with each other, both in FPMA and FPMB (see Table 4.6). We note that for the data reduction of the older *NuSTAR* observations we used the same procedure explained in §4.3.1, binning the data using OBS2 as a template (i.e. the August 2014 and February 2015 spectra have the same energy bins of the August 2017 one).

Table 4.6. Comparison of the 6 keV line component between old and new *NuSTAR* observations (Zaino et al. 2020).

	FPMA†	FPMB†
Aug 2014	1.8 ± 0.5	1.8 ± 0.5
Feb 2015	2.0 ± 0.4	2.0 ± 0.5
OBS1 (Jul 2017)	1.7 ± 0.5	2.3 ± 0.5
OBS2 (Aug 2017)	1.3 ± 0.5	2.4 ± 0.5
OBS3 (Nov 2017)	2.0 ± 0.5	2.1 ± 0.5
OBS4 (Feb 2018)	2.1 ± 0.5	2.1 ± 0.5

Note. † Normalization of the spurious line component, in units of 10^{-5} ph cm^{-2} s^{-1} keV^{-1}, fitting the data with Model E.

As a further step, we take advantage of the simultaneous *XMM-Newton* and *NuSTAR* observations performed in August 2014 (OBSID 0740060401 and 60302003004, respectively), to evaluate the possible presence of a line at ∼6 keV in data with higher spectral resolution. The *XMM-Newton* data were reduced using the latest CCF and the pn spectrum was extracted from a circular region with a 40 arcsec radius centered on the source, and binned in order to oversample the instrumental resolution by at least a factor of 3 and to have no less than 30 counts in each background-subtracted spectral channel. We note that the extraction region for the source spectrum is smaller than those used to extract the *NuSTAR* spectra, but no sources of emission were present beyond 40" within the EPIC images. Fitting both *XMM-Newton* and *NuSTAR* observations with a phenomenological model (i.e. `zpow+pexrav+several zgauss` components in `XSPEC`), we obtain the best fit in Figure 4.13. *XMM-Newton* data are well reproduced by the model, while significant residuals at ∼6 keV are clearly visible in *NuSTAR* spectra (see red and green spectral bins in panel (a)). To reproduce these residuals, an additional `gauss` component is needed. It is worth noting that the upper limit to the flux of an emission line at that energy in the *XMM-Newton* spectrum is much lower and inconsistent with the measurement in *NuSTAR* (see Table 4.7).

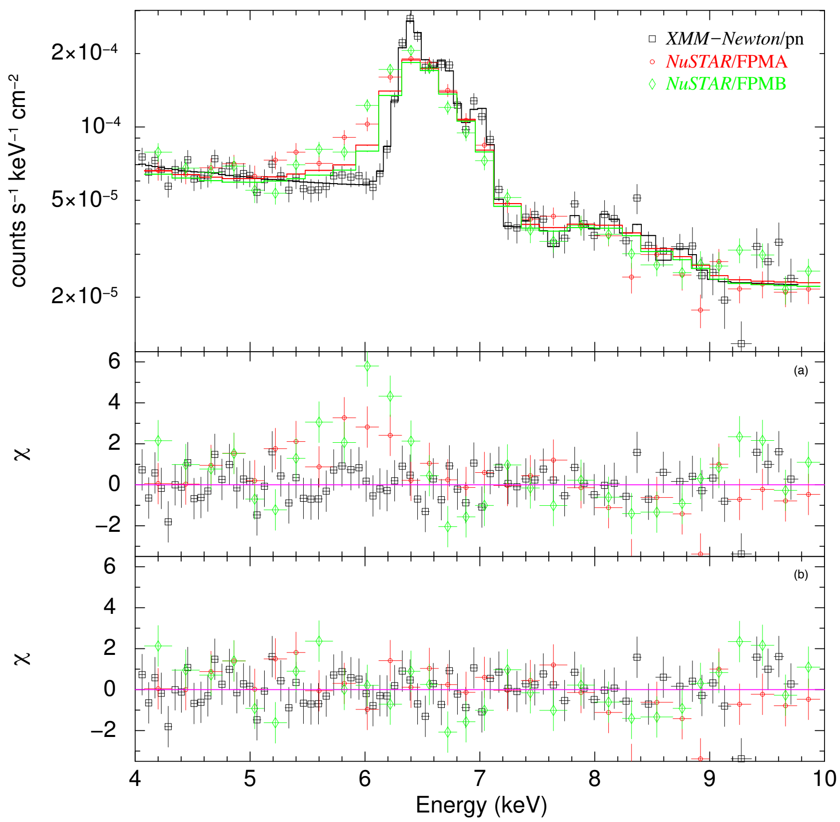

Figure 4.13. *Upper panel. XMM-Newton*/pn (black squares) and *NuSTAR*/FPMA (red circles) and FPMB (green diamonds) spectra of NGC 1068 performed simultaneously in August 2014, showing the 4-10 keV energy range. *Lower panels.* Residuals plotted in terms of sigmas with respect to the phenomenological model (panel (a)) and fitting the *NuSTAR* spectra with an additional emission line (panel (b)). We refer to the text for further details (Zaino et al. 2020).

Table 4.7. Energy and normalization of the 6 keV line component in the simultaneous *XMM-Newton* and *NuSTAR* observations performed in August 2014. Both spectra are fitted with a phenomenological model (Zaino et al. 2020).

	E (keV)	norm (ph cm^{-2} s^{-1} keV^{-1})
XMM-Newton	$6.0^{\dagger}$	$\leq 1.9 \times 10^{-6}$
NuSTAR/FPMA	6.0 ± 0.1	$(1.4 \pm 0.5) \times 10^{-5}$
NuSTAR/FPMB	6.1 ± 0.1	$(2.5 \pm 0.6) \times 10^{-5}$

Note. † Fixed value.

All the previous findings suggest that the significant residuals observed in Model A have no astrophysical origin, but are probably due to calibration issues; therefore, to account for them, we added a spurious emission line (modeled in `XSPEC` with a `gauss` component with $\sigma = 0$) in our best-fit model (Model E), leaving both its energy and flux free to vary between both the observations and the two *NuSTAR* focal planes.

An analogous feature is also observed in ESO 138-G1 (Zappacosta et al. in prep.), which is another Compton-thick AGN with a very large equivalent width of the Fe Kα line (e.g. Collinge & Brandt 2000, Piconcelli et al. 2011, De Cicco et al. 2015).

4.5 Discussion

Supposing that the intrinsic luminosity of the source did not vary during the whole monitoring, we attribute the spectral differences observed above 20 keV to X-ray emission piercing through a patchy dusty region. We observe the same column density variability on 6-month timescales already found by Marinucci et al. (2016) during the previous *NuSTAR* monitoring campaign (see red and blue data points with respect to grey and orange ones in Figure 4.14), suggesting the presence of a variable absorber on parsec-scale distance. However, the observational strategy of our monitoring campaign allowed us to probe shorter timescales with the aim of better constraining the location of the circumnuclear absorbing matter in NGC 1068.

According to our best-fit model, the values of the column density along the line of sight with their 1-sigma errors are $N_H = (7.4 \pm 0.6) \times 10^{24}$ cm^{-2}, $N_H = (5.6 \pm 0.5) \times 10^{24}$ cm^{-2}, $N_H = (6.2 \pm 0.5) \times 10^{24}$ cm^{-2} and $N_H \geq 8.6 \times 10^{24}$ cm^{-2} (corresponding to $N_H \geq 7.8 \times 10^{24}$ cm^{-2} at the 90 per cent confidence level, as reported in Table 4.4) for OBS1, OBS2, OBS3 and OBS4, respectively (see Figure 4.14). Thus, assuming the same intrinsic X-ray luminosity during the whole monitoring, we could clearly identify one unveiling and one eclipsing event: the first between July and August 2017 and the second between November 2017 and February 2018 with timescales lower than 27 days and 91 days, respectively. These events were ascribed to Compton-thick material with $N_H = (1.8 \pm 0.8) \times 10^{24}$ cm^{-2} and $N_H \geq (2.4 \pm 0.5) \times 10^{24}$ cm^{-2}, respectively, which moved temporarily across our line of sight, allowing or preventing the intrinsic nuclear radiation to pierce through the circumnuclear absorbing medium.

Considering a scenario in which the obscuring material is composed of individual spherical clouds orbiting with Keplerian velocities at a distance R from the SMBH, the distance of the cloud responsible for the unveiling/eclipsing event is given by

$$R = \frac{G M_{BH} (\Delta t)^2 n^2}{N_H^2}, \tag{4.1}$$

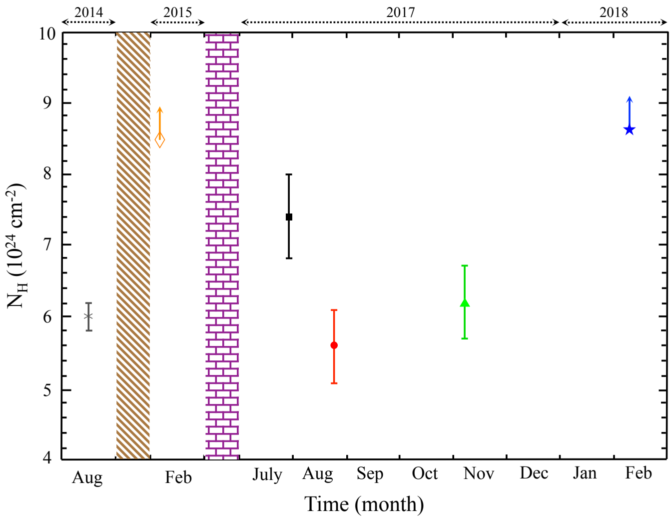

Figure 4.14. Values of the obscuring column density along the line of sight for the four 2017-2018 NuSTAR monitoring observations (black square, red circle, green triangle and blue star), when Model E is adopted. Old 2014-2015 measurements (grey asterisk and orange diamond) reproducing the same intrinsic luminosity are extrapolated from Figure 3 in Marinucci et al. (2016) and shown here for comparison. Errors correspond to the 68 per cent confidence level for one interesting parameter. Brown stripes and violet bricks indicate a period of 5 and 28 months, respectively, not covered by observations (Zaino et al. 2020).

where G is the gravitational constant, M_{BH} is the BH mass, Δt is the timescale of the column density variation, and n and N_H are the gas density and the column density of the cloud, respectively. Assuming a black hole mass $M_{BH} = 10^7$ M$_\odot$, as derived from water maser measurements (Greenhill et al. 1996), and a typical value for the gas density within the broad line region, such as $n = 10^{10}$ cm^{-3} (Wang et al. 2012), we estimate a size for the obscuring cloud of $D \sim 150\ R_g$ and find that the absorbers responsible for the unveiling and eclipsing event are located at a distance $R \leq (0.07 \pm 0.05)$ pc and $R \leq (0.46 \pm 0.14)$ pc, respectively.

According to Kaspi et al. (2005), the radius of the BLR is given by

$$\frac{R_{BLR}}{10\ lt - days} = 0.86 \times \left(\frac{L_{2-10\ keV}}{10^{43}\ erg\ s^{-1}}\right)^{0.544}, \tag{4.2}$$

leading to $R_{BLR} = \left(0.014^{+0.015}_{-0.007}\right)$ pc, using our spectral fitting parameters. Moreover, using the bolometric correction from Marconi et al. (2004), we inferred a bolometric luminosity $L_{bol} = (0.8^{+1.2}_{-0.6}) \times 10^{45}$ erg s^{-1}, in agreement with other studies (e.g. Pier et al. 1994; Woo & Urry 2002; Hönig et al. 2008) and leading to a dust sublimation radius $R_d = (0.36^{+0.27}_{-0.14})$ pc, if an average dust grain size of 0.05 μm with a temperature $T = 1500\ K$ is considered (Barvainis 1987). Assuming the torus inner walls to be at the dust sublimation radius, this value is consistent with the dimension of the dusty torus observed in infrared. Therefore, considering the gas density reported above, the obscuring clouds are constrained to be located in the innermost and hottest part of the dusty torus, or even further inside (i.e. in the BLR).

Finally, the inferred bolometric luminosity leads to a normalized accretion rate $\lambda = \frac{L_{\rm bol}}{L_{\rm Edd}} = 0.63^{+0.95}_{-0.48}$, which confirms the highly accreting nature of the source. Therefore, we cannot definitively rule out the hypothesis that at least part of the observed X-ray variability of the AGN in NGC 1068 is due to a change in the intrinsic luminosity of the central accretion disk. But, also in this latter case (i.e. Model D), a variation in N_H is expected, even though the column density in OBS4 is unconstrained. On the other hand, if we attributed the observed X-ray variability as due only to a change in the intrinsic AGN luminosity (i.e. Model F), we obtain a scenario equivalent to that suggested by our best-fit model from a statistical point of view. However, according to Shemmer et al. (2008), the normalized accretion rate resulting in OBS4 would correspond to a power-law slope $\Gamma = 1.82 \pm 0.01$, well below that observed in our analysis (i.e. $\Gamma = 2.1$). Furthermore, the uniform N_H - multiple L_X scenario predicts a column density well below the average value of 10^{25} cm^{-2} usually observed in NGC 1068 (e.g. Bauer et al. 2015), while our assumption of a constant intrinsic luminosity of the AGN on timescales of months is supported by mid-IR and optical data. Thus, our findings firmly rule out the scenario of a single, monolithic obscuring wall, and instead support the presence of a clumpy torus surrounding the nuclear region of NGC 1068.

4.6 What's next?

We have presented a spectral analysis of the latest *NuSTAR* monitoring campaign of the Compton-thick Seyfert 2 galaxy NGC 1068 composed of four ∼50 ks observations performed between July 2017 and February 2018 and probing timescales from 1 to 6 months. Our findings are summarized as follows.

- We detected one unveiling and one eclipsing event with timescales lower than 27 and 91 days, respectively, ascribed to Compton-thick material with $N_H = (1.8 \pm 0.8) \times 10^{24}$ cm^{-2} and $N_H \geq (2.4 \pm 0.5) \times 10^{24}$ cm^{-2} moving across our line of sight, allowing or preventing the intrinsic nuclear radiation from piercing through the circumnuclear matter. We can apparently locate the absorbing gas clouds to arise from the innermost part of the torus or closer, thus providing both tighter constraints on their location with respect to the previous *NuSTAR* monitoring campaign, and further evidence of the clumpy structure of the circumnuclear matter in this source.
- We reported a *Swift*-XRT detection of a transient X-ray source in February 2018, which is plausibly a strongly variable ULX located at ∼2 kpc from the nucleus of NGC 1068, with a peak X-ray intrinsic luminosity of $(3.0 \pm 0.4) \times 10^{40}$ erg s^{-1} in the 2-10 keV band.

Since its launch in June 2012, *NuSTAR* has observed NGC 1068 several times, sampling timescales ranging from ∼1 month to ∼5 years; further observations also performed simultaneously with future X-ray observatories, like *XRISM*, will be certainly helpful in refining and better constraining the scenario we discussed in §4.5. Furthermore, a leap in this field is expected to be achieved with the launch of the next future *High-Energy X-ray Probe* (*HEX-P* – Madsen et al. 2019) taking advantage of the complementary capability with the simultaneous *ATHENA* mission (Nandra et al. 2013; Barcons et al. 2017), providing the former a high-energy sensitivity with an improvement by a factor of 40 over *NuSTAR* in the 10-80 keV band, and the latter a high resolution spectroscopy below 10 keV. On the other hand, different information on the nature and geometry of the circumnuclear matter in NGC 1068 can be obtained from future X-ray polarimetry missions, such as the *Imaging X-ray Polarimeter Explorer* (*IXPE* - Weisskopf et al. 2016a and 2016b, scheduled to be launched at the end of 2021) and the enhanced X-ray Timing and Polarimetry mission (*eXTP* – Zhang et al. 2019, planned to be launched in 2027). In fact, in the 2-8 keV working band of the polarimeters on board these missions, the X-ray emission is dominated by reflection from the circumnuclear matter. A high polarization degree, dependent on the inclination and level of symmetry of the matter, is expected, with the polarization angle related to the symmetry axis. A comparison of such an axis to those of the spatially resolved inner tori and of the ionization cone will shed further light on the structure of the circumunuclear matter in NGC 1068.

Finally, as concerns the serendipitous discovery of the ULX discussed in §4.4.1, a search for its potential optical-ultraviolet counterpart has been planned for the next future using *Swift*-UVOT data. Indeed, multiwavelength studies can represent a key role to investigate the nature and the environment of these sources (e.g. Roberts et al. 2008). In particular, some constraints on the mass of the compact object or information about the accretion flow can be obtained from the radial velocity curve of the companion star (Kaaret et al. 2017). Moreover, several observations of point like counterparts with blue colors have already shown that some ULXs are associated with young star clusters or star forming regions (e.g. Liu et al. 2004; Soria et al. 2005; Avdan et al. 2016). However, even though the observed blue colors are consistent with emission from an irradiated accretion disk, it is worth noting that such a color may be partly due to contamination by reprocessed X-rays from both the accretion disc or the stellar surface (e.g. Madhusudhan et al. 2008; Patruno & Zampieri 2010; Vinokurov et al. 2018).

5

Probing the Compton-thin AGN in NGC 4507 through a *NuSTAR* monitoring

Contents

This chapter focuses on the analysis of a *NuSTAR* monitoring campaign of the Compton-thin Seyfert 2 galaxy NGC 4507. Composed of five 1-month spaced observations performed between May and September 2015, the campaign was aimed at solving any possible ambiguity on the variability of the intrinsic emission and amount of absorption within this source (Zaino et al. submitted). A short overview on NGC 4507 is discussed in §5.1, while §5.2 is devoted to the X-ray observations and the data reduction, with a particular attention to the *NuSTAR* spacecraft science data reduction used for the last observation (§5.2.1). The X-ray spectral analysis is described in §5.3, with §5.3.1 and §5.3.2 focused on the fits obtained modelling the circumnuclear matter with `pexrav` (Magdziarz & Zdziarski 1995) and `MYTorus` (Murphy & Yaqoob 2009) models, respectively. Finally, the results of the *NuSTAR* analysis are discussed in §5.4.1 and compared to the previous X-ray findings in §5.4.2, while §5.5 is devoted to a short summary and to any further future observations.

5.1 Past X-ray observations of NGC 4507

NGC 4507 is a nearby (z=0.0118) barred spiral galaxy, classified as SBab(rs) I (Sandage & Brucato 1979), and one of the X-ray brightest Seyfert 2 galaxies with an observed flux

$F_{2-10\ keV} \sim 2.1 \times 10^{-11}$ erg cm^{-2} s^{-1}, corresponding to an absorption-corrected luminosity $L_{2-10\ keV} \sim 3.7 \times 10^{43}$ erg s^{-1} in the 2-10 keV energy range (Comastri et al. 1998).

In the last 25 years, this source has been studied by all the main X-ray observatories. Evidence of multiple regions absorbing and reprocessing the primary emission has been observed within NGC 4507 and the variability in the X-ray band has been ascribed to either a variation in the intrinsic emission or to changes in the amount of absorption. A short overview of the main results obtained through X-ray observations is summarized as follows.

In 1994, *ASCA* observed NGC 4507 in a Compton-thin regime ($N_H \sim 3 \times 10^{23}$ cm^{-2}) detecting an iron Kα line at energy $E = 6.36 \pm 0.03$ keV consistent with transmission through cold distant matter, a strong soft excess and a further emission line at ∼0.9 keV identified as the Ne IX recombination line (Turner et al. 1997; Comastri et al. 1998).

Between December 1997 and January 1999, the source was then observed three times by *BeppoSAX*, showing a decreasing in the X-ray flux by a factor of about 2 (from 1.84×10^{-11} erg cm^{-2} s^{-1} to 0.87×10^{-11} erg cm^{-2} s^{-1}) over a 6-month timescale, which was ascribed to a change in the intrinsic emission of the source. No variations are indeed observed in the slope of the primary continuum nor in the amount of intrinsic absorption. At the same time, the Compton hump and the iron Kα line showed no significant variations despite the drop in the intrinsic emission, confirming that reprocessing features in NGC 4507 arised from distant matter at $D \geq 0.15$ pc (Lanzi et al. 2001; Risaliti 2002; Dadina 2007).

Two campaigns performed in 1996 and 2003 with *RXTE* observed the source in an intermediate flux state with respect to those observed by *BeppoSAX*. The values of the photon index and the column density were not different by more than ∼0.2 and a factor of 1.5, respectively, between the two satellites; however, the reflection fraction observed by *RXTE* was significantly lower. The reason of the discrepancy in the amount of reflection between *RXTE* and *BeppoSAX* data is not obvious; one possibility is that the high value of the reflection component measured by *BeppoSAX* could indicate a response to a higher past illuminating flux.

In 2001, NGC 4507 was observed by *XMM-Newton* and *Chandra* with two observations spaced by about two months, during which the flux of the source increased by a factor of 2, under the hypothesis of a constant absorbing column density ($N_H \sim 4 \times 10^{23}$ cm^{-2}). For the first time, the iron Kα Compton shoulder was detected and the observed shoulder-to-core ratio suggested that the bulk of the line originated in Compton-thick matter far away from the black hole. Thus, two different cold circumnuclear regions (i.e a Compton-thick reflector and a Compton-thin absorber) were required to explain the spectrum of the source at hard X-rays. Furthermore, at least two photoionized regions were needed to explain the large range of ionization states of the several emission lines detected in the soft X-rays (Matt et al. 2004).

In 2007, *Suzaku* caught the source in a highly absorbed state ($N_H \sim 9 \times 10^{23}$ cm^{-2}). A comparison with the previous *XMM-Newton* observations showed a variation both in the absorbing column density and in the intrinsic emission of the source. However, the spectral shape of NGC 4507 as observed by *XMM-Newton* cannot be reproduced without a significant change in the absorbing column density; thus, the main driver of the observed X-ray variability has been ascribed to a change in the obscuration level along the line of sight (Braito et al. 2013).

Finally, in 2010, *XMM-Newton* and *Chandra* performed a monitoring campaign of NGC 4507 composed of six observations and spanning a time period of about six months. A strong absorption variability on timescales of 1.5 - 4 months was detected ($|\Delta N_H| =$

$2.5 \times\ 10^{23}$ cm^{-2} at a 3σ confidence level – see Figure 5.1), suggesting the circumnuclear material to be composed of gas clouds on parsec-scale distance (Marinucci et al. 2013a).

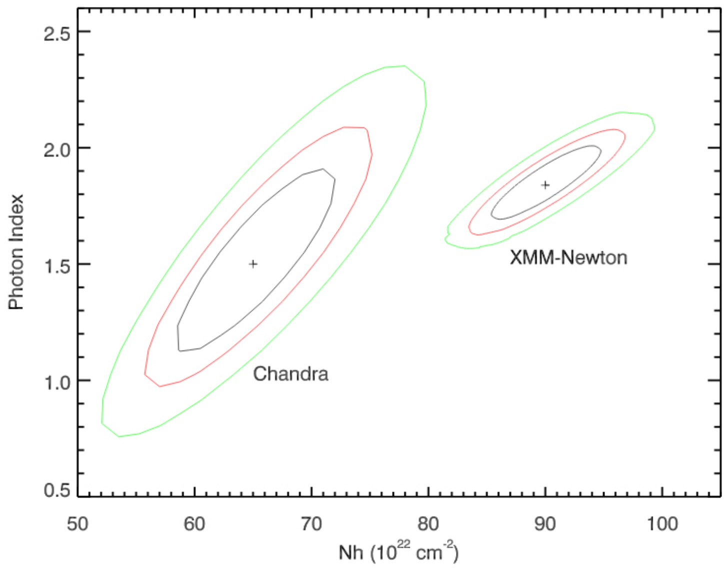

Figure 5.1. Γ-N$_H$ contour plots for the 5 combined *XMM-Newton* pointings and for the *Chandra* observation. The black crosses indicate the best-fit values, while solid black, red and green lines correspond to 1σ, 2σ and 3σ confidence levels, respectively (Marinucci et al. 2013a).

5.2 *NuSTAR* observations and data reduction

NGC 4507 was observed by *NuSTAR* (Harrison et al. 2013) with its two co-aligned X-ray telescopes, with corresponding Focal Plane Modules A (FPMA) and B (FPMB), during a monitoring campaign composed of five observations of about 30 ks each, performed between May and September 2015 (see Table 5.1).

Table 5.1. NuSTAR observation log for NGC 4507 (Zaino et al. submitted).

	obsID	Start time	Stop time	Total ontime[a] [ks]
OBS1	60102051002	2015-05-03 20:16:07	2015-05-04 12:01:07	32.3
OBS2	60102051004	2015-06-10 19:16:07	2015-06-11 14:21:07	37.1
OBS3	60102051006	2015-07-15 08:01:08	2015-07-16 01:11:08	34.6
OBS4	60102051008	2015-08-22 09:56:08	2015-08-23 01:51:08	33.2
OBS5	60102051009	2015-09-22 09:06:08	2015-09-23 04:06:08	—

Notes. [a] Total *NuSTAR* time on source, corresponding to the total Good Time Interval (GTI) for each obsID in Science mode. It is worth noting that the ontime differs from the exposure time, since the latter is corrected for the instrument livetime.

The Level 1 data products were processed using the *NuSTAR* Data Analysis Software (`NuSTARDAS`) package (version 1.8.0). Event files (Level 2 data products) were extracted using the `nupipeline` task, adopting standard filtering criteria and the latest calibration files available in the *NuSTAR* calibration database (`CALDB 20190627`). During the last observation (obsID=60102051009, hereafter OBS5), the star tracker on the optics bench that supplies absolute pointing data did not achieve a valid attitude solution; thus, we reduced the mode 06 files where the astrometry is calculated from the star trackers located on the spacecraft bus. A detailed discussion about this procedure is discussed in §5.2.1. We note that even if this method is not suitable for imaging studies, it provides spectra consistent with those obtained using standard science modes.

Each source spectrum was extracted from a circular region of radius 60 arcsec, corresponding to an encircled energy fraction (EEF) of about 75%, from both FPMA and FPMB, while the background data were extracted selecting two circular regions on the same chip, uncontaminated by source photons or background sources, with a radius of 60 arcsec each. Finally, the spectra were binned in order to have at least 100 counts in each background-subtracted spectral channel, and not to oversample the instrumental energy resolution by a factor larger than 3 (Kaastra & Bleeker 2016 and references therein). Net exposure times and the total count rates are reported in Table 5.2 for each observation and for both FPMA and FPMB, while spectra are shown in Figure 5.2.

Table 5.2. Net exposure time and net count rate of the *NuSTAR* monitoring of NGC 4507 (Zaino et al. submitted).

	Detector	Net exposure time [a] [ks]	Net count rate [b] [counts s^{-1}] 3-10 keV	10-40 keV	40-79 keV
OBS1	FPMA	30.1	0.226±0.003	0.347±0.003	0.018±0.001
	FPMB	30.1	0.214±0.003	0.320±0.003	0.018±0.001
OBS2	FPMA	34.5	0.245±0.003	0.351±0.003	0.016±0.001
	FPMB	34.4	0.231±0.003	0.328±0.003	0.015±0.001
OBS3	FPMA	31.4	0.217±0.003	0.353±0.003	0.019±0.001
	FPMB	31.4	0.212±0.003	0.324±0.003	0.017±0.001
OBS4	FPMA	30.9	0.226±0.003	0.328±0.003	0.017±0.001
	FPMB	30.9	0.223±0.003	0.329±0.003	0.016±0.001
OBS5	FPMA	37.5	0.292±0.003	0.399±0.003	0.018±0.001
	FPMB	36.2	0.296±0.003	0.394±0.003	0.019±0.001

Notes. [a] Net exposure time, after screening was applied on the data. [b] Net source count rate after screening and background subtraction, as observed in the 3-10 keV, 10-40 keV and 40-79 keV energy ranges.

5.2.1 The *NuSTAR* spacecraft science data reduction

NuSTAR spectral analyses are usually performed starting from the standard “science” data (known as mode 01), where the absolute pointing is determined using the on-board star tracker located on the X-ray optics bench (Camera Head Unit 4 – CHU4), which provides an aspect reconstruction accuracy of ±8 arcseconds. However, if blinded by either Earth-occultation or the presence of a bright target, CHU4 should not be available. In these cases, the spacecraft science mode (hereafter mode 06), where the source sky coordinates are derived using data from the three star trackers located on the spacecraft bus (CHU1, CHU2 and CHU3), can be used. This method causes a degradation in the accuracy to about ±2 arcminutes, which is mainly due to thermal flexing of the spacecraft bus star cameras, and results in multiple centroids in the reconstruction of the sky image of the source.

The three star trackers on the spacecraft bus (i.e. CHU1, CHU2, and CHU3) can be integrated in seven CHU combinations. Each of them is characterized by different offsets,

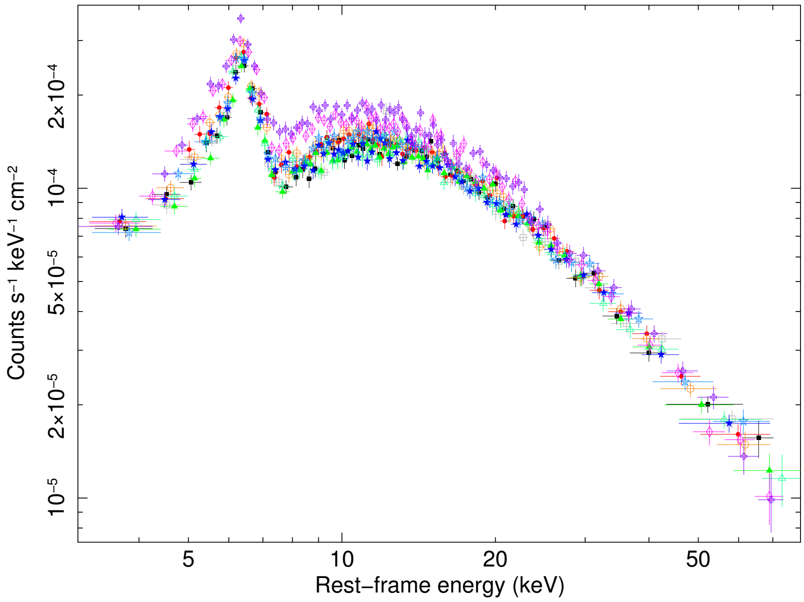

Figure 5.2. *NuSTAR* monitoring spectra of NGC 4507. OBS1, OBS2, OBS3, OBS4, and OBS 5 are shown in black and grey squares, red and orange circles, green and dark green triangles, blue and light blue stars, and magenta diamonds and violet crosses for FPMA and FPMB data, respectively. Data are rebinned for clarity purposes only (Zaino et al. submitted).

depending on several variables, such as the Solar aspect angle. This is the reason why mode 06 is not suitable for imaging studies. However, taking care of the optimal extraction region for each CHU combination, the spacecraft science mode can provide useful spectra when mode 1 is not available. Indeed, since all responses are calculated in the optics frame, whose relation to the detector plane is accurately tracked by a laser system, mode 06 spectra show no significant differences with respect to the standard science mode, as clearly shown in Figure 12 in Walton et al. (2016).

As concerns our *NuSTAR* monitoring, OBS5 is the only pointing for which the star tracker on the optics bench did not achieve a valid attitude solution. The spacecraft science data for this observation showed two centroids, which are about 45 arcseconds apart (see Figure 5.3).

To obtain the cleaned event files for both FPMA and FPMB, we made use of the `NuSTARDAS` software module `nusplitsc`, which decomposes the total mode 06 event file into distinct event files corresponding to a maximum of seven combinations of CHU1, CHU2 and CHU3. In our case, we obtained five event files (CHU2, CHU3, CHU12, CHU13, and CHU23). We then used the `nuproducts` software module to extract the energy spectra from the CHU# event files generated by `nusplitsc`. Since each CHU combination has a specific aspect reconstruction, we chose five different source extraction region files centered on the source as it appears in the corresponding decomposed mode 06 sky image. Finally, as recommended from the *NuSTAR* software analysis guide, we used `addspec` to combine the source and background PHA files as well as the RMFs and ARFs of each CHU combination. FPMA and FPMB spectra of NGC 4507, as obtained through this procedure, are shown in Figure 5.4.

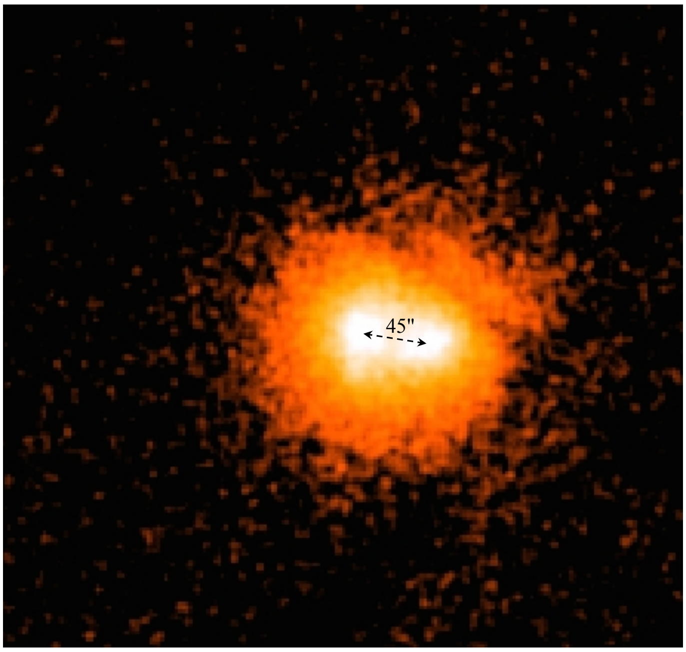

Figure 5.3. Sky image extracted from the full FPMA spacecraft science (mode 06) OBS5 event file, smoothed with a 2 pixels radius Gaussian filter. Due to the switch between different CHU combinations, two centroids at about 45 arcseconds apart are clearly evident (Zaino et al. submitted).

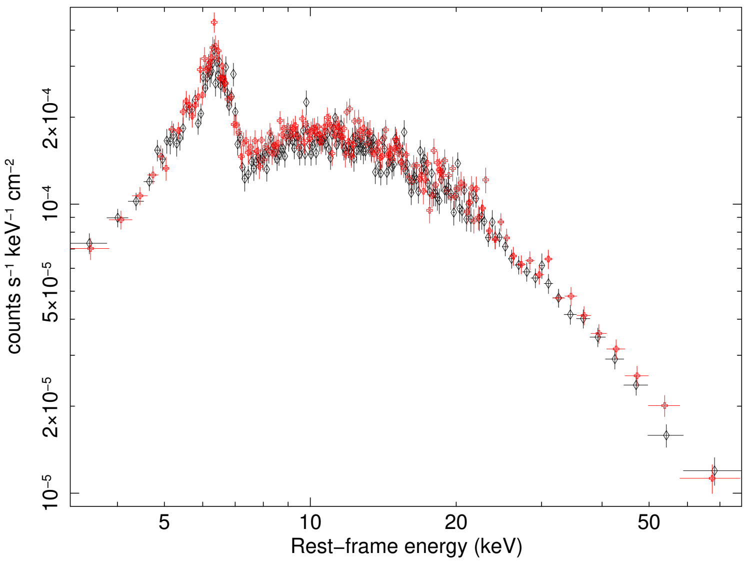

Figure 5.4. FPMA (black diamonds) and FPMB (red crosses) spectra of NGC 4507, as obtained after the *NuSTAR* spacecraft science (mode 06) data reduction (Zaino et al. submitted).

5.3 X-ray spectral analysis

The X-ray spectral analysis of NGC 4507 was performed using `XSPEC 12.10.1` (Arnaud 1996) and the χ^2 statistic. We assumed the photoelectric cross sections for all absorption components from Verner et al. (1996), while the element abundance pattern is from Wilms et al. (2000) and the metal abundance is fixed to solar. Unless stated otherwise, errors correspond to the 90 per cent confidence level for one interesting parameter ($\Delta\chi^2$=2.706).

5.3.1 Phenomenological approach

Following Matt et al. (2004), we fitted the *NuSTAR* 3-79 keV spectra with a model composed of an absorbed power-law plus Compton reflection continuum, a soft unabsorbed component and a Gaussian reproducing the iron Kα emission line at ~6.4 keV (Model P1). The reflection component is modeled with `pexrav` (Magdziarz & Zdziarski 1995), which accounts for a distant neutral reflector geometrically approximated as a slab, fixing the inclination angle to 30° (Matt et al. 2004; Braito et al. 2013). The fit was good (see Figure 5.5 – $\chi_r^2 = 1.06$) and, as concerns the iron line emission, we obtained values fully consistent between the observations, even though the rest-frame energies were lower than expected (see Model P1 in Table 5.3).

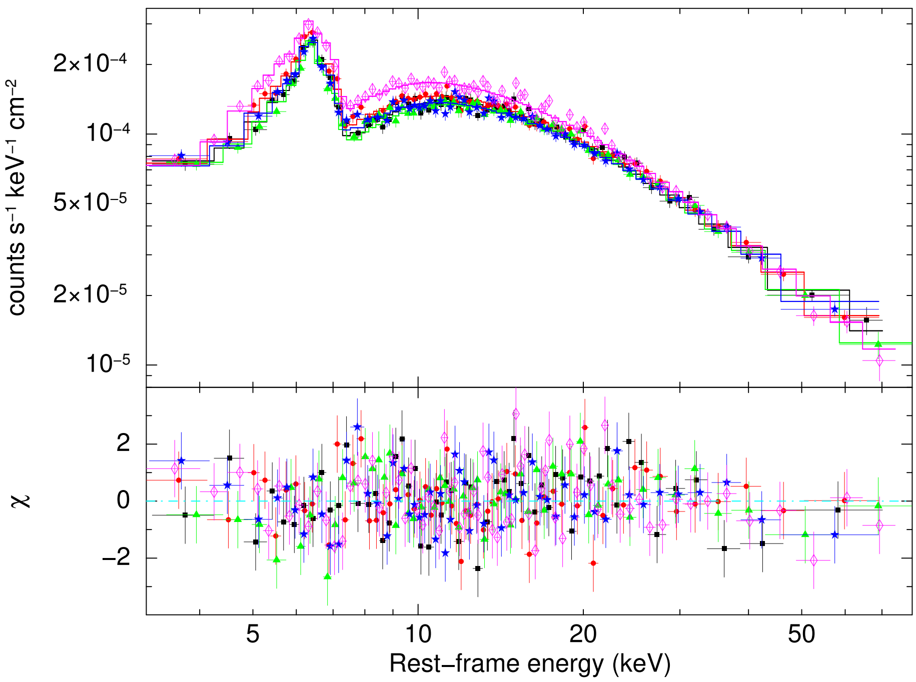

Figure 5.5. Spectra (top) and residuals (bottom) with respect to Model P1 (dash-dotted cyan line), plotted in terms of sigmas. OBS1, OBS2, OBS3, OBS4, and OBS 5 are shown in black squares, red circles, green triangles, blue stars, and magenta diamonds, respectively. Since residuals are similar in both *NuSTAR* focal planes, for clarity purposes only rebinned FPMA data are shown (Zaino et al. submitted).

As we already know, the iron Kα fluorescence line consists of a narrow core at about 6.4 keV and several Compton shoulders, due to the line photons emerging unscattered and after one or more scatterings, respectively (e.g. Matt 2002b). Since Chandra gratings observed the iron Kα line at the expected rest-frame energy within this source ($E = 6.403^{+0.021}_{-0.028}$ keV

Table 5.3. Summary of the `pexrav` models discussed in the text (Zaino et al. submitted).

Model P1: soft+primary+reflection+iron Kα line (χ^2/dof = 1305.6/1228)

	Γ	norm [ph cm^{-2} s^{-1} keV^{-1}]	N_H [10^{23} cm^{-2}]	|R|	$E_{K\alpha}$ [keV]	norm$_{K\alpha}$ [ph cm^{-2} s^{-1} keV^{-1}]
OBS1	1.68 ± 0.04	$(1.4 \pm 0.2) \times 10^{-2}$	7.67 ± 0.35	$0.15^{+0.13}_{-0.12}$	6.35 ± 0.03	$(4.8 \pm 0.7) \times 10^{-5}$
OBS2	$1.71^{+0.04}_{-0.03}$	$(1.5 \pm 0.2) \times 10^{-2}$	7.02 ± 0.30	$0.23^{+0.13}_{-0.11}$	6.33 ± 0.03	$(4.7 \pm 0.7) \times 10^{-5}$
OBS3	1.71 ± 0.04	$(1.5 \pm 0.2) \times 10^{-2}$	7.96 ± 0.36	$0.21^{+0.14}_{-0.12}$	6.33 ± 0.03	$(4.5^{+0.7}_{-0.6}) \times 10^{-5}$
OBS4	1.61 ± 0.04	$(1.1 \pm 0.1) \times 10^{-2}$	$6.77^{+0.34}_{-0.33}$	$0.16^{+0.13}_{-0.11}$	6.34 ± 0.03	$(4.4^{+0.6}_{-0.7}) \times 10^{-5}$
OBS5	1.81 ± 0.03	$(2.1 \pm 0.2) \times 10^{-2}$	6.70 ± 0.26	$0.32^{+0.12}_{-0.11}$	$6.32^{+0.03}_{-0.04}$	$(3.8^{+0.6}_{-0.7}) \times 10^{-5}$

Model P2: Model P1 + iron Kα Compton shoulder (χ^2/dof = 1306.4/1228)

Γ	norm [ph cm^{-2} s^{-1} keV^{-1}]	N_H [10^{23} cm^{-2}]	|R|	$E_{K\alpha}$ [keV]	norm$_{K\alpha}$ [ph cm^{-2} s^{-1} keV^{-1}]
During the whole monitoring, no significant changes appear in any parameters with respect to Model P1					

Model P3: Model P2 with gain (χ^2/dof = 1296.5/1228)

	Γ	norm [ph cm^{-2} s^{-1} keV^{-1}]	N_H [10^{23} cm^{-2}]	|R|	$E_{K\alpha}$ [keV]	norm$_{K\alpha}$ [ph cm^{-2} s^{-1} keV^{-1}]
OBS1	1.69 ± 0.04	$(1.5 \pm 0.2) \times 10^{-2}$	7.71 ± 0.35	0.16 ± 0.12	6.40 ± 0.03	$(3.8 \pm 0.6) \times 10^{-5}$
OBS2	1.72 ± 0.04	$(1.6 \pm 0.2) \times 10^{-2}$	7.10 ± 0.30	0.23 ± 0.12	6.40 ± 0.03	$(3.7 \pm 0.6) \times 10^{-5}$
OBS3	1.72 ± 0.04	$(1.5 \pm 0.2) \times 10^{-2}$	8.03 ± 0.36	0.21 ± 0.12	6.40 ± 0.03	$(3.5 \pm 0.5) \times 10^{-5}$
OBS4	1.63 ± 0.04	$(1.2 \pm 0.2) \times 10^{-2}$	6.86 ± 0.33	0.16 ± 0.12	6.40 ± 0.03	$(3.4 \pm 0.6) \times 10^{-5}$
OBS5	1.82 ± 0.03	$(2.3 \pm 0.2) \times 10^{-2}$	6.90 ± 0.25	0.29 ± 0.11	6.40 ± 0.03	$(2.9 \pm 0.6) \times 10^{-5}$

Model P4: Model P3 + nickel Kα line emission (χ^2/dof = 1255.1/1226)

	Γ	norm [ph cm^{-2} s^{-1} keV^{-1}]	N_H [10^{23} cm^{-2}]	|R|	$E_{K\alpha}$ [keV]	norm$_{K\alpha}$ [ph cm^{-2} s^{-1} keV^{-1}]
OBS1	1.71 ± 0.04	$(1.6 \pm 0.2) \times 10^{-2}$	7.92 ± 0.35	0.15 ± 0.12	6.40 ± 0.03	$(3.9 \pm 0.6) \times 10^{-5}$
OBS2	1.73 ± 0.04	$(1.6 \pm 0.2) \times 10^{-2}$	7.28 ± 0.30	0.22 ± 0.11	6.40 ± 0.03	$(3.8 \pm 0.6) \times 10^{-5}$
OBS3	1.73 ± 0.04	$(1.6 \pm 0.2) \times 10^{-2}$	8.26 ± 0.36	0.20 ± 0.12	6.40 ± 0.03	$(3.7 \pm 0.5) \times 10^{-5}$
OBS4	1.64 ± 0.04	$(1.2 \pm 0.2) \times 10^{-2}$	7.05 ± 0.33	0.16 ± 0.11	6.40 ± 0.03	$(3.5 \pm 0.5) \times 10^{-5}$
OBS5	1.83 ± 0.03	$(2.4^{+0.2}_{-0.3}) \times 10^{-2}$	7.05 ± 0.26	0.29 ± 0.11	6.40 ± 0.03	$(2.9 \pm 0.5) \times 10^{-5}$

Notes. Γ, norm: photon index and normalization of the intrinsic power-law; N_H: absorbing column density along the line of sight; |R|: solid angle Ω of the cold material visible from the Comptonizing source, in units of 2π; $E_{K\alpha}$ and norm$_{K\alpha}$: rest-frame energy and normalization of the iron Kα line; χ^2/dof: ratio between χ^2 and the degrees of freedom of the model. In model P2, the energy of the Compton shoulder is fixed at 6.32 keV, while its flux is fixed to be the 20% of the iron Kα line flux. In models P3 and P4, the energy and the flux of the Compton shoulder are fixed to be 0.08 keV lower than the line core energy, and the 20% of the iron Kα line flux, respectively. In model P3 and P4, the offset values were fixed to be g_1=-41 eV, g_2=-50 eV, g_3=-53 eV, g_4=-47 eV and g_5=-65 eV, for OBS1, OBS2, OBS3, OBS4 and OBS5, respectively. In model P4, the centroid energy and the normalization of the Ni Kα line are $E = 7.5 \pm 0.1$ keV and norm = $(0.7 \pm 0.2) \times 10^{-5}$ ph cm^{-2} s^{-1} keV^{-1}, respectively. In all models, the ratio between the soft and the intrinsic component is lower than 5%. Errors correspond to the 90 per cent confidence level for one interesting parameter.

– Matt et al. 2004), we supposed that the shift of the line observed in Model P1 (see Table 5.3) should be due to the presence of this feature not yet modelled. Therefore, we decided to add the first-order Compton shoulder (CS) to each observation, fixing its energy at $E = 6.32$ keV, as observed by *Chandra*, and its flux to be the 20% of the iron Kα line flux. However, this further component provide no significant variation in the description of our data. From a statistical point of view, the fit is equally good as the first one (Model P2 – $\chi^2_r = 1.06$), and also the other parameters show no significant changes. Only some residuals are visible in the 6.5-8 keV energy range (see Figure 5.6 – top panel).

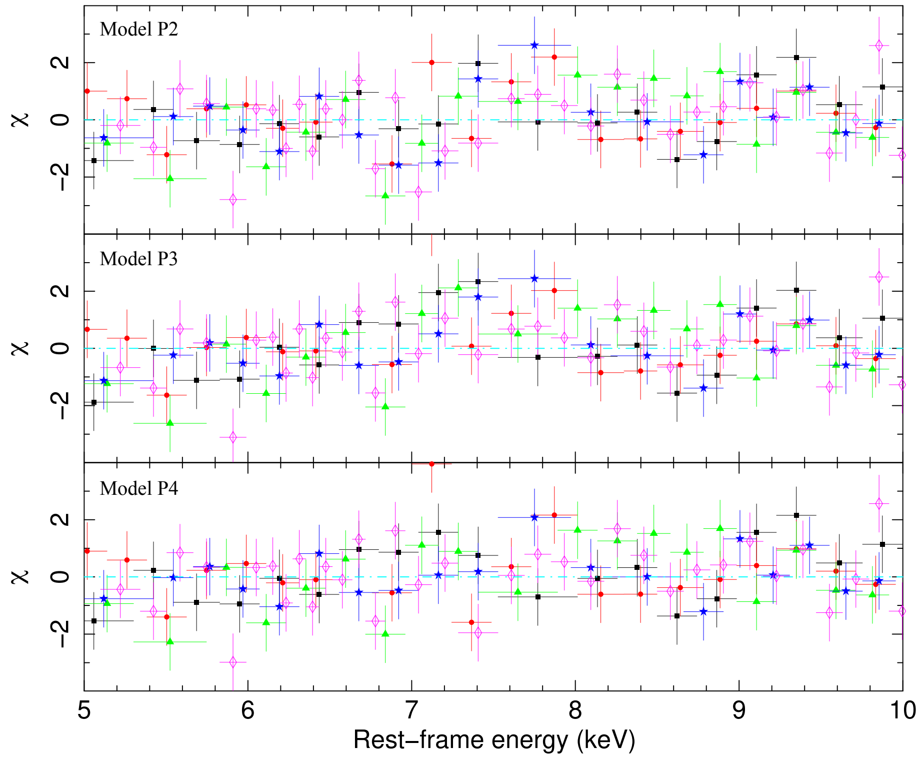

Figure 5.6. *From top to bottom.* Residuals in the 5-10 keV energy range with respect to Model P2, P3 and P4 (dash-dotted cyan line in all panels), plotted in terms of sigmas (Zaino et al. submitted). Both the color code and the symbols are the same as in Figure 5.5.

Even considering the redwards CS, the Fe Kα line appears redshifted during the whole monitoring. To take into account this discrepancy, hereafter, we added to each observation the shift needed to make consistent the line energies observed by *NuSTAR* with those observed with *Chandra*. This will also allow us to describe the circumnuclear matter with a more geometrically motivated configuration such as `MYTorus`, in which the iron Kα line energy is tabulated at 6.4 keV (see §5.3.2 for a detailed analysis). With respect to the previous model, we fixed the energy of the CS to be 0.08 keV lower than the line core energy (corresponding to the expected energy lost after one scattering), and we made use of the `gain` command in `XSPEC`, which shifts both the energies on which the response matrix and the ARF are defined (Model P3). In particular, the new energy E_f is calculated by $E_f = E_i/s - g$, where E_i is the input energy, while s and g are the response slope and the offset in units of keV, respectively. Thus, according to Model P2, the offset values were fixed to be g_1=-41 eV, g_2=-50 eV, g_3=-53 eV, g_4=-47 eV and g_5=-65 eV, for OBS1, OBS2, OBS3, OBS4 and OBS5, respectively. No significant changes appears in the goodness of the fit ($\chi_r^2 = 1.04$), nor in the observed parameters, except for the iron line which is now detected at its rest-frame energy in all the observations (see Model P3 in Table 5.3). This model results also to better reproduce the 6-7 keV energy range (see Figure 5.6 – middle panel).

Some positive residuals around $\sim$7.5 keV were still present; thus, we added a `zgauss` component to our previous model in order to mimic an emission feature (Model P4). The fit improved ($\Delta\chi^2 = 41$ for 2 additional parameters – see bottom panel in Figure 5.6), and the emission line is significant at the 99.9% confidence level, according to the F-test. The centroid energy is $E = 7.5 \pm 0.1$ keV, consistent with the nickel Kα transition, while the normalization is $norm = (0.7 \pm 0.2) \times 10^{-5}$ ph cm^{-2} s^{-1} keV^{-1}. We note that such a feature was already observed in this source (Braito et al. 2013).

5.3.2 A more geometrically motivated approach

Hereafter, we decided to use a more geometrically motivated torus model, such as `MYTorus` (Murphy & Yaqoob 2009), to self-consistenly describe the complex circumnuclear material within NGC 4507. In this model, the obscuring material is uniformly arranged in a toroidal structure around the central SMBH with an half-opening angle fixed to 60°, which corresponds to a covering factor $f_c = 0.5$ (i.e. the solid angle subtended by the torus at the X-ray source is $\Delta\Omega = 2\pi$). To reproduce this geometry, `MYTorus` is essentially composed of three tables. The first one is a multiplicative component applied to the power law modelling the intrinsic continuum, which accounts for both the photoelectric absorption and the Compton scattering attenuation and provides the neutral hydrogen equatorial column density (N_H^{eq}). The two additional tables account for the reprocessed photons and reproduce both the scattered continuum (i.e. photons reaching the observer after have been scattered one or more times by the circumnuclear matter) and the iron fluorescent lines (i.e. Fe Kα and Fe Kβ). The `MYTorus` model can be used in two different configurations: coupled and decoupled (Yaqoob 2012). The former assumes a uniform toroidal structure, while the latter takes into account the potential clumpiness of the circumnuclear matter.

Modelling a uniform toroidal structure

As a first step, we consider the `MYTorus` model in its standard coupled configuration (Yaqoob 2012), in which the torus inclination angle θ_{obs} (i.e. the angle between the axis of the torus and the line-of-sight) is left free to vary, but set to be the same for all three `MYTorus` components. Moreover, θ_{obs} is related to the column density $N_H^{l.o.s.}$ intercepted along the line of sight by:

$$N_H^{l.o.s.} = N_H^{eq}\left[1 - \left(\frac{1}{f_c}\right)^2 cos^2\theta_{obs}\right]^{\frac{1}{2}}, \tag{5.1}$$

where N_H^{eq} is the equatorial column density which is not expected to vary in case of a uniform toroidal structure. Furthermore, the normalizations of both the scattered continuum and the iron lines are set to be equal to the intrinsic one, being the latter free to vary between the observations. Therefore, in case of a variable intrinsic continuum, we assume that the X-ray reprocessor is compact enough for the Compton-scattered flux to respond to the intrinsic continuum on timescales much less than the integration time for the spectrum (Yaqoob 2012). With these assumptions, we obtained an acceptable fit from a statistical point of view ($\chi^2_r = 1.12$), whose parameters are shown in Table 5.4 (Model T1). In particular, $\theta_{obs} = (82 \pm 3)^\circ$, suggesting an edge-on view of the torus and corresponding to a column density intercepted along the line of sight $N_H^{l.o.s.} \sim 7.0 \times 10^{23}$ cm^{-2}.

Table 5.4. Summary of the coupled `MYTorus` models discussed in the text (Zaino et al. submitted).

Model T1: coupled `MYTorus` configuration (χ^2/dof = 1397.5/1250)			
	Γ	N_H^{eq} [10^{23} cm^{-2}]	$norm_{intr} = norm_{sc}$ [ph cm^{-2} s^{-1} keV^{-1}]
OBS1	1.64 ± 0.03		$(1.8^{+0.2}_{-0.1}) \times 10^{-2}$
OBS2	1.71 ± 0.02		$(2.4 \pm 0.2) \times 10^{-2}$
OBS3	$1.63^{+0.02}_{-0.03}$	$7.57^{+0.24}_{-0.29}$	$(1.7^{+0.2}_{-0.1}) \times 10^{-2}$
OBS4	$1.65^{+0.03}_{-0.02}$		$(1.9 \pm 0.2) \times 10^{-2}$
OBS5	1.81 ± 0.02		$(3.5^{+0.3}_{-0.2}) \times 10^{-2}$

Model T2: Model T1 with Fe XXVI Lyα absorption line (χ^2/dof = 1362.5/1248)		
Γ	N_H^{eq} [10^{23} cm^{-2}]	$norm_{intr} = norm_{sc}$ [ph cm^{-2} s^{-1} keV^{-1}]
During the whole monitoring, no significant changes appear in any parameters with respect to Model T1		

Notes. Γ: photon index of the intrinsic power-law; N_H^{eq}: neutral hydrogen equatorial column density; $norm_{intr}$, $norm_{sc}$: normalization of the intrinsic power-law and of the scattered continuum, respectively; χ^2/dof: ratio between χ^2 and the degrees of freedom of the model. The offset values were fixed to be g_1=-41 eV, g_2=-50 eV, g_3=-53 eV, g_4=-47 eV and g_5=-65 eV for OBS1, OBS2, OBS3, OBS4 and OBS5, respectively. All models include the Ni Kα emission line, whose energy and normalization are $E = 7.5 \pm 0.1$ keV and $norm = (0.7 \pm 0.2) \times 10^{-5}$ ph cm^{-2} s^{-1} keV^{-1}, respectively. In model T2, the centroid energy and the normalization of the Fe XXVI Lyα absorption line are E = 6.94 ± 0.06 keV and norm = $-(0.9^{+0.2}_{-0.3}) \times 10^{-5}$ ph cm^{-2} s^{-1} keV^{-1}, respectively. Errors correspond to the 90 per cent confidence level for one interesting parameter.

Only weak residuals are visible in the 6.5-7.0 keV energy range (see Figure 5.7 – top panel), which are suggestive of a possible absorption structure. Thus, we added a gaussian component with negative normalization to mimic an absorption feature at the redshift of the source (Model T2). The improvement of the fit ($\Delta\chi^2 = 35$ for 2 additional parameters) results only in a better modellization of the 6.5-7 keV energy range (see Figure 5.7 – bottom panel), being the main relevant parameters describing the source, such as the spectral slope, the equatorial column density and the normalization of the primary component, not significantly affected by this further component. The absorption line is significant at the 99.9% confidence level, according to the F-test. The centroid energy and the normalization of the absorption line are $E = 6.94 \pm 0.06$ keV and $norm = -(0.9^{+0.2}_{-0.3}) \times 10^{-5}$ ph cm^{-2} s^{-1} keV^{-1}, respectively, consistent with the Fe XXVI Lyα transition, while the relative confidence contours are shown in Figure 5.8. As concerns this feature, it is worth to note that absorption lines due both to Fe XXV and Fe XXVI were already observed in this source with both *Chandra* and *XMM-Newton* data (Matt et al. 2004; Bianchi et al. 2005).

Modelling a patchy torus distribution

Even though the `MYTorus` model in its coupled configuration provided a good description of the source from a statistical point of view, the column density variability already observed

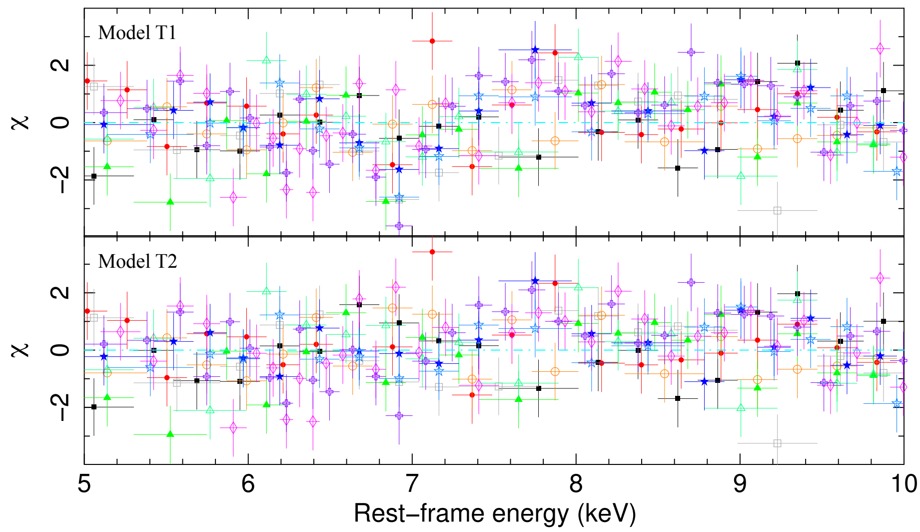

Figure 5.7. *From top to bottom.* Residuals with respect to Model T1 and T2 (dash-dotted cyan line in both panels) plotted in terms of sigmas (Zaino et al. submitted). Both the color code and the symbols are the same as in Figure 5.2.

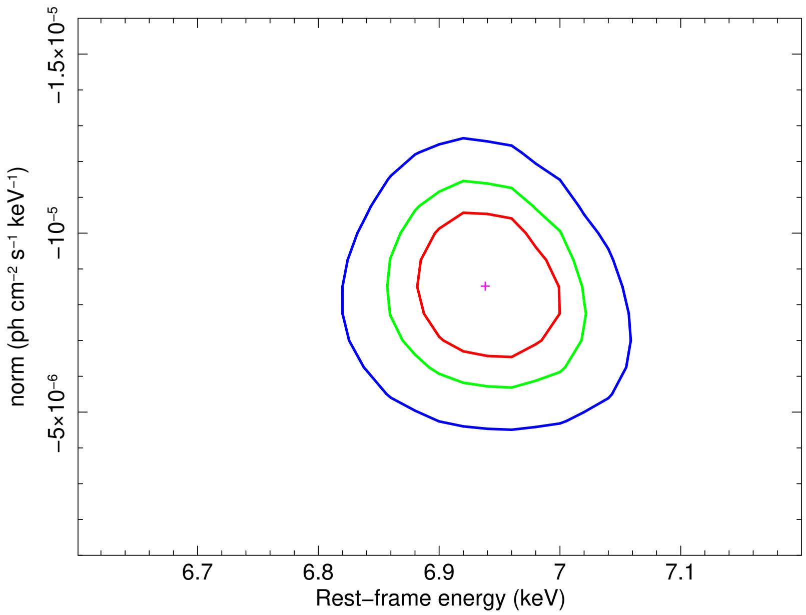

Figure 5.8. Confidence contours between the energy and the normalization of the Fe XXVI Lyα absorption line. Since this feature showed no significant variations during the whole monitoring, the two parameters were tied between the observations. Red, green and blue contours indicate 68 per cent, 90 per cent and 99 per cent confidence levels, while the magenta cross indicates the best-fit value (Zaino et al. submitted).

in NGC 4507 (Braito et al. 2013; Marinucci et al. 2013a) points towards a physical scenario in which the circumnuclear matter in general and the dusty torus in particular is clumpy. For this reason, we decided to model the circumnuclear matter with `MYTorus` in a decoupled configuration (Yaqoob 2012), in which the column density of the intrinsic and scattered components were no longer tied. In particular, we could separately model the column density along the line of sight $N_H^{l.o.s.}$ and the global average column density of the torus $N_{H,sc}$ due to the photons scattered from all directions into the observer line of sight. To reproduce this configuration, we fixed the viewing angle of the absorber to 90°, while the viewing angles of the reprocessed components (both the scattered continuum and the iron lines) were fixed to 0°. The photon index, the absorbing column density and the normalization of the primary continuum were left free to vary between the observations. Also the global average column density of the torus and the normalization of the scattered component were left free to vary, but assumed to be the same during the whole monitoring, since we expected no variations on such small timescales. Moreover, the normalization of the iron lines component were tied to the scattered continuum one.

Applying a decoupled `MYTorus` configuration to our data set, the fit improved ($\Delta\chi^2 = 83$ for 5 additional parameters – Model T3), suggesting the presence of a Compton-thick reflector ($N_{H,sc} = (2.5^{+0.5}_{-0.4}) \times 10^{24}$ cm^{-2}), while the absorbing matter along the line of sight is Compton-thin with values quite consistent with the ones observed when a `MYTorus` coupled configuration is assumed. The Fe XXVI Lyα absorption line was still present, showing no variation with respect to Model T2. Significant changes in the absorbing column density along the line of sight were observed during the whole monitoring (see Model T3 in Table 5.5). Also the normalization of the primary continuum in OBS5 appears to be higher with respect to the other observation; however this discrepancy could also be due to the fact that this value is clearly degenerate with Γ.

To avoid the degeneracy between variations in the absorbing column density and the intrinsic emission of the source, since Γ in OBS5 appears to be consistent within the errors with the other observations, we decided to assume the same spectral slope during the whole monitoring (Model T4). We obtained $\Gamma = 1.82^{+0.04}_{-0.03}$, which is fully consistent with the values previously found in all the observations. The fit was quite equivalent to Model T3 from a statistical point of view ($\chi^2_r = 1.05$). Both the reflector parameters and the intrinsic power-law normalization showed no significant changes during the monitoring, while some variations in the column density of the absorbing matter were still evident (see Model T4 in Table 5.5).

As the normalization of the primary continuum did not appear to significantly vary, we decided to assume the same intrinsic luminosity during the whole monitoring (Model T5). This assumption was also supported by the countrates observed in the 40-79 keV range (see Table 5.1). These values are indeed fully consistent in all the observations, thus suggesting no change in the intrinsic emission of the source. Under the above conditions, we obtained a good fit from a statistical point of view ($\chi^2_r = 1.06$), whose residuals are shown in Figure 5.9. Considering this scenario, the variability observed in the X-ray spectra of NGC 4507 can thus be ascribed to a change in the column density of the absorbing circumnuclear matter intercepting our line of sight. In particular, we obtained $N_H^{l.o.s.} = (7.77 \pm 0.13) \times 10^{23}$ cm^{-2}, $N_H^{l.o.s.} = (7.30 \pm 0.12) \times 10^{23}$ cm^{-2}, $N_H^{l.o.s.} = (7.98 \pm 0.13) \times 10^{23}$ cm^{-2}, $N_H^{l.o.s.} = (7.69 \pm 0.12) \times 10^{23}$ cm^{-2}, and $N_H^{l.o.s.} = (6.50 \pm 0.11) \times 10^{23}$ cm^{-2} for OBS1, OBS2, OBS3, OBS4, and OBS5, respectively.

Table 5.5. Summary of the decoupled `MYTorus` models discussed in the text (Zaino et al. submitted).

Model T3: decoupled `MYTorus` configuration (χ^2/dof = 1279.9/1243)					
	Γ	$N_H^{l.o.s.}$ [10^{23} cm^{-2}]	$norm_{intr}$ [ph cm^{-2} s^{-1} keV^{-1}]	$N_{H,sc}$ [10^{24} cm^{-2}]	$norm_{sc}$ [ph cm^{-2} s^{-1} keV^{-1}]
OBS1	$1.78^{+0.04}_{-0.03}$	7.57 ± 0.22	$(3.0 \pm 0.4) \times 10^{-2}$	$2.5^{+0.5}_{-0.4}$	$(1.4 \pm 0.2) \times 10^{-2}$
OBS2	$1.79^{+0.04}_{-0.03}$	7.11 ± 0.19	$(3.1 \pm 0.4) \times 10^{-2}$		
OBS3	$1.79^{+0.04}_{-0.03}$	7.83 ± 0.22	$(3.1 \pm 0.4) \times 10^{-2}$		
OBS4	1.78 ± 0.04	7.20 ± 0.21	$(2.7 \pm 0.4) \times 10^{-2}$		
OBS5	1.85 ± 0.03	6.97 ± 0.17	$(4.4 \pm 0.5) \times 10^{-2}$		
Model T4: Model T3 with the same photon index (χ^2/dof = 1309.5/1247)					
	Γ	$N_H^{l.o.s.}$ [10^{23} cm^{-2}]	$norm_{intr}$ [ph cm^{-2} s^{-1} keV^{-1}]	$N_{H,sc}$ [10^{24} cm^{-2}]	$norm_{sc}$ [ph cm^{-2} s^{-1} keV^{-1}]
OBS1	$1.82^{+0.04}_{-0.03}$	$7.74^{+0.18}_{-0.17}$	$(3.4^{+0.4}_{-0.3}) \times 10^{-2}$	$2.7^{+0.7}_{-0.4}$	$(1.5 \pm 0.2) \times 10^{-2}$
OBS2		$7.20^{+0.15}_{-0.14}$	$(3.3^{+0.4}_{-0.2}) \times 10^{-2}$		
OBS3		$7.95^{+0.18}_{-0.17}$	$(3.4^{+0.4}_{-0.3}) \times 10^{-2}$		
OBS4		7.46 ± 0.17	$(3.2^{+0.4}_{-0.2}) \times 10^{-2}$		
OBS5		6.68 ± 0.13	$(3.6^{+0.4}_{-0.3}) \times 10^{-2}$		
Model T5: Model T4 with the same intrinsic luminosity (χ^2/dof = 1330.8/1254)					
	Γ	$N_H^{l.o.s.}$ [10^{23} cm^{-2}]	$norm_{intr}$ [ph cm^{-2} s^{-1} keV^{-1}]	$N_{H,sc}$ [10^{24} cm^{-2}]	$norm_{sc}$ [ph cm^{-2} s^{-1} keV^{-1}]
OBS1	1.81 ± 0.03	7.77 ± 0.13	$(3.3 \pm 0.3) \times 10^{-2}$	2.5 ± 0.4	$(1.5 \pm 0.2) \times 10^{-2}$
OBS2		7.30 ± 0.12			
OBS3		7.98 ± 0.13			
OBS4		7.69 ± 0.12			
OBS5		6.50 ± 0.11			
Model T6: Model T3 with the same absorbing column density (χ^2/dof = 1316.3/1247)					
	Γ	$N_H^{l.o.s.}$ [10^{23} cm^{-2}]	$norm_{intr}$ [ph cm^{-2} s^{-1} keV^{-1}]	$N_{H,sc}$ [10^{24} cm^{-2}]	$norm_{sc}$ [ph cm^{-2} s^{-1} keV^{-1}]
OBS1	$1.77^{+0.03}_{-0.04}$	7.24 ± 0.10	$(2.6 \pm 0.3) \times 10^{-2}$	2.7 ± 0.5	$(1.4 \pm 0.2) \times 10^{-2}$
OBS2	1.81 ± 0.03		$(3.3 \pm 0.3) \times 10^{-2}$		
OBS3	$1.75^{+0.04}_{-0.03}$		$(2.5 \pm 0.3) \times 10^{-2}$		
OBS4	1.78 ± 0.03		$(2.8 \pm 0.3) \times 10^{-2}$		
OBS5	1.91 ± 0.03		$(5.0 \pm 0.4) \times 10^{-2}$		

Notes. Γ: photon index of the intrinsic power-law; $N_H^{l.o.s.}$, $N_{H,sc}$: neutral hydrogen line of sight and torus average column density, respectively; $norm_{intr}$, $norm_{sc}$: normalization of the intrinsic power-law and of the scattered continuum, respectively; χ^2/dof: ratio between χ^2 and the degrees of freedom of the model. The offset values were fixed to be g_1=-41 eV, g_2=-50 eV, g_3=-53 eV, g_4=-47 eV and g_5=-65 eV for OBS1, OBS2, OBS3, OBS4 and OBS5, respectively. All models include the Ni Kα emission line and the Fe XXVI Lyα absorption line. The centroid energy and normalization of the former are $E = 7.5 \pm 0.1$ keV and $norm = (0.7 \pm 0.2) \times 10^{-5}$ ph cm^{-2} s^{-1} keV^{-1}, while for the latter we have E $= 6.94 \pm 0.06$ keV and norm $= -(0.9^{+0.2}_{-0.3}) \times 10^{-5}$ ph cm^{-2} s^{-1} keV^{-1}, respectively. Errors correspond to the 90 per cent confidence level for one interesting parameter.

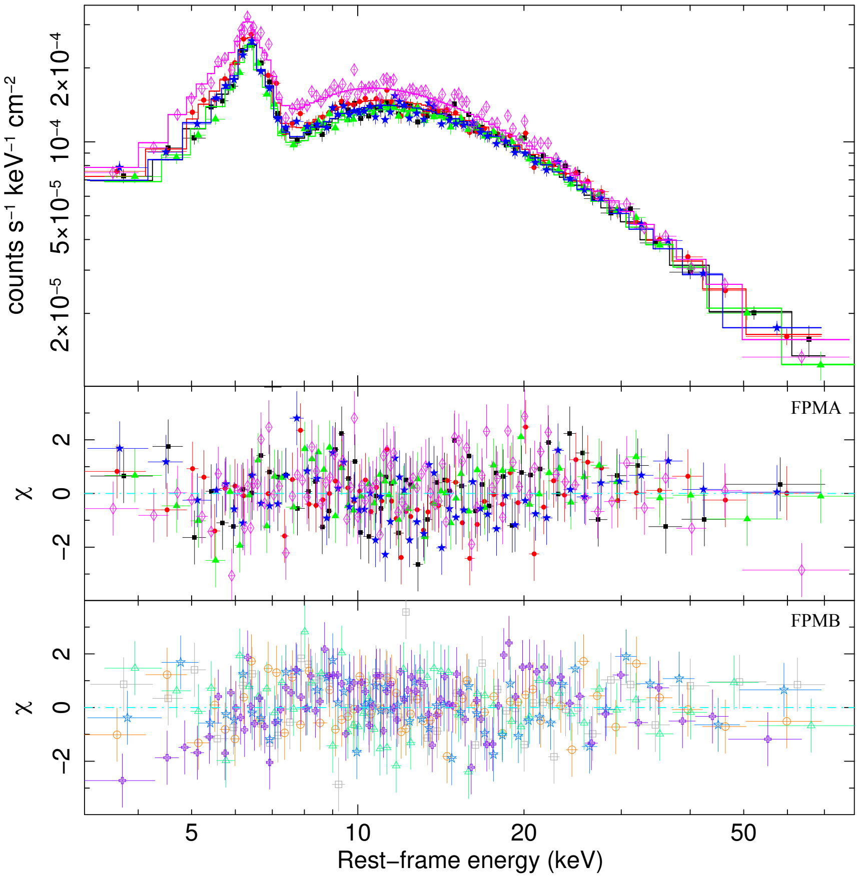

Figure 5.9. *NuSTAR* FPMA spectra (top panel) and residuals with respect to our best-fit model (Model T5 – dash-dotted cyan line) for both FPMA (middle panel) and FPMB (bottom panel) plotted in term of sigmas (Zaino et al. submitted). Both the color code and the symbols are the same as in Figure 5.2.

To test any possibility, we considered also a scenario in which the absorbing column density along the line of sight showed no changes, while the spectral slopes and the intrinsic luminosities were left free to vary during the monitoring (Model T6). The fit was acceptable from a statistical point of view (χ^2_r=1.06) and only weak variations are observed in the first 4 months of our monitoring, while significant changes in both the spectral slope and the intrinsic normalization are observed in OBS5 (see Model T6 in Table 5.5). It is worth noting that at least part of these variations could be due to the degeneracy affecting these two parameters. However, modelling the X-ray spectra allowing only the photon index or the normalization to be free to vary, resulted in a significant worsening of the fit in both cases ($\Delta\chi^2 = 366.2$ and $\Delta\chi^2 = 152.2$ for 4 additional parameters, respectively), suggesting that neither the photon index nor the normalization can alone account for the observed variability below 40 keV. Moreover, according to Model T6, the photon index in the last pointing is not only significantly higher with respect to the other observations, but also only marginally consistent with the value observed in Model T3, where no assumption was taken and all the parameters were left free to vary. Finally, an increase of the primary continuum by a factor of ~1.8, as observed in the last month of our monitoring, does not appear to be consistent with the stable countrates observed above 40 keV, where only the primary continuum is expected to be observed. Thus, the more natural explanation for the X-ray variability observed during our monitoring appears to be a variation in the absorbing column density. For this reason, we considered Model T5 as the most plausible scenario for NGC 4507, as observed during our 2015 *NuSTAR* monitoring.

5.4 Discussion

The X-ray spectral analysis of the latest *NuSTAR* monitoring of NGC 4507 allowed us to obtain new insights on the circumnuclear matter of this AGN, which are discussed in detail in §5.4.1. In particular, our data are well described by a physical scenario implying the presence of two circumnuclear cold regions, a Compton-thick emitter and a Compton-thin absorber. In general, such a configuration is not surprising in AGN, being already observed in other obscured sources, such as NGC 5506 (Matt et al. 2001; Bianchi et al. 2003) and NGC 1194 (Turner et al. 2020). However, NGC 4507 has not always shown such characteristics. On one hand, a similar circumnuclear matter is fully consistent with the one observed in 2001 from both *XMM-Newton* and *Chandra*, where the bulk of the iron Kα line is produced by Compton-thick matter, while the absorption occurred in a Compton-thin region with a low covering factor (Matt et al. 2004). On the other hand, our physical configuration appears to be at odds with the analysis of a *Suzaku* observation performed in 2007 in which only Compton-thin matter is required to describe the source (Braito et al. 2013). For further details, we refer to §5.4.2, in which we tested the consistency of our *NuSTAR* scenario with old *Suzaku* data.

5.4.1 The 2015 *NuSTAR* scenario

Our *NuSTAR* analysis allowed us to observe column density variations on timescales not yet probed for this source (i.e. from 1 to 4 months). In all pointings, NGC 4507 was caught in a high absorbed state, similar to what observed in 2007 by *Suzaku* (Braito et al. 2013). Assuming the same luminosity of the accretion disk during the whole monitoring (i.e. Model T5), we can attribute the variability observed in the X-ray spectra of NGC 4507 to gas clouds with different column densities moving temporarily across our line of sight.

In particular, we observed changes in the absorbing column density of the circumnuclear matter up to $\Delta N_H^{l.o.s.} = (1.2 \pm 0.2) \times 10^{23}$ cm^{-2} on timescales Δt lower than 31 days (see Table 5.6). The intrinsic de-absorbed X-ray luminosity in the 2-10 keV range inferred from our fits is $L_{2-10} = (3.5 \pm 0.3) \times 10^{43}$ erg s^{-1}, as already observed by Comastri et al. (1998). Using the bolometric correction from Marconi et al. (2004), we obtained a bolometric luminosity $L_{bol} = (0.8 \pm 0.1) \times 10^{45}$ erg s^{-1}, which leads to a normalized Eddington ratio $\lambda = \frac{L_{bol}}{L_{Edd}} = 0.15 \pm 0.02$. For such a value of λ, the expected spectral slope is given by $\Gamma = 1.84 \pm 0.04$, following the highly significant statistical relation between the X-ray spectral index Γ and the Eddington ratio λ of AGN found by Brightman et al. (2013). This value is fully consistent with the observed photon index in Model T5 (i.e. 1.81 ± 0.03), providing a good consistency test for our findings.

Table 5.6. Temporal distances Δt and column density variation along the line of sight $\Delta N_H^{l.o.s.}$ observed between each observation, assuming Model T5 (Zaino et al. submitted).

	Δt (10^6 s)	$\Delta N_H^{l.o.s}$ (10^{23} cm^{-2})
OBS1-OBS2	~ 3.3	0.5 ± 0.2
OBS2-OBS3	~ 3.0	0.7 ± 0.2
OBS3-OBS4	~ 3.3	0.3 ± 0.2
OBS4-OBS5	~ 2.7	1.2 ± 0.2

According to Kaspi et al. (2005), the radius of the BLR is given by

$$\frac{R_{BLR}}{10\ lt - days} = 0.86 \times \left(\frac{L_{2-10\ keV}}{10^{43}\ erg\ s^{-1}} \right)^{0.544}, \tag{5.2}$$

leading to $R_{BLR} \sim 0.01$ pc, using our spectral fitting parameters. We considered the obscuring material to be composed of individual spherical clouds orbiting with Keplerian velocities around the nuclear region. Their distance R from the SMBH is given by

$$R = \frac{GM_{BH}}{v^2}, \tag{5.3}$$

where G is the gravitational constant, M_{BH} is the BH mass and v is the transverse velocity of the obscuring matter. The latter is simply the ratio between the cloud dimension $D = N_H/n$ and the crossing time Δt, where N_H and n are the column density and the gas density of the cloud, respectively. Then, assuming a black hole mass $M_{BH} \sim 4.5 \times 10^7$ $M_\odot$, as derived from the $M_{BH} - \sigma$ relation (Tremaine et al. 2002), the velocity at which a given obscuring cloud crosses our line of sight is given by:

$$v \simeq \left[(GM_{BH})^2 \frac{\xi\ N_H}{L\ \Delta t} \right]^{\frac{1}{5}} \simeq 1000\ km\ s^{-1}, \tag{5.4}$$

where $\xi = L/nR^2 \lesssim 1$, as expected for neutral matter, and L is the 1-1000 Ryd ionizing luminosity (Tarter et al. 1969). Such a velocity implies a size $D \sim 45 R_G$ and a density $n \sim 4 \times 10^8$ cm^{-3} for the absorbing cloud. Moreover, according to Equation 5.3, the distance of the obscuring cloud results to be $R \gtrsim 5 \times 10^{17}$ cm from the SMBH. Thus, in our physical scenario the absorbing cloud is located at least at the outer BLR / inner torus boundary, or even a little further out.

5.4.2 Is the *NuSTAR* configuration consistent with old *Suzaku* data?

NGC 4507 was observed by *Suzaku* in December 2007 revealing the presence of Compton-thin matter surrounding the nuclear region with two distinct column densities, $N_H^{l.o.s.} = (9.38^{+0.25}_{-0.24}) \times 10^{23}$ cm^{-2} and $N_{H,sc} = (2.56^{+0.20}_{-0.17}) \times 10^{23}$ cm^{-2} along and out of the line of sight, respectively. The photon index was $\Gamma = 1.68 \pm 0.03$, while the normalization of both the primary and reflected component was $norm_{intr} = norm_{sc} = (1.91^{+0.16}_{-0.25}) \times 10^{-2}$ ph cm^{-2} s^{-1} (Braito et al. 2013).

In the following, we wanted to test if our *NuSTAR* scenario, in which the circumnuclear matter is composed of both a Compton-thin absorber and a Compton-thick emitter, can be supported by *Suzaku* data. To test this further configuration, we assumed the same decoupled `MYTorus` configuration explained in §5.3.2, with the only exception of the normalizations of the scattered components which are not only tied together, but also to the value of the intrinsic continuum, as observed by Braito et al. (2013). Furthermore, we limited our analysis to the energy range above 4 keV, to avoid the complexity of the soft-X-ray component, whose description is well beyond our goal. We obtained a good description of the *Suzaku* data, retrieving a $\chi^2/dof = 278.9/253$ (see Figure 5.10). The intrinsic continuum is well reproduced by a spectral slope $\Gamma = 1.68 \pm 0.05$ and a normalization $norm_{intr} = (1.2 \pm 0.2) \times 10^{-2}$ ph cm^{-2} s^{-1}, while the circumnuclear matter is well described by a Compton-thin absorber ($N_H^{l.o.s.} = (8.0 \pm 0.2) \times 10^{23}$ cm^{-2}) and an average global column density $N_{H,sc} = (1.6 \pm 0.3) \times 10^{24}$ cm^{-2}, whose confidence contours are shown in Figure 5.11. The flux and the intrinsic de-absorbed X-ray luminosity in the 2-10 keV range inferred from our fit are $F \sim 6.5 \times 10^{-12}$ erg cm^{-2} s^{-1} and $L_{2-10} \sim 1.6 \times 10^{43}$ erg s^{-1}, respectively. Thus, the *NuSTAR* configuration described in §5.4.1 seems to be well supported by *Suzaku* data.

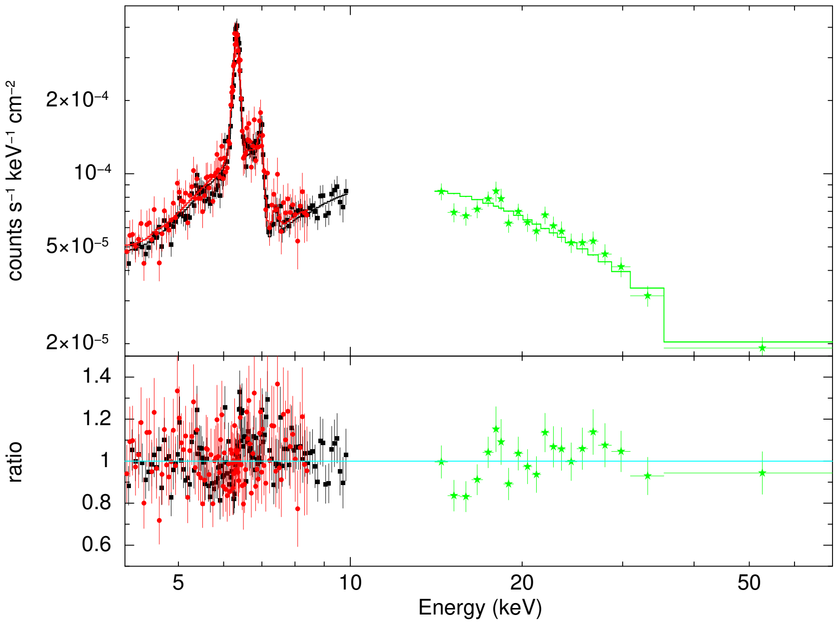

Figure 5.10. *Suzaku* XIS-FI (black squares), XIS1 (red circles) and HXD-PIN (green stars) spectra (top panel) and data-to-model ratio (bottom panel), modelling data with a `MYTorus` decoupled configuration (solid cyan line) reproducing a Compton-thin absorber and a Compton-thick reflector (Zaino et al. submitted).

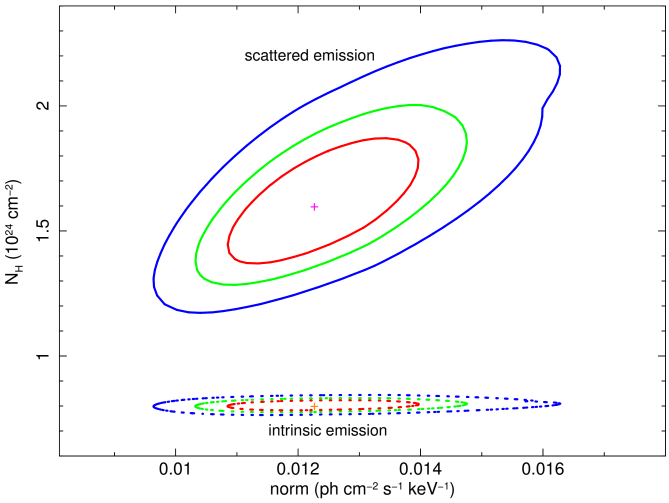

Figure 5.11. Confidence contours between the column density and the normalization of the intrinsic (dotted lines) and scattered (solid lines) emission, when modelling the 4-70 keV Suzaku data with a decoupled `MYTorus` configuration. Red, green and blue contours indicate 68 per cent, 90 per cent and 99 per cent confidence levels, while orange and magenta crosses indicate the best-fit values in the former and latter case, respectively (Zaino et al. submitted).

It is worth noting that the discrepancy in the physical properties of the circumnuclear matter out of the line of sight between our physical scenario and the one observed by Braito et al. (2013) would be explained by two main effects, which do not allow us to exclude any scenario. On one hand, *NuSTAR* provides no coverage of the soft-X-ray band below 3 keV, in contrast to *Suzaku* which probes a broader X-ray energy band (from 0.6 to 70 keV), although the *Suzaku* higher energy data are background-dominated. On the other hand, the gap between XIS and HXD in the 10-14 keV energy range may prevent a good spectral modelling of the reflection component. Indeed, it is around that energy range where the transmitted and reflected components intercept. For these reasons, further simultaneous observations covering both the soft and hard X-rays appear as mandatory to obtain a conclusive evidence of the physical properties of the circumnuclear reflector in NGC 4507.

5.5 Conclusions

We have presented a spectral analysis of the latest *NuSTAR* monitoring campaign of the Compton-thin Seyfert 2 galaxy NGC 4507 composed of five ~30 ks observations performed between May and September 2015. This campaign sampled timescales from one to four months with the aim of solving any possible ambiguity on the variability of the intrinsic emission and amount of absorption within the source. Our findings on the physical properties of both the absorber and the reflector can be summarized as follows.

- The most plausible explanation for the X-ray variability observed in the X-ray spectra of NGC 4507 is a change in the obscuration level along the line of sight up to $\Delta N_H^{l.o.s.} = (1.2 \pm 0.2) \times 10^{23}$ cm^{-2} in a 1-month timescale. These variations can be ascribed to absorbing gas clouds located at least at the outer BLR / inner torus boundary, or even a little further out, thus providing further evidence of the clumpy structure of the circumnuclear torus around NGC 4507.

- The physical scenario describing the circumnuclear matter surrounding the nuclear region of NGC 4507 is quite complex with reflection arising from gas with a Compton-thick global average column density and transmission of the continuum through variable Compton-thin matter. Even though already observed in other AGN, this description is at odds with the configuration drawn by analyzing older *Suzaku* data, which required only Compton-thin material to describe NGC 4507. Nonetheless, the *NuSTAR* scenario seems to well reproduce the *Suzaku* spectrum, at least above 4 keV. Even if *Suzaku* provides a more wider spectrum covering also the soft X-ray band, it is worth remarking that the data above 10 keV are background-dominated. Moreover, its lack of coverage in the 10-14 keV energy range where the reflection component begin to arise may prevent a robust spectral modelling of the reflector. For these reasons, future simultaneous observations with facilities covering both the soft and the hard X-rays may help in obtaining an in-depth view of the physical properties of the whole circumnuclear material within NGC 4507, checking our scenario for the Compton-thick reflector.

6

A short overview of polarimetry in the X-rays

Contents

Since the beginning of X-ray astronomy, X-ray polarimetry has been considered as a privileged tool for probing the physics and the geometry of astrophysical compact sources (e.g. Mészáros et al. 1988 and references therein). Unfortunately, the lack of polarimeters on-board space missions in the last 40 years has so far prevented X-ray polarimetry from evolving in parallel with X-ray imaging and spectroscopy.

The launch of the *Imaging X-ray Polarimetry Explorer* (*IXPE* – Weisskopf et al. 2016a and 2016b) mission, scheduled at the end of 2021, will re-open the polarimetry window in the X-ray energy band, allowing to add two fundamental parameters, such as the polarization degree and the polarization angle, to the direction, time and energy of incident photons. In particular, this incoming new era of X-ray polarimetry will give us the opportunity to explore the AGN scattering regions in a unique way, shedding further light on the geometry of the circumunuclear matter in heavily obscured sources, where the complete obscuration of the nuclear radiation, at least up to 10 keV (see §2.2.2), permits a clear view of the reprocessed features, which otherwise should be heavily diluted, often down to invisibility. In particular, clear measurements of several parameters, such as the half-opening angle of the torus, the inclination angle with respect to the line of sight and the column density, can be retrieved thanks to X-ray polarimetry (Goosmann & Matt 2011).

This chapter is designed to give some useful information about the scenario I have just drawn. In particular, §6.1 is devoted to introduce the Stokes parameters, through which we can completely describe the state of polarization of an electromagnetic wave. The physical process at the basis of a photoelectric polarimeter is discussed in §6.2, while its working mechanism is described in §6.3. Then, §6.4 focuses on the only few X-ray polarization measurements obtained so far, while §6.5 is devoted to introduce the next future *IXPE* mission.

6.1 The Stokes parameters

Without loss of generality, an electromagnetic wave can be expressed as the sum of two components which are linearly polarized in two orthogonal directions. In particular, the electric field $\vec{E}$ can be described by its orthogonal components, $\vec{E}_x$ and $\vec{E}_y$:

$$\vec{E} = \vec{E}_x(t) + \vec{E}_y(t) = \hat{x}E_x e^{-(i\omega t-\delta)} + \hat{y}E_y e^{-i\omega t}, \tag{6.1}$$

where $\hat{x}$ and $\hat{y}$ identify a frame of reference in the plane orthogonal to the direction of propagation and δ takes into account the phase difference between the two components (see Figure 6.1).

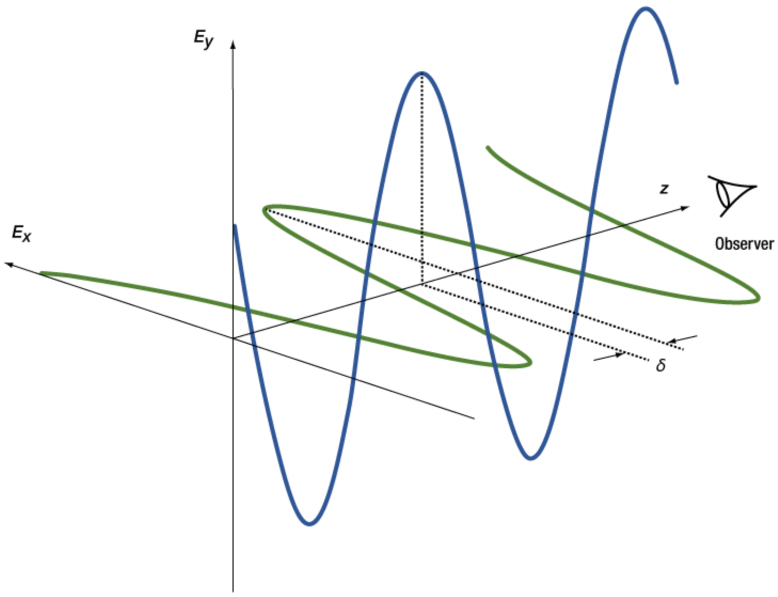

Figure 6.1. The superposition of the two orthogonal components $\vec{E}_x$ (in green) and $\vec{E}_y$ (in blue) with a phase difference δ gives the electric field $\vec{E}$ along the z-axis.

The evolution with time of the electric field in the plane xy can be obtained taking the real parts of $\vec{E}_x(t)$ and $\vec{E}_x(t)$:

$$\begin{cases} E_x = \mathcal{E}_x \cos\left(\omega t - \delta\right) \\ E_y = \mathcal{E}_y \cos\left(\omega t\right) \end{cases}, \tag{6.2}$$

which trace an ellipse in the xy plane, i.e. the so-called polarization ellipse (see Figure 6.2).

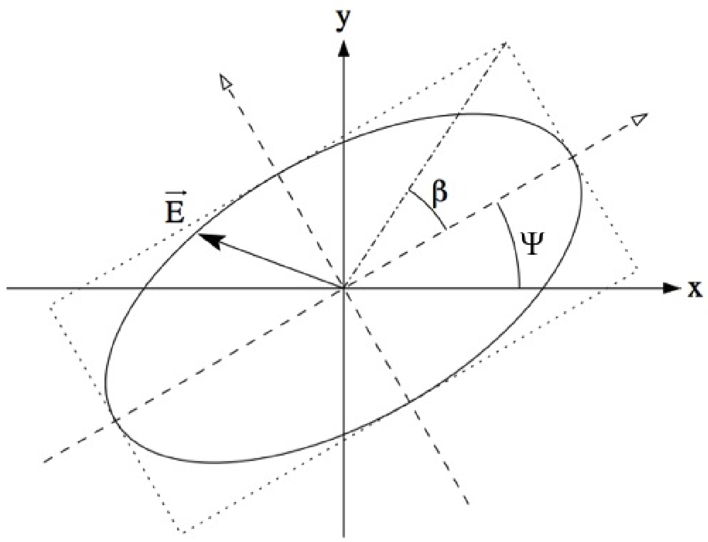

Figure 6.2. Polarization ellipse with orientation angle Ψ and angle of ellipticity β.

The state of polarization of an electromagnetic wave can be described by means of Stokes parameters, which completely describe the behavior of the electric field in the plane orthogonal to the direction of propagation. Having been introduced by George Gabriel Stokes in 1852, the four Stokes parameters can be defined by time averages of the electric field strength along the two orthogonal directions x and y:

$$I = \langle E_x^2 + E_y^2 \rangle, \tag{6.3}$$

$$Q = \langle E_x^2 - E_y^2 \rangle = E_0^2 \cos 2\beta \cos 2\Psi, \tag{6.4}$$

$$U = \langle 2E_x E_y \cos\delta \rangle = E_0^2 \cos 2\beta \sin 2\Psi, \tag{6.5}$$

$$V = \langle 2E_x E_y \sin\delta \rangle = E_0^2 \sin 2\beta, \tag{6.6}$$

where the the angle of ellipticity β and the polarization angle Ψ are defined in Figure 6.2 and $E_0^2 = \langle E_x^2 + E_y^2 \rangle$. In particular, both β and Ψ can be described as a function of the Stokes parameter through the following relations:

$$\tan 2\Psi = \frac{U}{Q}, \tag{6.7}$$

and

$$\sin 2\beta = \frac{V}{I}. \tag{6.8}$$

The Stokes parameters are useful because they relate to the physical properties of radiation: I represents the intensity of the wave, Q and U depend on the linear polarization properties, measuring the orientation of the polarization ellipse with respect to the x-axis, while V depends on the circular polarization properties. In particular, Q equals I $(-I)$ for a 100% linearly polarized wave with an E-field vector along the x-axis (y-axis), U equals I $(-I)$ for a 100% linearly polarized wave with an E-field vector along the diagonal between the x-axis and the y-axis (the negative x-axis and the y-axis), and V equals I $(-I)$ for 100% circularly right handed (left handed) polarized light, as shown in Figure 6.3 (Kislat et al. 2015).

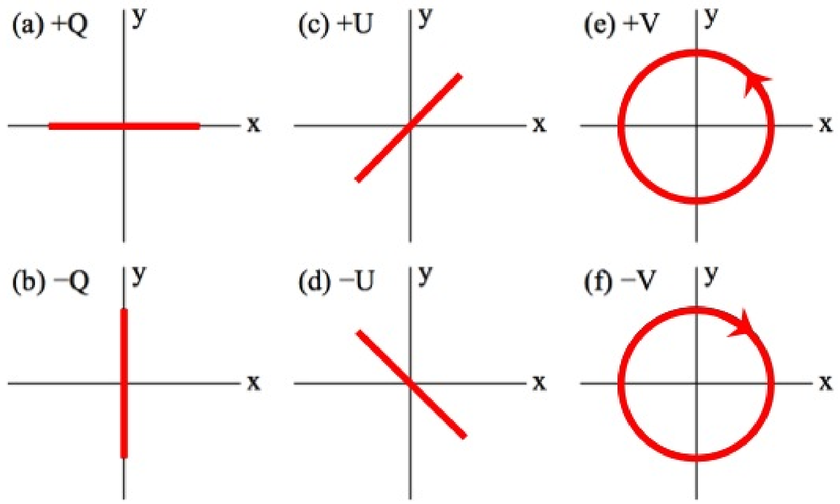

Figure 6.3. Polarization for different values of the Stokes parameters. (a) Q>0, U=0, V=0; (b) Q<0, U=0, V=0; (c) U>0, Q= 0, V=0; (d) U<0, Q=0, V=0; (e) V>0, Q=0, U=0; (f) V<0, Q=0, U=0.

The Stokes parameters are additive; therefore, for a partially polarized electromagnetic wave, we have:

$$\begin{bmatrix} I \\ Q \\ U \\ V \end{bmatrix} = \begin{bmatrix} \sqrt{Q^2+U^2+V^2} \\ Q \\ U \\ V \end{bmatrix} + \begin{bmatrix} I-\sqrt{Q^2+U^2+V^2} \\ 0 \\ 0 \\ 0 \end{bmatrix}, \tag{6.9}$$

with the first and the latter term of the sum representing a polarized and an unpolarized wave, respectively. Thus, for a completely polarized radiation, the polarization ellipse is characterized by only three quantities, being the I Stokes parameter given by

$$I = \sqrt{Q^2+U^2+V^2}, \tag{6.10}$$

while for unpolarized waves $I \neq 0$, $Q = U = V = 0$, and for partially polarized waves $I > \sqrt{Q^2+U^2+V^2}$.

In this context, the degree of polarization is defined as the ratio between the intensity of the polarized components and the total wave:

$$P = \frac{I_{pol}}{I_{tot}} = \frac{\sqrt{Q^2+U^2+V^2}}{I}, \tag{6.11}$$

while the polarization angle is given by

$$\Psi = \frac{1}{2}\tan^{-1}\left(\frac{U}{Q}\right). \tag{6.12}$$

Since current X-ray polarimeters are able to detect only linear polarization (V=0), Equation 6.11 reduces to

$$P = \frac{\sqrt{Q^2+U^2}}{I}. \tag{6.13}$$

6.2 The ideal physical process for X-ray polarimetry

The photoelectric effect is a promising basis for sensitive X-ray polarimeters. It is the dominant X-ray interaction mechanism below a few tens of keV in almost all materials (see Figure 6.4) and is highly sensitive to polarization.

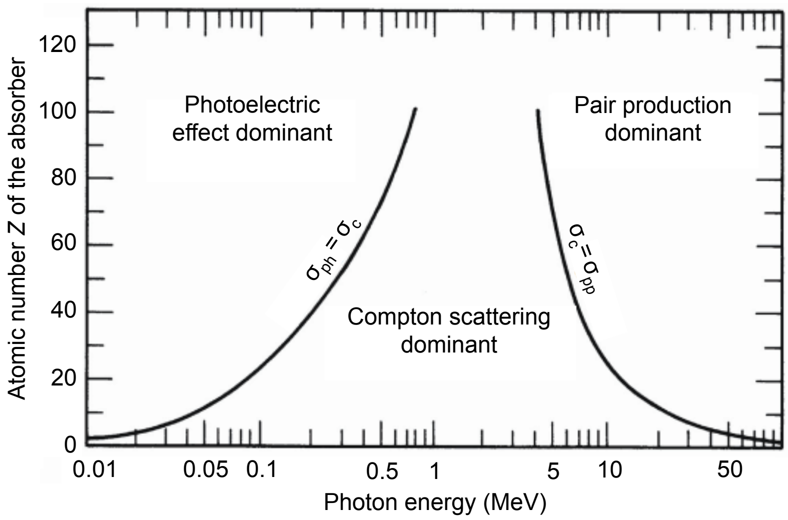

Figure 6.4. The relative importance of the three major types of interaction between radiation and matter. The lines show the values of Z and energy for which the two neighboring effects are just equal (adapted from Evans 1955).

When a photon is absorbed via photoelectric effect by an atom, a photoelectron is emitted with a kinetic energy $E_k = E_\gamma - E_b$, where E_γ and E_b are the energy of the absorbed photon and the binding energy of the photoelectron in its original shell, respectively. The direction of emission depends on the differential cross-section given by

$$\frac{d\sigma_{ph}}{d\Omega} \propto \frac{\sin^2\theta\cos^2\varphi}{(1-\beta\cos\theta)^4} \tag{6.14}$$

(Heitler 1954), where φ is the photoelectron azimuthal angle relative to the photon electric field vector, θ is the photoelectron emission angle relative to the photon momentum vector, and β is the photoelectron speed as a fraction of the speed of light (see Figure 6.5). Therefore, since for low energy photons (up to tens of keV) the photoelectron is preferentially emitted parallel to the photon electric field, i.e. the distribution peaks at $\varphi = 0°$, it is possible to determine the linear polarization of the incident photon by measuring the initial direction of the photoelectron. Moreover, being null the probability of ejecting a photoelectron perpendicular to the electric field vector, the photoelectric effect is an ideal polarization analyzer (Kaaret 2014).

6.3 The working mechanism of a photoelectric polarimeter

According to Equation 6.14, the angular distribution of the photoelectron emission is given by the product of independent functions of θ and φ; thus, we can measure the direction of the X-ray polarization from a 2-D photoelectron track projected onto a plane perpendicular to the direction of the incident X-ray radiation (Kitaguchi et al. 2018).

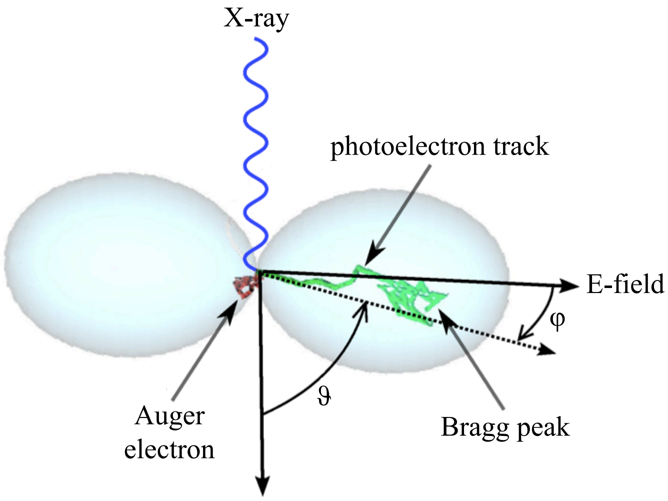

Figure 6.5. Angular distribution of the photoelectron emitted by interaction of a linearly polarized photon with an atom. Bothe the azimuthal angle φ relative to the photon electric field vector and the emission angle θ relative to the photon momentum vector are shown. The path of the photoelectron from its ejection to the stopping point is referred to as the "photoelectron track", while the concentrated energy loss near the end of the track is known as the "Bragg peak" (Kaaret 2014).

6.3.1 How to reconstruct the photoelectron track

Once the photoelectron is emitted, it interacts with the surrounding matter, leaving a trail of electron-ion pairs marking its path from the initial ejection to the final stopping point, which is known as the "photoelectron track". This ionization pattern is not straight because of the low mass of the electron, as shown in Figure 6.6. Thus, since the useful information needed for polarimetry is mostly stored in the initial part of the track, a correct reconstruction of the impact point of the photoelectron is crucial to determine the polarization of the incoming radiation (Li et al. 2017; Moriakov et al. 2020).

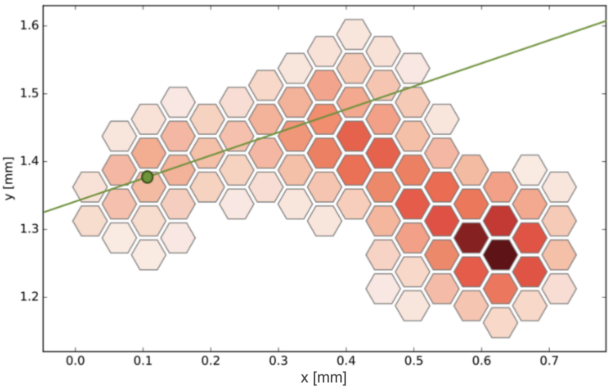

Figure 6.6. Example of an ionisation track collected by a photoelectric polarimeter: the color is darker for increasing value of charge deposition. The green dot represents the impact point of the incoming X-ray radiation, while the green line shows the direction of the photoelectron (Moriakov et al. 2020).

Since the photoelectron looses energy along the path at a rate that is inversely proportional to its instantaneous energy, the energy loss is lowest near the initial part of the track and highest at the end. This asymmetry in energy loss can be used to distinguish the photoelectric interaction point from the Bragg peak, which corresponds to the concentrated energy loss near the end of the track. Then, once the start of the track is identified, a fit of the track profile is needed to reconstruct the initial direction of the photoelectron (Kaaret 2014).

6.3.2 How to measure X-ray polarization

X-ray polarimeters convert the polarization of the absorbed photons in a $\cos^2$ modulation of their response. The functioning of a photoelectric polarimeter is shown in Figure 6.7. After the photoabsorption, the electron is emitted preferentially in the direction of the electric vector of the absorbed photon. The response of X-ray polarimeters is a modulation curve, which is the histogram of the azimuthal distribution of the events interacting with the detector (see Figure 6.8). The polarization angle is related to the phase φ_0 of the modulation curve, while the degree of polarization is proportional to the modulation amplitude. The constant of proportionality is given by the modulation factor μ, which is defined as the amplitude of the azimuthal modulation measured by the instrument for a 100% polarized beam.

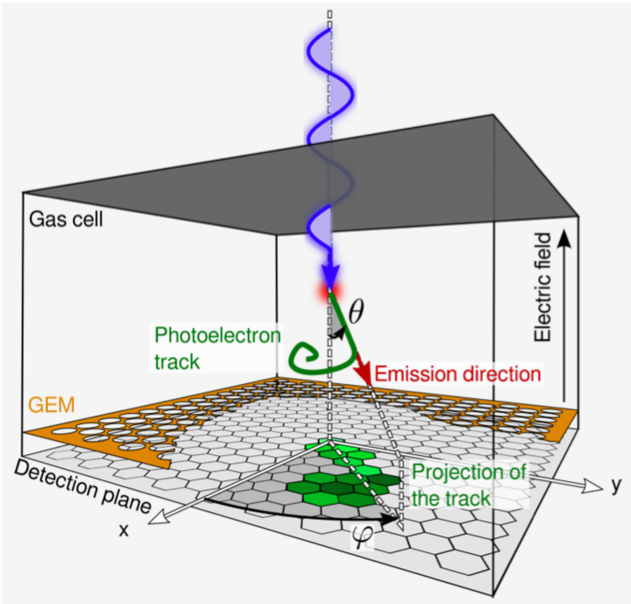

Figure 6.7. A schematic view of the functioning of a photoelectric polarimeter.

The classical approach used to derive a measure of the polarization from data is to fit the modulation curve with the function

$$\mathcal{M}(\varphi) = A + B\cos^2(\varphi - \varphi_0), \tag{6.15}$$

where φ_0 corresponds to the polarization angle Ψ_0 in case of a photoelectric polarimeter. The amplitude modulation is given by

$$M = \frac{\mathcal{M}_{max} - \mathcal{M}_{min}}{\mathcal{M}_{max} + \mathcal{M}_{min}} = \frac{B}{B + 2A}, \tag{6.16}$$

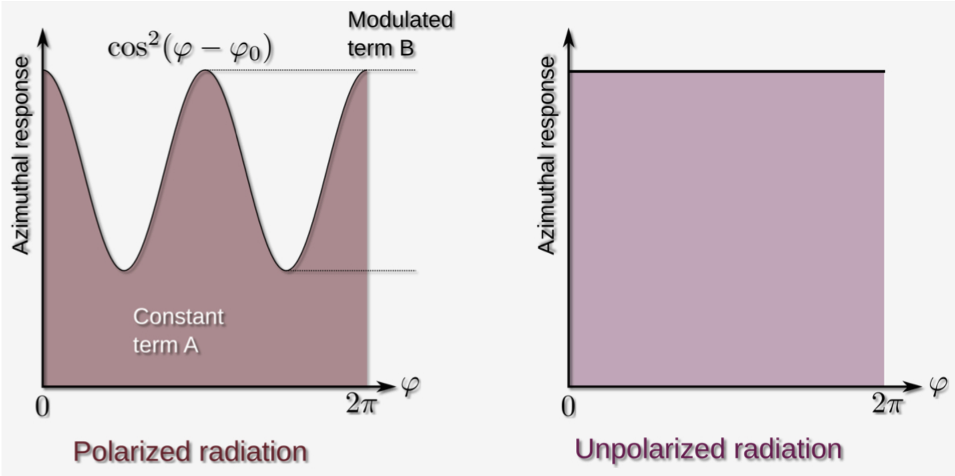

Figure 6.8. Response of the X-ray polarimeter in case of polarized (left) or unpolarized (right) radiation.

and the degree of polarization is given by rescaling M by the modulation factor μ:

$$P = \frac{M}{\mu} = \frac{1}{\mu}\frac{B}{B+2A}. \tag{6.17}$$

In this classical approach, the polarization degree and angle are treated as independent parameters; however, since they are correlated with each other, the use of Stokes parameters appears to be a more convenient way to analyze the polarization measured in the X-rays.

Stokes parameters can be derived from data in two different (yet equivalent) approaches:

- fitting the modulation curve with a function depending explicitly on Stokes parameters:
$$\mathcal{M}(\varphi) = I[1 + Q\cos 2\varphi + U\sin 2\varphi], \tag{6.18}$$
(Strohmayer & Kallman 2013), which is similar to the classical method described above;

- through a photon-by-photon estimate (Kislat et al. 2015), which is the approach used by *IXPE*.

In both cases, the degree of polarization is given by

$$P = \frac{2}{\mu}\frac{\sqrt{Q^2+U^2}}{I}, \tag{6.19}$$

where the factor $2/\mu$ results from the fact that the observed Stokes parameters are both influenced by the modulation factor of the instrument, and derived from the emission angle distribution of photoelectrons. Since the latter follows a sinusoidal distribution with a 180° period, the derived Stokes parameters are indeed reduced by a factor of 2 with respect to the true Stokes parameters of the incident photons.

6.4 Past X-ray polarization measurements

Despite the scientific potential of X-ray polarimetry, to date only few measurements were made, mainly focused on the Crab Nebula.

Novick et al. (1972) detected for the first time a linear polarization from the Crab nebula at a statistical confidence of 99.7 %, taking advantage from two polarimeters on-board a sounding rocket based on Thomson scattering at 90° and Bragg diffraction at 45°. The modulation signal detected at twice the rotation frequency on the rocket (see Figure 6.9) is the hint of a linear X-ray polarization. Under the assumption that the polarization is independent of the energy, these results lead to a degree of polarization $P = (18.2 \pm 6.1)\%$ at a position angle of $(155 \pm 10)°$. If combined with a previous experiment detecting only an upper limit for the polarization of the Crab Nebula (P<27% – Wolff et al. 1969), the total polarization of the Crab Nebula results to be $P = (15.4 \pm 5.2)\%$ at a position angle of $(156 \pm 10)°$, being in excellent agreement with the optical polarization and providing conclusive evidence that the X-ray emission from the Crab Nebula is produced by a synchrotron mechanism.

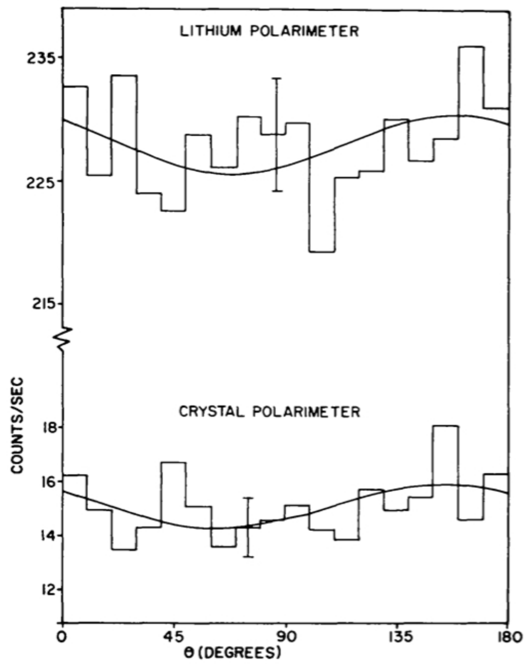

Figure 6.9. Flight data from the lithium and crystal polarimeters versus the position angle θ modulo 180°. The solid lines are the best fits to a function periodic at twice the rotation frequency of the rocket (Novick et al. 1972).

Few years later, Weisskopf et al. (1978) reported the results of the first measurement of the X-ray polarization of the Crab Nebula independent of the pulsed component. Exploting the characteristics of the Bragg polarimeter on board the *OSO-8* satellite launched in 1978, which is the only dedicated satellite-borne X-ray polarimeter having flown so far, a nebular polarization of $P = (19.2 \pm 1.0)\%$ at a position angle of $(156.4 \pm 1.4)°$ and $P = (19.5 \pm 2.8)\%$ at a position angle of $(152.6 \pm 4.0)°$ was observed at 2.6 keV and 5.2 keV, respectively (see Figure 6.10).

Recently, Dean et al. (2008) measured the polarization of the emission from the Crab nebula at higher energies ($E = 0.1 - 1.0$ MeV) with the SPI instrument on-board the *INTEGRAL* satellite. Analyzing more than three years of data (consisting of 600 observations of the Crab Nebula), a linear polarization $P = (46 \pm 10)\%$ has been measured at a position angle $(123 \pm 11)°$, closely aligned with the jet seen in the X-rays (see Figure 6.11), and in agreement with optical polarization measurement (Kanbach et al. 2005).

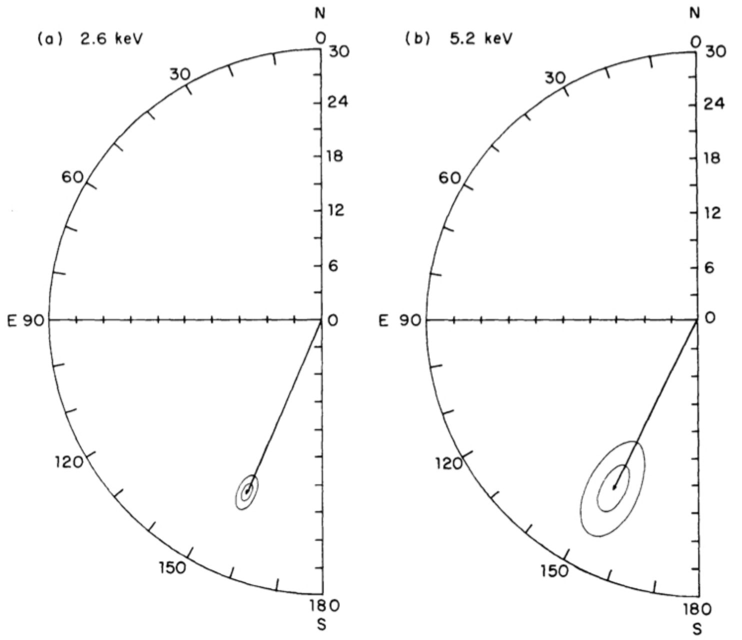

Figure 6.10. The polarization vectors for the Crab Nebula at (a) 2.6 keV and (b) 5.2 keV. Surrounding the vectors in order of increasing size are the 67% and 99% confidence contours. The radial scale is the polarization in percent (Weisskopf et al. 1978).

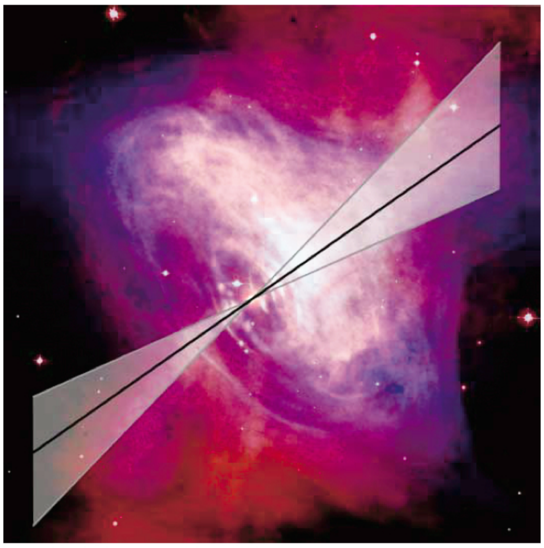

Figure 6.11. The γ-ray polarization vector measured by INTEGRAL/SPI, whose limits are shown by the shading, is superimposed to a composite X-ray (in blue) and optical (in red) image of the Crab Nebula (Dean et al. 2008).

The discovery of the polarized emission of the Crab nebula has been the only firm result achieved by X-ray polarimetry so far in the classical X-ray band. No evidence for a polarized signal in the emission of the Crab pulsar was observed at the 3σ confidence level (Silver et al. 1978), while only low time-averaged polarizations for both Sco X-1 (Long et al. 1979) and Cygnus X-1 (Long et al. 1980), and upper limits for ten strong sources belonging to different classes (Hughes et al. 1984) were provided by later analyses of the *OSO-8* data.

6.5 The *Imaging X-ray Polarimetry Explorer* mission

The *Imaging X-ray Polarimetry Explorer* (*IXPE* – Weisskopf et al. 2016a and 2016b) has been selected to be part of NASA's small explorer (SMEX) program in January 2017, and is now in the Project Phase D, which comprises system assembly, integration and test, and launch.

Expected to be launched at the end of 2021 from Kennedy Space Center (KSC) on the SpaceX Falcon 9 in a stowed configuration, *IXPE* will be placed into a circular low Earth orbit (LEO) at an altitude of 570 km and an inclination of 0 degrees. Once in orbit, a 4-meter extensible boom will be fully deployed matching the required separation between the mirrors and the focal plane detectors (see Figure 6.12).

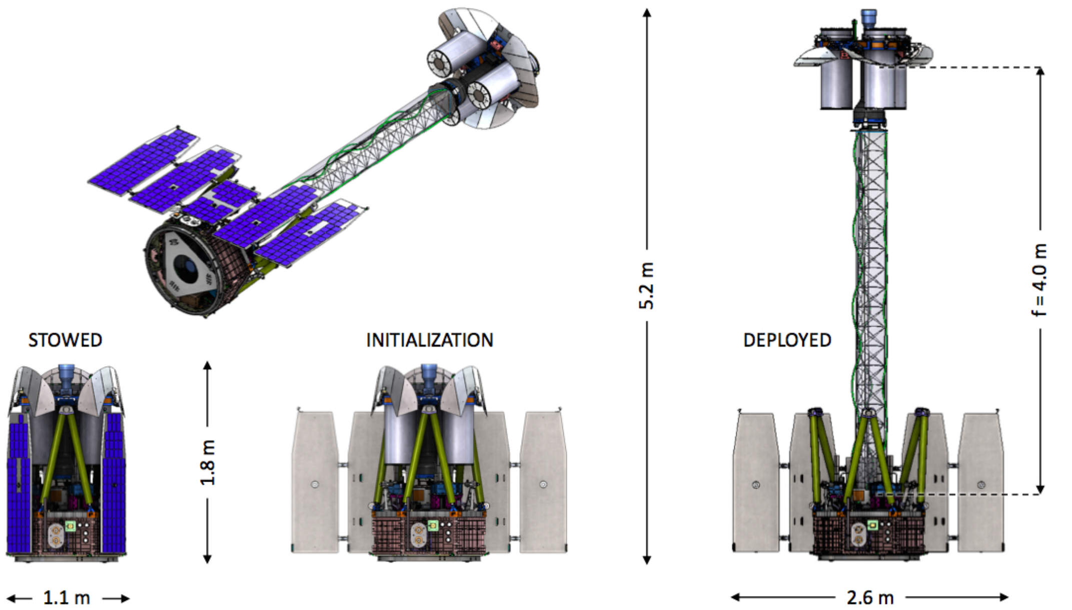

Figure 6.12. *From left-to-right.* The *IXPE* observatory stowed for launch, partially deployed for initialization of spacecraft operations, and fully deployed for science observations (O'Dell et al. 2019).

The *IXPE* mission is an international collaboration (see Figure 6.13) led by NASA Marshall Space Flight Center (MSFC) and including the Italian Space Agency (ASI) and Ball Aerospace as major international partners. In particular, MSFC provides the X-ray mirror module assemblies (MMAs – §6.5.1), while the Italian Space Agency (ASI) provides the unique polarization-sensitive detector units (DUs – §6.5.2) built by the Italian Institute Nuclear Physics (INFN) in collaboration with the Italian Institute of Astrophysics (INAF), and the detectors service unit (DSU), as well as the primary ground station, located in Malindi (Kenya). Ball Aerospace is responsible for the spacecraft, payload mechanical elements and flight metrology along with payload, spacecraft and system I&T followed by launch and operations, while the mission operations center (MOC) is located at CU/LASP.

Figure 6.13. The international partnership and the specific role of each institute involved in the *IXPE* mission.

The *IXPE* observatory consists of a spacecraft and two payload modules separated by a deployable boom (see Figure 6.14) and composed of three identical X-ray telescopes, each comprising a grazing-incidence MMA and a polarization-sensitive gas pixel X-ray DU. Completely dedicated to the measurement of the linear polarization in the X-ray band in the 2-8 keV energy range, it will also provide a moderate spectral and angular resolution, and an excellent timing accuracy (see Table 6.1).

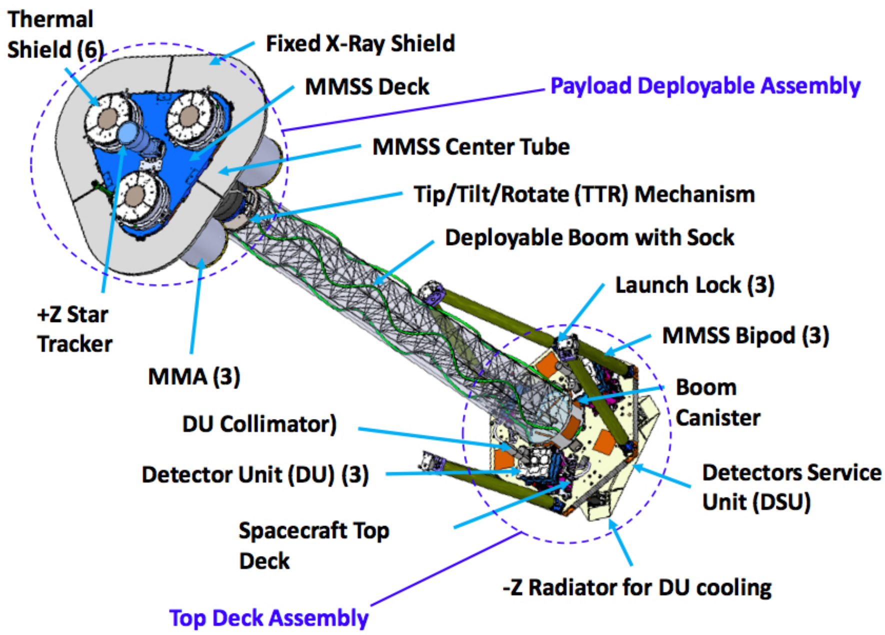

Figure 6.14. An *IXPE* telescope system view, showing key payload and spacecraft components (Deninger et al. 2020).

Table 6.1. IXPE performance parameters.

Parameter	Value
Launch vehicle	Falcon 9
Orbit	LEO 570 km with 0.1 deg inclination
Sky coverage per orbit	30%
Ground stations	primary: Malindi; secondary: Singapore
Operational phase	2 years + possible extension
Energy band	2-8 keV
Polarization sensitivity (MDP)	$<$5.5% for 1×10^{-11} erg cm^{-2} s^{-1} (10 days observation)
Spurious modulation	$<$0.3%
Field of view (FoV)	10 arcmin diameter overlapping for 3 telescopes
Spectral resolution	$\sim$20% @ 5.9 keV
Timing accuracy	20 μs with GPS

The baseline *IXPE* mission will last 2 years, following a 1-month commissioning phase. All scientific data will be publicly available through NASA's High-Energy Astrophysics Science Archive Research Center (HEASARC) at GSFC. If approved, IXPE will continue beyond 25 months, initiating a HEASARC-administered general observer (GO) program.

6.5.1 The X-ray mirror module assemblies

The *IXPE* observatory features three identical X-ray mirror module assemblies (MMAs – Ramsey et al. 2019) containing 24 nested nickel-cobalt shells, each of which includes the primary and secondary grazing-incidence mirror surfaces to achieve a 4001-mm focal length. MMAs are shown in Figure 6.15, while their main characteristics of MMAs are listed in Table 6.2.

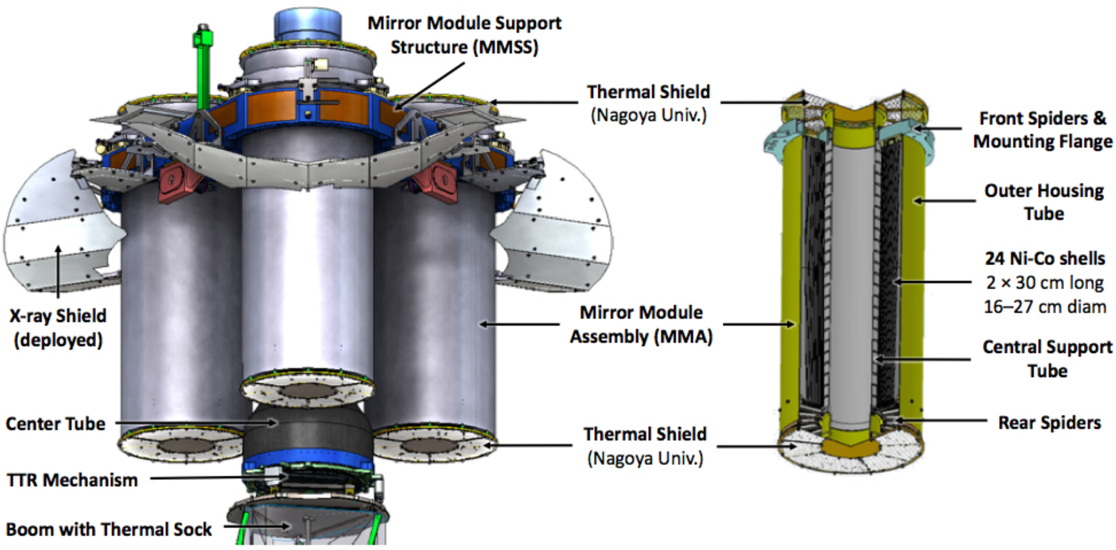

Figure 6.15. *IXPE* X-ray optics, comprising three identical MMAs mounted into the mirror module support structure (MMSS), along with other payload elements. A cut-away view of an MMA is shown on the right (O'Dell et al. 2019).

Table 6.2. Configuration and performance specification of the *IXPE* mirror module assemblies (adapted from Ramsey et al. 2019).

Parameter	Value
Mirror modules	3
Number of shells per mirror module	24
Focal lenght	4.001 m
Total shell lenght	600 mm
Inner/outer shell diameter	162 mm / 272 mm
Inner/outer shell thickness	178 μm / 254 μm
Shell material	Nickel cobalt alloy
X-ray optical coating	None (bare Ni-Co)
Effective area per mirror module	183 cm^2 @ 2.3 keV; >210 cm^2 @ 3-6 keV
Angular resolution	$\leq$25 arcsec HPD
Detector limited FoV	12.9 arcmin square

Produced by MSFC, the MMAs are based on the replica from mandrels technique, and equipped with thermal shields provided by the Nagoya University and heaters supplied by Ball Aerospace useful to control their temperature once in orbit. The most important breakthrough of this technology is the possibility to construct very thin shells, allowing to achieve a large collecting area also in a small mission like *IXPE* (see Figure 6.16).

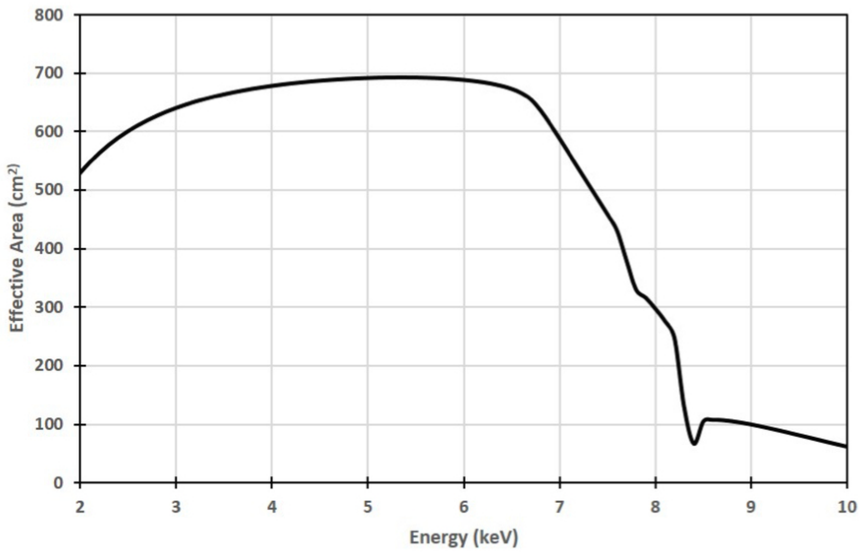

Figure 6.16. Expected pre-detector effective area of the three MMA optics, including attenuation by the thermal shields (Ramsey et al. 2019).

6.5.2 The X-ray instrument

The X-ray instrument onboard *IXPE* is composed of three identical polarization-sensitive Detector Units (DUs), whose main characteristics are listed in Table 6.3, and a single Detectors Service Unit (DSU), through which the DUs interface with the space-craft (see Figure 6.17).

Table 6.3. Performance specification of the *IXPE* detector units.

Parameter	Value
Sensitive area	15 mm × 15 mm
Fill gas and composition	Dimethyl ether (DME) @ 1 atm
Detector window	50-μm thick beryllium
Spatial resolution (FWHM)	$\leq$123 μm (6.4 arcsec) @ 2 keV
Energy resolution (FWHM)	0.54 kev @ 2 keV

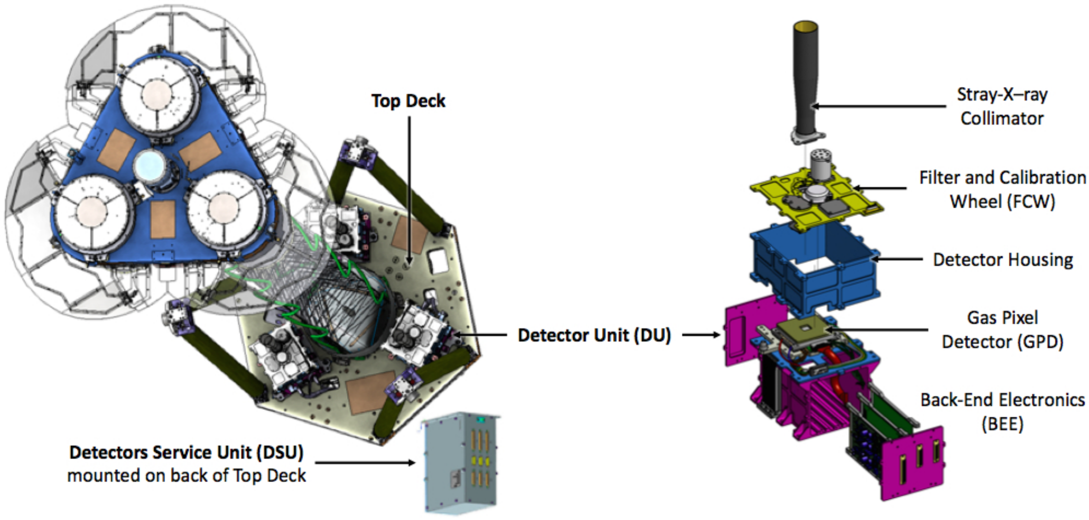

Figure 6.17. X-ray instrument onboard the *IXPE* observatory, composed on three DUs aligned with the MMAs and a DSU (left image). On the right, the main DU components, i.e. Stray X-ray Collimator, Filter and Calibration Wheel, Detector Housing, Gas Pixel Detector, and Back-End Electronics, are shown (O'Dell et al. 2019).

The Gas Pixel Detector (GPD) hosted inside each DU has been developed in Italy by INFN in collaboration with INAF. The working principle is shown in Figure 6.18 (left image). When a photon is absorbed in the gas cell, a photoelectron is emitted in the direction of the electric field and propagates in the gas producing electron-ion pairs by ionization along the path. These charges are then multiplied in an electric field generated by a Gas Electron Multiplier (GEM) and then collected on the top layer of a dedicated ASIC. The response of the instrument is the track of the photoelectron path (right image in Figure 6.18), whose reconstruction is useful to derive its emission direction, which is related to the polarization of the absorbed photon. In particular, when the photons are linearly polarized, the distribution of the photoelectrons is not uniform, but shows a $\cos^2$ modulation where the maximum corresponds to the angle of polarization.

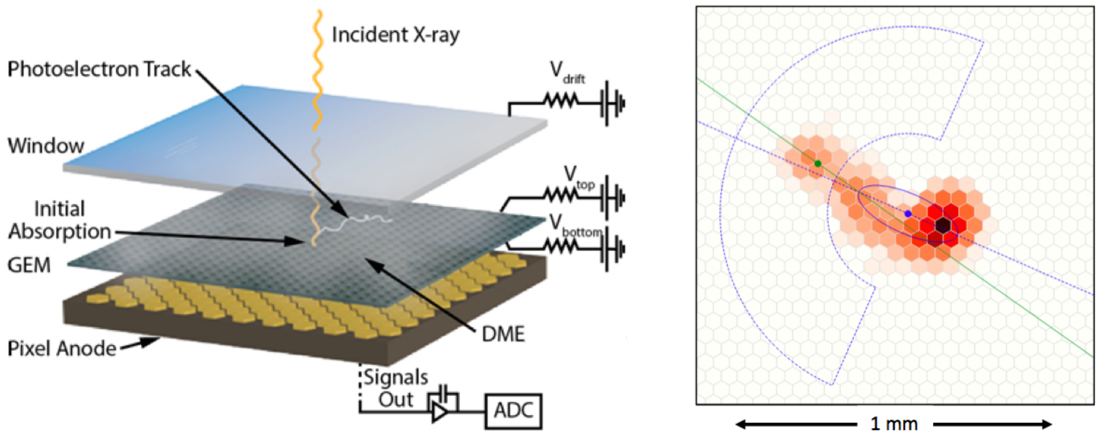

Figure 6.18. A schematic representation of the working principle of the Gas Pixel Detector is shown on the left, while a ionization track resulting from absorption of a 5.9 keV X-ray photons, as amplified by the GEM and imaged onto the GPD's pixelated anode is shown on the right (O'Dell et al. 2019).

Each DU is also equipped with a filter calibration wheel, hosting a few filters and four calibration sources. The filters are expected to be used only in case of extremely bright sources to prevent any damage on the detectors, while the calibration sources will be used routinely during *IXPE* observations. In particular, three of them are not polarized and will be useful for calibration and for checking response on polarized radiation, while the last one is able to produce polarized X-rays at 3.0 keV and 5.9 keV.

7

The polarimetric X-ray view of the Circinus Galaxy

Contents

Due to their large scattering-induced polarization, Compton-thick AGN are obvious candidates for X-ray polarization measurements. Since the Circinus Galaxy is the brightest Compton-thick AGN in the sky in the 2-8 keV band, as shown in Table 7.1, it has been included in the first year *IXPE* observing plan.

Table 7.1. Brightest Compton-thick AGN in the 2-8 keV *IXPE* band.

Target	F_{2-8keV} (erg cm^{-2} s^{-1})
Circinus Galaxy	1.1×10^{-11}
Mrk 3	5.0×10^{-12}
NGC 1068	4.2×10^{-12}
NGC 7582	1.7×10^{-12}

In this context, this chapter focuses on the expected polarimetric X-ray view of the Circinus Galaxy. In particular, §7.1 is devoted to shortly summarize what we already know about the spectroscopic X-ray view of this source, while §7.2 focuses on the main spectral components observed in its X-ray spectrum. Then, the expected polarization degree due to each spectral component and the relative *IXPE* simulations are discussed in §7.3. Finally, §7.4 and §7.5 are devoted to discuss the best observational strategy needed to disentangle the contribution of the AGN to the polarization signal from the one due to contamination from other X-ray sources within the field of view.

7.1 The spectroscopic X-ray view of the Circinus Galaxy

The Circinus Galaxy (hereafter Circinus) is a Sb-Sd spiral galaxy located at low Galactic latitude (b=-3.8°) in a region of relatively low Galactic extinction ($A_v \sim 1.5$ – Freeman et al. 1977). Several evidences of intense extranuclear activity, such as a luminous watermaser (Gardner & Whiteoak 1982) and IR nucleus (Moorwood & Glass 1984), two starburst rings at ∼2 and ∼10 arcsec from the nucleus (Wilson et al. 2000 and references therein), an overall complex extended radio structure (Elmouttie et al. 1998; Curran et al. 2008), and a spectacular [OIII] ionization cone (Marconi et al. 1994), suggest the presence of an obscured active nucleus. Moreover, being a nearby ($D = 4.2 \pm 0.8$ Mpc, Freeman et al. 1977) X-ray bright Seyfert 2 galaxy, it has been largely observed by all the main X-ray observatories in the last 25 years.

Circinus was observed for the first time in the X-rays in 1994 during the *ROSAT* All Sky Survey (RASS – Brinkmann et al. 1994), which measured a corrected for absorption X-ray flux $F \sim 1.3 \times 10^{-11}$ erg cm^{-2} s^{-1} in the 0.1-2.4 keV energy band. The first pointed X-ray observation was made by *ASCA* one year later showing a spectrum dominated by a pure Compton reflection component with a very flat continuum ($\Gamma < 1$), a prominent iron Kα emission line ($EW \sim 2$ keV) and several other fluorescence lines from lighter elements, such as Ne, Mg, Si, and S (Matt et al. 1996). The Compton-thick nature of the source suggested by *ASCA* data was confirmed few years later by *BeppoSAX*, which observed the source for the first time above 10 keV. The emerging of the primary continuum at hard X-rays has indeed been ascribed to the presence of a screen of absorbing matter with $N_H \sim 4 \times 10^{24}$ cm^{-2} through which the nuclear region is observed Guainazzi et al. 1999; Matt et al. 1999). The properties of the nuclear emission has been investigated also with better angular resolution X-ray satellites such as *Chandra* (Sambruna et al. 2001a and 2001b; Marinucci et al. 2013b, Kawamuro et al. 2019) and *XMM-Newton* (Molendi et al. 2003; Massaro et al. 2006), suggesting that the soft X-rays are due to nuclear emission reprocessed from both photoionized and photoexcited plasma. Finally, *NuSTAR* observations performed in 2013 observed a nuclear spectrum consistent with Compton-scattering by an optically-thick torus with $N_H > 6 \times 10^{24}$ cm^{-2} (Arévalo et al. 2014).

7.2 Modelling the X-ray spectrum of the Circinus Galaxy

For my analysis, I took advantage of the spectrum of Circinus observed by *XMM-Newton* in 2001 (obsID=0111240101), discussed in Massaro et al. (2006). The spectral continuum is well reproduced by a combination of two models: a power-law accounting for the soft X-ray emission, and a pure Compton reflection component describing the high energy part of the spectrum which is modelled in `XSPEC` with `pexrav` (Magdziarz & Zdziarski 1995), assuming solar abundances for all the elements. Several emission lines are then added to the continuum model, as required by the inspection of residuals (see Table 2 in Massaro et al. 2006 for a complete list). Therefore, the baseline model can be roughly expressed by the following general formula:

$$F(E) = e^{-\sigma_{ph}(E)\ N_H}\ [AE^{-\Gamma} + R(\Gamma) + \sum_i G_i(E)], \tag{7.1}$$

where $\sigma_{ph}(E)$ is the photoelectric cross-section with abundances as in Wilms et al. (2000), and N_H is the cold absorption along the line of sight, which includes absorption from our own Galaxy plus possible contributions from the Circinus galaxy itself. A is the normalization of the power-law with slope Γ accounting for the reflection of the nuclear radiation from ionized matter, $R(\Gamma)$ is the pure reflection continuum arising from cold matter within the torus, and $G_i(E)$ are the Gaussian profiles used to reproduce the emission lines. The photon index and the high energy cut-off of the power-law are fixed to be $\Gamma = 1.56$ and $E_c = 56$ keV, as in Matt et al. (1999) and Bianchi et al. (2001), and the best-fit is shown in Figure 7.1. Assuming such a model (see Figure 7.2), the total flux of Circinus in the 2-8 keV *IXPE* energy band is $\sim 1.1 \times 10^{-11}$ erg cm^{-2} s^{-1}, being divided into each spectral components as follows.

- warm reflection continuum: $F_{2-8keV} = 4.5 \times 10^{-12}$ erg cm^{-2} s^{-1};
- cold reflection continuum: $F_{2-8keV} = 4.9 \times 10^{-12}$ erg cm^{-2} s^{-1};
- emission lines: $F_{2-8keV} = 1.1 \times 10^{-12}$ erg cm^{-2} s^{-1}.

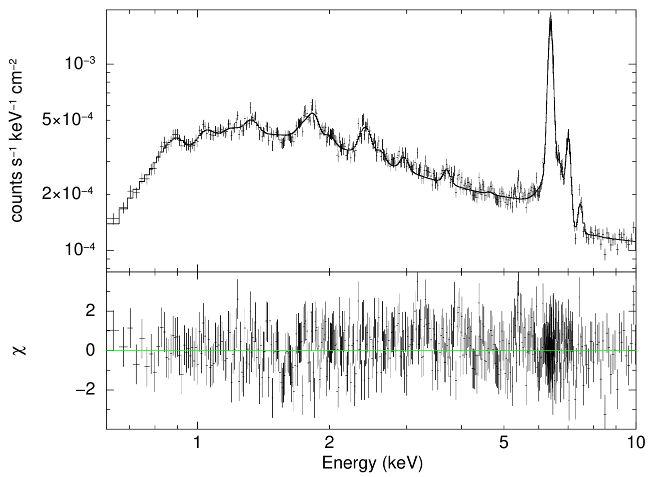

Figure 7.1. *XMM-Newton* EPIC-pn spectrum of the Circinus Galaxy (top panel) and residuals with respect the baseline model discussed throughout the text.

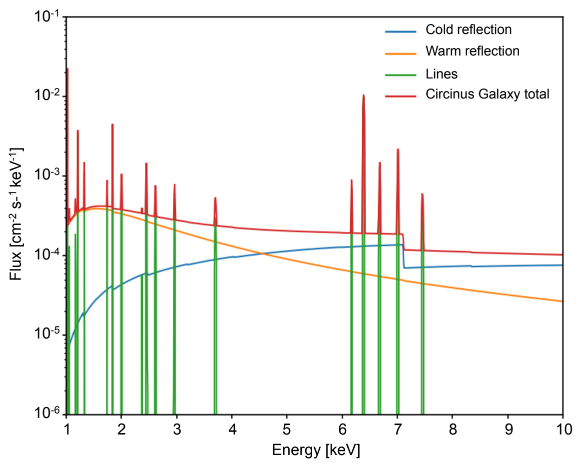

Figure 7.2. 1-10 keV baseline model reproducing the X-ray spectrum of the Circinus Galaxy (red solid line), which is composed of a warm reflection continuum coming from the ionization cones (in orange), a cold reflection continuum arising from the torus (in blue), and several emission lines (in green), due to both warm and cold matter.

7.3 *IXPE* simulations of the nuclear region of the Circinus Galaxy

Assuming a geometry in which the ionization cone is perpendicular to the torus' plane, the contribution of each component to the total expected polarization degree is calculated as follows.

The polarization of the cold reflection continuum is obtained through simulations performed with the Monte Carlo code `STOKES` (Marin 2018), assuming a central isotropic and unpolarized point source surrounded by a torus with a flared geometry, having an inner radius $R_{in} = 0.01$ pc, and an outer radius $R_{out} = 5$ pc. Different half-opening angles of the torus and inclination angles with respect to the torus axis have been considered. According to several literature works, two inclination angles are considered, i.e. $i = 65°$ from radio (Freeman et al. 1977) and *ALMA* data (Zschaechner et al. 2016; Izumi et al. 2018) and $i = 75°$ from VLT MIDI observations (Tristram et al. 2014) and SED analysis (Wada et al. 2016). Since our line of sight have to intercept the torus, we considered two different half-opening angles of the torus, i.e. $\theta = 30°$ or $\theta = 40°$, as measured from the equatorial plane.

When such a configuration is assumed, the expected polarization degree due to the cold reflection component is shown in Figure 7.3 for each combination of θ and i. The mean value of the cold polarization is of the order of 10% and 35%, when the half opening angle of the torus is 30° or 40°, respectively, while no significant dependence on the inclination is expected at a given θ. For this reason, only the case in which $i = 75°$ will be considered for the *IXPE* simulations described in the following.

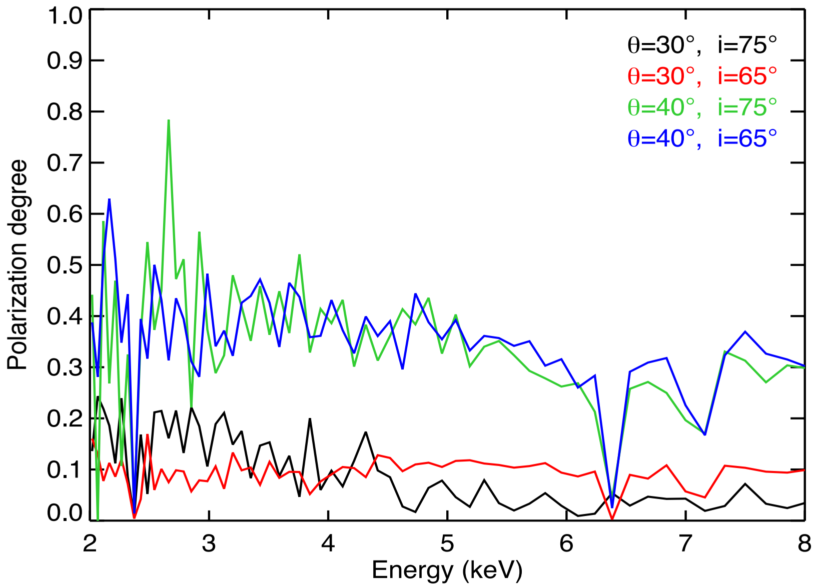

Figure 7.3. Expected polarization degree due to the cold reflection continuum for the Circinus Galaxy. Four cases are shown, combining the different values of both the inclination of the line of sight and the half-opening angle of the torus. No significant differences appear for different inclination at a given θ.

Concerning the warm reflection due to the ionization cone, its polarization P_w is given by

$$P_w = P_w(\gamma, i) = \frac{\sin^2 i}{2\alpha + \sin^2 i}, \tag{7.2}$$

(Brown & McLean 1977), where, assuming optically thin matter and a conical geometry with half-opening angle θ_c (see Figure 7.4):

$$\begin{cases} \alpha = \frac{1+\gamma}{1-3\gamma} \\ \gamma = \frac{1-\mu_c^3}{3(1-\mu_c)} \\ \mu_c = \cos\theta_c \end{cases} . \tag{7.3}$$

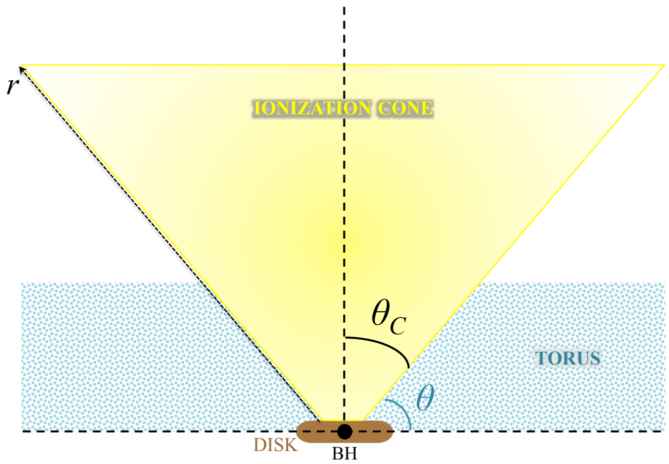

Figure 7.4. Sketch of the conical geometry assumed for the warm reflection component. The distribution of optically thin matter is assumed to be constant within the ionization cone and null elsewhere.

With our geometry, and assuming $\theta_c = \pi/2 - \theta$, i.e. that the ionization cone is funneled by the torus, the polarization of the warm reflector is expected to be of the order of 28% or 41% for $\theta = 30°$ or $\theta = 40°$ respectively, while the emission lines are considered as unpolarized. The polarization is found to be perpendicular to the torus axis ($\Psi = 0°$) for all the spectral components.

The expected polarization degree for each component in the two different configurations is summarized in Table 7.2, while the total polarization is shown in Figure 7.5 for both cases.

Several simulations has been performed in order to estimate the exposure time needed to obtain an MDP=5%, good enough given the expected values. Figure 7.6 clearly shows that our goal can be reached through an 800 ks *IXPE* observation. It is worth noting that the significant decrease of the polarization at high energies is mainly due to the unpolarized flux of the iron Kα line. The blue dots are the simulated data for a given configuration, while the orange dotted line reproduces the expected polarization for the opposite configuration. Plotting data in this way allows to clearly check that a measure of the X-ray polarization could lead to a direct measure of the half-opening angle of the torus.

Table 7.2. Expected polarization degree induced from the Compton-thick AGN within the Circinus Galaxy for cold, warm and line component, when an inclination angle of 75° is assumed.

	Torus half-opening angle	
	$\theta = 30°$	$\theta = 40°$
Cold polarization	10%	35%
Warm polarization	28%	41%
Line polarization	0%	0%

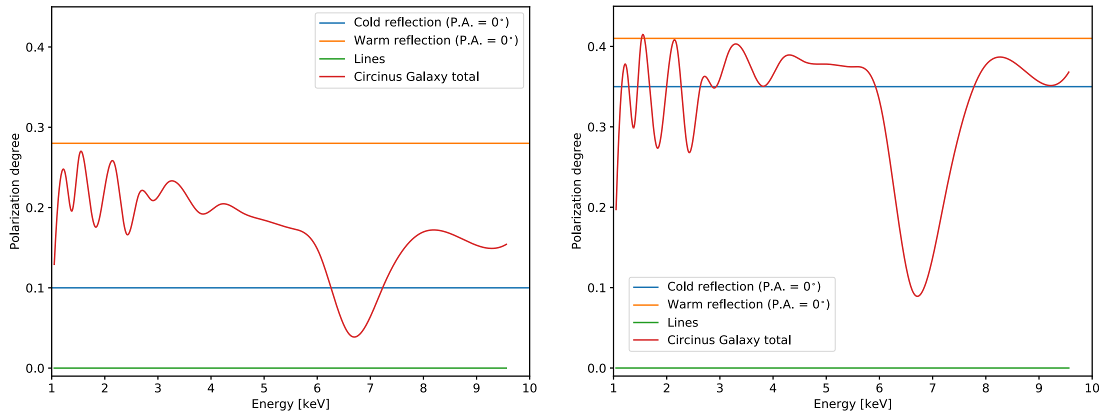

Figure 7.5. Total expected polarization degree for $\theta = 30°$ (left panel) and $\theta = 40°$ (right panel), when an inclination angle of 75° and the baseline model discussed in §7.2 are assumed.

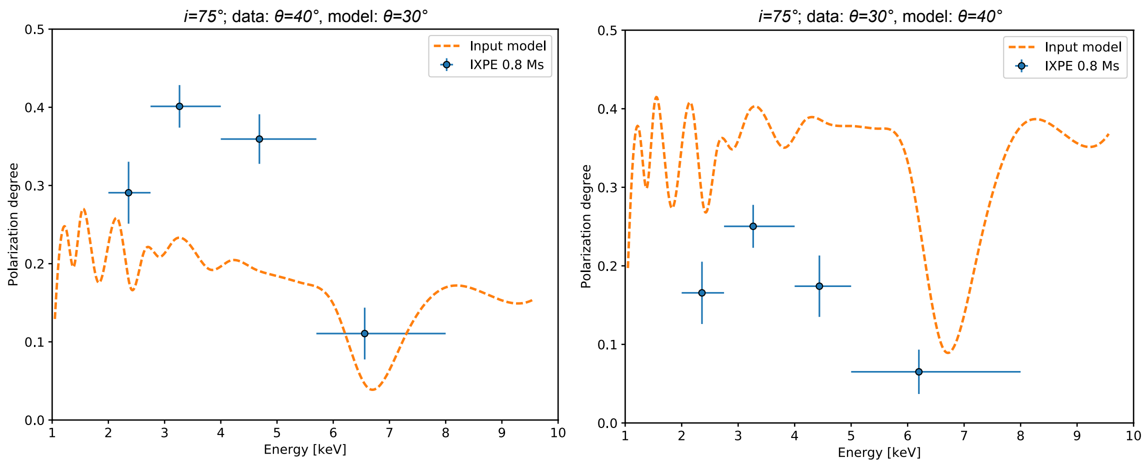

Figure 7.6. 800 ks *IXPE* simulation for the Circinus Galaxy. The polarization degree is shown as a function of the energy. Simulated data (in blue) are plotted together with the expected polarization for the opposite configuration.

7.4 The observational strategy

In order to obtain the best observational strategy for the *IXPE* pointing of Circinus, it is mandatory to take into account any possible source of contamination. Since the central region of the Circinus Galaxy is heavily populated by ULXs (Bauer et al. 2001; Smith & Wilson 2001) that cannot be spatially resolved by *IXPE*, it is fundamental to simultaneously monitor their flux level, in order to disentangle the contribution of the ULXs within the field of view from the one of the AGN to the total polarization signal measured by *IXPE*.

Among the 15 sources detected within a 1 arcmin aperture radius of the nucleus (Bauer et al. 2001), the brightest ones are CXOU J141312.3-652013 (hereafter CG X-1) and CXOU J141310.0-652044 (hereafter CG X-2), at angular distances of 15" north-east and 25" south from the AGN (see Figure 7.7). In particular, CG X-1 is an eclipsing X-ray binary system with a Wolf-Rayet donor star, a period $P \sim 7.2$ hr and a 2-8 keV flux which varies from a few percent to $\sim 45\%$ of the one of the AGN on timescales of weeks (Esposito et al. 2015; Qiu et al. 2019). On the other hand, CG X-2 is a young supernova remnant candidate (SN 1996cr – Bauer et al. 2008) with a stable flux of a few percent with respect to the nuclear one.

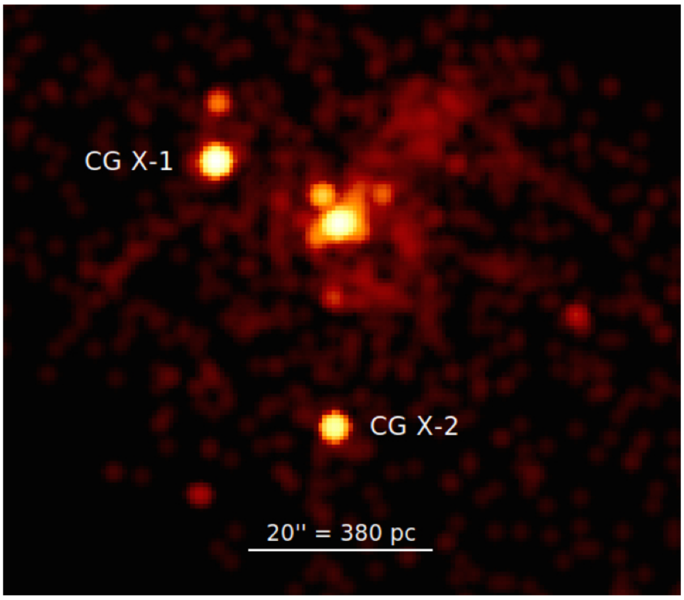

Figure 7.7. Archival *Chandra* ACIS-S (ObsID 365) image of the central region of the Circinus Galaxy in the 0.3-8 keV energy band, with the two brightest ULXs marked. North is up and east to the left. Some smoothing has been applied for the sake of visual clarity.

Spectra of both the AGN and the two ULXs were obtained from an ACIS-S observation performed on March 14, 2000 (ObsID 365), with a net exposure time of ~5 ks. In this pointing CG X-1 was observed at its brightest flux level. The spectra were extracted using circular regions with 2" radii, while a 5" radius was used for the background. As concerns the AGN, the spectrum was modelled as described in §7.2, resulting in a 2-8 keV flux $F_{AGN} = (1.0 \pm 0.1) \times 10^{-11}$ erg cm^{-2} s^{-1}. On the other hand, the spectra of CG X-1 and CG X-2, are both modelled with an absorbed power-law, whose parameter are shown in Table 7.3. Using such a model, the observed flux are $F_{1,h} = (4.5 \pm 0.5) \times 10^{-12}$ erg cm^{-2} s^{-1} and $F_2 = (1.1 \pm 0.4) \times 10^{-12}$ erg cm^{-2} s^{-1} for CG X-1 in its highest flux state and

CG X-2, respectively (see Figure 7.8). Thus, when CG X-1 is at its brightest level, the combined fluxes of the two ULXs represent $\sim 50\%$ of the flux of the AGN.

Table 7.3. Best-fit values obtained through a 10 ks *Chandra* simulation.

Target	Γ	N_H (10^{22} cm^{-2})	F_{2-8keV} (10^{-12} erg cm^{-2} s^{-1})
CG X-1	1.45 ± 0.15	1.0 ± 0.2	4.5 ± 0.5
CG X-2	1.5 ± 0.4	0.9 ± 0.4	1.1 ± 0.4

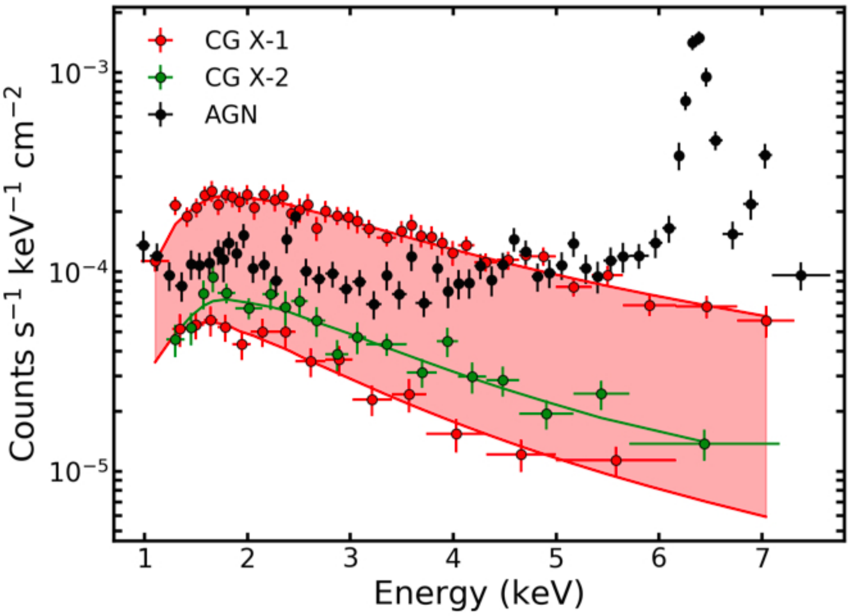

Figure 7.8. 10 ks simulated data for the AGN (in black) and for both CG X-1 (in red) and CG X-2 (in green). The pink region denotes the range of spectral variability for CG X-1. At its high and low flux levels, CG X-1 has a relative 2-8 keV flux of $\sim 45\%$and $\sim 7\%$ compared to the AGN, respectively.

A low flux state of CG X-1 is reported in Arévalo et al. (2014) and modelled with an absorbed power-law with spectral index $\Gamma = 1.80 \pm 0.04$ and column density $N_H = (1.03 \pm 0.03) \times 10^{22}$ cm^{-2}, resulting in a 2-8 keV flux $F_{1,l} \sim 7 \times 10^{-13}$ erg cm^{-2} s^{-1}.

Since we aim at measuring the 2-8 keV flux of CG X-1 in the low flux state (i.e. $F_{1,l}$) with an uncertainty lower than 20%, we performed several ACIS-S simulations of the spectra of the three sources. Testing different exposure times and using the most updated RMFs/ARFs, due to the recent degradation of the ACIS-S detector at energies below 2 keV, we obtained that a 10 ks *Chandra* observation is needed to reach our goal.

The results from the fits of the simulated data with the baseline model are reported in Figure 7.8. The red and green solid lines show the best fit models over-imposed to the simulated data of the ULXs, whilst the pink region denotes the range of spectral and flux variability for CG X-1. Uncertainties of 15% and 6% are retrieved on the 2-8 keV flux in the faint and bright states of CG X-1, respectively. An uncertainty of 10% is then obtained on the 2-8 keV flux of CGX-2.

Since CG X-1 varies on timescales of weeks, an ACIS-S snapshot at the beginning and another one at the end of the *IXPE* pointing (which is about 20 days long) appears to be the best observational strategy in order to

- spatially resolve the two brightest ULXs within the field of view;
- monitor any possible flux or spectral variability of CG X-1;
- study the contamination of the two sources to the polarization measurement induced from the Compton-thick AGN, as discussed in the next section.

7.5 Which is the contribution of the contaminating sources to the total polarization signal?

As discussed in §7.4, the most important contaminating sources during the future *IXPE* observation of the Circinus Galaxy are the ULXs CG X-1 and CG X-2, located at a distance of ∼285 pc and ∼375 pc from the AGN, respectively. In particular, CG X-1 has a variable flux, which is ∼ 7% and ∼ 45% of the AGN flux in the 2-8 keV *IXPE* band, when observed in its brightest and faintest state, respectively. On the other hand, CG X-2 has a more stable flux of a few percent with respect to the nuclear one. Thus, accounting for the large range of variability of CG X-1 (see Figure 7.8), two different contamination levels have been considered for the ULXs, i.e. 10% and 50% of the AGN flux in the 2-8 keV *IXPE* band, in order to estimate the ULX contamination level to the total polarization signal measured during the future *IXPE* observation.

Considering a half-opening angle of the torus $\theta = 40°$, an inclination angle $i = 75°$ with respect to our line of sight, and assuming the emission from the ULXs as unpolarized, the expected polarization signals obtained through a 800 ks *IXPE* observation are shown in Figure 7.9. In case of a null contribution from the ULXs to the 2-8 keV flux, the polarization degree is P=5-43%. The larger value is due to the warm reflection component from the ionization cone at soft energies, while the low polarization observed at high energies is mainly due to the unpolarized flux of the iron Kα fluorescence emission line at 6.4 keV. On the other hand, the highest polarization degree decreases to 38% and 27%, in case of a 10% or 50% contamination level from the ULXs. These simulated data clearly show that the coordination with *Chandra* is fundamental to correct the total polarization signal measured by *IXPE* for the contribution of the ULXs within the field of view. In this context, a *Chandra* proposal aimed at tracking the ULX population activity in the Circinus Galaxy during the *IXPE* observation has been already approved.

Thus, the observational strategy discussed in §7.4, which includes two *Chandra* observations to be performed at the beginning and at the end of the *IXPE* observation, appears as the best way to obtain a good estimate of the polarization induced by the AGN within the Circinus Galaxy. Otherwise, since we cannot spatially resolve the three sources (i.e. the AGN and the two ULXs) with the *IXPE* pointing only, we would run the risk of overestimating the polarization of the only Compton-thick source that will be observed during the first year *IXPE* observing plan.

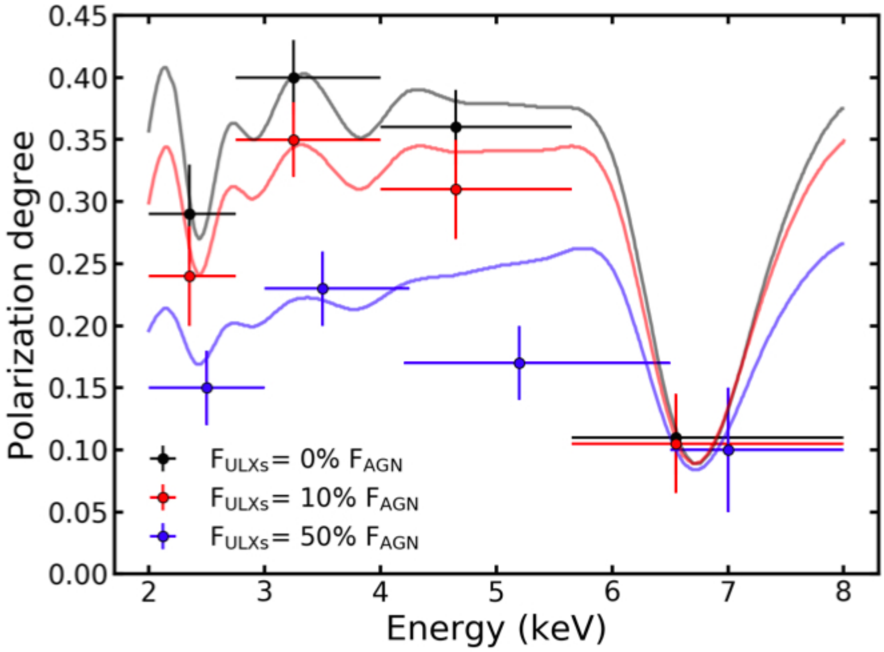

Figure 7.9. *IXPE* simulations and models for different contamination levels. The expected polarization degree in case of a null contribution from the ULXs is shown in black, while a 10% and a 50% ULX contamination is indicated in red and blue, respectively.

8
Conclusions and future perspectives

Contents

In this last chapter, I shortly summarize the main results obtained during my thesis work, which was aimed at mapping the circumnuclear matter in obscured AGN. To achieve this aim, both spectroscopic data from several current X-ray observatories and simulations of future X-ray polarimetric measurements have been analyzed and discussed in detail in Chapter 4, 5, and 7.

8.1 Obscured AGN through X-ray spectroscopy

As concerns X-ray spectroscopy, I focused my attention on two bright sources: the Compton-thick AGN in NGC 1068 and the Compton-thin Seyfert 2 galaxy NGC 4507.

For my research project, the AGN within NGC 1068 appeared as a very interesting source because in 2014 experienced an unveiling event, in which Compton-thick material moved temporarily out from our line of sight, allowing for the first time the nuclear radiation to pierce through the circumnuclear medium. However, the 6-month separation between the observations prevented us to put tigther constraints on the location of the circumnuclear absorbing clouds (Marinucci et al. 2016). This is the reason why a further *NuSTAR* monitoring was performed in 2017-2018 sampling shorter timescales from 1 to 6 months.

The main results of the spectral analysis of this campaign, which revealed variability both in the soft X-rays below 5.5 keV and in the hard X-ray band above 20 keV, are summarized as follows.

▷ The soft X-ray variability has been ascribed to a transient X-ray source detected by *Swift*-XRT, which is plausibly a strongly variable ULX. Located at ∼2 kpc from the nucleus of NGC 1068, it reached a peak X-ray intrinsic luminosity $L_{2-10keV} = (3.0 \pm 0.4) \times 10^{40}$

erg s^{-1} in the 2-10 keV band. No robust identification with previously detected sources has been observed, and only an upper limit of ~3 months can be given on its X-ray variability timescale.

▷ The hard X-ray variability has been ascribed to one unveiling and one eclipsing event with timescales lower than 27 and 91 days, respectively, due to Compton-thick matter moving across our line of sight. Assuming the circumnuclear material to be composed of individual spherical clouds orbiting with Keplerian velocities at a distance R from the SMBH, we can locate the absorbing gas clouds in the innermost part of the torus or closer (i.e. in the BLR), providing both tighter constraints on their location with respect to the previous *NuSTAR* monitoring campaign, and further evidence of the clumpy structure of the circumnuclear matter NGC 1068.

It is worth remarking that this analysis has been published by the Monthly Notices of the Royal Astronomical Society (MNRAS) in March 2020 (Zaino et al. 2020). Moreover, the results discussed in detail in Chapter 4 and summarized above have been presented at several national and international conferences, and a preliminary version of them has been discussed by seminar at the Strasbourg Observatory in January 2019.

The second source on which I focused my attention during my research work is NGC 4507. During past observations, this bright Seyfert 2 galaxy showed variability in the X-ray band and evidence of multiple regions that absorb and reprocess the primary emission of the AGN. In order to solve any possible ambiguity on the variability of the intrinsic emission and amount of absorption within this source, a *NuSTAR* monitoring campiagn was performed in 2015.

The analysis of these data revealed a hard X-ray variability below 40 keV, while stable countrates were observed above this energy during the whole monitoring. This suggests that no variations are expected to be observed in the primary continuum and that the most plausible explanation for the variability observed in the X-ray spectra is a change in the obscuration level along the line of sight (Zaino et al. submitted). The main results obtained on the physical properties of the circumnuclear matter, which are discussed in detail in Chapter 5, can be summarized as follows.

▷ The main driver of the X-ray variability is ascribed to Compton-thin absorbing gas clouds crossing our line of sight in a 1-month timescale and located between the outer BLR and the inner torus boundary or even a little further out.

▷ A quite complex physical scenario describes the circumnuclear matter surrounding the nuclear region of NGC 4507 with reflection arising from gas with a Compton-thick global average column density and transmission of the continuum through variable Compton-thin matter. Even if such a configuration is not surprisingly in AGN (e.g. Matt 2001; Bianchi et al. 2003; Turner et al. 2020), for NGC 4507 it appears at odds with the only Compton-thin material observed by *Suzaku* eight year before (Braito et al. 2013). This discrepancy could be due to the *Suzaku* lack of coverage in the 10-14 keV energy range, which may prevent a robust spectral modelling of the reflector; however, future simultaneous observations with facilities covering both the soft and the hard X-rays are expected to obtain a conclusive evidence about the physical properties of the reflector within this source.

8.2 Obscured AGN via X-ray polarimetry

As Science Participant of the *IXPE* team in the Topical Working Group on radio-quiet AGN, I was involved in the scientific investigation, including modeling, simulation, planning, analysis and interpretation of the future *IXPE* scientific observations. In this context, I performed several simulations on the brightest Compton-thick AGN with the aim of

1. selecting the best candidate to observe with *IXPE* in order to obtain information about the geometry of the circumnuclear material in highly obscured AGN;

2. studying the best observational strategy providing a good estimate of the polarization induced by the AGN, corrected for the presence of any contaminating source.

Mainly due to its highest brightness in the 2-8 keV working band of the polarimeters on board this observatory, the Circinus Galaxy resulted to be the best Compton-thick candidate to include in the first year *IXPE* observing plan. Several simulations have clearly shown that a useful MDP=5% can be obtained through an 800 ks *IXPE* observation, also taking into account the presence of contaminating source within the field of view (Zaino et al. in preparation). It is indeed well known that the central region of the Circinus Galaxy is heavily populated by ULXs (Bauer et al. 2001; Smith & Wilson 2001) that might potentially contaminate the measurement of the polarization signal from the AGN.

Since the *IXPE* Point Spread Function prevent us to spatially resolve these sources, a coordination with *Chandra* is mandatory to correct the total polarization signal measured by *IXPE* for the contribution of the ULXs within the field of view. Moreover, due to the variability on timescale of weeks already shown by one of these ULXs, the observational strategy for the Circinus Galaxy will require two *Chandra* snapshots, one at the beginning and another one at the end of the *IXPE* pointing (which is about 20 days long). In this context, it is worth to note that a *Chandra* proposal based on the simulations described in detail in Chapter 7 and aimed at tracking the ULX population activity in the Circinus Galaxy during the *IXPE* observation has been already approved.

References for this thesis

Chapter 4

Zaino A., Bianchi S., Marinucci A., Matt G., Bauer F. E., Brandt W. N., Gandhi P., Guainazzi M., Iwasawa K., Puccetti S., Ricci C., Walton D. W., *"Probing the circumnuclear absorbing medium of the buried AGN in NGC 1068 through NuSTAR observations"*, 2020, MNRAS, 492, 3872

Chapter 5

Zaino A., Braito V., Bianchi S., Matt G., Severgnini P., Della Ceca R., Marinucci A., Reeves J. N., Ballo L., Turner T. J., *"A NuSTAR X-ray spectral analysis of the circumnuclear matter within NGC 4507"*, 2020, submitted to MNRAS.

Chapter 7

Zaino A., Marin F., Bianchi S., Marinucci A., Matt G., *"X-ray polarization in Compton-thick AGN: the Circinus Galaxy"*, 2021, in preparation.

Bibliography

Aird J., Coil A. L., Georgakakis A., Nandra K., Barro G. and Pérez-González P. G., 2015, MNRAS, 451, 1892

Antonucci R., 1993, ARA&A, 31, 473

Antonucci R. R. J. and Miller J. S., 1985, ApJ, 297, 621

Arévalo P., Bauer F. E., Puccetti S., Walton D. J., Koss M., Boggs S. E., Brandt W. N., Brightman M., Christensen F. E., Comastri A., Craig W. W., Fuerst F., Gandhi P., Grefenstette B. W., Hailey C. J., Harrison F. A., Luo B., Madejski G., Madsen K. K., Marinucci A., Matt G., Saez C., Stern D., Stuhlinger M., Treister E., Urry C. M. and Zhang W. W., 2014, ApJ, 791, 81

Arnaud K. A., Branduardi-Raymont G., Culhane J. L., Fabian A. C., Hazard C., McGlynn T. A., Shafer R. A., Tennant A. F. and Ward M. J., 1985, MNRAS, 217, 105

Arnaud, K. A. 1996, in Astronomical Society of the Pacific Conference Series, Vol. 101, Astronomical Data Analysis Software and Systems V, G. H. Jacoby & J. Barnes eds., p. 17

Aschenbach B. and Braeuninger H., 1988, Proc. SPIE, 982, 10

Avdan S., Akyuz A., Vinokurov A., Aksaker N., Avdan H., Fabrika S., Valeev A., Akkaya-Oralhan I. and Balman, Ş., 2019, ApJ, 875, 68

Baldwin J. A., Hamann F., Korista K. T., Ferland G. J., Dietrich M. and Warner C., 2003, ApJ, 583, 649

Bambi C., 2018, Annalen der Physik, 530, 1700430

Barcons X., Barret D., Decourchelle A., den Herder J. W., Fabian A. C., Matsumoto H., Lumb D., Nandra K., Piro L., Smith R. K. and Willingale R., 2017, Astronomische Nachrichten, 338, 153

Bardeen J. M., Press W. H. and Teukolsky S. A., 1972, ApJ, 178, 347

Barthelmy S. D., Barbier L. M., Cummings J. R., Fenimore E. E., Gehrels N., Hullinger D., Krimm H. A., Markwardt C. B., Palmer D. M., Parsons A., Sato G., Suzuki M., Takahashi T., Tashiro M. and Tueller J., 2005, Space Science Reviews, 120, 143

Barvainis R., 1987, ApJ, 320, 537

Bauer F. E., Brandt W. N., Sambruna R. M., Chartas G., Garmire G. P., Kaspi S. and Netzer H., 2001, AJ, 122, 182

Bauer F. E., Dwarkadas V. V., Brandt W. N., Immler S., Smartt S., Bartel N. and Bietenholz M. F., 2008, ApJ, 688, 1210

Bauer F. E., Arévalo P., Walton D. J., Koss M. J., Puccetti S., Gandhi P., Stern D., Alexander D. M., Baloković M., Boggs S. E., Brandt W. N., Brightman M., Christensen F. E., Comastri A., Craig W. W., Del Moro A., Hailey C. J., Harrison F. A., Hickox R., Luo B., Markwardt C. B., Marinucci A., Matt G., Rigby J. R., Rivers E., Saez C., Treister E., Urry C. M. and Zhang W. W., 2015, ApJ, 812, 116

Bearden J. A. and Burr A. F., 1967, Rev. Mod. Phys., 39, 125

Beckmann, V. and Shrader, C., 2012, in Active Galactic Nuclei, 1° edition, ed. Wiley-VCH

Bianchi S., Matt G. and Iwasawa K., 2001, MNRAS, 322, 669

Bianchi S., Balestra I., Matt G., Guainazzi M. and Perola G. C., 2003, A&A, 402, 141

Bianchi S., Matt G., Nicastro F., Porquet D. and Dubau J., 2005, MNRAS, 357, 599

Bianchi S., La Franca F., Matt G., Guainazzi M., Jimenez Bailón E., Longinotti A. L., Nicastro F. and Pentericci L., 2008, MNRAS, 389, L52

Bianchi S., Piconcelli E., Chiaberge M., Bailón E. J., Matt G. and Fiore F., 2009, ApJ, 695, 781

Bianchi S., Maiolino R., Risaliti G., 2012, Adv. Astron, 2012, id. 782030

Bland-Hawthorn J., Gallimore J. F., Tacconi L. J., Brinks E., Baum S. A., Antonucci R. R. J. and Cecil G. N., 1997, Ap&SS, 248, 9

Bostroem K. A., Valenti S., Sand D. J., Andrews J. E., Van Dyk S. D., Galbany L., Pooley D., Amaro R. C., Smith N., Yang S., Anupama G. C., Arcavi I., Baron E., Brown P. J., Burke J., Cartier R., Hiramatsu D., Dastidar R., Derkacy J. M., Dong Y., Egami E., Ertel S., Filippenko A. V., Fox O. D., Haislip J., Hosseinzadeh G., Howell D. A., Gangopadhyay A., Jha S. W., Kouprianov V., Kumar B., Lundquist M., Milisavljevic D., McCully C., Milne P., Misra K., Reichart D. E., Sahu D. K., Sai H., Singh A., Smith P. S., Vinko J., Wang X., Wang Y., Wheeler J. C., Williams G. G., Wyatt S., Zhang J. and Zhang X., 2019, arXiv:1909.07304

Braito V., Ballo L., Reeves J. N., Risaliti G., Ptak A. and Turner T. J., 2013, MNRAS, 428, 2516

Brightman M., Silverman J. D., Mainieri V., Ueda Y., Schramm M., Matsuoka K., Nagao T., Steinhardt C., Kartaltepe J., Sanders D. B., Treister E., Shemmer O., Brandt W. N., Brusa M., Comastri A., Ho L. C., Lanzuisi G., Lusso E., Nandra K., Salvato M., Zamorani G., Akiyama M., Alexander D. M., Bongiorno A., Capak P., Civano F., Del Moro A., Doi A., Elvis M., Hasinger G., Laird E. S., Masters D., Mignoli M., Ohta K., Schawinski K. and Taniguchi Y., 2013, MNRAS, 433, 2485

Brinkman A. C., van Rooijen J. J., Bleeker J. A. M., Dijkstra J. H., Heise J., de Korte P. A. J., Mewe R. and Paerels F., 1987, Astrophysical Letters and Communications, 26, 73

Brinkmann W., Siebert J. and Boller T., 1994, A&A, 281, 355

Brown J. C. and McLean I. S., 1977, A&A, 57, 141

Buchner J., Georgakakis A., Nandra K., Brightman M., Menzel M. -L., Liu Z., Hsu L. -T., Salvato M., Rangel C., Aird J., Merloni A. and Ross N., 2015, ApJ, 802, 89

Buchner J. and Bauer F. E., 2017, MNRAS, 465, 4348

Burrows D. N., Hill J. E., Nousek J. A., Kennea J. A., Wells A., Osborne J. P., Abbey A. F., Beardmore A., Mukerjee K., Short A. D. T., Chincarini G., Campana S., Citterio O., Moretti A., Pagani C., Tagliaferri G., Giommi P., Capalbi M., Tamburelli F., Angelini L., Cusumano G., Bräuninger H. W., Burkert W. and Hartner G. D., 2005, Space Science Reviews, 120, 165

Burtscher L., Meisenheimer K., Tristram K. R. W., Jaffe W., Hönig S. F., Davies R. I., Kishimoto M., Pott J.-U., Röttgering H., Schartmann M., Weigelt G. and Wolf S., 2013, A&A 558, A149

Canizares C. R., Davis J. E., Dewey D., Flanagan K. A., Galton E. B., Huenemoerder D. P., Ishibashi K., Markert T. H., Marshall H. L., McGuirk M., Schattenburg M. L., Schulz N. S., Smith H. I. and Wise M., 2005, PASP, 117, 1144

Cash W., 1976, A&A, 52, 307

Celotti A., Fabian A. C. and Rees M. J., 1992, MNRAS, 255, 419

Celotti A., 2004, in *"Accretion Disks, Jets, and High Energy Phenomena in Astrophysics"*. Les Houches-École d'Été de Physique Theorique, 78, 491, eds. Beskin V., Henri G., Menard F., Pelletier G. and Dalibard J., Springer, Berlin, Heidelberg

Chartas G., Kochanek C. S., Dai X., Poindexter S. and Garmire G., 2009, ApJ, 693, 174

Christensen F. E., Jakobsen A. C., Brejnholt N. F., Madsen K. K., Hornstrup A., Westergaard N. J., Momberg J., Koglin J., Fabricant A. M., Stern M., Craig W. W., Pivovaroff M. J. and Windt D., 2011, Proc. SPIE, 8147, 81470U

Collin-Souffrin S., Czerny B., Dumont A. -M. and Życki P. T., 1996, A&A, 314, 393

Collinge M. J. and Brandt W. N., 2000, MNRAS, 317, L35

Comastri A., Vignali C., Cappi M., Matt G., Audano R., Awaki H. and Ueno S., 1998, MNRAS, 295, 443

Costa E., Soffitta P., Bellazzini R., Brez A., Lumb N. and Spandre G., 2001, Nature, 411, 662

Crummy J., Fabian A. C., Gallo L. and Ross R. R., 2006, MNRAS, 365, 1067

Curran S. J., Koribalski B. S. and Bains I., 2008, MNRAS, 389, 63

Czerny B., Nikołajuk M., Różańska A., Dumont A. -M., Loska Z. and Życki P. T., 2003, A&A, 412, 317

Czerny B., Różańska A., Dovčiak M., Karas V., Dumont A. -M., 2004, A&A, 420, 1

Dadina M., 2007, A&A, 461, 1209

De Cicco M., Marinucci A., Bianchi S., Piconcelli E., Violino G., Vignali C. and Nicastro F., 2015, MNRAS, 453, 2155

Dean A. J., Clark D. J., Stephen J. B., McBride V. A., Bassani L., Bazzano A., Bird A. J., Hill A. B., Shaw S. E. and Ubertini P., 2008, Science, 321, 1183

Deininger W. D., Kalinowski W., Masciarelli J., Gray S., Peterson C., Hibbard G., Wedmore J., Bladt J., Weisskopf M. C., Ramsey B., O'Dell S. L., Tennant A., Mize R., Foster M., Soffitta P., Muleri F., Santoli F., Del Monte E., Baldini L., Pinchera M., Latronico L., Trois A. and Osborne D., 2020, Proceedings of the 2020 IEEE Aerospace Conference

den Herder J. W., Brinkman A. C., Kahn S. M., Branduardi-Raymont G., Thomsen K., Aarts H., Audard M., Bixler J. V., den Boggende A. J., Cottam J., Decker T., Dubbeldam L., Erd C., Goulooze H., Güdel M., Guttridge P., Hailey C. J., Janabi K. A., Kaastra J. S., de Korte P. A. J., van Leeuwen B. J., Mauche C., McCalden A. J., Mewe R., Naber A., Paerels F. B., Peterson J. R., Rasmussen A. P., Rees K., Sakelliou I., Sako M., Spodek J., Stern M., Tamura T., Tandy J., de Vries C. P., Welch S. and Zehnder A., 2001, A&A, 365, L7

Dewangan G. C., Griffiths R. E., Dasgupta S. and Rao A. R., 2007, ApJ, 671, 1284

Done C., Gierliński M., Sobolewska M. and Schurch N., 2007, ASP Conference Series, 373, 121

Dovčiak M., Bianchi S., Guainazzi M., Karas V. and Matt G., 2004, MNRAS, 350, 745

Dovčiak M., Karas V. and Yaqoob T., 2004, ApJS, 153, 205

Elmouttie M., Haynes R. F., Jones K. L., Sadler E. M. and Ehle M., 1998, MNRAS, 297, 1202

Elvis M., Wilkes B. J., McDowell J. C., Green R. F., Bechtold J., Willner S. P., Oey M. S., Polomski E. and Cutri R., 1994, ApJS, 95, 1

Elvis M., Risaliti G., Nicastro F., Miller J. M., Fiore F. and Puccetti S., 2004, ApJ, 615, L25

Elvis M., 2012, Journal of Physics: Conference Series, 372, 012032

Esposito P., Israel G. L., Milisavljevic D., Mapelli M., Zampieri L., Sidoli L., Fabbiano, G. and Rodríguez Castillo G. A., 2015, MNRAS, 452, 1112

Evans R. D., 1955, *"The Atomic Nucleus"*, ed. McGraw-Hill

Fabian A. C., 1999, PNAS, 96, 4749

Fabian A. C., Iwasawa K.,Reynolds C. S. and Young A. J., 2000, PASP, 112, 1145

Fabian A. C. Miniutti G., 2005, arXiv: astro-ph/0507409

Fanaroff B. L. and Riley J. M., 1974, MNRAS, 167, 31P

Feltre A., Hatziminaoglou E., Fitz J. and Franceschini A., 2012, MNRAS, 426, 120

Freeman K. C., Karlsson B., Lynga G., Burrell J. F., van Woerden H., Goss W. M. and Mebold U., 1977, A&A, 55, 445

Fritz J., Franceschini A. and Hatziminaoglou E., 2006, MNRAS, 366, 767

Gallimore J. F., Baum S. A. and O'Dea C. P., 2004, ApJ, 613, 794

Gandhi P., Horst H., Smette A., Hönig S., Comastri A., Gilli R., Vignali C. and Duschl W., 2009, A&A, 502, 457

Gandhi P., Hönig S. F. and Kishimoto M., 2015, ApJ, 812, 113

García-Burillo S., Combes F., Ramos Almeida C., Usero A., Alonso-Herrero A., Hunt L. K., Rouan D., Aalto S., Querejeta M., Viti S., van der Werf P. P., Fuente A., Colina L., Martín-Pintado J., Henkel C., Martín S., Gratadour D., Neri R. and Tacconi L. J., 2019, arXiv:1909.00675

Gardner F. F. and Whiteoak J. B., 1982, MNRAS, 201, 13

Garmire G. P., Bautz M. W., Ford P. G., Nousek J. A., Ricker Jr. G. R., 2003, Proc. SPIE, 4851, 28

Gaskell C. M. and Klimek E. S., 2003, Astronomical & Astrophysical Transactions, 22, 661

Gehrels N., Chincarini G., Giommi P., Mason K. O., Nousek J. A., Wells A. A., White N. E., Barthelmy S. D., Burrows D. N., Cominsky L. R., Hurley K. C., Marshall F. E., Mészáros P., Roming P. W. A., Angelini L., Barbier L. M., Belloni T., Campana S., Caraveo P. A., Chester M. M., Citterio O., Cline T. L., Cropper M. S., Cummings J. R., Dean A. J., Feigelson E. D., Fenimore E. E., Frail D. A., Fruchter A. S., Garmire G. P., Gendreau K., Ghisellini G., Greiner J., Hill J. E., Hunsberger S. D., Krimm H. A., Kulkarni S. R., Kumar P., Lebrun F., Lloyd-Ronning N. M., Markwardt C. B., Mattson B. J., Mushotzky R. F., Norris J. P., Osborne J., Paczynski B., Palmer D. M., Park H. -S., Parsons A. M., Paul J., Rees M. J., Reynolds C. S., Rhoads J. E., Sasseen T. P., Schaefer B. E., Short A. T., Smale A. P., Smith I. A., Stella L., Tagliaferri G., Takahashi T., Tashiro M., Townsley L. K., Tueller J., Turner M. J. L., Vietri M., Voges W., Ward M. J., Willingale R., Zerbi F. M. and Zhang W. W., 2004, ApJ, 611, 1005

George I. M. and Fabian A. C., 1991, MNRAS, 249, 352.

Ghisellini G., Haardt F. and Matt G., 1994, MNRAS, 267, 743

Ghisellini G., Haardt F. and Matt G., 2004, A&A, 413, 535

Gierliński M. and Done C., 2004, MNRAS, 349, L7

Gilli R., Comastri A. and Hasinger G., 2007, A&A, 463, 79

Gladstone J. C., Roberts T. P. and Done C., 2009, MNRAS, 397, 1836

Gofford J., Reeves J. N., Tombesi F., Braito V., Turner J., Miller L. and Cappi M., 2013, MNRAS, 430, 60

Goosmann R. W. and Matt G., 2011, MNRAS, 415, 3119

Greenhill L. J., Gwinn C. R., Antonucci R. and Barvainis R., 1996, ApJ, 472, L21

Groves B., 2007, ASP Conference Series, 373, 511

Guainazzi M., Matt G., Antonelli L. A., Bassani L., Fabian A. C., Maiolino R., Marconi A., Fiore F., Iwasawa K. and Piro L., 1999, MNRAS, 310, 10

Guilbert P. W. and Rees M. J., 1988, MNRAS, 233, 475

Haardt F. and Maraschi L., 1991, ApJ, 380, L51

Haardt F., Maraschi L. and Ghisellini G., 1994, ApJ, 432, L95

Hailey C. J., An H., Blaedel K. L., Brejnholt N. F., Christensen F. E., Craig W. W., Decker T. A., Doll M., Gum J., Koglin J. E., Jensen C. P., Hale L., Mori K., Pivovaroff M. J., Sharpe M., Stern M., Tajiri G. and Zhang W. W., 2010, Proc. SPIE, 7732, 77320T

Hamann F. and Ferland G., 1999, ARA&A, 37, 487

Hamann F., Korista K. T., Ferland G. J., Warner C. and Baldwin J., ApJ, 564, 592

Harrison C., 2014, *"Observational constraints on the influence of active galactic nuclei on the evolution of galaxies"*. "Durham theses, Durham University. Available at Durham E-Theses Online: http://etheses.dur.ac.uk/10744"

Harrison F. A., Craig W. W., Christensen F. E., Hailey C. J., Zhang W. W., Boggs S. E., Stern D., Cook W. R., Forster K., Giommi P., Grefenstette B. W., Kim Y., Kitaguchi T., Koglin J. E., Madsen K. K., Mao P. H., Miyasaka H., Mori K., Perri M., Pivovaroff M. J., Puccetti S., Rana V. R., Westergaard N. J., Willis J., Zoglauer A., An H., Bachetti M., Barrière N. M., Bellm E. C., Bhalerao V., Brejnholt N. F., Fuerst F., Liebe C. C., Markwardt C. B., Nynka M., Vogel J. K., Walton D. J., Wik D. R., Alexander D. M., Cominsky L. R., Hornschemeier A. E., Hornstrup A., Kaspi V. M., Madejski G. M., Matt G., Molendi S., Smith D. M., Tomsick J. A., Ajello M., Ballantyne D. R., Baloković M., Barret D., Bauer F. E., Blandford R. D., Brandt W. N., Brenneman L. W., Chiang J., Chakrabarty D., Chenevez J., Comastri A., Dufour F., Elvis M., Fabian A. C., Farrah D., Fryer C. L., Gotthelf E. V., Grindlay J. E., Helfand D. J., Krivonos R., Meier D. L., Miller J. M., Natalucci L., Ogle P., Ofek E. O., Ptak A., Reynolds S. P., Rigby J. R., Tagliaferri G., Thorsett S. E., Treister E. and Urry C. M., 2013, ApJ, 770, 103

Heckman T. M., 1980, ApJ, 87, 152

Heitler W., 1954, *"The Quantum Theory of Radiation"*, Oxford University Press

Henri G. and Petrucci P. O., 1997, A&A, 326, 87

Hickox R. C. and Alexander D. M., 2018, ARA&A, 56, 625

Hönig S. F., Prieto M. A. and Beckert T., 2008, A&A, 485, 33

Hughes J. P., Long, K. S., Novick R., 1984, ApJ, 280, 255

Jaffe W., Meisenheimer K., Rottgering H. J. A., Leinert Ch., Richichi A., Chesneau O., Fraix-Burnet D., Glazenborg-Kluttig A., Granato G.-L., Graser U., Heijligers B., Kohler R., Malbet F., Miley G.K., Paresce F., Pel J.-W., Perrin G., Przygodda F., Schoeller M., Sol H., Waters L.B.F.M., Weigelt G., Woillez J. and de Zeeuw P.T., 2004, Nature, 429, 47

Jansen F., Lumb D., Altieri B., Clavel J., Ehle M., Erd C., Gabriel C., Guainazzi M., Gondoin P., Much R., Munoz R., Santos M., Schartel N., Texier D. and Vacanti G., 2001, A&A, 365, L1

Kaaret P., 2014, arXiv:1408.5899

Kaaret P., Feng H., and Roberts T. P., 2017, ARA&A, 55, 303

Kaastra J. S. and Bleeker J. A. M., 2016, A&A, 587, A151

Kalberla P. M. W., Burton W. B., Hartmann D., Arnal E. M., Bajaja E., Morras R. and Pöppel W. G. L., 2005, A&A, 440, 775

Kallman T. R., Palmeri P., Bautista M. A., Mendoza C. and Krolik J. H., 2004, ApJS, 155, 675

Kanbach G., Słowikowska A., Kellner S. and Steinle H., 2005, AIP Conference Procedings, 801, 306

Kaspi S., Smith P. S., Netzer H., Maoz D., Jannuzi B. T. and Giveon U., 2000, ApJ, 533, 631

Kaspi S., Maoz D., Netzer H., Peterson B. M., Vestergaard M. and Jannuzi B. T., 2005, ApJ, 629 61

Kato Y., Mineshige S. and Shibata K., 2004, ApJ, 605, 307

Kawamuro T., Izumi T. and Imanishi M., 2019, PASJ, 71, 68

Kelley R. L., Mitsuda K., Allen C. A., Arsenovic P., Audley M. D., Bialas T. G., Boyce K. R., Boyle R. F., Breon S. R., Brown G. V., Cottam J., Dipirro M. J., Fujimoto R., Furusho T., Gendreau K. C., Gochar G. G., Gonzalez O., Hirabayashi M., Holt S. S., Inoue H., Ishida M., Ishisaki Y., Jones C. S., Keski-Kuha R., Kilbourne C. A., McCammon D., Morita U., Moseley S. H., Mott B., Narasaki K., Ogawara Y., Ohashi T., Ota N., Panek J. S., Porter F. S., Serlemitsos A., Shirron P. J., Sneiderman G. A., Szymkowiak A. E., Takei Y., Tveekrem J. L., Volz S. M., Yamamoto M. and Yamasaki N. Y., 2007, PASJ, 59, S77

Kellermann K. I., Sramek R., Schmidt M., Shaffer D. B. and Green R., 1989, AJ, 98, 1195

Kellermann K. I., Sramek R. A., Schmidt M., Green R. F. and Shaffer D. B., 1994, AJ, 108, 1163

Kerr R. P., 1963, Physical Review Letters, 11, 237

Khachikian E. Ye. and Weedman D. W., 1974, ApJ, 192, 581

King A. R., Pringle J. E., West R. G. and Livio M., 2004, MNRAS, 348, 111

Kislat F., Clark B., Beilicke M. and Krawczynski H., 2015, Astroparticle Physics, 68, 45

Kitaguchi T., Black K., Enoto T., Fukazawa Y., Hayato A., Hill J. E., Iwakiri W. B., Jahoda K., Kaaret P., McCurdy R., Mizuno T., Nakano T. and Tamagawa T., 2018, Nuclear Instruments and Methods in Physics Research, A, 880, 188

Koyama K., Tsunemi H., Dotani T., Bautz M. W., Hayashida K., Tsuru T. G., Matsumoto H., Ogawara Y., Ricker G. R., Doty J., Kissel S. E., Foster R., Nakajima H., Yamaguchi H., Mori H., Sakano M., Hamaguchi K., Nishiuchi M., Miyata E., Torii K., Namiki M., Katsuda S., Matsuura D., Miyauchi T., Anabuki N., Tawa N., Ozaki M., Murakami H., Maeda Y., Ichikawa Y., Prigozhin G. Y., Boughan E. A., Lamarr B., Miller E. D., Burke B. E., Gregory J. A., Pillsbury A., Bamba A., Hiraga J. S., Senda A., Katayama H., Kitamoto S., Tsujimoto M., Kohmura T., Tsuboi Y. and Awaki H., 2007, PASJ, 59, S23

Krolik J. H., 1998, ApJ, 498, L13

Kuncic Z., Celotti A. and Rees M. J., 1997, MNRAS, 284, 717

Ilić D., Popović L. Č., Ciroi S., La Mura G. and Rafanelli P., 2010, Journal of Physics: Conference Series, 257, 012034

Imanishi M., Nakanishi K., Izumi T. and Wada K., 2018, ApJ, 853, L25

Impellizzeri C. M. V., Gallimore J. F., Baum S. A., Elitzur M., Davies R., Lutz D., Maiolino R., Marconi A., Nikutta R., O'Dea C. P. and Sani E., 2019, arXiv:1908.07981

Ishibashi W., Courvoisier T. J.-L., 2010, A&A, 512, A58

Iwasawa K., Miniutti G. and Fabian A. C., 2004, MNRAS, 355, 1073

Izumi T., Wada K., Fukushige R., Hamamura S. and Kohno K., 2018, ApJ, 867, 48

Lamastra A., Bianchi S., Matt G., Perola G. C., Barcons X. and Carrera F. J., 2009, A&A, 504, 73

Lanzi R., Comastri A. and Vignali C., Mem. SAIt, 72, 61

Li T., Zeng M., Feng H., Cang J., Li H., Zhang H., Zeng Z., Cheng J., Ma H. and Liu Y., 2017, Nuclear Instruments and Methods in Physics Research, A, 858, 62

Lightman A. P. and White T. R., 1988, ApJ, 335, 57

Liu J.-F., Bregman J. N. and Seitzer P., 2004, ApJ, 602, 249

Liu T., Tozzi P., Wang J.-X., Brandt W. N., Vignali C., Xue Y., Schneider D. P., Comastri A., Yang G., Bauer F. E., Paolillo M., Luo B., Gilli R., Wang Q. D., Giavalisco M., Ji Z., Alexander D. M., Mainieri V., Shemmer O., Koekemoer A. and Risaliti G., 2017, ApJS, 232, 8

Long K. S., Chanan G. A., Ku W. H. -M. and Novick R., 1979, ApJ, 232, L107

Long K. S., Chanan G. A. and Novick R., 1980, ApJ, 238, 710

López-Gonzaga N., Asmus D., Bauer F. E., Tristram K. R. W. Burtscher L., Marinucci A., Matt G. and Harrison F. A., 2017, A&A, 602, A78

Lynden-Bell D., 1969, Nature, 223, 690

Madhusudhan N., Rappaport S., Podsiadlowski Ph. and Nelson L., 2008, ApJ, 688, 1235

Madsen K. K., Alexander D., Bachetti M., Ballantyne D., Baloković M., Boggs S., Boorman P., Brandt N. W., Brenneman L., Christensen F., Civano F., Connors R., Descalle M., Elvis M., Fabian A., Ferreira D., Fornasini F., Fuerst F., García J., Gellert N., Grefenstette B., Grindlay J., Heida M., Hickox R., Miyasaka H., Hornschmeier A., Hornstrup A., Jaodand A., Kamraj N., Krawczynski H., Lansbury G., Lohfink A., Matt G., Middleton M., Miller J., Pottschmidt K., Ricci C., Stern D., Vogel J., Walton D., Wilms J., Wik D., Windt D. and Zhang W., 2019, Astro2020: Decadal Survey on Astronomy and Astrophysics, APC white papers, no. 166; Bulletin of the American Astronomical Society, Vol. 51, Issue 7, id. 166

Magdziarz P., Blaes O. M., Zdziarski A. A., Johnson W. N. and Smith D. A., 1998, MNRAS, 301, 179

Magdziarz P. and Zdziarski A. A., 1995, MNRAS, 273, 837

Maio U., Dott M., Petkova M., Perego A. and Volonteri M., 2003, ApJ, 767, 37

Maiolino R. and Risaliti G., 2007, ASP Conference Series, 373, 447

Malkan M. A., Gorjian V. and Tam R., 1998, ApJS, 117, 25

Malzac J. and Celotti A., 2002, MNRAS, 335, 23

Marconi A., Moorwood A. F. M., Origlia L. and Oliva E., 1994, The Messenger, 78, 20

Marconi A., Risaliti G., Gilli R. Hunt L. K., Maiolino R. and Salvati M., 2004, MNRAS, 351, 169

Marconi, A., Axon, D. J., Maiolino, R., et al. 2009, ApJ, 698, L103

Markowitz A. G., Krumpe M. and Nikutta R., 2014, MNRAS, 439, 1403

Marin F., 2018, A&A, 615, 171

Marinucci A., Risaliti G., Wang J., Bianchi S., Elvis M., Matt G., Nardini E. and Braito V., 2013, MNRAS, 429, 2581

Marinucci A., Miniutti G., Bianchi S., Matt G. and Risaliti G., 2013, MNRAS, 436, 2500

Marinucci A., Bianchi S., Matt G., Alexander D. M., Baloković M., Bauer F. E., Brandt W. N., Gandhi P., Guainazzi M., Harrison F. A., Iwasawa K., Koss M., Madsen K. K., Nicastro F., Puccetti S., Ricci C., Stern D. and Walton D. J., 2016, MNRAS, 456, L94

Mason K. O., Breeveld A., Much R., Carter M., Cordova F. A., Cropper M. S., Fordham J., Huckle H., Ho C., Kawakami H., Kennea J., Kennedy T., Mittaz J., Pandel D., Priedhorsky W. C., Sasseen T., Shirey R., Smith P. and Vreux J. -M., 2001, A&A, 365, L36

Massaro F., Bianchi S., Matt G., D'Onofrio E. and Nicastro F., 2006, A&A, 455, 153

Matt G., Perola G. C. and Piro L., 1991, A&A, 247, 25

Matt G., Fiore F., Perola G. C., Piro L., Fink H. H., Grandi P., Matsuoka M., Oliva E. and Salvati M., 1996, MNRAS, 281, L69

Matt G., Fabian A. C., Reynolds C. S., 1997, MNRAS, 289, 175

Matt G., Guainazzi M., Maiolino R., Molendi S., Perola G. C., Antonelli L. A., Bassani L., Brandt W. N., Fabian A. C., Fiore F., Iwasawa K., Malaguti G., Marconi A. and Poutanen J., 1999, A&A, 341, L39

Matt G., Fabian A. C., Guainazzi M., Iwasawa K., Bassani L. and Malaguti G., 2000, MNRAS, 318, 173

Matt G., 2001, AIP Conference Proceedings, 599, 209

Matt G., Guainazzi M., Perola G. C., Fiore F., Nicastro F., Cappi M. and Piro L., 2001, A&A, 377, L31

Matt G., 2002a, Roy. Soc. London Philosoph. Trans. Ser. A, 360, 2045

Matt G., 2002b, MNRAS, 337, 147

Matt G., Guainazzi M. and Maiolino R., 2003, MNRAS, 342, 422

Matt G., Bianchi S., D'Ammando F. and Martocchia A., 2004, A&A, 421, 473

Matzeu G. A., Reeves J. N., Braito V., Nardini E., McLaughlin D. E., Lobban A. P., Tombesi F. and Costa M. T., 2017, MNRAS, 472, L15

McHardy I. M., 2013, MNRAS, 430, L49

Merloni A., Malzac J., Fabian A. C. and Ross R. R., 2006, MNRAS, 370, 1699

Mészáros P., Novick R., Szentgyorgyi A., Chanan G. A. and Weisskopf M. C., 1988, ApJ, 324, 1056

Middleton M. J., Sutton A. D., Roberts T. P., Jackson F. E. and Done C., 2012, MNRAS, 420, 2969

Middleton M. J., Miller-Jones J. C. A., Markoff S., Fender R., Henze M., Hurley-Walker N., Scaife A. M. M., Roberts T. P., Walton D. J., Carpenter J., Macquart J.-P., Bower G. C., Gurwell M., Pietsch W., Haberl F., Harris J., Daniel M., Miah J., Done C., Morgan J. S., Dickinson H., Charles P., Burwitz V., Della Valle M., Freyberg M., Greiner J., Hernanz M., Hartmann D. H., Hatzidimitriou D., Riffeser A., Sala G., Seitz S., Reig P., Rau A., Orio M., Titterington D. and Grainge K., 2013, Nature, 493, 187

Miller J. S. and Antonucci R. R. J., 1983, ApJ, 271, L7

Miller J. S., Goodrich R. W. and Mathews W. G., 1991, ApJ, 378, 47

Miniutti G., Ponti G., Dadina M., Cappi M., Malaguti G., Fabian A. C. and Gandhi P., 2006, MNRAS, 373, L1

Mitsuda K., Bautz M., Inoue H., Kelley R. L., Koyama K., Kunieda H., Makishima K., Ogawara Y., Petre R., Takahashi T., Tsunemi H., White N. E., Anabuki N., Angelini L., Arnaud K., Awaki H., Bamba A., Boyce K., Brown G. V., Chan K.-W., Cottam J., Dotani T., Doty J., Ebisawa K., Ezoe Y., Fabian A. C., Figueroa E., Fujimoto R., Fukazawa Y., Furusho T., Furuzawa A., Gendreau K., Griffiths R. E., Haba Y., Hamaguchi K., Harrus I., Hasinger G., Hatsukade I., Hayashida K., Henry P. J., Hiraga

J. S., Holt S. S., Hornschemeier A., Hughes J. P., Hwang U., Ishida M., Ishisaki Y., Isobe N., Itoh M., Iyomoto N., Kahn S. M., Kamae T., Katagiri H., Kataoka J., Katayama H., Kawai N., Kilbourne C., Kinugasa K., Kissel S., Kitamoto S., Kohama M., Kohmura T., Kokubun M., Kotani T., Kotoku J., Kubota A., Madejski G. M., Maeda Y., Makino F., Markowitz A., Matsumoto C., Matsumoto H., Matsuoka M., Matsushita K., McCammon D., Mihara T., Misaki K., Miyata E., Mizuno T., Mori K., Mori H., Morii M., Moseley H., Mukai K., Murakami H., Murakami T., Mushotzky R., Nagase F., Namiki M., Negoro H., Nakazawa K., Nousek J. A., Okajima T., Ogasaka Y., Ohashi T., Oshima T., Ota N., Ozaki M., Ozawa H., Parmar A. N., Pence W. D., Porter F. S., Reeves J. N., Ricker G. R., Sakurai I., Sanders W. T., Senda A., Serlemitsos P., Shibata R., Soong Y., Smith R., Suzuki M., Szymkowiak A. E., Takahashi H., Tamagawa T., Tamura K., Tamura T., Tanaka Y., Tashiro M., Tawara Y., Terada Y., Terashima Y., Tomida H., Torii K., Tsuboi Y., Tsujimoto M., Tsuru T. G., Turner M. J. L., Ueda Y., Ueno S., Ueno M., Uno S., Urata Y., Watanabe S., Yamamoto N., Yamaoka K., Yamasaki N. Y., Yamashita K., Yamauchi M., Yamauchi S., Yaqoob T., Yonetoku D. and Yoshida A., 2007, PASJ, 59, S1

Molendi S., Bianchi S. and Matt G., 2003, MNRAS, 343, L1

Moorwood A. F. M. and Glass I. S., 1984, A&A, 135, 281

Moriakov N., Samudre A., Negro M., Gieseke F., Otten S. and Hendriks L., 2020, arXiv:2005.08126

Morrison R. and McCammon D., 1983, ApJ, 270, 119

Murphy K. D. and Yaqoob T., 2009, MNRAS, 397, 1549

Murray S. S., Chappell J. H., Kenter A. T., Kobayashi K., Kraft R. P., Meehan G. R., Zombeck M. V., Fraser G. W., Pearson J. F., Lees J. E., Brunton A. N., Pearce S. E., Barbera M., Collura A. and Serio S., 1997, Proc. SPIE, 3114, 11

Mushotzky R. F., Done C. and Pounds K. A., 1993, ARA&A, 31, 717

Nagao T., Marconi A. and Maiolino R., 2006, A&A, 447, 157

Nandra K. and Pounds K. A., 1994, MNRAS, 268, 405

Nandra K., 2001, Advances in Space Research, 28, 295

Nandra K., Barret D., Barcons X., Fabian A., den Herder J.-W. et al., 2013, arXiv:1306.2307

Narayan R. and Yi I., 1994, ApJ, 428, L13

Narayan R., 2005, New J. Phys., 7 199

Nayakshin S. and Melia F., 1997, ApJ, 490, L13

Nenkova M., Sirocky M. M., Nikutta R., Ivezić Z. and Elitzur M., 2008a, ApJ, 685, 147

Nenkova M., Sirocky M. M., Nikutta R., Ivezić Z. and Elitzur M., 2008b, ApJ, 685, 160

Netzer H., 1990, *"Active Galactic Nuclei"*. Courvoisier T. J.-L. & Mayor M. eds. (Berlin: Springer-Verlag)

Netzer H., 2006, in *"Physics of Active Galactic Nuclei at All Scales"*, Alloin D., Johnson R., Lira P. eds. (Berlin: Springer)

Netzer H., 2015, ARA&A, 53, 365

Novick R., Weisskopf M. C., Berthelsdorf R., Linke R. and Wolff R. S., 1972, ApJ, 174, L1

O'Dell S. L., Attinà P., Baldini L., Barbanera M., Baumgartner W. H., Bellazzini R., Bladt J., Bongiorno S. D., Brez A., Cavazzuti E., Citraro S., Costa E., Deininger W. D., Del Monte E., Dietz K. L., Di Lalla N., Donnarumma I., Elsner R. F., Fabiani S., Ferrazzoli R., Guy L., Kalinowski W., Kaspi V. M., Kelley A. R., Kolodziejczak J. J., Latronico L., Lefevre C., Lucchesi L., Manfreda A., Marshall H. L., Masciarelli J., Matt G., Minuti M., Muleri F., Nasimi H., Nuti A., Orsini L., Osborne D., Perri M., Pesce-Rollins M., Peterson C., Pinchera M., Puccetti S., Ramsey B. D., Ratheesh A., Romani R. W., Santoli F., Sciortino A., Sgrò C., Smith B. T., Spandre G., Soffitta P., Tennant A. F., Tobia A., Trois A., Wedmore J., Weisskopf M. C., Xie F., Zanetti F., Alexander C., Allen D. Z., Amici F., Antoniak S., Bonino R., Borotto F., Breeding S., Brienza D., Bygott H. K., Caporale C., Cardelli C., Ceccanti M., Centrone M., Di Persio G., Evangelista Y., Ferrie M., Footdale J., Forsyth B., Foster M., Gunji S., Gurnee E., Hibbard G., Johnson S., Kelly E., Kilaru K., La Monaca F., Le Roy S., Loffredo P., Magazzu G., Marengo M., Marrocchesi A., Massaro F., McCracken J., McEachen M., Mereu P., Mitchell S., Mitsuishi I., Morbidini A., Mosti F., Negro M., Oppedisano C., Pacheco R., Paggi A., Pavelitz S. D., Pentz C., Piazzola R., Porter B., Profeti A., Ranganathan J., Rankin J., Root N., Rubini A., Ruswick S., Sanchez J., Scalise E., Schindhelm S., Speegle C. O., Tamagawa T., Tardiola M., Walden A. L., Weddendorf B. and Welch D., 2019, Proc. SPIE, 11118, 111180

Osterbrock D. E., 1981, ApJ, 249, 462

Osterbrock D. E. and Pogge R. W., 1985, ApJ, 297, 166

Osterbrock D. E. and Ferland G. J., 2006, *"Astrophysics of gaseous nebulae and active galactic nuclei"*, Sausalito, CA: University Science Books

Page K. L., Schartel N., Turner M. J. L. and O'Brien P. T., 2004, MNRAS, 352, 523

Padovani P., 1997, in *"Very High Energy Phenomena in the Universe"*, ed. Y. Giraud-Héraud & J. Trân Thanh Vân (Paris: Ed. Frontières), 7

Page K. L., Reeves J. N., O'Brien P. T. and Turner M. J. L., 2005, MNRAS, 364, 195

Palmeri P., Mendoza C., Kallman T. R., Bautista M. A. and Meléndez M., 2003, A&A, 410, 359

Patruno A. and Zampieri L., 2010, MNRAS, 403, L69

Perola G. C., Matt G., Cappi M., Fiore F., Guainazzi M., Maraschi L., Petrucci P.-O. and Piro L., 2002, A&A, 389, 802

Peterson B. M., 1997, *"An introduction to active galactic nuclei"*, Cambridge University Press

Petrucci P. -O., Gronkiewicz D., Rozanska A., Belmont R., Bianchi S., Czerny B., Matt G., Malzac J., Middei R., De Rosa A., Ursini F. and Cappi M., 2020, A&A, 634, 85

Piconcelli E., Jiménez-Bailón E., Guainazzi M., Schartel N., Rodríguez-Pascual P. M., Santos-Lleó M., 2005, A&A, 432, 15

Piconcelli E., Bianchi S., Vignali C., Jiménez-Bailón E. and Fiore F., 2011, A&A, 534, A126

Pier E. A. and Krolik J. H., 1992, ApJ, 401, 99

Pier E. A. and Krolik J. H., 1993, ApJ, 418, 673

Pier E. A., Antonucci R., Hurt T., Kriss G. and Krolik J., 1994, ApJ, 428, 124

Pinto C., Alston W., Parker M. L., Fabian A. C., Gallo L. C., Buisson D. J. K., Walton D. J., Kara E., Jiang J., Lohfink A. and Reynolds C. S., 2018, MNRAS, 476,1021

Pintore F., Zampieri L., Stella L., Wolter A., Mereghetti S. and Israel G. L., 2017, ApJ, 836, 113

Pintore F., Belfiore A., Novara G., Salvaterra R., Marelli M., De Luca A., Rigoselli M., Israel G., Rodriguez G., Mereghetti S., Wolter A., Walton D. J., Fuerst F., Ambrosi E., Zampieri L., Tiengo A. and Salvaggio C., 2018, MNRAS, 477, L90

Pogge R. W., 1988, ApJ, 328, 519

Pogge R. W., 2000, New Astronomy Reviews, 44, 381

Poutanen J. and Fabian A. C., 1999, MNRAS, 306, L31

Puccetti S., Fiore F., Risaliti G., Capalbi M., Elvis M. and Nicastro F., 2007, MNRAS, 377, 607

Qiu Y., Soria R., Wang S., Wiktorowicz G., Liu, J., Bai Y., Bogomazov A., Di Stefano R., Walton D. J. and Xu X., 2019, ApJ, 877, 57

Raban D., Jaffe W., Röttgering H., Meisenheimer K. and Tristram, K. R. W., 2009, MNRAS, 394, 1325

Ramos Almeida C. and Ricci C., 2017, Nature Astronomy, 1, 679

Ramsey B. D., Bongiorno S. D., Kolodziejczak J. J., Kilaru K., Alexander C., Baumgartner W. H., Elsner R. F., McCracken J., Mitsuishi I., Pavelitz S. D., Ranganathan J., Sanchez J., Speegle C. O., Weddendorf B. and O'Dell S. L., 2019, Proc. SPIE, 11119, 1111903

Reeves J. N. and Turner M. J. L., 2000, MNRAS, 316, 234

Reynolds C. S., 1997, MNRAS, 286, 513

Reynolds C. S., 1998, arXiv:astro-ph/9810018

Reynolds C. S. and Nowak M. A., 2003, Physics Reports, 377, 389

Risaliti G., 2002, A&A, 386, 379

Risaliti G., Elvis M. and Nicastro F., 2002, ApJ, 571, 234

Risaliti G. and Elvis M., 2004, in *"Supermassive Black Holes in the Distant Universe"*, 308, 187

Risaliti G., Elvis M., Fabbiano G., Baldi A. and Zezas A., 2005, ApJ, 623, L93

Rivers E., Markowitz A. and Rothschild R., 2011, ApJS, 193, 3

Rivers E., Risaliti G., Walton D. J., Harrison F., Arévalo P., Bauer F. E., Boggs S. E., Brenneman L. W., Brightman M., Christensen F. E., Craig W. W., Furst F., Hailey C. J., Hickox R. C., Marinucci A., Reeves J., Stern D. and Zhang W. W., 2015a, ApJ, 804, 107

Rivers E., Baloković M., Arévalo P., Bauer F. E., Boggs S. E., Brandt W. N., Brightman M., Christensen F. E., Craig W. W., Gandhi P., Hailey C. J., Harrison F., Koss M., Ricci C., Stern D., Walton D. J. and Zhang W. W., 2015b, ApJ, 815, 55

Roberts T. P., Levan A. J. and Goad M. R., 2008, MNRAS, 387, 73

Roming P. W. A., Kennedy T. E., Mason K. O., Nousek J. A., Ahr L., Bingham R. E., Broos P. S., Carter M. J., Hancock B. K., Huckle H. E., Hunsberger S. D., Kawakami H., Killough R., Koch T. S., McLelland M. K., Smith K., Smith P. J., Soto J. C., Boyd P. T., Breeveld A. A., Holland S. T., Ivanushkina M., Pryzby M. S., Still M. D. and Stock, J., 2005, Space Science Reviews, 120, 95

Ross R. R. and Fabian A. C., 2005, MNRAS, 358, 211

Rowan-Robinson M., 1977, ApJ, 213, 635

Rybicki G. B. and Lightman A.P., 1979, *"Radiative processes in astrophysics"*, Wiley New York

Sambruna R. M., Brandt W. N., Chartas G., Netzer H., Kaspi S., Garmire G. P., Nousek J. A. and Weaver K. A., 2001a, ApJ, 546, L9

Sambruna R. M., Netzer H., Kaspi S., Brandt W. N., Chartas G., Garmire G. P., Nousek J. A. and Weaver K. A., 2001b, ApJ, 546, L13

Sandage A. and Brucato R., 1979, AJ, 84, 472

Sanders D. B., Phinney E. S., Neugebauer G., Soifer B. T. and Matthews K., 1989, ApJ, 347, 29

Schwarzschild K., 1916, Königlich Preuβische Akademie der Wissenschaften (Berlin). Sitzungsberichte (1916), 189

Serlemitsos P. J., Soong Y., Chan K.-W.; Okajima T., Lehan J. P., Maeda Y., Itoh K., Mori H., Iizuka R., Itoh A., Inoue H., Okada S., Yokoyama Y., Itoh Y., Ebara M., Nakamura, R., Suzuki K., Ishida M., Hayakawa A., Inoue C., Okuma S., Kubota R., Suzuki M., Osawa T., Yamashita K., Kunieda H., Tawara Y., Ogasaka Y., Furuzawa A., Tamura K., Shibata R., Haba Y., Naitou M. and Misaki K., 2007, PASJ, 59, S9

Shakura N. I. and Sunyaev R. A., 1973, A&A, 24, 337

Shapiro S. L., Lightman A. P. and Eardley D. M., 1976, ApJ, 204, 187

Shemmer O., Brandt W. N., Netzer H., Maiolino R. and Kaspi S., 2008, ApJ, 682, 81

Silver E. H., Weisskopf M. C., Kestenbaum H. L., Long K. S., Novick R. and Wolff R. S., 1978, ApJ, 225, 221

Smith D. A. and Wilson A. S., 2001, ApJ, 557, 180

Smith D. A. and Wilson A. S., 2003, ApJ, 591, 138

Sobolewska M. A. and Done C., 2006, MNRAS, 374, 150

Soria R., Cropper M., Pakull M., Mushotzky R. and Wu K., 2005, MNRAS, 356, 12

Stalevski M., Fritz J., Baes M., Nakos T. and Popović, L. Č., 2012, MNRAS 420, 2756

Stern B. E., Poutanen J., Svensson R., Sikora M. and Begelman M. C., 1995, ApJ, 449, L13

Stobbart A. -M., Roberts T. P. and Wilms J., 2006, MNRAS, 368, 397

Strohmayer T. E. and Kallman T. R., 2013, ApJ, 773, 103

Strüder L., Briel U., Dennerl K., Hartmann R., Kendziorra E., Meidinger N., Pfeffermann E., Reppin C., Aschenbach B., Bornemann W., Bräuninger H., Burkert W., Elender M., Freyberg M., Haberl F., Hartner G., Heuschmann F., Hippmann H., Kastelic E., Kemmer S., Kettenring G., Kink W., Krause N., Müller S., Oppitz A., Pietsch W., Popp M., Predehl P., Read A., Stephan K. H., Stötter D., Trümper J., Holl P., Kemmer J., Soltau H., Stötter R., Weber U., Weichert U., von Zanthier C., Carathanassis D., Lutz G., Richter R. H., Solc P., Böttcher H., Kuster M., Staubert R., Abbey A., Holland A., Turner M., Balasini M., Bignami G. F., La Palombara N., Villa G., Buttler W., Gianini F., Lainé R., Lumb D. and Dhez P., 2001, A&A, 365, L18

Takahashi T., Abe K., Endo M., Endo Y., Ezoe Y., Fukazawa Y., Hamaya M., Hirakuri S., Hong S., Horii M., Inoue H., Isobe N., Itoh T., Iyomoto N., Kamae T., Kasama D., Kataoka J., Kato H., Kawaharada M., Kawano N., Kawashima K., Kawasoe S., Kishishita T., Kitaguchi T., Kobayashi Y., Kokubun M., Kotoku J., Kouda M., Kubota A., Kuroda Y., Madejski G., Makishima K., Masukawa K., Matsumoto Y., Mitani T., Miyawaki R., Mizuno T., Mori K., Mori M., Murashima M., Murakami T., Nakazawa K., Niko H., Nomachi M., Okada Y., Ohno M., Oonuki K., Ota N., Ozawa H., Sato G., Shinoda S., Sugiho M., Suzuki M., Taguchi K., Takahashi H., Takahashi I., Takeda S., Tamura K., Tamura T., Tanaka T., Tanihata C., Tashiro M., Terada Y., Tominaga S., Uchiyama Y., Watanabe S., Yamaoka K., Yanagida T. and Yonetoku D., 2007, PASJ, 59, S35

Tarter C. B., Tucker W. H. and Salpeter E. E., 1969, ApJ, 156, 943

Telesco C. M. and Decher R., 1988, ApJ, 334, 573

Terashima Y. and Wilson A. S., 2003, ApJ, 583, 145

Thorne K. S., 1974, ApJ, 191, 507

Titarchuk L. and Lyubarskij Y., 1995, ApJ, 450, 876

Tombesi F., Cappi M., Reeves J. N., Palumbo G. G. C., Yaqoob T., Braito V. and Dadina M., 2010, A&A, 521, A57

Tombesi F., Cappi M., Reeves J. N., Nemmen R. S., Braito V., Gaspari M. and Reynolds C. S., 2013, MNRAS, 430, 1102

Tortosa A., Bianchi S., Marinucci A., Matt G. and Petrucci P. O., 2018, A&A, 614, 37

Tremaine S., Gebhardt K., Bender R., Bower G., Dressler A., Faber S. M., Filippenko A. V., Green R., Grillmair C., Ho, L. C., Kormendy J., Lauer T. R., Magorrian J., Pinkney J. and Richstone D., 2002, ApJ, 574, 740

Treister E. and Urry C. M., 2012, Advances in Astronomy, 2012, 516193

Tristram K. R. W., Burtscher L., Jaffe W., Meisenheimer K., Hönig S. F., Kishimoto M., Schartmann M. and Weigelt G., 2014, A&A, 563, A82

Tully R. B., 1988, *"Nearby Galaxies Catalog"*, Cambridge and New York, Cambridge Univ. Press

Turner M. J. L., Abbey A., Arnaud M., Balasini M., Barbera M., Belsole E., Bennie P. J., Bernard J. P., Bignami G. F., Boer M., Briel U., Butler I., Cara C., Chabaud C., Cole R., Collura A., Conte M., Cros A., Denby M., Dhez P., Di Coco G., Dowson J., Ferrando P., Ghizzardi S., Gianotti F., Goodall C. V., Gretton L., Griffiths R. G., Hainaut O., Hochedez J. F., Holland A. D., Jourdain E., Kendziorra E., Lagostina A., Laine R., La Palombara N., Lortholary M., Lumb D., Marty P., Molendi S., Pigot C., Poindron E., Pounds K. A., Reeves J. N., Reppin C., Rothenflug R., Salvetat P., Sauvageot J. L., Schmitt D., Sembay S., Short A. D. T., Spragg J., Stephen J., Strüder L., Tiengo A., Trifoglio M., Trümper J., Vercellone S., Vigroux L., Villa G., Ward M. J., Whitehead S. and Zonca E., 2001, A&A, 365, L27

Turner T. J. and Pounds K. A., 1988, MNRAS, 232, 463

Turner T. J., George I. M., Nandra K. and Mushotzky R. F., 1997, ApJS, 113, 23

Turner T. J., Reeves J. N., Braito V., Yaqoob T., Kraemer S. B. and Severgnini P., 2020, MNRAS, 498, 1983

Ueda Y., Akiyama M., Hasinger G., Miyaji T. and Watson M. G., 2014, ApJ, 786, 104

Urry C. M. and Padovani P., 1995, PASP, 107, 803

van Speybroeck L. P., Jerius D., Edgar R. J., Gaetz T. J., Zhao P. and Reid P. B., 1997, Proc. SPIE, 3113, 89

Vaughan S., Edelson R., Warwick R. S. and Uttley P., 2003, MNRAS, 345, 1271

Verner D. A., Ferland G. J., Korista K. T. and Yakovlev D. G., 1996, ApJ, 465, 487

Vinokurov A., Fabrika S. and Atapin K., 2018, ApJ, 854, 176

Volonteri M., Sikora M., Lasota J.-P. and Merloni A., 2013, ApJ, 775, 94

Wada K., Schartmann M. and Meijerink R., 2016, ApJL, 828, L19

Walton D. J., Harrison F. A., Bachetti M., Barret D., Boggs S. E., Christensen F. E., Craig W. W., Fuerst F., Grefenstette B. W., Hailey C. J., Madsen K. K., Middleton M. J., Rana V., Roberts T. P., Stern D., Sutton A. D., Webb N. and Zhang W., 2015, ApJ, 799, 122

Walton D. J., Tomsick J. A., Madsen K. K., Grinberg V., Barret D., Boggs S. E., Christensen F. E., Clavel M., Craig W. W., Fabian A. C., Fuerst F., Hailey C. J., Harrison F. A., Miller J. M., Parker M. L., Rahoui F., Stern D., Tao L., Wilms J. and Zhang W., 2016, ApJ, 826, 87

Walton D. J., Fürst F., Heida M., Harrison F. A., Barret D., Stern D., Bachetti M., Brightman M., Fabian A. C. and Middleton M. J., 2018, ApJ, 856, 128

Wang Y., Ferland G. J., Hu C., Wang J.-M. and Du P., 2012, MNRAS, 424, 2255

Ward M., Elvis M., Fabbiano G., Carleton N. P., Willner S. P. and Lawrence A., 1987, ApJ, 315, 74

Weisskopf M. C., Silver E. H., Kestenbaum H. L., Long K. S. and Novick R., 1978, ApJ, 220, L117

Weisskopf M. C., Tananbaum H. D., Van Speybroeck L. P. and O'Dell S. L., 2000, Proc. SPIE, 4012, 2

Weisskopf M. C., Ramsey B., O'Dell S. L., Tennant A., Elsner R., Soffitta P., Bellazzini R., Costa E., Kolodziejczak J., Kaspi V., Muleri F., Marshall H., Matt G. and Romani R., 2016a, Proc. SPIE 9905, Space Telescopes and Instrumentation 2016: Ultraviolet to Gamma Ray, 990517

Weisskopf M. C., Ramsey B., O'Dell S. L., Tennant A., Elsner R., Soffitta P., Bellazzini R., Costa E., Kolodziejczak J., Kaspi V., Muleri F., Marshall H., Matt G. and Romani R., 2016b, Results in Physics, 6, 1179

Wik D. R., Hornstrup A., Molendi S., Madejski G., Harrison F. A., Zoglauer A., Grefenstette B. W., Gastaldello F., Madsen K. K., Westergaard N. J., Ferreira D. D. M., Kitaguchi T., Pedersen K., Boggs S. E., Christensen F. E., Craig W. W., Hailey C. J., Stern D. and Zhang W. W., 2014, ApJ, 792, 48

Wilms J., Allen A. and McCray R., 2000, ApJ, 542, 914

Wilson A. S., Shopbell P. L., Simpson C., Storchi-Bergmann T., Barbosa F. K. B., Ward M. J., 2000, AJ, 120, 1325

Winkler H., 1992, MNRAS, 257, 677

Wittkowski M., Kervella P., Arsenault R., Paresce F., Beckert T. and Weigelt G., 2004, A&A, 418, L39

Wolff R. S., Angel J. R. P., Novick R. and Vanden Bout P., 1969, ApJ, 160, L21

Woo J.-H. and Urry C. M., 2002, ApJ, 579, 530

Yang G., Brandt W. N., Luo B., Xue Y. Q., Bauer F. E., Sun M. Y., Kim S., Schulze S., Zheng X. C., Paolillo M., Shemmer O., Liu T., Schneider D. P., Vignali C., Vito F. and Wang J. -X., 2016, ApJ, 831, 145

Yaqoob T., 2012, MNRAS, 423, 3360

Yaqoob T., Tatum M. M., Scholtes A., Gottlieb A. and Turner T. J., 2015, MNRAS, 454, 973

Zaino A., Bianchi S., Marinucci A., Matt G., Bauer F. E., Brandt W. N., Gandhi P., Guainazzi M., Iwasawa K., Puccetti S., Ricci C. and Walton D. J., 2020, MNRAS, 492, 3872

Zhang, S.-N., 2013, Frontiers of Physics, 8, 630

Zhang S.-N., Santangelo A., Feroci M., Xu Y., Lu F. et al., 2019, Science China Physics, Mechanics & Astronomy, 62, 29502

Zhao X., Marchesi S., Ajello M., Marcotulli L., Cusumano G., La Parola V. and Vignali C., 2019, ApJ, 870, 60

Zheng W., Kriss G. A., Wang J. X., Brotherton M., Oegerle W. R., Blair W. P., Davidsen A. F., Green R. F., Hutchings J. B. and Kaiser M. E., 2001, ApJ, 562, 152

Zschaechner L. K., Walter F., Bolatto A., Farina E. P., Kruijssen J. M. D., Leroy A., Meier D. S., Ott J. and Veilleux S., 2016, ApJ, 832, 142